

Fullerene Molecules as Building Blocks for Nanomaterials

A Dissertation

Presented to
the faculty of the School of Engineering and Applied Science
University of Virginia

in partial fulfillment
of the requirements for the degree

Doctor of Philosophy

by

Ehsan Monazami

May

2017

APPROVAL SHEET

The dissertation
is submitted in partial fulfillment of the requirements
for the degree of
Doctor of Philosophy



AUTHOR

The dissertation has been read and approved by the examining committee:

Petra Reinke

Advisor

Leonid V. Zhigilei

Haydn N. Wadley

Stephen J. McDonnell

Ian Harrison

William C. Johnson

Accepted for the School of Engineering and Applied Science:



Craig H. Benson, Dean, School of Engineering and Applied Science

May
2017

Abstract

The study of surfaces at the atomic and molecular scale has improved our understanding of many physical and chemical processes such as oxidation, carburization and has contributed critically to advancements in nanoscience and technology. In this thesis, fullerene (C_{60}) molecules were used as a critical building block for modification, enhancement, and material synthesis for two distinct material systems.

The first material system included in this study was graphene on copper substrates. Intercalation of C_{60} molecules at the interface between copper and graphene by annealing was used to modulate the electronic properties of graphene. The intercalation was confirmed by comparing topography and electronic properties of the graphene- C_{60} -copper system with graphene wrinkles and moiré patterns. The intercalated molecules create a local strain/deformation on the graphene layer, and its magnitude is controlled by the intermolecular distance. This study provided a pathway to control local strain, which can influence the electronic properties of graphene.

Tungsten carbide thin films were the second material system studied in this thesis. These thin films were synthesized by co-deposition of C_{60} molecules as carbon precursor and tungsten atoms on a MgO(100) substrate, which was held at 1073 K. Prior to thin film synthesis, a number of experiments designed to study the interaction between C_{60} and W during annealing at moderate temperature revealed remarkable results about this interaction. Scanning tunneling microscopy/spectroscopy (STM/STS) measurements demonstrated that the surface band gap of the C_{60} molecular layer can be adjusted from a wide band gap (>2.5 eV) to a metallic molecular surface during annealing from 300 to 800 K. Density functional theory calculations were used to

develop possible reaction pathways and explain the experimentally observed electronic structure modulation. Tungsten carbide shows a unique combination of properties and exhibits catalytic activity, which makes this material an attractive substitute for expensive noble metal catalysts. However, the use of tungsten carbide thin films is limited by surface oxidation, which is accompanied by a depression of activity. In this thesis, non-stoichiometric carbon rich tungsten carbide thin films were prepared to study the possibility of carburization of the oxidized regions via embedded free carbon in the thin films. Thin films with different C:W ratios were synthesized to illustrate the effect of free carbon on surface morphology and susceptibility to oxidation. Several oxidation/ carburization cycles were performed on carbon rich tungsten carbide films and the results indicated that the annealing of these films results in diffusion of free carbon from lower layers and re-carburization of the oxidized area. Therefore, this is a viable method to significantly increase the lifetime of the catalytic surface of tungsten carbide. For this study, synchrotron-based ambient pressure x-ray photoelectron spectroscopy (AP-XPS) and STM/STS measurements, were performed.

Acknowledgments

There are so many people that without their help this thesis could not happen. First and foremost, I would like to thank my Ph.D. advisor Prof. Petra Reinke for her limitless support, and standing by me through the entire process. For her help and guidance over the last 5 years and all the extra work. I have always enjoyed our conversations and my experience of working in her group has been incredible.

I would also like to acknowledge Prof. William C. Johnson, who took the chance on me and gave me the opportunity to come to University of Virginia at first place. I am extremely grateful for his support. And my dissertation committee members for their valuable time.

I would like to thank my colleagues at UVA for providing a friendly environment. Prof. Leonid Zhigilei for all his help and support. Jatin Amatya and Robert Golden for our study group. My lab mates were a huge resource for scientific discussions. Gopal and Brandon who taught me how to work with STM, and Cameron and Darwin for being amazing friends. Balaji, Bernard, Nathaniel, Will, and all my good friends at UVA, who made the last 5 years of my life an incredible experience. Richard White for teaching me about SEM and TEM, and great work experience in the first year of my PhD. Kim, for the emotional support and helping me with all the small and big problems.

I also acknowledge the contributions of all the other collaborators that made this thesis possible. First, Brandon for his exploratory experiments for nanospheres and tungsten carbides. Petra Rudolf and Luca Bignardi for providing graphene samples. Prof Joachim Schnadt and his group for hosting me and Petra during our visit in MaxLab. Prof James Rondinelli for our DFT discussions and answering my questions.

I would also like to thank my girlfriend Marybeth for her patience and great support. My brother Reza and my amazing family for always believing in me through my whole life and encouraging me to pursue my dreams. My parents, none of this would be possible without their continuous support.

Finally, I gratefully acknowledge support of this work by the National Science Foundation through Award DMR-1005809 by the Division of Materials Research (Ceramics) and Award CHE-1507986 by the Division of Chemistry (Macromolecular/ Supramolecular and Nanochemistry).

Publication List

- (1) Monazami, E.; Bignardi, L.; Rudolf, P.; Reinke, P. Strain Lattice Imprinting in Graphene by C₆₀ Intercalation at the Graphene/Cu Interface. *Nano Lett.* **2015**.
- (2) Monazami, E.; McClimon, J. B.; Rondinelli, J.; Reinke, P. Electronic Structure and Band Gap of Fullerenes on Tungsten Surfaces: Transition from a Semiconductor to a Metal Triggered by Annealing. *ACS Appl. Mater. Interfaces* **2016**.
- (3) Monazami, E.; McClimon, J. B.; Reinke, P. Oxidation and Carburization of Carbon Rich Tungsten Carbide. *in preparation*.
- (4) Monazami, E.; Ramalingam, G.; Reinke, P. Optimization of STS maps for Investigation of Surface Reactions at Nanoscales. *in preparation*.
- (5) McClimon, J. B.; Monazami, E.; Reinke, P. Interaction of C₆₀ with Tungsten: Modulation of Morphology and Electronic Structure on the Molecular Length Scale. *J. Phys. Chem. C* **2014**, *118* (42), 24479–24489.
- (6) Volders, C.; Monazami, E.; Ramalingam, G.; Reinke, P. Alternative Route to Silicene Synthesis via Surface Reconstruction on H-MoSi₂ Crystallites. *Nano Lett.* **2017**, *17* (1), 299–307.
- (7) Ramalingam, G.; Monazami, E.; Reinke, P. Evolution of Atomic and Electronic Structure of Ni(001) Surface during Oxidation. *in preparation*.
- (8) Krauss, S. T.; Remcho, T. P.; Monazami, E.; Thompson, B. L.; Reinke, P.; Begley, M. R.; Landers, J. P. Inkjet Printing on Transparency Films for Reagent Storage with Polyester-Toner Microdevices. *Anal Methods* **2016**.

Table of Contents

Abstract	1
Acknowledgments	iii
Publication List	v
Table of Contents	vi
List of Figures	viii
List of Tables	xvi
1. Introduction	2
1.1. References	6
2. Materials	9
2.1. Graphene	9
2.1.1. Electronic and Band Structure of Graphene	12
2.1.2. Graphene Synthesis	14
2.2. Fullerene (C ₆₀)	15
2.2.1. Crystalline C ₆₀	17
2.2. Tungsten Carbide	19
2.3. Reference	21
3. Experimental and Theoretical Techniques	24
3.1. Ultrahigh Vacuum System (UHV)	24
3.2. Scanning Tunneling Microscopy (STM)	25
3.3. Scanning Tunneling Spectroscopy (STS)	28
3.4. X-Ray Photoemission Spectroscopy (XPS)	30
3.4.1. Ambient Pressure X-Ray Photoemission Spectroscopy (AP-XPS)	33
3.5. Atomistic Simulations	35
3.6. References	42
4. Substrate Materials	45
4.1. C ₆₀ on Copper	45
4.2. Magnesium Oxide (MgO)	47
4.3. Tungsten (W)	49
4.4. References	51
5. STS Maps for Investigation of Surface Reaction at Nanoscale	53
5.1. Introduction	53

5.2. Methods	55
5.3. References	62
6. Strain Lattice Imprinting in Graphene by C ₆₀ Intercalation	65
6.1. Abstract	65
6.2. Introduction	66
6.3. Methods	67
6.4. Results and Discussion	70
6.5. References	88
7. Electronic Structure and Band Gap of Fullerenes on Tungsten Surfaces	93
7.1. Abstract	93
7.2. Introduction	94
7.3. Methods	95
7.4. Results and Discussions	97
7.4. Conclusions	111
7.5. References	114
7.7. Supporting Information	117
7.7.1. DFT Calculation of C ₆₀ / W	117
7.7.2. C ₆₀ / W-bulk Energies and Adsorption Geometries	117
7.7.3. Electronic structure of C ₆₀ / W(110) and C ₆₀ / W(100)	121
7.7.4. C ₆₀ Molecule Motion at Room Temperature	124
7.7.5. Single Molecules on the W-surface	126
7.7.6. References	128
8. Oxidation and Carburization of Carbon Rich Tungsten Carbide Thin Films	130
8.1. Introduction	130
8.2. Methods	131
8.3. Results	132
8.3.1 STM/STS Results and Discussions	132
8.3.2. AP-XPS Results Discussions	144
8.5. Conclusions	162
8.6. Future work	163
8.7. References	164

List of Figures

Figure 2.1: Schematic representation of carbon allotropes. Taken from Reference [1].	9
Figure 2.2: MD simulation results for a graphene flake at 180 K. a) Snapshot of top-view of the graphene and distribution of valley and hills after 23 ps. b) Histogram distribution of the height profile extracted from (a). c) Snapshot of top-view of the graphene and distribution of valley and hills after 30 ps. d) Histogram distribution of the height profile extracted from (c).	11
Figure 2.3: STM image of graphene on copper, several of the hexagons in the honeycomb structure of graphene are indicated in this image. a_1 and a_2 are the primitive lattice vectors of graphene. b) Corresponding 2D-fast Fourier transform of the STM image in (a), the FFT peaks are colored by light blue, the 1 st BZ of graphene is indicated by the red hexagons. b_1 and b_2 are the basis vectors of the reciprocal lattice.	12
Figure 2.4: The electronic structure of graphene. a) The graphene energy dispersion. b) Graphene band structure and local density of states projected on s (red), p_x and p_y (black), and p_z (blue) orbitals, calculated by DFT method.	14
Figure 2.5: Schematics of two different orientation of C_{60} molecule. a) When the h-h bond is on top b) When the h-p bond is on top	16
Figure 2.6: a) STM image of 5 ML of C_{60} molecules on graphite. The marked region shows the conventional unit cell for this structure. b) 3D Illustration of solid C_{60} .	17
Figure 2.7: STM images of the C_{60} monolayer on $WO_2/W(110)$ substrate at different temperatures. (a) $12 \times 14 \text{ nm}^2$ image acquired at $T = 78 \text{ K}$. (b) $19 \times 16 \text{ nm}^2$ images of the same C_{60} film acquired at $T = 315 \text{ K}$. Taken from Reference [34].	18
Figure 2.8: STM images of C_{60} molecules on tungsten surface a) Before anneal. b) After anneal at $T=623 \text{ K}$. The molecules in after anneal surface, exhibit two or three surface grooves which are correlated to the molecular orbital in C_{60} (image size $8 \times 15 \text{ nm}^2$).	19
Figure 2.9: a) W-C phase diagram. Taken from reference [36]. Structural representation of b) hexagonal WC and c) hexagonal W_2C .	20
Figure 3.1: View of the UHV system equipped with STM. (1), (2), (3), and (4) Deposition sources slots. Various types of deposition source can be used in these sections (E-beam source for tungsten and thermal evaporation source for C_{60} molecules), and these materials can be evaporated directly in UHV system. 5) Transferring manipulator. 6) Sample stage. This stage is capable of direct current and e-beam heating up to $T=1473 \text{ K}$. 7) Preparation chamber, this section is used for deposition, heating, and oxidation processes. 8) STM chamber. 9) Eddy current damping system to minimize the vibration during the STM/STS measurements.	24
Figure 3.2: Principle of operation of the constant current mode in STM. a) illustration of STM operation to obtain atomic resolution. b) STM operation in larger scale. The dashed line indicates	

the measured height (z) during the scan over a step edge (1), and a contamination spot (2) with different LDOS in comparison to the rest of surface. Taken from references [3,4]. 26

Figure 3.3: Visualization of tunneling between the tip and a metallic sample with one dimensional potential energy diagrams. a) Sample and the tip at equilibrium and separated by small barrier thickness. b) A positive bias voltage is applied to the tip and therefore, electrons tunnel from tip to empty states of the sample. c) A negative bias voltage is applied to the tip and therefore, electrons tunnel from filled states of the sample to the tip..... 27

Figure 3.4: Scanning tunneling spectroscopy. a) Visualization of spectra acquired for every five points in a 512x512 pixel image. b) Two example for I-V curve measured by STS. These two spectra are measured on nanospheres surface and they are explained in chapter 7. c) The normalized dI/dV curves calculated from curves shown in (b). 30

Figure 3.5: Schematic representation of the three-step model of the photo emission process. 1. Excitation of the electron to a Bloch final state inside the crystal, 2. Transport of the electron to the surface, 3. Escape of the electron into the vacuum. (schematic is taken from ref [16]). 32

Figure 3.6: (a) Drawing of the APXPS instrument at the MAX IV Laboratory. (b) Cross-section drawing of the high-pressure cell. At the front in green is the door which is opened for sample transfer. The nozzle is depicted in a golden color and points at the sample (in brown). Sample heating is achieved through the wall behind the sample by electron bombardment. The double set-up of bellows makes it possible to move the sample during measurement. (c) High- pressure cell using approach to the analyzer. (d) Sample loading into the high-pressure cell docked to the analyzer. (Pictures and the caption are taken from reference [16]) 34

Figure 3.7: The flow chart of calculation process in DFT. 39

Figure 3.8: $C_{59}W$ hetrofullerene configuration. a) Initial configuration. b) relaxed configuration from two different view angles. c) Schlegel diagram of $C_{59}W$ 40

Figure 3.9: $C_{60}W$ hetrofullerene configurations. a) Schlegel diagram of hetrofullerene, the possible initial configurations which were considered in the simulations are labeled from 1-5. b) The total energy calculated for each configuration in (a). The minimum total energy was chosen as zero eV energy. c) Initial structure of configuration #1 d) relaxed structure of configuration #1 from two different view angles. 41

Figure 4.1: Charge transfer and variation of local density of states (LDOS) on Cu/C_{60} surface. a) Topography image, which includes a region with coverage of <1 ML C_{60} (bottom), Cu surface (center), and a C_{60} multilayer island (top). b) Differential conductance map for $V=0.40$ V. The blue color indicates lower LDOS state and the red color regions show surface area with higher LDOS. c) The linescan profile extracted from topography image (green dashed line in (a)). It shows the height variation across the sample and is aligned with the three regions marked in the topography image. d) Averaged spectra extracted from three regions marked in (a) and (b). The spectra are averaged over 20 individual spectra. The green arrows indicate the LUMO energies, and the dashed line at zero volt is the Fermi energy. 46

Figure 4.2: photo taken from MgO on STM sample plate. A drop of silver glue was place on top of MgO and Ta strips to ensure the electrons pathway.....	47
Figure 4.3: AFM images of MgO substrate; a) After 30 sec etching and then 1273 K annealing for 10 hr. several of Ca spires are indicated by black circles. b): After additional etching and annealing step.	48
Figure 4.4: a) 50 nm W thin film on MgO(100) deposited at 1073 K. b) Extracted profile from the linescan in (a). c) Schematic representation of W(110) and MgO (100).....	50
Figure 5.1: Spectrum acquired from graphene on copper sample. a) I-V curve. c) The normalization parameter (I/V), where a divergence is observed at $V \sim 0$. c) After differentiation of I-V curve and before normalization. d) Normalized dI/dV for several ϵ values.....	57
Figure 5.2: Spectrum acquired from multilayer of C_{60} molecules on graphene. The dashed line indicates the Fermi energy. a) Determination of the band gap by method I. the cutoff value is determined by noise level in instrument. b) Determination of the band gap by method II.	59
Figure 5.3: Snapshot of the GUI designed for grid STS analysis. The red square in top-left contour map highlights the area that the spectra were extracted.	61
Figure 6.1: STM topography images of (a) graphene surface, (b) Cu(001), (c) moiré pattern with superimposed graphene honeycomb lattice, and (d) linescan along the diagonal of (c). The bottom row shows the corresponding Fourier transforms illustrating the hexagonal and square lattices, respectively. The green circles mark graphene spots, and the white circle marks the moiré pattern with its longer wavelength. (E) Geometric simulation of the moiré pattern for a 5° rotation between graphene and Cu lattice, which corresponds to the one seen in (c). The scalebar is 1 nm in all images.	70
Figure 6.2: (a) 3D image of a four-way wrinkle in graphene, (b) 3D image of a single wrinkle with atomically resolved graphene lattice as shown in (c), which was recorded at the center of the wrinkle. (d) Top view of the same wrinkle shown in (b) (scale bar = 5 nm); the green (blue) line corresponds to the line along which the ST spectra from (f) were collected and averaged. (e) STS map for $V_{bias} = 9.2$ mV within the boxed area marked in (d). The wrinkle coincides with the higher dI/dV values in agreement with the spectra displayed in (f), which includes the spectra averaged along the lines indicated in (d). (f) Displays representative dI/dV spectra; the error bars indicate the variation in the spectra used for averaging: parallel to the wrinkle axis on top of the wrinkle (green), and at the edge of the wrinkle (blue). The spectrum for graphene on Cu prior to C_{60} intercalation (black) is included for comparison. The spectrum for the C_{60} layer prior to intercalation is identical to spectra shown in the literature ^{47,48} and has a bandgap of 2.3 eV.	72
Figure 6.3: (a) 3D STM topography image of an amorphous intercalated structure; the graphene lattice on top of the C_{60} molecules is resolved (Note: this image was Fourier filtered to reduce noise, image b is an unfiltered 2D image of same sample). (b) Image section of the amorphous intercalated structure and two linescans are shown below the image. Molecules along line A (line B) are separated by 3 nm (4.1 nm) and dA (dB) in the linescans indicates the apparent height for the respective intermolecular distances. (c) Summary of average feature heights observed for graphene on Cu, moiré patterns such as the one shown in Figure 6.1, and the wide range of feature	

heights observed in the intercalated structures. Isolated fullerene molecules will have an apparent height of about 0.8 nm when buried beneath graphene. 75

Figure 6.4: (a) shows a crystalline intercalated structure and a linescan for V_{bias} of 0.085 and 0.3 V of the same image section. The corresponding data points are included in (b) for 3.4 nm intermolecular distance. (b) Reduced apparent height calculated by division of the apparent height (AH) of the molecules by the maximum AH measured for the largest molecule distance at the same V_{bias} . The reduced apparent height for three bias voltages is included and they collapse onto a single step-like function. The drawing on the right-hand side visualizes the high and low strain states. 78

Figure 6.5: (a) and (b) Representative STM topography images of the crystalline intercalated structure (scale bar = 40 nm). The image region marked with a purple rectangle is enlarged and shown in a different color scheme to enhance image contrast. The white circle marks a vacancy in the intercalant lattice. (c) ST spectra from the crystalline intercalated structure (Gr on C_{60} , red) and graphene on Cu for comparison (Gr on copper, black). The arrows mark the position of the spectral minimum, most likely the Dirac energy, and the two minima associated with the superlattice peaks from the crystalline intercalated structure. The spectroscopy map at $V_{\text{bias}} = 37$ mV reflects the spatial distribution of the crystalline intercalation region with a higher dI/dV (red and yellow color) and includes a section with graphene on Cu at the bottom of the frame with a significantly lower dI/dV value (blue) in agreement with the spectra. The ST spectra were obtained by averaging over the area indicated by the black and white squares in the map (see text for details). 80

Figure 7.1: Summary of surfaces observed before and after deposition of C_{60} on W/MgO(100) surfaces (a–c) and after annealing of this surface to 673 K (d1) and 773 K (d2). The MgO sample is etched with phosphoric acid and subjected to a two-step annealing process to minimize the development of Ca spires and achieve a smooth surface. The MgO terraces are prior to W deposition on average 100×100 nm in size and provide smooth terraces for W thin-film growth (a and b). The fullerene layer (c) is composed of regions with high crystallinity (FCC packing) and amorphous regions (right-hand side of the image). After annealing (d1 and d2), the surface morphology of the fullerenes is maintained, and the majority of the molecules exhibit two or three surface grooves, which are consistent with a 6–6 orientation (d1 and d2; image size 8×15 nm). 99

Figure 7.2: Topography and LDOS including a band-gap map for C_{60} layers on W. (a) Topography image, which has regions with single-layer and multilayer C_{60} , as evidenced by the line scan at the center of the image. The regions marked in the image correspond to the following structure: region 1 is a C_{60} single layer, region 2 is a C_{60} double layer, and region 3 is an amorphous structure. (b) Band-gap map. The gap was determined from the I–V curves measured at 102×102 image points. (d) Representative examples of the normalized dI/dV spectra. The error bar is the standard error of the data set. (c) Distributions of band gaps measured in part b in the form of a histogram. All data points from the band-gap map are included. Labels 1–3 in the histogram correspond to the respective regions in the image. 102

Figure 7.3: Modulation of LDOS as a function of the annealing temperature (300–700 K) and topography image in addition to the normalized dI/dV map for 673 K. (a) LDOS derived from

spectroscopy maps for C_{60} layers annealed at the temperatures indicated in the figure. The width of the error bar is related to the spatial homogeneity of the respective map and the experimental error in STS acquisition. Data points with clearly unphysical excursions and noise were removed (%10). The topography image in part b and the corresponding normalized dI/dV map in part c illustrate the spatial variation of the LDOS for an annealing step at 673 K. Examples for normalized dI/dV spectra for the two regions marked in the map are included (blue and green). For comparison, the normalized conductance spectrum for the W surface is included (yellow). 104

Figure 7.4: Distribution of the molecule diameter as a function of the annealing temperature. Each distribution includes several hundred molecules, and the annealing steps are identical with those discussed in Figures 2 and 3. The distribution is normalized to the unit height. 106

Figure 7.5: Band-gap evolution as a function of the temperature from 300 to 773 K. (a) Band-gap distributions measured after annealing at the temperature indicated in the graph. The distributions measured for several images are included for each temperature. The distribution at 300 K is relatively broad, which can directly be traced back to the differences between the single, double, and amorphous C_{60} layers shown in Figure 7.1. The distributions are normalized to the unit height, and for 700 K, only metallic spectral signatures are observed. (b) Corresponding band-gap maps. Each representative strip is 20×80 nm in size and part of a larger map. (c) Change of the average gap and normalized conductance at E_F as a function of the temperature. 107

Figure 7.6: Results from DFT calculations for the most stable $C_{59}W$ and $C_{58}W_2$ substitutional configurations and $C_{60}W$ with W atoms added on the outside of the C_{60} cage. The calculations for C_{60} are included for comparison. For the open-shell structures $C_{60}W$, $C_{59}W$, and $C_{58}W_2$, spin-resolved DOS is depicted, with the spin-up DOS marked in blue and the spin-down DOS marked in red. The DOS is summed over the entire molecule. Gray and light-blue atoms indicate C and W, respectively. 110

Figure 7.7: Possible adsorption orientation for C_{60} molecule on substrate. The red circles show the closest carbon atoms to the W-substrate. (a) h-h bridge between two hexagons (b) p-h bridge between a hexagon and pentagon (c) pentagon face (d) hexagon face. 118

Figure 7.8: Considered adsorption geometries of C_{60} molecule on a) W(110) and b) W(100) surface. To display the adsorption position clearly, only the lowest 14 carbon atoms from C_{60} are shown. (a) Four possible adsorption site for W(110) where the h-h bond in C_{60} positioned at (#1) at the center (#2) at the center with 45o rotation (#3) on bridge (#4) on top .(b) Four possible adsorption site for W(100) where the h-h bond in C_{60} positioned at (#1) the center (#2) at the center with 45o rotation (#3) on bridge (#4) on top..... 119

Figure 7.9: Total energy analysis of the systems to find the most stable adsorption configuration/distance for C_{60} molecules on (a) W(100) and (b) W(110) (c) the relaxed configuration for W(110) (d)the relaxed configuration for W(100) 121

Figure 7.10: Configuration and calculated projected density of states (DOS) on C_{60} molecules after adsorption on W(110) surface. (a) the most stable molecule orientation with the h-h bond facing the W-surface - top and side view. The LUMO for C_{60} on W(110) is depicted in the same orientation and reflects the molecule as it is seen on the vacuum-facing side imaged with STM, in

which blue and red represent the positive and negative wave function. (b) DOS of the C_{60} molecule, and C_{60} positioned on W(110) in the orientation shown in (a) before smoothing and after smoothing with a Gaussian with a full half width of 0.1 eV. The dashed vertical line indicates E_F 123

Figure 7.11: Configuration and calculated projected density of states (DOS) on C_{60} molecules after adsorption on W(100) surface. (a) the most stable molecule adsorption geometry with the h-h bond facing the W-surface - top and side view. The LUMO for C_{60} on W(100) is depicted in the same orientation and reflects the molecule as it is seen on the vacuum-facing side imaged with STM, in which blue and red represent the positive and negative wave function. (b) DOS of the C_{60} molecule, and C_{60} positioned on W(100) in the orientation shown in (a) before smoothing and after smoothing with a Gaussian with a full half width of 0.1 eV. The dashed vertical line indicates E_F 124

Figure 7.12: Sequential image frames of C_{60} molecules on a W-surface ($V_{bias}=1$ V $I=0.02$ nA). Frame 1 (a) and 2 (b) were recorded sequentially. The molecule positions are marked in the images, and their position is isolated in frames shown in the bottom row. 126

Figure 7.13: Topography image, and differential conductance maps for V_{bias} of -1.76 V (filled states) and +1.2 V (empty states) recorded simultaneous. The C_{60} coverage is ~ 0.3 ML and the molecules are marked with circles to allow for ease of comparison between image and maps. Every 5th image pixel corresponds to a ST spectrum. The enhanced LDOS at the molecule positions is readily apparent against the constant LDOS from the metal substrate. The section in the center bottom of the image, which corresponds to a substrate inhomogeneity yields a higher LDOS from the metal substrate and the fullerene molecules are hard to locate in this region for the empty states, but easily seen in the filled state map. 127

Figure 8.1: STM images from two different 50/50 tungsten carbide thin films (S1 and S2). a,b) 2000×2000 nm² images. The long ordering observed at this magnification is imprinted by the morphology of the underlying MgO substrate. c,d) Higher magnification images which show the fine structure on the surface. The image size of (c) is (145×145 nm²) and the image size of (d) is (500×500 nm²). 134

Figure 8.2: High resolution STM images (8×8 nm²) of S1 and S2 samples. 135

Figure 8.3: STM images from 40/60 tungsten carbide thin films (S3). a,b) 2000×2000 nm² images. The majority of the islands have smooth edges. c,d) Higher magnification where the nanoclusters inside each island are visible. The image size of (c) is (500×500 nm²) and the image size of (d) is (80×100 nm²). e,f) High resolution STM images (15×15 nm²). 136

Figure 8.4: a) STM image from 40/60 tungsten carbide thin films (7×12 nm²). The majority of the surface area is covered by graphene and graphite. b) the corresponding derivative STM image to highlight the striped regions from (a). c) The corresponding FFT illustrating the hexagonal lattices. d) The schematic representation of carbon atoms in graphite/graphene. The dashed lines show bottom layer and the solid lines show the top layer of carbon sheet. 138

Figure 8.5: STM images of the 25/75 tungsten carbide thin films (S5). a,b) image size (2000×2000 nm²). The large mobile islands are attributed to segregated graphite patches. c,d) Atomic resolution STM images, where the surface is covered by graphite. 139

Figure 8.6: STM images from 40/60 tungsten carbide thin films. (a), (c), and (e) are STM images recorded before oxidation and (b), (d), and (f) are the STM images after oxidation. a,b) 2000×2000 nm² image size. c,d) 100×100 nm² STM images. e,f) High resolution STM images (15×15 nm²).
..... 140

Figure 8.7: a) STM image of oxidized surface b) The corresponding bandgap of (a). c) Spectra extracted from regions marked by black rectangles in (a,b). The average spectrum is shown by the red line and all other spectra are displayed by blue dots. The inset is the average curve at (-2.5 – 0 V) energy range. d) The band gap histogram. 142

Figure 8.8: a) STM image of the S5 sample after UHV annealing of the oxidized surface. b) The corresponding bandgap of (a). c) Spectra extracted from region marked by black square in (a). All spectra are shown by blue dots and the average spectrum is shown by the red line. d) The band gap profile extracted from region marked by the white square in (c). 143

Figure 8.9: The processes performed on S9 sample. The blue/red circles indicate the time and temperature of recorded spectra during carburization/oxidation, respectively. 145

Figure 8.10: a) The intensity contour plot of the W4f spectra ($h\nu = 400$ eV) for S9 sample during oxidation/carburization cycles. b) Selected spectra from (a). The processing parameters (time and temperature) for this experiment are shown in Figure 8.9. 146

Figure 8.11: Several examples of the results for the fitting process. The spectra at the left-hand side were recorded during carburization and the ones at the right-hand side were measured during oxidation. The raw data (dark green), carbide doublet (dark blue), W5p peak from carbide doublet (light blue), oxide doublet (red), and the Shirley background is shown with the dashed line. The residuals are shown at the bottom of each graph where the blue color indicates an overestimation of the fitted results and the red color indicates an underestimation of the fitted curve. The numbers at the top of each graph specifies the number of XPS spectra recorded during experiment (same as Figure 8.8). 149

Figure 8.12: The calculated residuals after fitting. The star symbols indicate the spectra shown in Figure 8.11. 150

Figure 8.13: Evolution of the carbide component in XPS spectra for the S9 sample. These results obtained after fitting with two doublets. The red bars indicate the carbide concentration in presence of oxygen in the cell (oxidation). The blue bars show the carbide concentration during annealing in UHV (carburization). The green circles show the temperature when the spectra were measured. 152

Figure 8.14: a) Two examples of XPS data from S10 sample. This sample has the same carbon to tungsten ratio as S9 (W:C 25:75). b) The difference between the spectra shown in (a). 154

Figure 8.15: several examples of the results after the fitting process. The left-hand side spectra are recorded during carburization and the right-hand side spectra during oxidation. The raw data (dark green), carbide doublet (dark blue), W5p peak from carbide doublet (light blue), oxide doublet (red), and the Shirley background is shown with the dashed line. The residual for each curve is included at the bottom of each graph where the blue color indicates an overestimation of the fitted

results and the red color indicates an underestimation of the fitted curve. The numbers at the top of each graph specifies the number of XPS spectra recorded during experiment (same as Figure 8.10).	156
Figure 8.16: The red bars indicate the ratio of the carbide area in presence of oxygen in the cell. The blue bars show the ratio of carbide area during annealing at UHV (carburization). The oxidation/carburization cycles are labeled from I-VII.	157
Figure 8.17: Several examples of linear fitting of the data shown in Figure 8.14. the vertical axis for all the graphs is area $(WC+WC_{1-x})$ /total area.	158
Figure 8.18: Calculated carburization rate from XPS data. Recall that the concentration of free carbon in both S9 and S10 is 50%, S8 is 20%, and S7 is 0%.	159
Figure 8.19: The red bars indicate the ratio of the several oxide components in presence of oxygen in the cell. The blue bars show the ratio of those oxide components during annealing at UHV (carburization). The oxidation/carburization cycles are labeled from I-VII.	161

List of Tables

Table 3.1: Binding energy for several oxidation states in tungsten.	32
Table 8.1: Summary of carbide thin films used in this work. The term C_{ext} represent the ratio of extra carbon in thin films if tungsten and carbon form WC. This assumption is confirmed by XPS analysis.....	132
Table 8.2: XPS parameters used in fitting. (*) The BE energy of W^{6+} in WO_3 during the oxidation was always slightly lower and positioned at 35.55 ± 0.2 eV.....	148
Table 8.3: Intensity of individual peaks in carbide and oxide doublet for two distinct spectra .	153
Table 8.4: list of parameters used in fitting procedure.	154

Chapter 1

Introduction

1. Introduction

Over the past decades, the progress in vacuum technology and instrumentation has made it possible to study materials surface in atomic scale,¹ which improves our understanding about the physical and chemical processes/reactions and contributes critically to the advancement in nanoscience and technology. Discovery of graphene by Novoselov and Geim is an example of the importance and the power of atomic scale investigation, which was recognized by the 2010 Nobel prize in physics.²

The main characterization technique in this thesis is the scanning tunneling microscopy (STM). STM is a powerful tool, which provides information about topographic and electronic properties of the surface. In addition, in-situ STM studies are used to investigate the chemical reactions and the changes in the surface morphology. In this thesis, modulation of electronic properties, surface diffusion, interaction between molecular layer with its substrate, nucleation of the oxide and carbide nuclei, and the surface reactions at atomic scale are studied. For this purpose, scanning tunneling spectroscopy (STS) as a complementary technique was used, and to process the acquired spectroscopy data, a software was developed. The details of this software are described in chapter 5.

This work provides new information about the mechanism of reaction/interaction for several materials at atomic scales, which can eventually use in development and optimization of complex materials with a wide range of applications. In this work, fullerene (C_{60}) molecules are used to manipulate and create nanostructured materials for (i) imprinting deformation/strain lattice on graphene (ii) use metal fullerene interaction to tailor surface electronic structure (iii) synthesis of tungsten carbide. This molecule was discovered by Kroto et al in 1985.³ In this work, the closed shell structure of C_{60} molecules were synthesized by laser vaporization of a graphite sample. Since

then, this molecule has become a common building block for synthesis of nanomaterials, molecular electronics, and devices.⁴⁻⁹

This thesis organized as follows: At first, the intercalation of this molecule at the interface of graphene/Cu as a method for graphene modulation is discussed,¹⁰ then the effect of the annealing on the electronic properties of C₆₀ molecules on tungsten surface is investigated,^{11,12} and at last, this molecule was used in synthesis of carbon rich tungsten carbide.

CVD graphene on copper is the first material system studied in this thesis, which is discussed in chapter 6. Unlike conventional bulk semiconductors such as silicon and germanium, modulating the electronic properties of graphene is not a trivial task. Due to the dimensional limitations of graphene, doping with a foreign atom is a difficult task and often causes defects and the loss of coveted electronic properties.¹³⁻¹⁵ The linear E(K) dispersion relation near the K-points in graphene band structure, which is called the Dirac cone, drives the properties of graphene, therefore its preservation is critical in the manipulation process. Graphene's two-dimensional structure allows modulation of its properties through the interaction with the substrate or by surface adsorbates. This approach is highly versatile and can modify graphene's properties while simultaneously conserving the Dirac cone. The main challenge for this approach is to find suitable pathways to achieve the desired graphene modulation. In this work, an approach for the intercalation of C₆₀ molecules at the graphene-Cu interface, which leads to the formation of amorphous and crystalline strain lattice, is presented, and the impact of this strain on electronic properties of graphene is reviewed.

Tungsten carbide thin films are the second material system that was studied in this work. These thin films were synthesized by co-deposition of C₆₀ molecules as carbon precursor and tungsten atoms on MgO(100) substrate which was held at high temperatures (<1073 K). The results

related to the carbide thin films are reviewed in chapter 8. At the initial stages of this project, interesting observations about the interaction/reaction between tungsten and C₆₀ molecules at lower temperature range (300 - 800 K) laid the foundation for a separate study. It was observed that during the annealing of C₆₀ molecule layers on tungsten surface, the bandgap of the molecules gradually decrease while the overall shape of molecule conserves. This reaction causes a transformation in electronic properties of the molecules in a way that the C₆₀ molecules layers with band gap of (~2.5 eV) at room temperature, will behave as metallic nanospheres after annealing at temperature above (680 K). STM/STS measurements in addition to density functional theory (DFT) calculation were performed to reveal the mechanism of this reaction. The results related to this project are discussed in chapter 7.

Tungsten Carbide thin films show a unique combination of properties and exhibit catalytic activity, which makes them an attractive substitute for expensive noble metal catalysts.¹⁶⁻¹⁹ However, the use of tungsten carbide thin films is limited by surface oxidation, which is accompanied by a depression of activity. In this work, the investigation of oxidation process of tungsten carbides was combined with the development of a method to recover the carbide surface. Non-stoichiometric carbides with a high concentration of carbon were synthesized to study whether an excess amount of carbon in thin films can be utilized to provide a pathway for recovery of surface carbide. This self-healing process (re-carburization) is accomplished by annealing of the thin films, which will cause the extra carbon from lower layers to diffuse towards surface and form new carbide regions by replacing oxygen atoms in the oxide components. The oxidation and carburization cycles were repeated several times, which showed this method is a viable pathway to significantly increase the life time of a catalytic surface. In this work, in addition to STM/STS

measurements, Ambient Pressure-XPS was performed to unravel the chemical bonding and kinetics of this reaction.

1.1. References

- (1) Oura, K.; Lifshits, V. G.; Saranin, A.; Zotov, A. V.; Katayama, M. *Surface Science: An Introduction*; Springer Science & Business Media, 2013.
- (2) Novoselov, K. S.; Geim, A. K.; Morozov, S. V.; Jiang, D.; Zhang, Y.; Dubonos, S. V.; Grigorieva, I. V.; Firsov, A. A. Electric Field Effect in Atomically Thin Carbon Films. *Science* **2004**, *306* (5696), 666–669.
- (3) Kroto, H. W.; Heath, J. R.; O'Brien, S. C.; Curl, R. F.; Smalley, R. E. C₆₀: Buckminsterfullerene. *Nature* **1985**, *318* (6042), 162–163.
- (4) Ling, Q.-D.; Lim, S.-L.; Song, Y.; Zhu, C.-X.; Chan, D. S.-H.; Kang, E.-T.; Neoh, K.-G. Nonvolatile Polymer Memory Device Based on Bistable Electrical Switching in a Thin Film of Poly(N-Vinylcarbazole) with Covalently Bonded C₆₀. *Langmuir* **2007**, *23* (1), 312–319.
- (5) Brumbach, M.; Placencia, D.; Armstrong, N. R. Titanyl Phthalocyanine/C₆₀ Heterojunctions: Band-Edge Offsets and Photovoltaic Device Performance. *J. Phys. Chem. C* **2008**, *112* (8), 3142–3151.
- (6) Kouwenhoven, L. Nanotechnology: Bouncing a C₆₀ Ball. *Nature* **2000**, *407* (6800), 35–36.
- (7) Park, H.; Park, J.; Lim, A. K. L.; Anderson, E. H.; Alivisatos, A. P.; McEuen, P. L. Nanomechanical Oscillations in a Single-C₆₀ Transistor. *Nature* **2000**, *407* (6800), 57–60.
- (8) Joachim, C.; Gimzewski, J. K.; Aviram, A. Electronics Using Hybrid-Molecular and Mono-Molecular Devices. *Nature* **2000**, *408* (6812), 541–548.
- (9) Nakashima, N.; Nonaka, Y.; Nakanishi, T.; Sagara, T.; Murakami, H. A C₆₀-Embedded Artificial Bilayer Membrane Film Electrode Device: Phase-Transition-Dependent Electrochemistry. *J. Phys. Chem. B* **1998**, *102* (38), 7328–7330.
- (10) Monazami, E.; Bignardi, L.; Rudolf, P.; Reinke, P. Strain Lattice Imprinting in Graphene by C₆₀ Intercalation at the Graphene/Cu Interface. *Nano Lett.* **2015**.
- (11) Monazami, E.; McClimon, J. B.; Rondinelli, J.; Reinke, P. Electronic Structure and Band Gap of Fullerenes on Tungsten Surfaces: Transition from a Semiconductor to a Metal Triggered by Annealing. *ACS Appl. Mater. Interfaces* **2016**.
- (12) McClimon, J. B.; Monazami, E.; Reinke, P. Interaction of C₆₀ with Tungsten: Modulation of Morphology and Electronic Structure on the Molecular Length Scale. *J. Phys. Chem. C* **2014**, *118* (42), 24479–24489.
- (13) Agnoli, S.; Favaro, M. Doping Graphene with Boron: A Review of Synthesis Methods, Physicochemical Characterization, and Emerging Applications. *J. Mater. Chem. A* **2016**, *4* (14), 5002–5025.
- (14) Meyer, J. C.; Kurasch, S.; Park, H. J.; Skakalova, V.; Künzel, D.; Groß, A.; Chuvilin, A.; Algara-Siller, G.; Roth, S.; Iwasaki, T.; Starke, U.; Smet, J. H.; Kaiser, U. Experimental Analysis of Charge Redistribution due to Chemical Bonding by High-Resolution Transmission Electron Microscopy. *Nat. Mater.* **2011**, *10* (3), 209–215.
- (15) Urban, K. W. Electron Microscopy: The Challenges of Graphene. *Nat. Mater.* **2011**, *10* (3), 165–166.
- (16) Yang, X.; Kimmel, Y. C.; Fu, J.; Koel, B. E.; Chen, J. G. Activation of Tungsten Carbide Catalysts by Use of an Oxygen Plasma Pretreatment. *ACS Catal.* **2012**, *2* (5), 765–769.
- (17) Elezović, N. R.; Babić, B. M.; Gajić-Krstajić, L.; Ercius, P.; Radmilović, V. R.; Krstajić, N. V.; Vračar, L. M. Pt Supported on Nano-Tungsten Carbide as a Beneficial Catalyst for the Oxygen Reduction Reaction in Alkaline Solution. *Electrochimica Acta* **2012**, *69*, 239–246.

- (18) Decker, S.; Löfberg, A.; Bastin, J.-M.; Frennet, A. Study of the Preparation of Bulk Tungsten Carbide Catalysts with C₂H₆/H₂ and C₂H₄/H₂ Carburizing Mixtures. *Catal. Lett.* **1997**, *44* (3–4), 229–239.
- (19) Ren, H.; Chen, Y.; Huang, Y.; Deng, W.; Vlachos, D. G.; Chen, J. G. Tungsten Carbides as Selective Deoxygenation Catalysts: Experimental and Computational Studies of Converting C₃ Oxygenates to Propene. *Green Chem.* **2014**, *16* (2), 761–769.

Chapter 2

Materials

2. Materials

2.1. Graphene

Graphene is a two-dimensional array of carbon atoms in a honeycomb lattice that is just one atom thick (densely packed in a honeycomb lattice), where each carbon atom has sp^2 bonding with three neighboring atoms. Graphene can be described as the basic building material for other carbon allotropes including: graphite, and carbon nanotubes (CNT), and C_{60} . Graphite can be described as several layers of graphene stacked on each other, CNT is a graphene layer which rolled around itself, and C_{60} molecule is a section of graphene that wrapped around itself and forms a closed shell structure by introducing several pentagons (Figure 2.1).¹

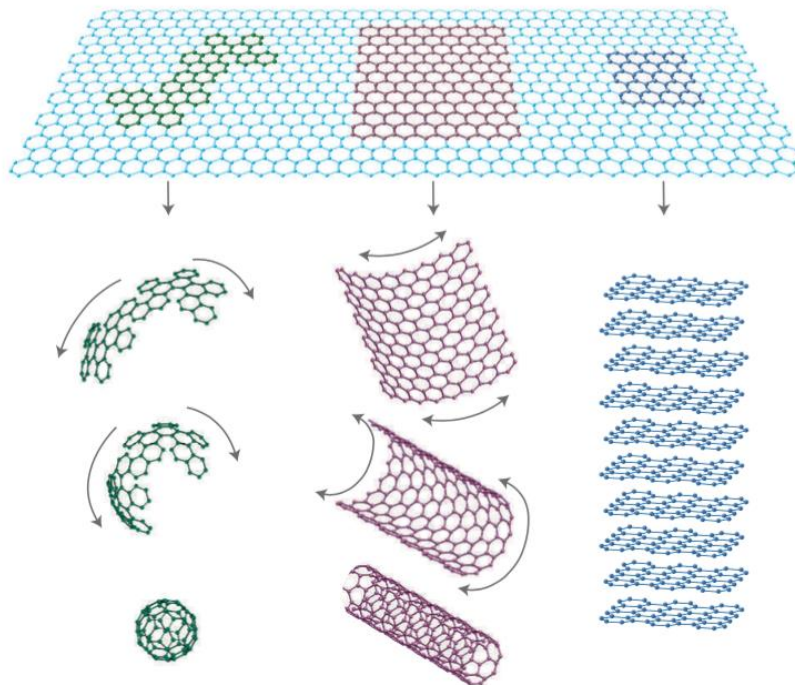


Figure 2.1: Schematic representation of carbon allotropes. Taken from Reference [1].

Even though graphene has been known as a fundamental material for all the other carbon allotropes, it was always assumed that an isolated layer of graphene in the free state is not stable and it was only studied as a theoretical material.¹ This hypothesis developed about 80 years ago, after Landau and Peierls discussed the existence of 2D materials in two separate articles.^{2,3} The authors of these works argued that at any finite temperature, a divergent thermal fluctuation in 2D crystals will cause a displacement in the atomic structure of the 2D crystals. This displacement is comparable to the interatomic distances, thus the crystal melts. Later, these claims were confirmed by several experimental observations and theoretical works. For instance, the decrease in the melting point of thin films as the thickness decreases.^{4,5} After the discovery of graphene by Novoselov and Geim in 2004, this generally accepted theory was rejected.⁶

During the past decades, several methods have been developed to grow or prepare 2D crystals. In addition to synthesizing 2D materials on various substrates, single layer of freestanding graphene, BN, and MoS₂ has been prepared and studied. In addition to experimental observation, which has proved that a continuous layer of 2D material can exist at finite temperature, the existence of these 2D structures can be rationalized in theory too. Figure 2.2 shows the results for molecular dynamic (MD) simulation performed on a small flake of graphene with 2808 atoms. The C-C in-plane bonds in this simulation were defined by Tersoff potential.^{7,8} In this simulation, we start with a perfectly flat 2D layer of graphene at 0 K as the initial structure. Then, the stability of this flake at higher temperature was studied by increasing the velocity distribution of the atoms. These results show that after increasing the temperature of the system to 180 K, which causes a thermal fluctuation in the system, the graphene flake remains stable. This stability can be explained by small fluctuation that are formed in the 3rd dimension (z-axis) of graphene. This roughening in the system is essential for stability of 2D crystals at any finite temperature (formation of hills and

valleys (ripples)). Similar observations have been reported by several other theoretical work and experimental observation.^{9–15}

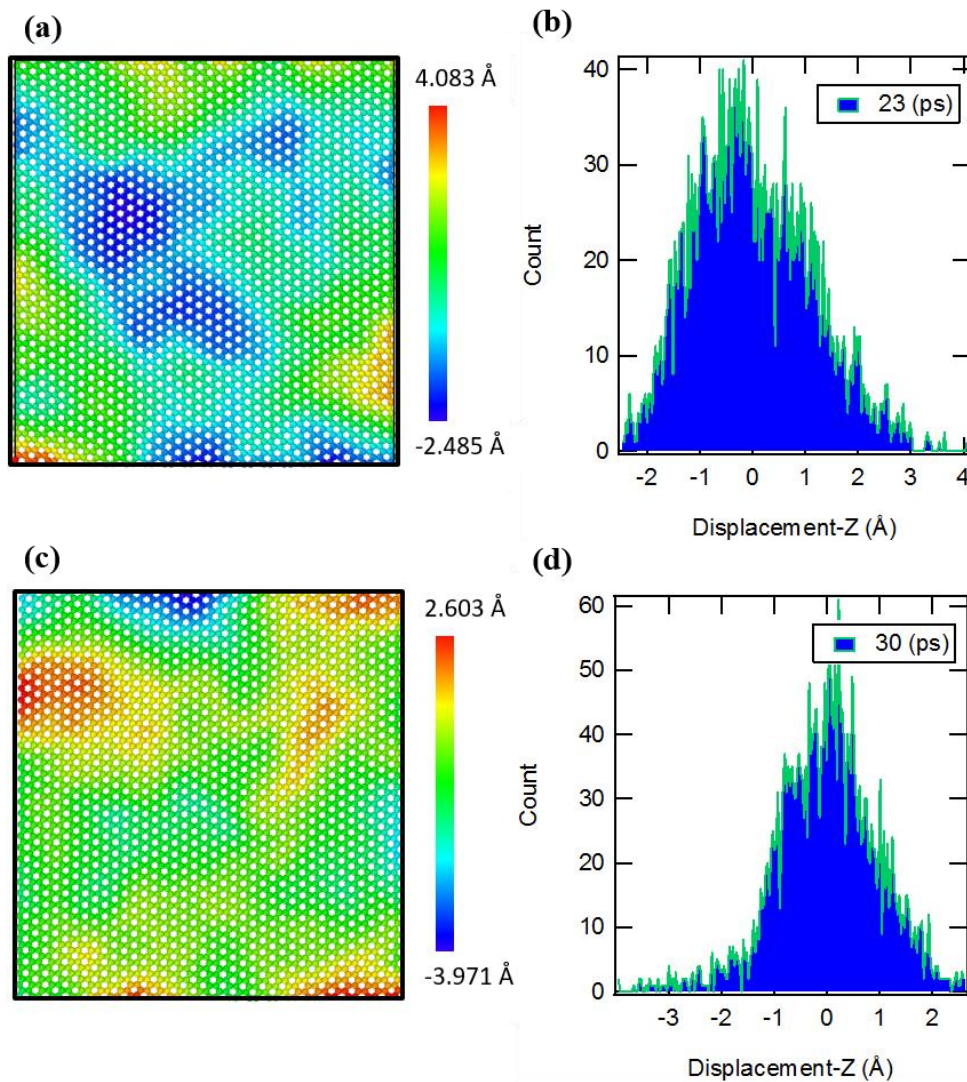


Figure 2.2: MD simulation results for a graphene flake at 180 K. a) Snapshot of top-view of the graphene and distribution of valley and hills after 23 ps. b) Histogram distribution of the height profile extracted from (a). c) Snapshot of top-view of the graphene and distribution of valley and hills after 30 ps. d) Histogram distribution of the height profile extracted from (c).

2.1.1. Electronic and Band Structure of Graphene

In chapter 6 of this work, the effect of strain in graphene and formation of super lattice in graphene by C_{60} molecules are discussed. Therefore, here we briefly introduce some important concepts about band structure of graphene and the chemical vapor deposition (CVD) techniques to grow graphene.

Graphene is a 2D honeycomb structure (hexagonal Bravais lattice) of carbon atoms with the average nearest neighbor distance of 1.42 \AA . This structure contains a two-atom basis set which are labeled as A and B in Figure 2.3(a). Figure 2.3(b) shows the 2D-fast Fourier transform of the STM graphene image with the first Brillouin zone (1^{st} BZ) of graphene (red hexagon) with the two inequivalent corners of K and K' (Dirac points).

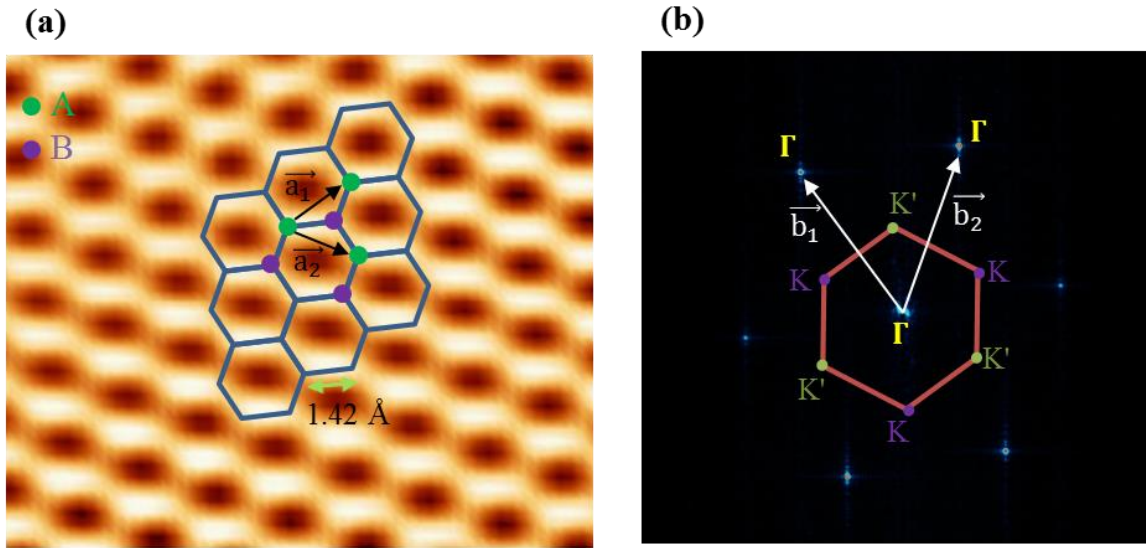


Figure 2.3: STM image of graphene on copper, several of the hexagons in the honeycomb structure of graphene are indicated in this image. \vec{a}_1 and \vec{a}_2 are the primitive lattice vectors of graphene. b) Corresponding 2D-fast Fourier transform of the STM image in (a), the FFT peaks are colored by light blue, the 1^{st} BZ of graphene is indicated by the red hexagons. \vec{b}_1 and \vec{b}_2 are the basis vectors of the reciprocal lattice.

Because of the symmetry relations in the graphene structure, the corners of 1st BZ are pairwise equivalent and the positions of these corners in the K-space are given by:

$$K = \frac{2\pi}{3a} \left(1, \frac{1}{\sqrt{3}}\right) \text{ and } K' = \frac{2\pi}{3a} \left(1, \frac{-1}{\sqrt{3}}\right)$$

Where a is the nearest neighbor C-C spacing and is 1.424Å.

Figure 2.4 illustrates the band structure and the projected density of states (DOS) of graphene calculated by DFT method. This calculation was performed with Atomistic Toolkit (ATK 2015.rc2) package and the local density approximation (LDA) with the Perdew–Zunger exchange–correlation parametrization was used.¹⁶ In graphene, three electrons per carbon atoms participate in formation of strong in plane covalent bonds (σ), which are formed by sp^2 hybridization of s -orbital and the degenerated p_x and p_y orbitals; and one electron per atom will form an orthogonal weaker bond (π), which is formed by the sp^2 hybridization of s -orbital and p_z orbital. The π electrons form energy bands at lower energy (near the Fermi energy) and σ electrons form energy bands at higher energies.¹⁷ Therefore, the electronic behavior of the graphene at near fermi energy is a result of π electrons (Figure 2.4).

As the consequence of the crystallographic structure of graphene, its band structure is exactly symmetric near Fermi energy, with DOS zero at its Dirac point. This band structure leads to the fact that non-doped graphene is a perfect semimetal with zero band gap and the Fermi energy and Dirac point coincide. Also, the energy dispersion relation (E_k) for graphene is linear around the Dirac point and this leads to the unique electronic properties of graphene, including; ultra-high charge carrier mobility for electron and holes. Low energy excitons of this system can be described

by the Dirac equation in two spatial dimensions where the electrons can be treated as Dirac particles and thus behave like photons.^{18,19}

$$E = \hbar v_f \sqrt{k_x^2 + k_y^2}$$

Where v_f is the Fermi velocity of the electrons and is 1×10^6 m/s.

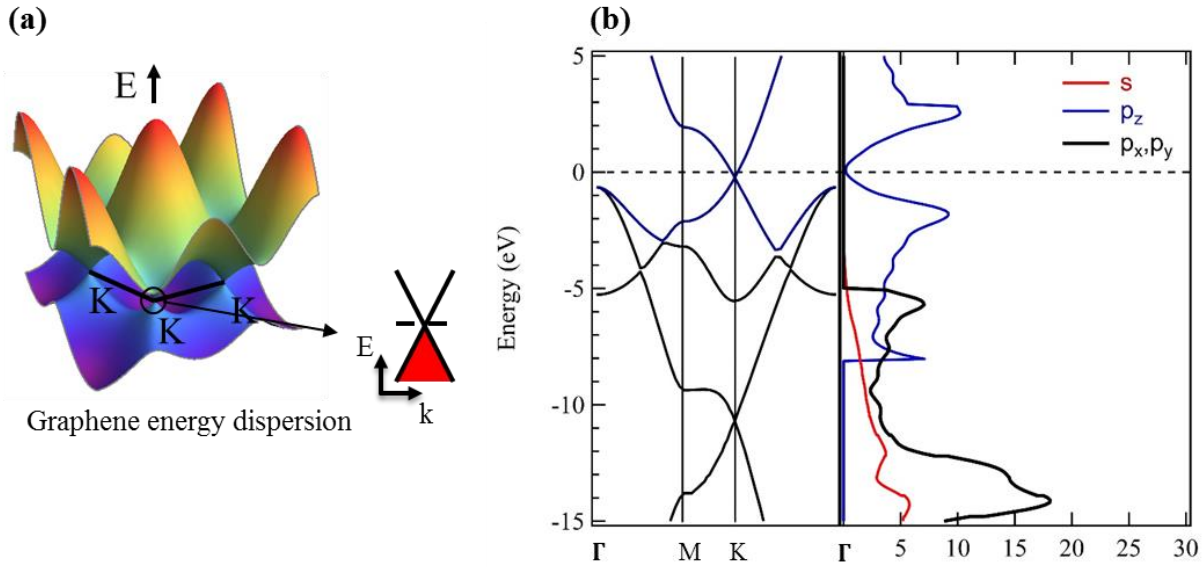


Figure 2.4: The electronic structure of graphene. a) The graphene energy dispersion. b) Graphene band structure and local density of states projected on s (red), p_x and p_y (black), and p_z (blue) orbitals, calculated by DFT method. (this simulation was performed by ATK package)

2.1.2. Graphene Synthesis

Graphite and few layers of graphene have been studied for several decades, but only in 2004, Andre Geim and colleagues were able to separate a single layer of graphene using a simple exfoliation method (micromechanical cleavage). This method is performed by exfoliation of graphene layers from graphite, using a scotch tape and transferring to the target substrate.

Since the discovery of graphene by mechanical exfoliation technique, several methods of graphene synthesis including: chemical exfoliation of graphite,²⁰ reduction of graphene oxide,^{21–23} epitaxial growth on SiC and BN,^{24,25} and CVD techniques have been introduced and studied.^{26–28} Among these techniques, CVD graphene has emerged as the most common method for the preparation and production of graphene layers since it was first reported in 2008.²⁹

Two different set of graphene on polycrystalline copper samples were used in this work, both synthesized by the CVD method. The first CVD graphene sample was provided by Luca Bignardi at University of Groningen, Netherlands,³⁰ and the second sample was purchased from Graphene Supermarket. The common steps in the growth process of these samples are listed as follows: 1) a thin Cu foil (thickness < 25 mm) is introduced to a low vacuum furnace ($P < 10^{-5}$ mbar). 2) the Cu foil is annealed in a H_2/Ar reducing environment to remove the native oxide layer on Cu (Cu_2O and CuO). 3) In this step, the Cu foil which is held at high temperatures (1180–1358 K) is exposed to a mixture of gasses containing Ar, H_2 and CH_4 for few minutes, during this step graphene is formed by decomposition of hydrocarbon. 4) subsequently the sample is cooled down to room temperature. The surface of these samples was dominated by single layer graphene. In addition, both samples show extended regions of Cu (100) grains between graphene islands.

2.2. Fullerene (C_{60})

The C_{60} molecule consist of 60 carbon atoms located at the vertices of a truncated icosahedron where each carbon atom is triangularly bonded with the 3 adjacent carbon atoms. An icosahedron consists of 20 hexagons and 12 pentagons where each pentagon is surrounded by 5 hexagons. This configuration is consistent with Euler's theorem and the isolated pentagon rule.³¹ In a regular icosahedron all the 90 edges have an equal length while the situation in fullerene cage is slightly different. There are two different bond lengths (length of the edges) in a fullerene cage

and therefore the C_{60} is referred as a truncated icosahedron. The C-C bond between hexagons and pentagons (h-p) is referred to as an electron poor bond (single bond) and has a length of 1.46 (Å); the bond between two hexagons (h-h) is shorter, 1.40 (Å), and is referred to as an electron rich bond (double bond).³² These bond lengths are highlighted in Figure (2.5).

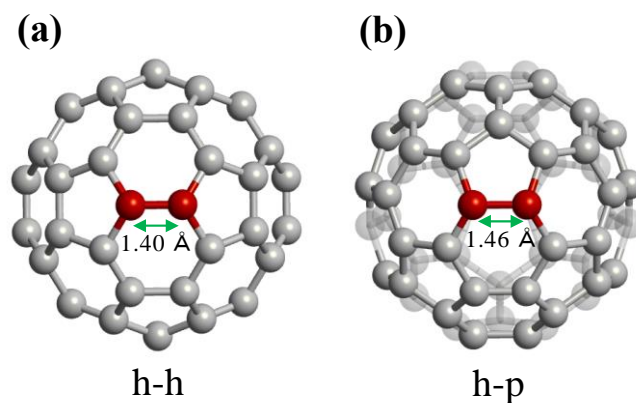


Figure 2.5: Schematics of two different orientation of C_{60} molecule. a) When the h-h bond is on top b) When the h-p bond is on top.

The size of C_{60} molecule is about 7 (Å), which results in a diameter of about 10.35 (Å) during STM measurements. This size difference (3.35 Å) is explained by considering the π electron cloud around a C_{60} molecule.³³

In C_{60} , the bonding requirements for all valence electrons is satisfied therefore all the molecular levels are fully filled (closed shell structure). Each carbon atom in C_{60} structure is bonded with the 3-adjacent carbon atoms in an sp^2 derived bonding configuration similar to graphite. Although, in contrast to graphite where these bonds are truly planar, the sp^2 bonds in C_{60} occur on a curved surface. This curvature results in a mixture of sp^2 with sp^3 bonding.³³

2.2.1. Crystalline C₆₀

Deposition of C₆₀ molecules on a metal substrates or graphite results in formation of a full coverage of the surface. In this structure, C₆₀ molecules are arranged in a face center cubic (fcc) lattice. The primitive unit cell of this structure contains one molecule per unit cell and the conventional unit cell of this structure includes four molecules per unit cell. The lattice constant of bulk C₆₀ is about $a=14.17$ (Å) with a nearest neighbor C₆₀-C₆₀ distance of $d=10.32$ (Å) (Figure 2.6). These values can change depending on the type of substrates and number of molecular layers.

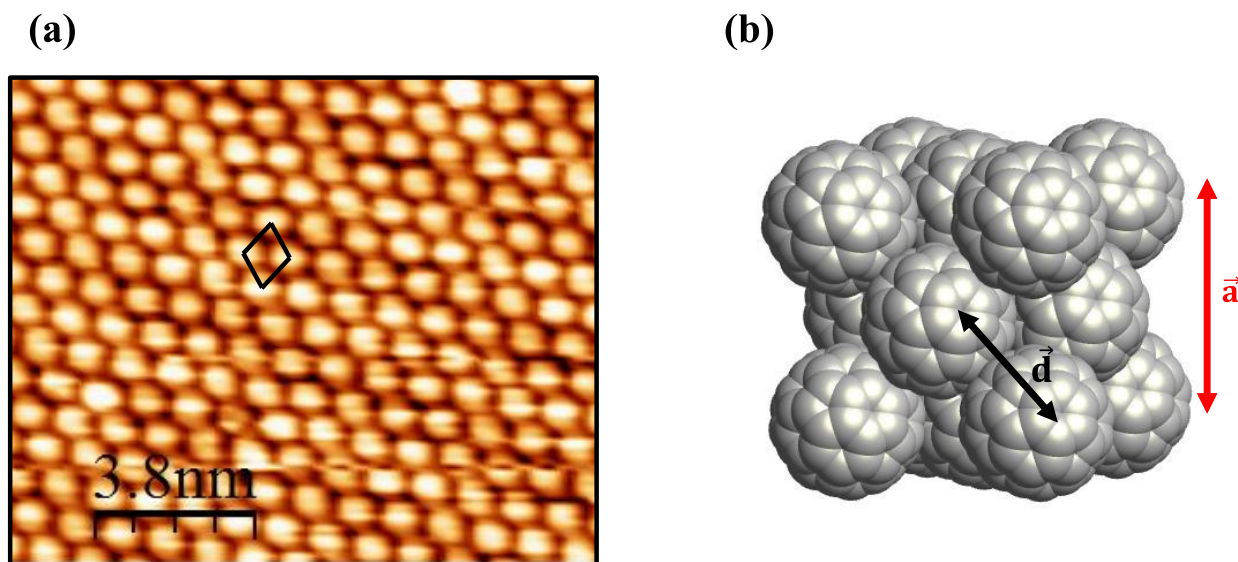


Figure 2.6: a) STM image of 5 ML of C₆₀ molecules on graphite. The marked region shows the conventional unit cell for this structure. b) 3D Illustration of solid C₆₀.

At room temperature, the C₆₀ molecule are rotating rapidly with three degrees of rotational freedom. The rotational period for fullerenes is about 10^{-11} s.³³ Therefore, all molecules exhibit a featureless equivalent structure during STM measurement unless this rotation is ceased. Temperature has a strong effect on the rotation of C₆₀ molecules. Figure 2.7 Illustrates the difference between the STM images when the molecules on tungsten oxide substrates are rotating

at room temperature and when the rotation of the molecules is stopped at 77 K. As a result of the interruption of the rotation at low temperature it is possible to image the molecular orbitals of C_{60} molecules. These orbitals, often appear as groove shape structure in individual molecule in STM images.

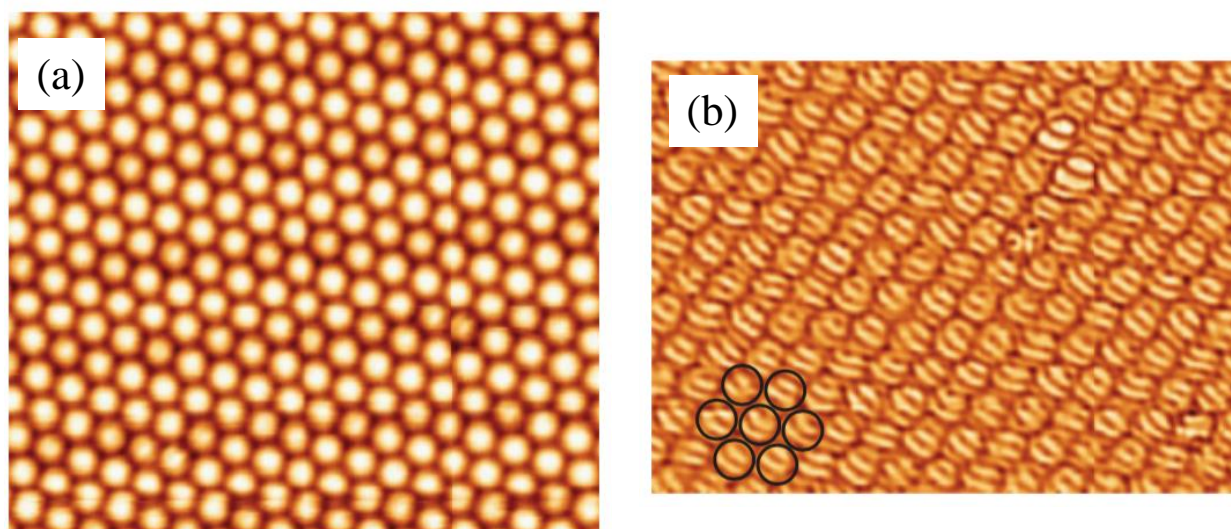


Figure 2.7: STM images of the C_{60} monolayer on $WO_2/W(110)$ substrate at different temperatures. (a) 19×16 nm² images of the same C_{60} film acquired at $T = 315$ K. (b) 12×14 nm² image acquired at $T = 78$ K. Taken from Reference [34].

In addition, if the C_{60} molecules are anchored to the substrate due to strong interaction between molecule-substrate, similar results can be observed. Figure 2.8 shows the STM images for molecules on tungsten substrate before and after initiation of the interaction between the substrate and molecules. The annealing process is the trigger for this interaction and the results regarding to this process is described in Chapter 7.

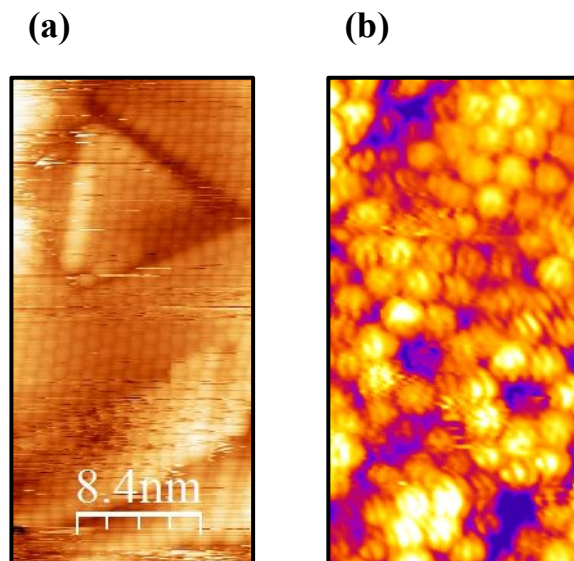


Figure 2.8: STM images of C_{60} molecules on tungsten surface a) Before anneal. b) After anneal at $T=623$ K. The molecules in after anneal surface, exhibit two or three surface grooves which are correlated to the molecular orbital in C_{60} (image size 8×15 nm²).

2.2. Tungsten Carbide

A study of nonstoichiometric carbon rich tungsten carbide thin films is presented in chapter 8. In order to control the carbon inventory in these thin films, an unusual synthesis pathway was used. Tungsten carbide thin films were grown by co-deposition of C_{60} and tungsten on MgO(100) substrates over the temperature range 873-1073 K. During this process, the fullerene cage breaks down into individual carbon atoms and then incorporate with tungsten atoms to form tungsten carbide. This non-traditional method for tungsten carbide synthesis via fullerene and pure tungsten precursors allows for a fine control over concentration of tungsten and carbon inventory in the thin films. Also, employing fullerene molecules as a carbon source inhibits any possible hydrogen contamination that can modify reaction pathways.

Figure 2.9 shows the W-Carbon phase diagram with green circles indicating the composition of tungsten carbide thin-films that are used in this work. These compositions were obtained by

controlling the deposition rate of tungsten and fullerene (as carbon precursor). For compositions and temperature ranges of interest, W, α -W₂C, WC, amorphous carbon and graphite are the phases to consider. Some metastable phases like cubic β -WC_{1-x} (NaCl structure) can exist instead of the thermodynamically stable hexagonal WC phase even at low temperatures, but formation of this phase depends on deposition rate and the crystallographic orientation of substrate.³⁵

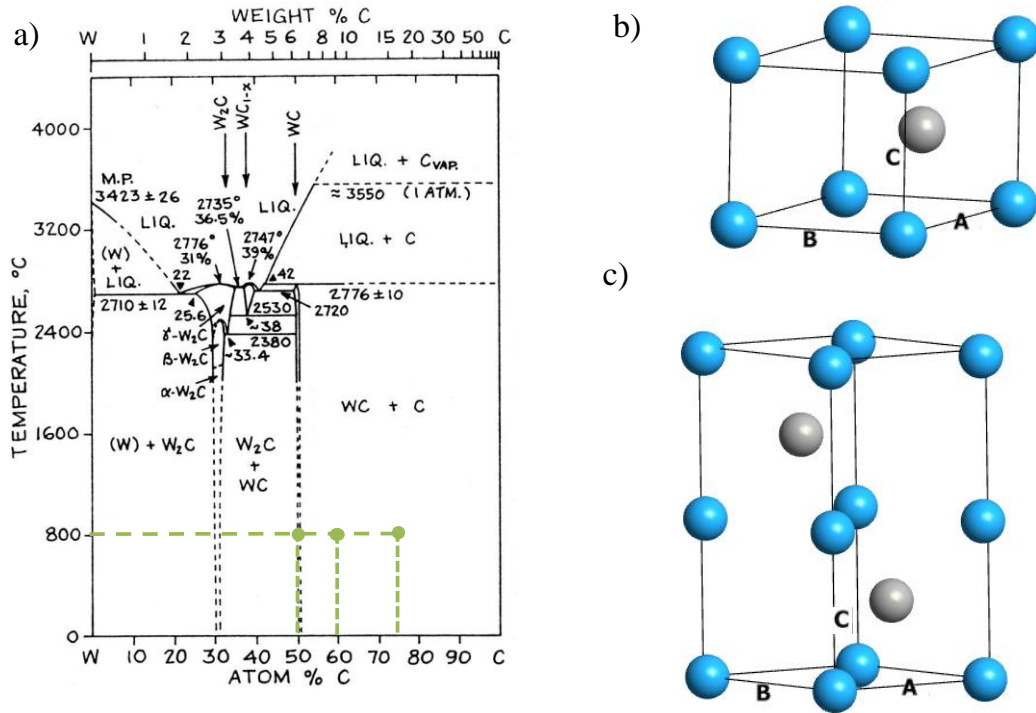


Figure 2.9: a) W-C phase diagram. Taken from reference [36]. Structural representation of b) hexagonal WC and c) hexagonal W₂C.

2.3. Reference

- (1) Geim, A. K.; Novoselov, K. S. The Rise of Graphene. *Nat. Mater.* **2007**, 6 (3), 183–191.
- (2) Landau, L. D. Zur Theorie Der Phasenumwandlungen II. *Phys. Z. Sowjetunion* **1937**, 11, 26–35.
- (3) Peierls, R. Quelques propriétés typiques des corps solides. *Ann. Inst. Henri Poincaré* **1935**, 5 (3), 177–222.
- (4) Venables, J. A.; Spiller, G. D. T.; Hanbucken, M. Nucleation and Growth of Thin Films. *Rep. Prog. Phys.* **1984**, 47 (4), 399.
- (5) Mermin, N. D. Crystalline Order in Two Dimensions. *Phys. Rev.* **1968**, 176 (1), 250–254.
- (6) Novoselov, K. S.; Geim, A. K.; Morozov, S. V.; Jiang, D.; Zhang, Y.; Dubonos, S. V.; Grigorieva, I. V.; Firsov, A. A. Electric Field Effect in Atomically Thin Carbon Films. *Science* **2004**, 306 (5696), 666–669.
- (7) Lindsay, L.; Broido, D. A. Optimized Tersoff and Brenner Empirical Potential Parameters for Lattice Dynamics and Phonon Thermal Transport in Carbon Nanotubes and Graphene. *Phys. Rev. B* **2010**, 81 (20), 205441.
- (8) Yoon, C. S.; Megusar, J. Molecular Dynamic Simulation of Amorphous Carbon and Graphite Interface. *Interface Sci.* **1995**, 3 (1), 85–100.
- (9) Moura, M. J. B.; Marder, M. Tearing of Free-Standing Graphene. *Phys. Rev. E* **2013**, 88 (3), 32405.
- (10) Neek-Amal, M.; Xu, P.; Schoelz, J. K.; Ackerman, M. L.; Barber, S. D.; Thibado, P. M.; Sadeghi, A.; Peeters, F. M. Thermal Mirror Buckling in Freestanding Graphene Locally Controlled by Scanning Tunnelling Microscopy. *Nat. Commun.* **2014**, 5, 4962.
- (11) Sidorenkov, A. V.; Kolesnikov, S. V.; Saletsky, A. M. Molecular Dynamics Simulation of Graphene on Cu(111) with Different Lennard-Jones Parameters. *Eur. Phys. J. B* **2016**, 89 (10).
- (12) Xu, P.; Dong, L.; Neek-Amal, M.; Ackerman, M. L.; Yu, J.; Barber, S. D.; Schoelz, J. K.; Qi, D.; Xu, F.; Thibado, P. M.; Peeters, F. M. Self-Organized Platinum Nanoparticles on Freestanding Graphene. *ACS Nano* **2014**, 8 (3), 2697–2703.
- (13) Huei, L. M.; Yoon, T. L.; Soon, Y. Y.; Lim, T. L. Molecular Dynamics Simulation of Melting of Finite and Infinite Size Graphene. *ArXiv161104161 Cond-Mat* **2016**.
- (14) Ackerman, M. L.; Kumar, P.; Neek-Amal, M.; Thibado, P. M.; Peeters, F. M.; Singh, S. Anomalous Dynamical Behavior of Freestanding Graphene Membranes. *Phys. Rev. Lett.* **2016**, 117 (12), 126801.
- (15) Xu, P.; Yang, Y.; Barber, S. D.; Ackerman, M. L.; Schoelz, J. K.; Qi, D.; Kornev, I. A.; Dong, L.; Bellaiche, L.; Barraza-Lopez, S.; Thibado, P. M. Atomic Control of Strain in Freestanding Graphene. *Phys. Rev. B* **2012**, 85 (12), 121406.
- (16) Brandbyge, M.; Mozos, J.-L.; Ordejón, P.; Taylor, J.; Stokbro, K. Density-Functional Method for Nonequilibrium Electron Transport. *Phys. Rev. B* **2002**, 65 (16), 165401.
- (17) Nakada, K.; Ishii, A. DFT Calculation for Adatom Adsorption on Graphene. InTech, **2011**.
- (18) Xue, J.; Sanchez-Yamagishi, J.; Bulmash, D.; Jacquod, P.; Deshpande, A.; Watanabe, K.; Taniguchi, T.; Jarillo-Herrero, P.; LeRoy, B. J. Scanning Tunnelling Microscopy and Spectroscopy of Ultra-Flat Graphene on Hexagonal Boron Nitride. *Nat. Mater.* **2011**, 10 (4), 282–285.
- (19) Novoselov, K. S.; Geim, A. K.; Morozov, S. V.; Jiang, D.; Katsnelson, M. I.; Grigorieva, I. V.; Dubonos, S. V.; Firsov, A. A. Two-Dimensional Gas of Massless Dirac Fermions in Graphene. *Nature* **2005**, 438 (7065), 197–200.

- (20) Parvez, K.; Wu, Z.-S.; Li, R.; Liu, X.; Graf, R.; Feng, X.; Müllen, K. Exfoliation of Graphite into Graphene in Aqueous Solutions of Inorganic Salts. *J. Am. Chem. Soc.* **2014**, *136* (16), 6083–6091.
- (21) Chua, C. K.; Pumera, M. Chemical Reduction of Graphene Oxide: A Synthetic Chemistry Viewpoint. *Chem. Soc. Rev.* **2013**, *43* (1), 291–312.
- (22) Thema, F. T.; Moloto, M. J.; Dikio, E. D.; Nyangiwe, N. N.; Kotsedi, L.; Maaza, M.; Khenfouch, M. Synthesis and Characterization of Graphene Thin Films by Chemical Reduction of Exfoliated and Intercalated Graphite Oxide. *J. Chem.* **2012**, *2013*, e150536.
- (23) Zhu, Y.; Murali, S.; Cai, W.; Li, X.; Suk, J. W.; Potts, J. R.; Ruoff, R. S. Graphene and Graphene Oxide: Synthesis, Properties, and Applications. *Adv. Mater.* **2010**, *22* (35), 3906–3924.
- (24) Berger, C.; Song, Z.; Li, X.; Wu, X.; Brown, N.; Naud, C.; Mayou, D.; Li, T.; Hass, J.; Marchenkov, A. N.; Conrad, E. H.; First, P. N.; Heer, W. A. de. Electronic Confinement and Coherence in Patterned Epitaxial Graphene. *Science* **2006**, *312* (5777), 1191–1196.
- (25) Yang, W.; Chen, G.; Shi, Z.; Liu, C.-C.; Zhang, L.; Xie, G.; Cheng, M.; Wang, D.; Yang, R.; Shi, D.; Watanabe, K.; Taniguchi, T.; Yao, Y.; Zhang, Y.; Zhang, G. Epitaxial Growth of Single-Domain Graphene on Hexagonal Boron Nitride. *Nat. Mater.* **2013**, *12* (9), 792–797.
- (26) Lee, H. C.; Liu, W.-W.; Chai, S.-P.; Mohamed, A. R.; Lai, C. W.; Khe, C.-S.; Voon, C. H.; Hashim, U.; Hidayah, N. M. S. Synthesis of Single-Layer Graphene: A Review of Recent Development. *Procedia Chem.* **2016**, *19*, 916–921.
- (27) Mattevi, C.; Kim, H.; Chhowalla, M. A Review of Chemical Vapour Deposition of Graphene on Copper. *J. Mater. Chem.* **2011**, *21* (10), 3324–3334.
- (28) Li, X.; Cai, W.; An, J.; Kim, S.; Nah, J.; Yang, D.; Piner, R.; Velamakanni, A.; Jung, I.; Tutuc, E.; Banerjee, S. K.; Colombo, L.; Ruoff, R. S. Large-Area Synthesis of High-Quality and Uniform Graphene Films on Copper Foils. *Science* **2009**, *324* (5932), 1312–1314.
- (29) Reina, A.; Jia, X.; Ho, J.; Nezich, D.; Son, H.; Bulovic, V.; Dresselhaus, M. S.; Kong, J. Large Area, Few-Layer Graphene Films on Arbitrary Substrates by Chemical Vapor Deposition. *Nano Lett.* **2009**, *9* (1), 30–35.
- (30) Bignardi, L.; Dorp, W. F. van; Gottardi, S.; Ivashenko, O.; Dudin, P.; Barinov, A.; Hosson, J. T. M. D.; Stöhr, M.; Rudolf, P. Microscopic Characterisation of Suspended Graphene Grown by Chemical Vapour Deposition. *Nanoscale* **2013**, *5* (19), 9057–9061.
- (31) Kroto, H. W. The Stability of the Fullerenes C_n , with $N = 24, 28, 32, 36, 50, 60$ and 70 . *Nature* **1987**, *329* (6139), 529–531.
- (32) David, W. I. F.; Ibberson, R. M.; Matthewman, J. C.; Prassides, K.; Dennis, T. J. S.; Hare, J. P.; Kroto, H. W.; Taylor, R.; Walton, D. R. M. Crystal Structure and Bonding of Ordered C_{60} . *Nature* **1991**, *353* (6340), 147–149.
- (33) Dresselhaus, M. S.; Dresselhaus, G.; Eklund, P. C. *Science of Fullerenes and Carbon Nanotubes: Their Properties and Applications*; Academic Press, 1996.
- (34) Bozhko, S. I.; Krasnikov, S. A.; Lübken, O.; Murphy, B. E.; Radican, K.; Semenov, V. N.; Wu, H. C.; Bulfin, B.; Shvets, I. V. Rotational Transitions in a C_{60} Monolayer on the $WO_2/W(110)$ Surface. *Phys. Rev. B* **2011**, *84* (19), 195412.
- (35) Palmquist, J.-P.; Czigány, Z.; Hultman, L.; Jansson, U. Epitaxial Growth of Tungsten Carbide Films Using C_{60} as Carbon Precursor. *J. Cryst. Growth* **2003**, *259* (1–2), 12–17.
- (36) Moffatt, W. G. *The Handbook of Binary Phase Diagrams*; General Electric Company, Corporate Research and Development, Technology Marketing Operation, 1981.

Chapter 3

Experimental and Theoretical Techniques

3. Experimental and Theoretical Techniques

3.1. Ultrahigh Vacuum System (UHV)

The majority of the experiments in this thesis were performed with an Omicron Variable Temperature (VT) ultra-high vacuum scanning probe microscope (Figure 3.1), with a base pressure of $\leq 2 \times 10^{-10}$ mbar.

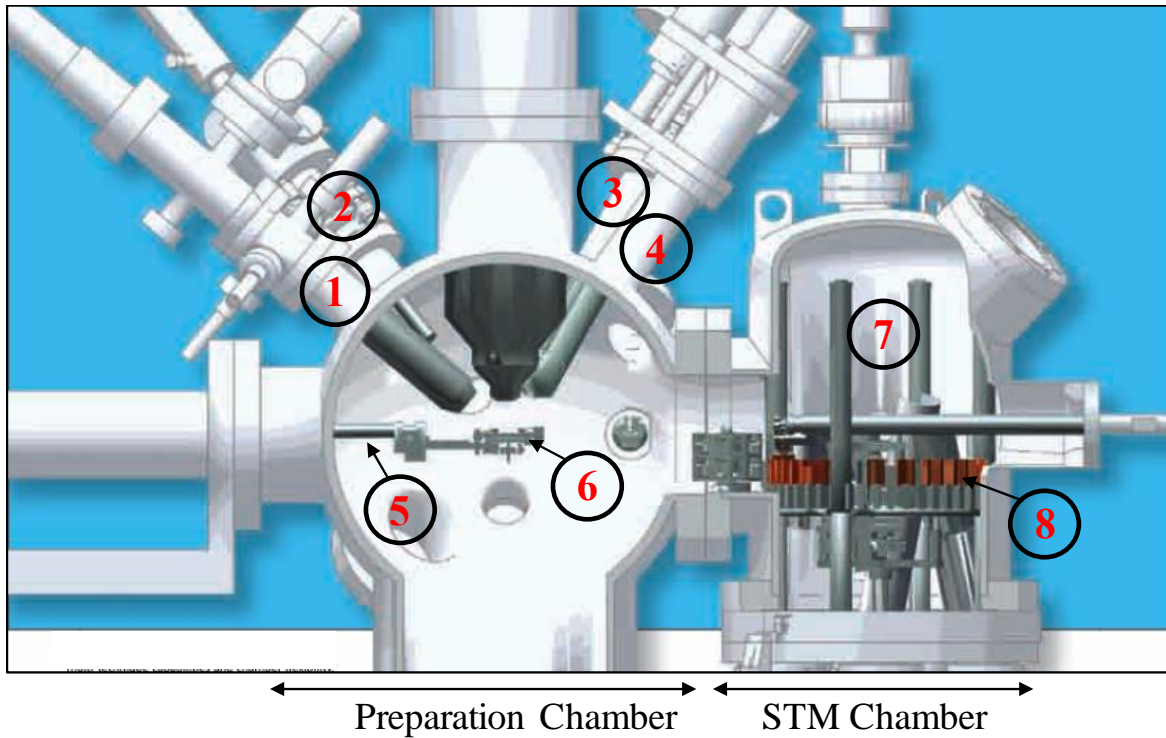


Figure 3.1: View of the UHV system equipped with STM. (1), (2), (3), and (4) Deposition sources slots. Various types of deposition source can be used in these sections (E-beam source for tungsten and thermal evaporation source for C_{60} molecules), and these materials can be evaporated directly in UHV system. 5) Transferring manipulator. 6) Sample stage. This stage is capable of direct current and e-beam heating up to $T=1473$ K. 7) Preparation chamber, this section is used for deposition, heating, and oxidation processes. 8) STM chamber. 9) Eddy current damping system to minimize the vibration during the STM/STS measurements

This UHV system includes three different chambers: a small volume load lock, a preparation chamber, and a microscope chamber. The load lock chamber is separated from the preparation chamber with a manual gate valve. This chamber is located behind the preparation

chamber and cannot be seen in Figure 3.1. The sample preparation, heating, and deposition were all performed in the preparation chamber. This configuration keeps the sample under UHV conditions for the entirety of the experiment including deposition, heating, and imaging; which is necessary for surface science studies, preparation of an atomically clean surface, and monitoring the initial stage of oxidation.^{1,2}

3.2. Scanning Tunneling Microscopy (STM)

STM is the primary characterization technique which was used in this thesis. This powerful tool can provide topography and electronic structure information with atomic resolution for the surface of materials with sufficient conductivity. STM measurements shown in this thesis are performed in constant current imaging (CCI) mode. This mode is the first and most used mode in STM, and the basic concept of it was introduced by Binnig and Rohrer at 1982.³ In this mode, a sharp metallic tip is brought in close proximity of a conductive sample's surface. Afterwards, by applying a voltage between the tip and sample, electron can tunnel from the sample to the tip or vice versa. This tunneling current is controlled by a feedback loop that adjusts the height of the tip at fixed bias voltage to maintain a constant current while the tip raster across the surface. The contour map produced by this method ($z(x,y)$) is not determined solely by the arrangement of the atom on the surface, but rather reflects a constant current surface.^{3,4} This phenomenon is shown in Figure 3.2, where a contamination on the surface with no height difference relative to its surrounding but different local density of states (LDOS) appears with altered apparent height in STM image.

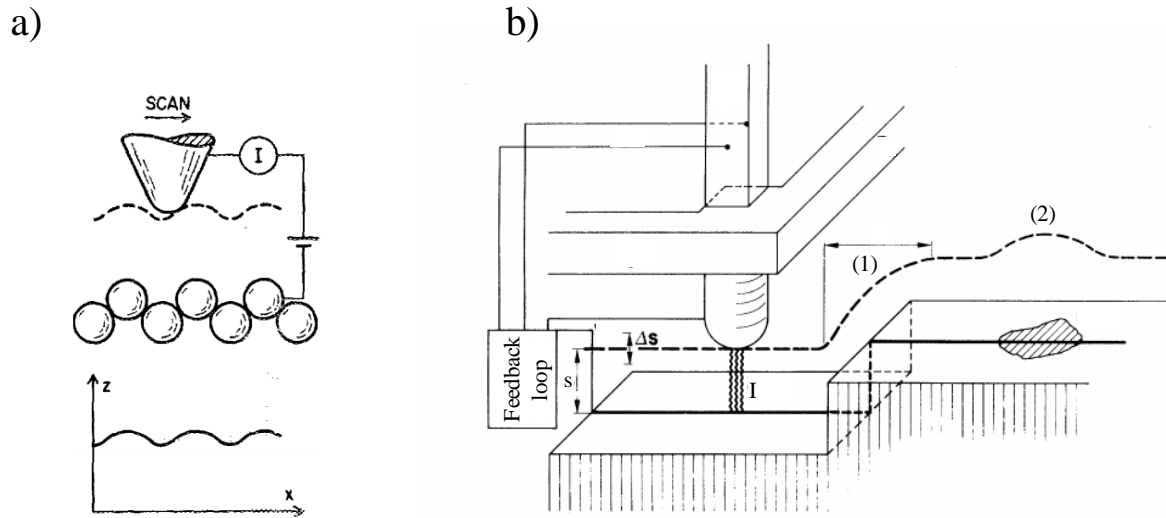


Figure 3.2: Principle of operation of the constant current mode in STM. a) illustration of STM operation to obtain atomic resolution. b) STM operation in larger scale. The dashed line indicates the measured height (z) during the scan over a step edge (1), and a contamination spot (2) with different LDOS in comparison to the rest of surface. Taken from references [3,4].

After STM tip approach to a sample and when sample's surface and tip are separated by small vacuum gap, without presence of any voltage, the Fermi energy of the tip and sample will be at the same level and electrons cannot tunnel through the barrier thickness (Figure 3.3a). However, by applying a bias voltage (V_{bias}) between tip and sample, the Fermi energy position of tip in respect to the sample will change and therefore, the electrons will tunnel through the vacuum barrier. The direction of electric field (or the signs of the bias voltage) determines whether electrons tunnel from the tip to the sample and probing the empty states (conduction band) of the sample (Figure 3.3b) or from the sample to the tip and probing the filled states (valence band) of the sample (Figure 3.3c).⁵

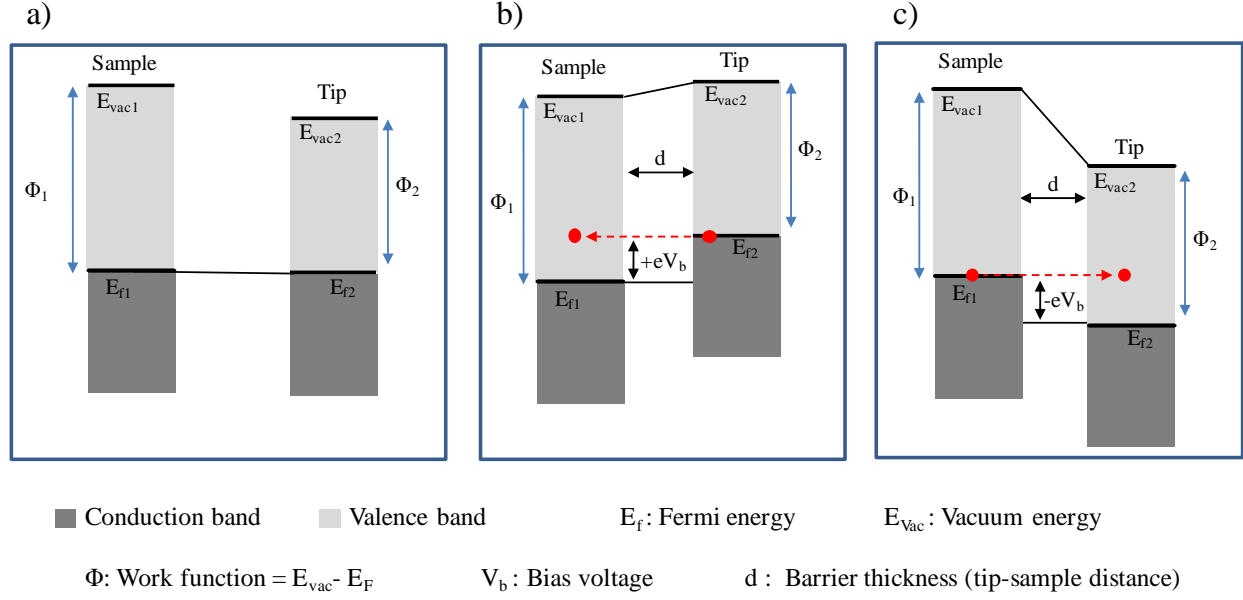


Figure 3.3: Visualization of tunneling between the tip and a metallic sample with one dimensional potential energy diagrams. a) Sample and the tip at equilibrium and separated by small barrier thickness. b) A positive bias voltage is applied to the tip and therefore, electrons tunnel from tip to empty states of the sample. c) A negative bias voltage is applied to the tip and therefore, electrons tunnel from filled states of the sample to the tip.

This tunneling current can be derived by the Wentzel Kramers Brillouin (WKB) approximation and is given by following expression:^{5,6}

$$I \propto \int_0^{eV} \rho_s(E) \rho_t(E + eV_b) T(E, eV_b) dE \quad (3.1)$$

Where $\rho_s(E)$ is the LDOS of the sample, $\rho_t(E + eV)$ is the LDOS of the tip, $T(E, eV)$ is the transmission coefficient of the electron, E is energy of states relative to the Fermi level, and eV is the applied bias voltage. The transmission coefficient is given by:⁷

$$T(E, eV_b) = \exp \left(-2(d + R) \left[\frac{2m}{\hbar^2} \left(\frac{\Phi_t + \Phi_s}{2} + \frac{eV_b}{2} - E \right) \right]^{\frac{1}{2}} \right) \quad (3.2)$$

Where R is the effective tip radius, and d is the distance between the tip and sample. The equation 3.2 shows that the tunneling current is exponentially dependent on the barrier distance. With the assumption that during the measurements, the DOS of the tip remain constant, the equation 3.1 can be written as following:⁸

$$I \propto \int_0^{eV} \rho_s(r, E) T(E, eV_b) dE \quad (3.3)$$

Therefore, the tunneling current depends on the barrier distance, bias voltage, and DOS of the sample. Thus, each STM image includes information about topography (tip-sample distance) and electronic structure of sample (ρ_s). The equation (3.2) and (3.3) indicate that the tunneling current is exponential dependent on the barrier distance. Therefore, even small changes in the barrier distance (in order of angstroms) can be measured by monitoring the tunneling current and as a result, a high resolution topographic contour map of a surface can be obtained.

3.3. Scanning Tunneling Spectroscopy (STS)

In section 3.2. it was shown that the tunneling current measured in STM depends on the barrier distance, LDOS of the sample, and the bias voltage applied between the tip and sample. In STS, the explicit LDOS of the sample is measured by utilizing this bias voltage dependency.

STS is performed by varying the potential difference determined by V_b while measuring the tunneling current; therefore, the I-V characteristics are measured at a specific X-Y position on the surface and the derivative of this result (dI/dV) is then proportional to the LDOS at the point of measurement on the surface.^{6,9,10} With this method, LDOS of the sample can be measured in the range of several eV around the Fermi energy (E_f). To be able to compare the results measured

from different experiments and to correct the dI/dV curves measured from different tip-sample distance, these curves were normalized by following equation:

$$\text{normalized spectra } (I): \frac{\frac{dI}{dV}}{I \sqrt{V + \varepsilon}} \quad (3.4)$$

Where ε is an offset value to avoid singularity at the band edges and at $V=0$. The normalization process and more details about spectroscopy methods used in this thesis are discussed in chapter 5.

Two different approaches of STS measurements are used in this thesis: a) point spectroscopy where an I-V characteristic are measured for one single point in an image area b) spectroscopy maps where I-V measurements distributed at equidistant intervals on the surface. Each topography image in this work includes 512×512 pixels. During STS mapping, I-V characteristics are usually recorded for every 5th pixel, as it is shown in Figure 3.4, and in total 103×103 I-V spectra are measured. In this type of STS map, 50 voltage steps in single I-V characteristic are frequently used. This results for each scanning direction (forward and backward) 21,218 I-V curves in one single map. By mapping the dI/dV values at a specific voltage, a conductivity or bandgap map can be created. In these types of maps, about 10-20% of the I-V curves show a significant noise often due to changes in tip shape, surface contamination and etc. These noisy curves were removed and were not included in spectra averaging.

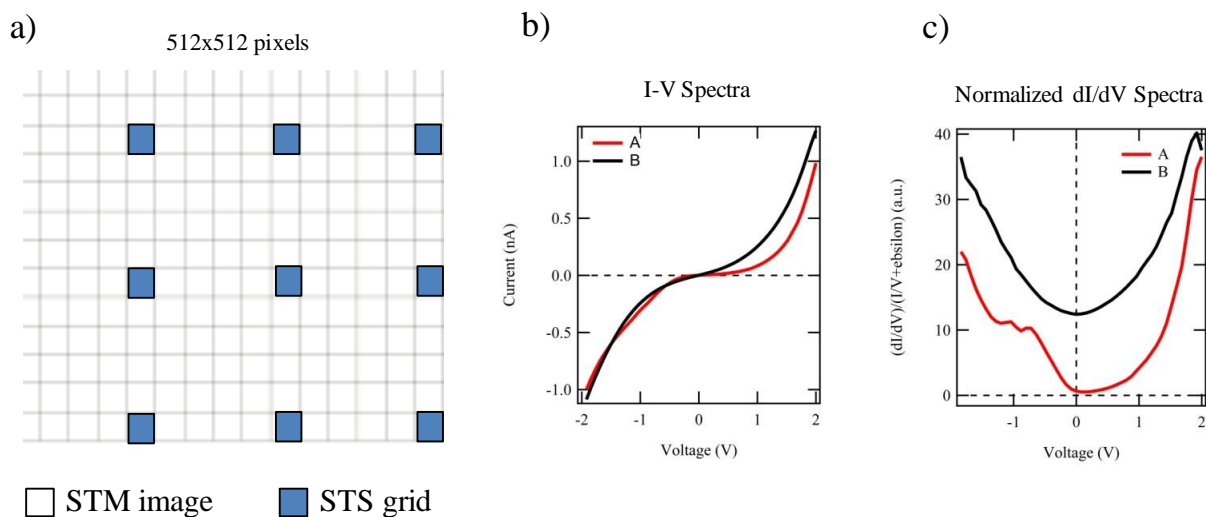


Figure 3.4: Scanning tunneling spectroscopy. a) Visualization of spectra acquired for every five points in a 512x512 pixel image. b) Two example for I-V curve measured by STS. These two spectra are measured on nanospheres surface and they are explained in chapter 7. c) The normalized dI/dV curves calculated from curves shown in (b).

Prior to each measurement, STS data sets were measured on graphite and gold (Au) to confirm reproducibility and reliability of the tip performance. STM and STS data were analyzed with WSxM 5.0,¹¹ Igor Pro 6.22, and a MATLAB program that was developed in this thesis for analysis and visualization of STS maps.

3.4. X-Ray Photoemission Spectroscopy (XPS)

In chapter 8 of this thesis, the oxidation/carburization of carbon rich tungsten carbide thin films is examined. One of the characterization techniques, which was used for these thin films is X-ray photoelectron spectroscopy (XPS). For this purpose, W4f, C1s, and O1s core levels were measured.

XPS is one of the most important techniques for surface science studies. The short mean free path of electrons over the energy range from a few eV to few thousand eV in condensed

matter, makes XPS a very surface sensitive method.¹² The three-step model has been used successfully to describe the photoemission process and serves as the basis to the interpretation of photoelectron spectra (Figure 3.5). This model describes the photoemission process as following: 1) excitation of the photoelectron in the bulk solid. 2) transport of the excited electron from the bulk to the surface. 3) transmission through the surface potential barrier to the vacuum and eventually to the detector where its kinetic energy is measured.¹³ The binding energy of electron is calculated by:

$$BE = h\nu - E_{kin} - \phi \quad , \quad E_{photon} = h\nu \quad (3.5)$$

Where the BE is the binding energy of the electron, h is the Plank's constant, ν is the photon frequency, E_{kin} is the kinetic energy of electron as measured by the electron analyzer, ϕ is the work function of the spectrometer, and E_{photon} is the photon energy.

For each element and core level orbital, a characteristic binding energy is associated. Therefore, each atomic orbital result in a characteristic set of peaks in XPS. The binding energy of an electron depends on the core level that the photoemission occurs from and the local chemical/physical environment of the atom. Any change in chemical/physical environment of an atom, give rise to a shift in binding energy associated to the atom.¹⁴ For example, the XPS spectra in several oxidation states of tungsten is given in Table 3.1. The capability to differentiate between different chemical states of an element is considered as one of the major strengths of XPS.

three-step model

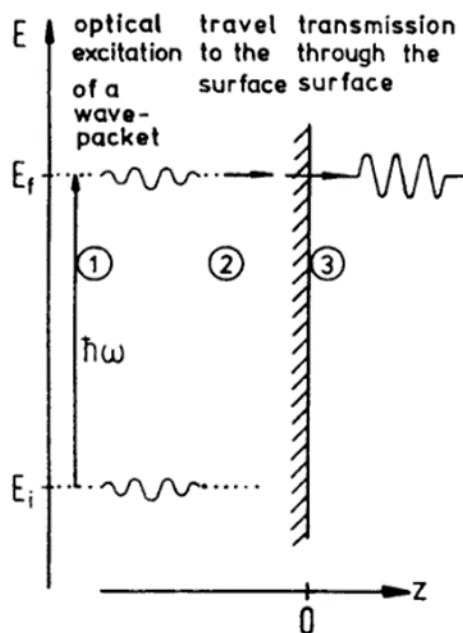


Figure 3.5: Schematic representation of the three-step model of the photo emission process. 1. Excitation of the electron to a Bloch final state inside the crystal, 2. Transport of the electron to the surface, 3. Escape of the electron into the vacuum. (schematic is taken from ref [16]).

Oxidation State	Binding Energy (eV)
W^0 in elemental W	31.0 ± 0.1
W^{4+} in WO_2	33.2 ± 0.2
W^{5+} in W_2O_5	34.6 ± 0.2
W^{6+} in WO_3	35.75 ± 0.2

Table 3.1: Binding energy for several oxidation states in tungsten.

In XPS, core levels are usually identified by means of their quantum numbers, the nomenclature nl_j notation; where n is the principle quantum number, l is the orbital angular momentum, and j is the overall angular momentum. The overall angular momentum is defined by $j = l + s$, where s is the spin angular momentum and it can be either $1/2$ or $-1/2$. For all orbitals except

s orbital ($l=0$), the coupling between spin angular momentum and the angular momentum of orbital results in orbital splitting.^{14,15} Because of this splitting, each orbital (p,d,f) results to two possible states with different binding energy. For example, in tungsten the 4f orbital ($j=3\pm1/2$) give rise to $4f_{5/2}$ and $4f_{7/2}$ peaks which are separated by 2.1 ± 0.1 eV. The relative intensity of the components of this doublet, known as multiplicity factor (M.P), is depend on their relative degeneracy which are given by expression $(2j+1)$. Hence, the relative intensity of the doublet components in 4f orbital is $4f_{5/2} : 4f_{7/2}$ is 6:8.¹⁴

3.4.1. Ambient Pressure X-Ray Photoemission Spectroscopy (AP-XPS)

During the past decade, the AP-XPS (ambient pressure XPS) instruments overcome the strong inelastic scattering in gasses mainly by two methods: an electrostatic lens system which allows differential pumping, and a third-generation synchrotron radiation source which provides a much higher photon flux.

XPS and AP-XPS measurements in this thesis were performed at the SPECIES beamline at Max-Lab located at Lund University in collaboration with Prof. J. Schnadt. This instrument consists of separate analysis and preparation chambers in addition to a high-pressure cell. This instrument can provide a photon energy in range of 27-900 eV. XPS measurements were performed at both relatively high pressure (3 mbar) and UHV environment. The in-situ oxidation measurements were performed after transferring the sample to a retractable ‘high-pressure cell’ (Figures 3.6b–d), which can be docked to the front aperture of the electron analyzer. During oxidation cycles, the high-pressure cell was filled by oxygen gas, while the rest of system retains a pressure of around 10^{-6} mbar.¹⁶

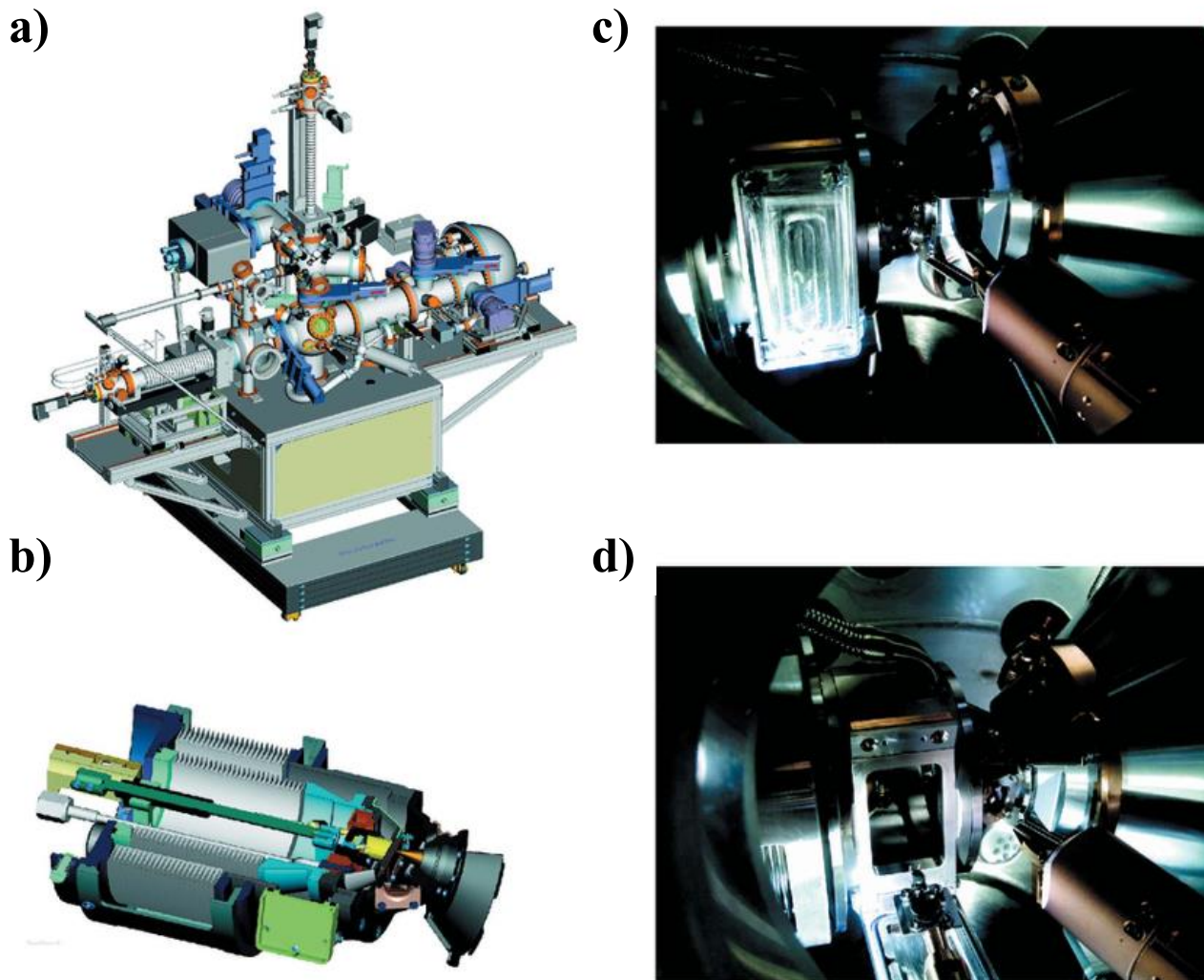


Figure 3.6: (a) Drawing of the APXPS instrument at the MAX IV Laboratory. (b) Cross-section drawing of the high-pressure cell. At the front in green is the door which is opened for sample transfer. The nozzle is depicted in a golden color and points at the sample (in brown). Sample heating is achieved through the wall behind the sample by electron bombardment. The double set-up of bellows makes it possible to move the sample during measurement. (c) High- pressure cell using approach to the analyzer. (d) Sample loading into the high-pressure cell docked to the analyzer. (Pictures and the caption are taken from reference [16])

With this setup, several oxidation/carburization cycles on carbon-rich tungsten carbide samples were performed and these results are discussed in chapter 8. All samples were synthesized in UHV environment in our lab and later transferred to Max-Lab for AP-XPS studies.

Consequently, the formation of a thin residual oxide layer on the surface due to exposure of the surface to atmospheric pressure was inevitable.

3.5. Atomistic Simulations

The interpretation of the experimental results on C₆₀-W interactions required additional atomistic simulation modeling. In this thesis, the geometry, bonding, band gap, and stability of several C₆₀-W bonding combinations including C₅₈W₂, C₅₈W, C₅₉W, C₆₀W, C₆₀ on W(110) and C₆₀ on W(100) were studied within the framework of density functional theory (DFT). The results for these configurations is presented in chapter 7 in addition to the experimental results. All of the simulations were carried out using local spin density approximation (LSDA) as implemented in the Atomistic Toolkit (ATK 2015.rc2) package. In this section, few important concepts about electronic structure methods and DFT are briefly discussed and for more information the reader is referred to the ATK manual.¹⁷

Total Energy

In atomistic simulations, the total energy of the system is used to calculate the bond energy, stability of atomic/molecular structure, chemical reactions mechanism, and etc. To calculate the total energy of a system the kinetic and potential energy of both nuclei and electrons have to be considered.

$$E_{tot} = K_{nuc} + K_{ele} + U_{ele-ele} + U_{nuc-nuc} + U_{ele-nuc} \quad (3.3)$$

Where K_{nuc} is the kinetic energy of nuclei, K_{ele} is the kinetic energy of electrons, and $U_{ele-ele}$, $U_{nuc-nuc}$, $U_{ele-nuc}$ terms are the electron-electron, nuclei-nuclei, and electron nuclei potential, respectively. The terms in total energy equations can be calculated from Schrodinger equation, and the simplest form of it can be written as an energy eigenvalue equation:

$$\hat{H} \Psi = E \Psi \quad (3.4)$$

Where Ψ is the eigenfunction (wave function) and E is the eigenvalue (total energy) of the Hamiltonian (\hat{H}). By consideration of both electrons and nuclei the Schrodinger equation can be written as:

$$\hat{H}\Psi(\{r_i\}, \{R_I\}) = E\Psi(\{r_i\}, \{R_I\}) \quad (3.5)$$

Where $\{r_i\}$ is the coordinates of electrons and $\{R_I\}$ is the coordinates of nuclei. An analytic solution for this complex equation is not possible, and to be able to solve this equation some approximation needs to be made.

Born-Oppenheimer Approximation:

Max Born and J. Robert Oppenheimer developed this approximation and a full description of it can be find in following references.^{21,22} This approximation is based on the fact that the mass of nuclei is much larger than the mass of electrons; therefore, the motion of nuclei is much smaller than the motion of electrons, i.e. kinetic energy of nuclei is negligible in compare to electron's kinetic energy. Thus, it is possible to decouple the motion of the nuclei and electrons in equation of motion. We can therefore express the wave function of electron and nuclei as following:²³

$$\Psi(\{r_i\}, \{R_I\}) = \Psi(\{r_i\}; \{R_I\})\Phi\{R_I\} \quad (3.6)$$

Where $\Psi(\{r_i\}; \{R_I\})$ is the wave function of electron and parametrically depends on nuclear position R_I , and $\Phi\{R_I\}$ is the wave function of the nuclear with the coordinate sets of R_I . Now we can write the overall Schrodinger equation separately for electrons and nuclei.

$$\text{Nuclei Schrodinger equation: } \hat{H}_{nuc}\Phi\{R_I\} = E_{nuc}\Phi\{R_I\} \quad (3.7)$$

$$\text{Electrons Schrodinger equation: } \hat{H}_{ele}\Psi(\{r_i\}; \{R_I\}) = E\Psi(\{r_i\}; \{R_I\}) \quad (3.8)$$

Where the \hat{H}_{nuc} , \hat{H}_{ele} are the Hamiltonian for nuclei and electrons respectively. The \hat{H}_{ele} can be written as:

$$\hat{H}_{\text{ele}} = -\frac{1}{2} \sum_i \nabla_i^2 + \sum_{i < j} \frac{e^2}{|r_i - r_j|} + \sum_{iI} \frac{eZ_I}{|r_i - r_I|} \quad (3.9)$$

Where the first term is the kinetic energy of electrons, the second term is the electron-electron interaction, and the third term is the electron-nuclei interaction. The second term in the Hamiltonian equation (3.9), the electron-electron interaction, is the critical term and the root of difficulty in solving the equation. As the result of this electron-electron interaction, the individual electron wave function only can be found by simultaneously considering the individual electron wave function of all the other electrons, and this consideration leads to a many body problem.^{18,23}

DFT

DFT calculations are based on two main theorems: Hohenberg–Kohn and Kohn-Sham..²⁴ The first part of the Hohenberg–Kohn theorem states that the ground state energy (in Schrodinger equation) is a unique functional of the charge density. They showed the ground state charge density uniquely determines the external potential (particularly the electron-electron interaction) of the system. Consequently, the ground-state charge density uniquely determines the electron wave function, and energy of ground state. This reduces the number of variables in Schrodinger equation from $3N$ variables wave function, to charge density with only 3 spatial variables. Second part of Hohenberg–Kohn results states that the energy calculated for any charge density is always equal or greater than the ground state energy of the system.^{18,23,24} This part of theory allows us to treat the charge density as a variational variable in search of true ground state energy. The last step to provide a practical method was provided by Kohn-Sham.²⁵ They proved that it is possible to define

a functional of charge density which contains all the many body interaction terms, termed as exchange-correlation functional, and separate this functional from single body terms. These results are stated in following equation:

$$\left[-\frac{\hbar}{2m} \nabla^2 + V_{eff}(r) \right] \Psi_i(r) = \varepsilon_i \Psi_i(r) \quad (3.10)$$

$$V_{eff} = V_{el}(r) + V_{Har}[n(r)] + V_{XC}[n(r)] \quad (3.11)$$

$$V_{XC}[n(r)] = \int dr n(r) \varepsilon_{XC}[n(r)] \quad (3.12)$$

$$E_{DFT}[n(r)] = E_{KE} + \int dr n(r) V_{el}(r) + V_{Har}[n(r)] + V_{XC}[n(r)] \quad (3.13)$$

Where the first term in equation (3.10) is the kinetic energy of non-interacting electrons E_{KE} , the second term $V_{eff}(r)$ is the effective potential and is defined in (3.11). In this equation, the $V_{el}(r)$ is the potential energy of an electron from interaction between an electron and collection of atom nuclei, the $V_{Har}[n(r)]$ is the Hartree potential and is defined as Coulomb repulsion between an electron and the total electron density, and the last term $V_{XC}[n(r)]$ is the exchange-correlation potential and is the key part in DFT calculation. The simplest approach to find the exchange-correlation term is local spin-density approximation (LSDA), which often referred as LDA. In LDA the exchange-correlation energy at each position is defined as exchange-correlation energy of homogenous electron gas at electron density observed at that position (local density).^{25,26} The flow chart shown in Figure 3.7 describes the algorithm use in DFT method to compute the target quantities.

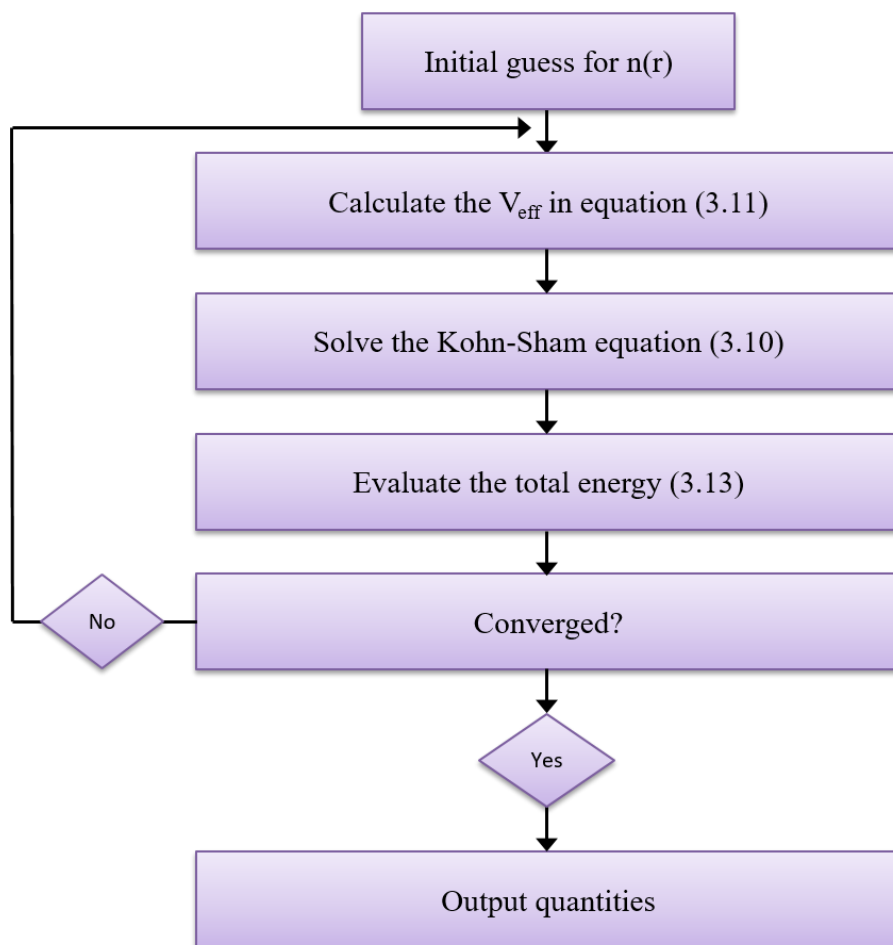


Figure 3.7: The flow chart of calculation process in DFT.

DFT calculations in this thesis, which are discussed in more depth in chapter 7, are categorized in two sections: At First section, a study of the stability and electronic structure properties of several hetrofullerenes including $C_{58}W_2$, $C_{59}W$, and $C_{60}W$ are studied. To generate $C_{59}W$ hetrofullerene, a carbon atom from C_{60} molecule was replaced with a tungsten atom. Figure 3.8 illustrates the configuration of $C_{59}W$. Due to the fact that all the carbon atoms in C_{60} molecule are equivalent, only one initial configuration for $C_{59}W$ is possible. This configuration was relaxed by limited-memory Broyden–Fletcher–Goldfarb–Shanno (LBFGS) algorithm until the maximum

force on all atoms was less than 0.05 eV/\AA .²⁷ The structure of C_{59}W hetrofullerene after optimization is shown in Figure 3.8b.

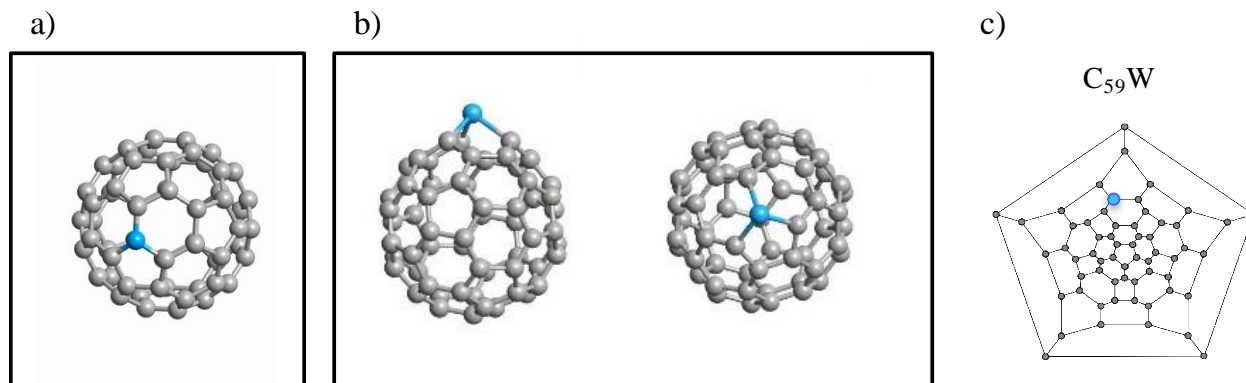


Figure 3.8: C_{59}W hetrofullerene configuration. a) Initial configuration. b) relaxed configuration from two different view angles. c) Schlegel diagram of C_{59}W .

In contrast to C_{59}W structure, there are several initial possible configurations for C_{60}W hetrofullerene. These possible configurations and their total energy after relaxation are shown in Figure 3.9. It was found out the most stable C_{60}W hetrofullerene configuration is obtained by placing a W-atom at center of a hexagon of C_{60} molecule (configuration #1 in Figure 3.9a).

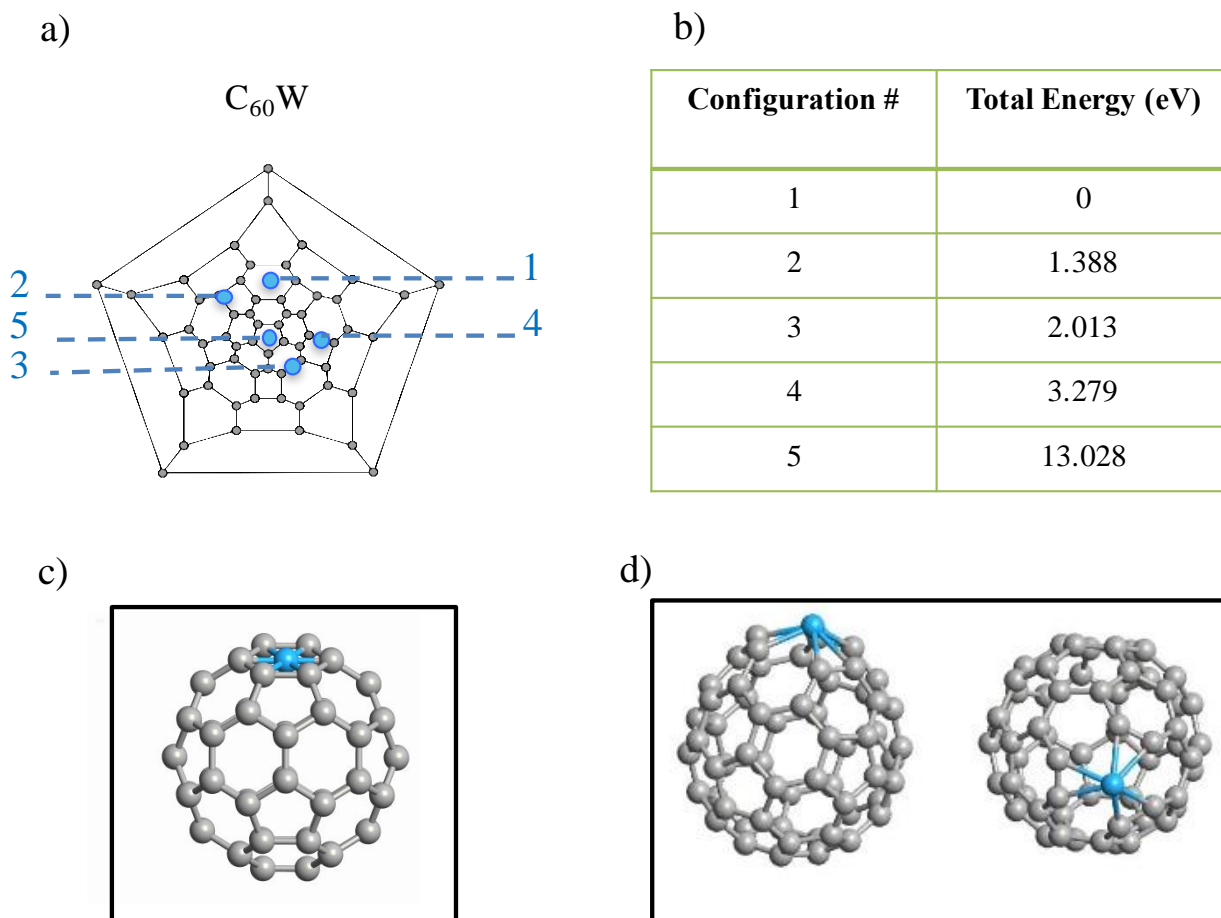


Figure 3.9: $C_{60}W$ hetrofullerene configurations. a) Schlegel diagram of hetrofullerene, the possible initial configurations which were considered in the simulations are labeled from 1-5. b) The total energy calculated for each configuration in (a). The minimum total energy was chosen as zero eV energy. c) Initial structure of configuration #1 d) relaxed structure of configuration #1 from two different view angles.

At second section, the possible adsorption geometries and orientations of C_{60} on W(110) and C_{60} on W(100) are studied. These configurations and the effect of tungsten substrate on electronic structures of C_{60} molecule are discussed in chapter 7.

3.6. References

- (1) Tersoff, J.; Lang, N. D. 1 - THEORY OF SCANNING TUNNELING MICROSCOPY A2 - Stroscio, Joseph A. In *Scanning Tunneling Microscopy*; Kaiser, W. J., Ed.; Academic Press: San Diego, 1993; pp 1–29.
- (2) Meyer, E.; Hug, H. J.; Bennewitz, R. *Scanning Probe Microscopy: The Lab on a Tip*; Springer-Verlag Berlin Heidelberg: Berlin, 2004.
- (3) Binnig, G.; Rohrer, H.; Gerber, C.; Weibel, E. Surface Studies by Scanning Tunneling Microscopy. *Phys. Rev. Lett.* **1982**, 49 (1), 57–61.
- (4) Binnig, G.; Rohrer, H. Scanning Tunneling Microscopy - from Birth to Adolescence. *Reveiwis Mod. Phys.* **1987**, 59 (3), 615–625.
- (5) Wiesendanger, R. *Scanning Probe Microscopy: Analytical Methods*; Springer Science & Business Media, 1998.
- (6) Hamers, R. J. Atomic-Resolution Surface Spectroscopy with the Scanning Tunneling Microscope. *Annu. Rev. Phys. Chem.* **1989**, 40 (1), 531–559.
- (7) Tersoff, J.; Hamann, D. R. Theory and Application for the Scanning Tunneling Microscope. *Phys. Rev. Lett.* **1983**, 50 (25), 1998–2001.
- (8) Feenstra, R. M.; Stroscio, J. A.; Fein, A. P. Tunneling Spectroscopy of the Si(111)2 × 1 Surface. *Surf. Sci.* **1987**, 181 (1–2), 295–306.
- (9) Baratoff, A.; Binnig, G.; Fuchs, H.; Salvan, F.; Stoll, E. Tunneling Microscopy and Spectroscopy of Semiconductor Surfaces and Interfaces. *Surf. Sci.* **1986**, 168 (1), 734–743.
- (10) Becker, R. S.; Golovchenko, J. A.; McRae, E. G.; Swartzentruber, B. S. Tunneling Images of Atomic Steps on the Si(111)7×7 Surface. *Phys. Rev. Lett.* **1985**, 55 (19), 2028–2031.
- (11) Horcas, I.; Fernández, R.; Gómez-Rodríguez, J. M.; Colchero, J.; Gómez-Herrero, J.; Baro, A. M. WSXM: A Software for Scanning Probe Microscopy and a Tool for Nanotechnology. *Rev. Sci. Instrum.* **2007**, 78 (1), 13705–013705–013708.
- (12) Szajman, J.; Liesegang, J.; Jenkin, J. G.; Leckey, R. C. G. Is There a Universal Mean-Free-Path Curve for Electron Inelastic Scattering in Solids? *J. Electron Spectrosc. Relat. Phenom.* **1981**, 23 (1), 97–102.
- (13) Spicer, W. E. Photoemissive, Photoconductive, and Optical Absorption Studies of Alkali-Antimony Compounds. *Phys. Rev.* **1958**, 112 (1), 114–122.
- (14) Watts, J. F.; Wolstenholme, J. *An Introduction to Surface Analysis by XPS and AES*; Wiley, 2003.
- (15) Briggs, D.; Grant, J. T. *Surface Analysis by Auger and X-Ray Photoelectron Spectroscopy*; SurfaceSpectra, 2003.
- (16) Schnadt, J.; Knudsen, J.; Andersen, J. N.; Siegbahn, H.; Pietzsch, A.; Hennies, F.; Johansson, N.; Mårtensson, N.; Öhrwall, G.; Bahr, S.; Mähl, S.; Schaff, O. The New Ambient-Pressure X-Ray Photoelectron Spectroscopy Instrument at MAX-Lab. *J. Synchrotron Radiat.* **2012**, 19 (5), 701–704.
- (17) ATK Manual — QuantumWise 2016.4 documentation
<http://docs.quantumwise.com/manuals/manual.html> (accessed Jan 2, 2017).
- (18) Sholl, D.; Steckel, J. A. *Density Functional Theory: A Practical Introduction*; John Wiley & Sons, 2011.
- (19) *Molecular Quantum Mechanics - Part 3 An Introduction to Quantum Chemistry*; Clarendon Press, 1970.

- (20) Boys, S. F. Electronic Wave Functions. I. A General Method of Calculation for the Stationary States of Any Molecular System. *Proc. R. Soc. Lond. Math. Phys. Eng. Sci.* **1950**, 200 (1063), 542–554.
- (21) Born, M.; Oppenheimer, R. Zur Quantentheorie Der Molekeln. *Ann. Phys.* **1927**, 389 (20), 457–484.
- (22) *Electrons and Phonons*.
- (23) Brázdová, V.; Bowler, D. R. *Atomistic Computer Simulations: A Practical Guide*; John Wiley & Sons, 2013.
- (24) Hohenberg, P.; Kohn, W. Inhomogeneous Electron Gas. *Phys. Rev.* **1964**, 136 (3B), B864–B871.
- (25) Kohn, W.; Sham, L. J. Self-Consistent Equations Including Exchange and Correlation Effects. *Phys. Rev.* **1965**, 140 (4A), A1133–A1138.
- (26) Barth, U. von; Hedin, L. A Local Exchange-Correlation Potential for the Spin Polarized Case. I. *J. Phys. C Solid State Phys.* **1972**, 5 (13), 1629.
- (27) Liu, D. C.; Nocedal, J. On the Limited Memory BFGS Method for Large Scale Optimization. *Math. Program.* **1989**, 45 (1–3), 503–528.

Chapter 4

Substrate Materials

4. Substrate Materials

4.1. C₆₀ on Copper

To gain insight in the interaction between C₆₀ and the Cu-substrate we performed additional experiments where C₆₀ was deposited on a section of the polycrystalline-Cu substrate, which was not covered by graphene. The presence of the Cu (001) surface is confirmed by atomic resolution topography images. This experiment yields information on the C₆₀-Cu interaction, the position of highest occupied molecular orbital (HOMO) and lowest unoccupied molecular orbital (LUMO) peaks and quantitative information about the bandgap compression in C₆₀ single layer islands.¹⁻³ The thickness of the C₆₀ layers varied across the sample, which provides opportunity to measure Cu surface, terraces with less than 1 monolayer (ML) coverage of C₆₀, and regions with a multilayer coverage of C₆₀ in a single image frame.

The spectroscopy and topography data are summarized in the Figure 4.1, which shows a spectroscopy map at 0.4 V and the corresponding topography image. The center section of the topography image is the exposed Cu surface, which is recognized with a high differential conductivity appearing in red color in dI/dV map. The bottom section corresponds to less than 1ML layer of C₆₀ molecules on copper surface, shown in light blue color in dI/dV map. Region located at the top of the image is a C₆₀ multilayer and it is represented with dark blue in dI/dV map. The normalized differential conductance spectra, average on the indicated regions (I,II, and III) are shown in Figure 4.1d; the superimposed error bar expresses the variation of the spectra in selected regions. The bandgap for the multilayer C₆₀ (III) is about 2.3 eV with E_F positioned slightly closer to the conduction band, and the HOMO and LUMO peaks can clearly be identified. In section (II) where the coverage is < 1 ML, the bandgap is decreased (~ 1 eV) and a slight shift of the LUMO (indicated by green arrows) to lower energies is observed.

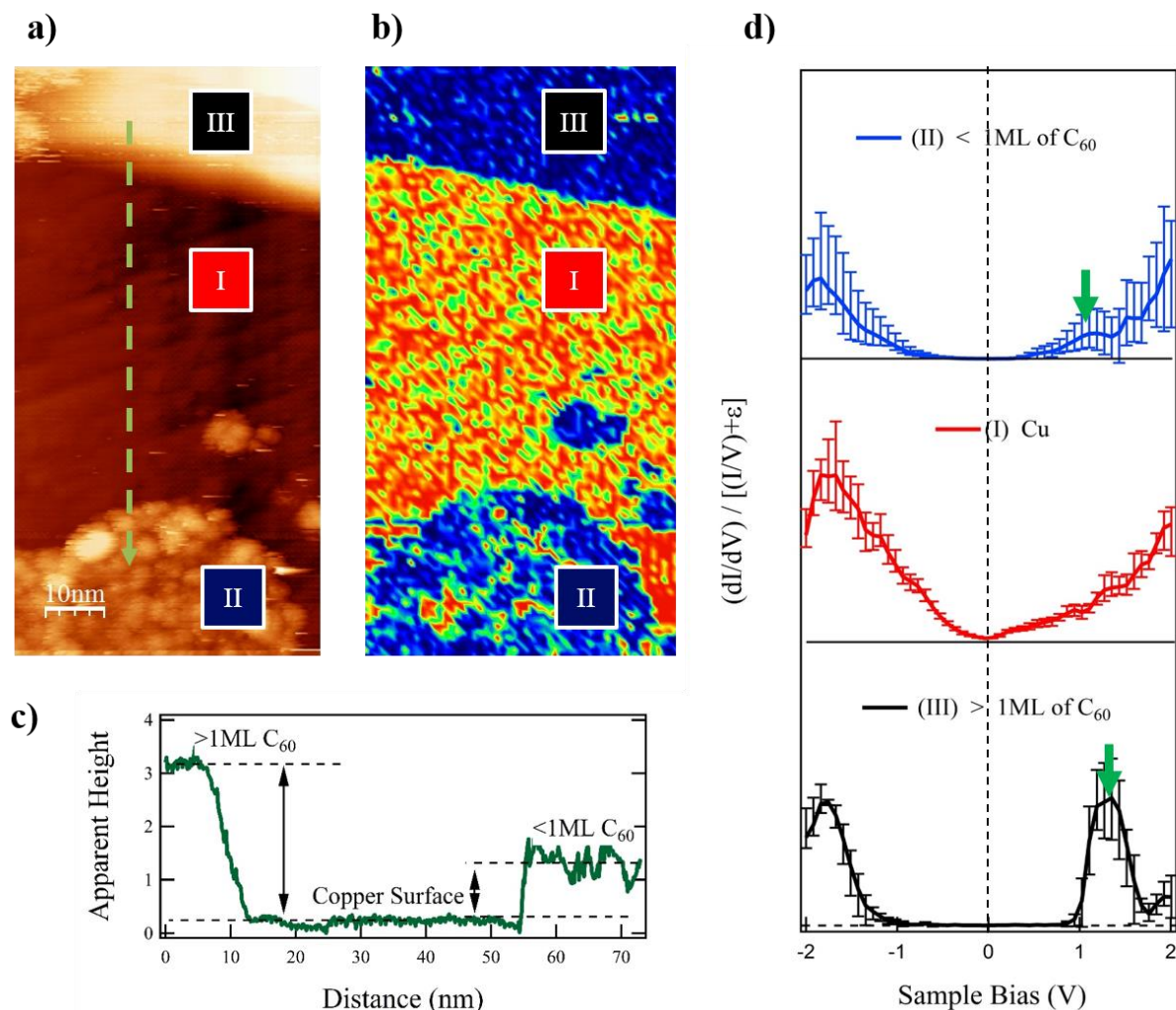


Figure 4.1: Charge transfer and variation of local density of states (LDOS) on Cu/C₆₀ surface. a) Topography image, which includes a region with coverage of <1 ML C₆₀ (bottom), Cu surface (center), and a C₆₀ multilayer island (top). b) Differential conductance map for V=0.40 V. The blue color indicates lower LDOS state and the red color regions show surface area with higher LDOS. c) The linescan profile extracted from topography image (green dashed line in (a)). It shows the height variation across the sample and is aligned with the three regions marked in the topography image. d) Averaged spectra extracted from three regions marked in (a) and (b). The spectra are averaged over 20 individual spectra. The green arrows indicate the LUMO energies, and the dashed line at zero volt is the Fermi energy.

The bandgap compression is common in the molecule layer in contact with a metal substrate and can be linked to several contributions including a charge transfer, image

charge/screening effects, and hybridization between the metal d-band and the molecules electronic states.^{2,4}

No significant contribution from the molecular orbitals is detected in the region of the superlattice peaks described in chapter 6. The spectra for the intercalated C_{60} are therefore not controlled by the molecules electronic states which supports the interpretation of superlattice spectra presented in the chapter 6.

4.2. Magnesium Oxide (MgO)

Single crystal MgO(100) is frequently used as a substrate for the growth of a wide range of thin films, and epitaxial growth can be observed for many metals. In the present work MgO(100) was used as a substrate for the growth of tungsten and tungsten carbide thin films (chapter 7 and 8). MgO substrate is chemically stable against the oxidation and annealing temperature performed in this work. The MgO substrates were clamped to the STM sample plate by two tantalum (Ta) strips as shown in Figure 4.2. For this configuration, in order to ensure a conductive pathway necessary for STM measurements, a small drop of silver paste was placed in the corner of the MgO substrates and extended to Ta stipes.

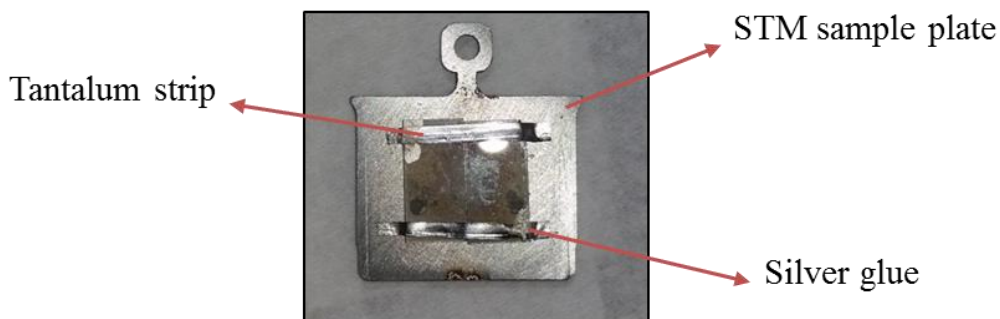


Figure 4.2: photo taken from MgO on STM sample plate. A drop of silver glue was place on top of MgO and Ta strips to ensure the electrons pathway.

To prepare MgO substrates with clean and atomically smooth surfaces extensive amount of work was done in our group.^{5,6} The summary of surface preparation for MgO is described as follows: as received MgO samples (CrysTec) was first exposed to a 30 s etch in 14.6 M H₃PO₄, then rinsed with deionized water and acetone, and finally underwent a 10 hr annealing in air at 1273 K in a box furnace. After this step, the MgO surface was dominated by atomically flat cubic terraces as well as numerous spires up to 40 nm in height which are usually attributed to segregation of calcium contamination to the surface.^{7,8} Several of these spires are indicated by black circles in Figure 4.3, where these can be clearly seen as small circular protrusions. To remove these spires, an additional etching step following by a 5 hr annealing in air was performed. Figure 4.3 shows atomic force microscopy (AFM) images of the MgO substrates after the first and second anneal.

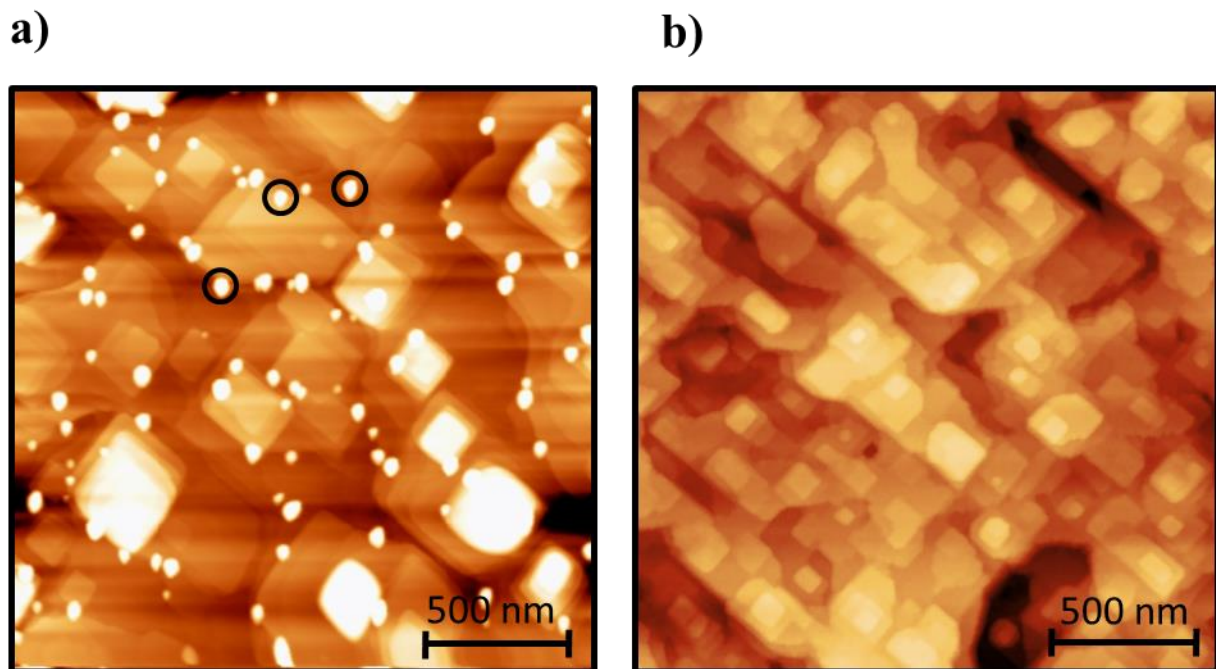


Figure 4.3: AFM images of MgO substrate; a) After 30 sec etching and then 1273 K annealing for 10 hr. several of Ca spires are indicated by black circles. b): After additional etching and annealing step.

4.3. Tungsten (W)

Tungsten thin films were deposited on MgO (100) substrate, which was held at 873-1073K, by electron beam evaporation of tungsten rod. The deposition rate was calibrated with a quartz crystal monitor (QCM) and kept between 0.5-0.8 nm/min. The tungsten thin films with thicknesses between 50-80 nm were synthesized. The W layer, which is grown at 1073 K, shows a relatively smooth surface with height variation as small as 3 Å over each grain and 10 Å at grain boundaries (Figure 4.4). The presence of small grains (100x100 Å²) and short range surface roughness is an indication of limited diffusion of W atoms at 1073 K.

Although the epitaxial growth of a magnetron sputtered W surface on MgO has been reported previously,⁹ for the tungsten surfaces in this work, it is difficult to confirm the epitaxial growth solely from STM data. The MgO(100) surface shows a potential epitaxial relationship to W(110). For this epitaxy, the W(110) is parallel to MgO(100). In a purely geometric model where the interfacial energies are not considered, the misfit of this configuration is about 5.9%. Another possible orientation of W-MgO is for W(100) to be parallel to MgO (100), but the misfit would be much larger (about 22%) in this case. For the purpose of density functional theory simulations, both W(100) and W(110) are considered (chapter 7). In general, the epitaxy of MgO(100) with both BCC and FCC metals has been reported for Fe, Ni, Cu, Pd, Pt, and Pb.^{10,11}

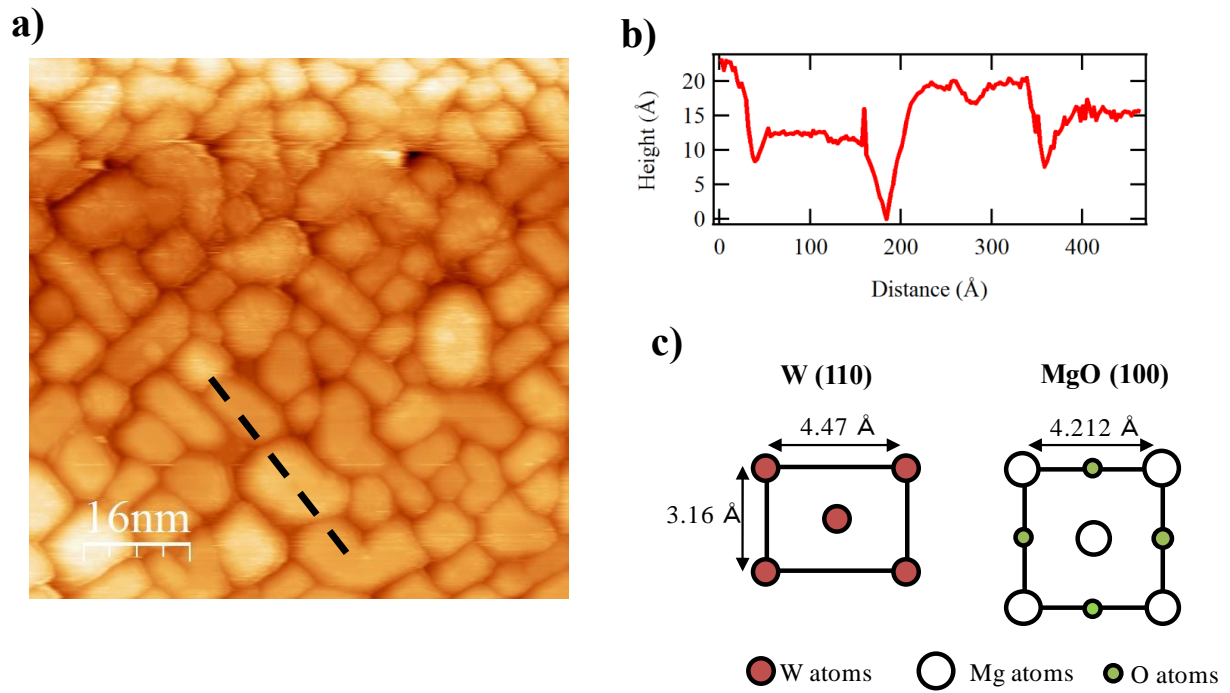


Figure 4.4: a) 50 nm W thin film on MgO(100) deposited at 1073 K. b) Extracted profile from the linescan in (a). c) Schematic representation of W(110) and MgO (100).

4.4. References

- (1) Neaton, J. B.; Hybertsen, M. S.; Louie, S. G. Renormalization of Molecular Electronic Levels at Metal-Molecule Interfaces. *Phys. Rev. Lett.* **2006**, *97* (21), 216405.
- (2) Orientation Dependence of Charge Transfer for C₆₀ on Cu(100). *Appl. Phys. Lett.* **2011**, *98* (13), 133303.
- (3) Sau, J. D.; Neaton, J. B.; Choi, H. J.; Louie, S. G.; Cohen, M. L. Electronic Energy Levels of Weakly Coupled Nanostructures: C₆₀-Metal Interfaces. *Phys. Rev. Lett.* **2008**, *101* (2), 26804.
- (4) Tamai, A.; Seitsonen, A. P.; Baumberger, F.; Hengsberger, M.; Shen, Z.-X.; Greber, T.; Osterwalder, J. Electronic Structure at the C₆₀ Metal Interface: An Angle-Resolved Photoemission and First-Principles Study. *Phys. Rev. B* **2008**, *77* (7), 75134.
- (5) Synthesis and oxidation of non-stoichiometric tungsten carbide studied by scanning tunneling microscopy/spectroscopy. Master. University of Virginia (2014). Print. <http://libra.virginia.edu/catalog/libra-oa:3096> (accessed Jul 20, 2015).
- (6) Growth of Ni and Ni-Cr Alloy Thin Films on MgO(001): Effect of Alloy Composition on Surface Morphology. *J. Appl. Phys.* **2016**, *120* (22), 225302.
- (7) Minamikawa, T.; Suzuki, T.; Yonezawa, Y.; Segawa, K.; Morimoto, A.; Shimizu, T. Annealing Temperature Dependence of MgO Substrates on the Quality of YBa₂Cu₃O_x Films Prepared by Pulsed Laser Ablation. *Jpn. J. Appl. Phys.* **1995**, *34* (8R), 4038.
- (8) Cukauskas, E. J.; Kirchoefer, S. W.; Chang, W. Morphology and Dielectric Properties of Ba_{0.5}Sr_{0.5}TiO₃ Thin Films on Annealed (1 0 0) MgO. *J. Cryst. Growth* **2002**, *236* (1–3), 239–247.
- (9) Palmquist, J.-P.; Czigany, Z.; Odén, M.; Neidhart, J.; Hultman, L.; Jansson, U. Magnetron Sputtered W–C Films with C₆₀ as Carbon Source. *Thin Solid Films* **2003**, *444* (1–2), 29–37.
- (10) Thürmer, K.; Koch, R.; Weber, M.; Rieder, K. H. Dynamic Evolution of Pyramid Structures during Growth of Epitaxial Fe (001) Films. *Phys. Rev. Lett.* **1995**, *75* (9), 1767–1770.
- (11) M KATO, M. W. Overview No. 78 Epitaxy of Cubic Crystals on (001) Cubic Substrates. *Acta Metall.* **1989**, *37* (3), 749–756.

Chapter 5

STS Maps for Investigation of Surface Reaction at Nanoscale

5. STS Maps for Investigation of Surface Reaction at Nanoscale

5.1. Introduction

Scanning tunneling microscopy/spectroscopy (STM/STS) is a powerful tool to characterize the geometric and electronic structure of a surface, and to investigate surface chemical reactions with atomic resolution. In addition to topography measurements in STM, it is also possible to explicitly study the surface local density of states (LDOS) through STS measurements. STS is performed by acquiring tunneling current while varying the bias voltage as the distance between tip and sample is kept constant and the current voltage characteristics are measured (described in Chapter 3 in more details). STS data are typically acquired in two different modes:

(a) point spectroscopy: where I-V curves are measured at specific point on the image area

(b) grid spectroscopy: where I-V curves are measured within a given image area on a predefined and regularly spaced grid. In order to obtain simultaneously information about topography and electronic structure of the surface, a scanning tunneling (ST) spectrum is recorded at every STS grid points (n) with the feedback loop open (turned off), and for all the points between STS grid positions (n - n+1), the feedback loop is closed (turned on) and STM topography is recorded. The the I-V curves recorded at the STS grid points will be process to yield conductance (dI/dV) and band gap maps, and these maps can be correlated with the topographic image.

The tunneling current measured in STM can be derived within the Wentzel Kramers Brillouin (WKB) approximation and is given by following expression:^{1,2}

$$I \propto \int_0^{eV_b} \rho_s(E) \rho_t(E + eV_b) T(E, eV_b) dE \quad (5.1)$$

Where $\rho_s(E)$ is the local density of states (LDOS) of the sample, $\rho_t(E + eV)$ is the LDOS of the tip, $T(E, eV)$ is the transmission coefficient of the electron throughout the tunnel barrier, E is energy of states relative to the Fermi level, and eV is the applied bias voltage. At a fixed sample to tip distance, the change in transmission coefficient with applied bias voltage is monotonic.^{3,4} Hence, the derivation of equation 5.2 can be written as:

$$\frac{dI}{dV} \propto \rho_s(r, E) \rho_t(E + eV_b) T(d, E, eV_b) \quad (5.2)$$

Therefore, the dI/dV is a good approximation to the LDOS of the sample at the point of measurement on the surface.^{1,5,6} The dI/dV curves can be obtained either by numerical differentiation of I-V curves or measured directly using the lock-in technique. The lock-in technique is performed by applying a high frequency sinusoidal modulation voltage that is superimposed on the bias voltage. Therefore, a STS measurement by using the lock-in technique requires longer time for data acquisition (~5 times longer than without lock-in), and thermal drift during the STS measurements becomes an important factor that it need to be considered. Hence, this technique is often utilized in STS measurements at low temperatures (<77 K). Because of the small thermal drift at low temperature, it is possible to measure dI/dV curves several times at specific point of a surface, which results in an excellent signal-to-noise ratio. The capability of acquiring high quality STS spectrum is the main advantage of this method. A grid spectroscopy with lock-in technique is possible, however it requires several hours. Therefore, the grid STS by using lock-in is not suitable for the targeted observation of surface reactions with several intermediate steps in a relatively narrow time window.

In this work, the surface reactions as a function of annealing temperature and gaseous environments (in UHV or in presence of oxygen) for several complex material systems is investigated. In these types of studies, time and temperature are the critical parameters. Therefore, grid STS measurements were performed at room temperature and the dI/dV curves were obtained with numerical differentiation. In this thesis, this method is referred to as “rapid acquisition technique”. The relatively short data acquisition time in this technique allows for assessment of several reaction steps on a single sample (<24 hours). However, the signal-to-noise ratio achieved in this method is smaller than in the lock-in technique. This disadvantage is balanced by the acquisition of a large number of spectra within a grid. The maps acquired by this technique have been utilized to study nanostructure synthesis, nanomaterial growth, C₆₀ molecule interaction with the metallic surface (chapter 7), graphene manipulation (chapter 6), and processing assessment (chapter 8).^{7–10}

5.2. Methods

The topographic STM images are often measured with a resolution of 512×512 pixels and the STS grid can be at the same resolution as the image, i.e. 1×1 grid which gives 512×512 STS curves; To decrease the acquisition time and avoid a large thermal drift, the number of pixels at STS grid are often smaller than the simultaneously measured topographic image. The most common STS grid that was used in this work is a 5×5 grid, where STS curves are recorded at every 5th point of the topographic images, and bias voltage resolution was at 51 points. This STS grid results in 103×103 I-V curves and ~500,000 data points for each map. Therefore, to manage and process these large amount of data, a MATLAB code and a graphical user interface (GUI) was developed. This GUI is capable of generating conductance and band gap maps, and performing several normalization methods.

The first step in the analysis of the I-V characteristics obtained by rapid acquisition technique is a numerical differentiation which yields dI/dV. Due to direct relation between dI/dV values and transmission coefficient (equation 5.2), the dI/dV spectra depend exponentially on separation distance between tip and sample. Therefore, to remove this exponential dependence a normalization method has to be performed.¹¹⁻¹⁴ Several normalization methods for dI/dV spectra are available in this GUI. Here we discuss briefly the two most frequently used normalization methods.

The most commonly used normalization factor is the tunneling resistance (I/V), which provide an estimate for transmission function. In this method, the (dI/dV) curves are divided by the ratio of the measured current over voltage. It has been shown that (dI/dV)/(I/V) is proportional to LDOS of the sample.¹⁵ Figure 5.1 shows the various stages of this normalization process for a spectrum acquired from graphene on copper sample.

With this normalization, for the current values close to zero or around the noise level (I~0), the (I/V) parameter becomes noisy and diverges, resulting in an artificial peak in the normalized curves (Figure 5.1c). To fix this issue a small constant (ϵ) is added to the denominator.¹⁶ This offset is used to avoid singularity at the band edges and at V=0. Thus, the final equation for the normalized dI/dV converts to the following:

$$\text{normalized spectra (I)}: \frac{\frac{dI}{dV}}{\frac{I}{V} + \epsilon} \quad (5.3)$$

Figure 5.1d illustrate the influence of ϵ on a normalized curve. By increasing the value of ϵ the magnitude of the artificial peak at V~0 decreases and eventually at $\epsilon=1.5$ (nA/V) the artificial peak disappears without any change in overall shape of curve. This normalization works on the

dI/dV curves obtained from both metallic and semiconducting surfaces and it was the method of choice in this work.

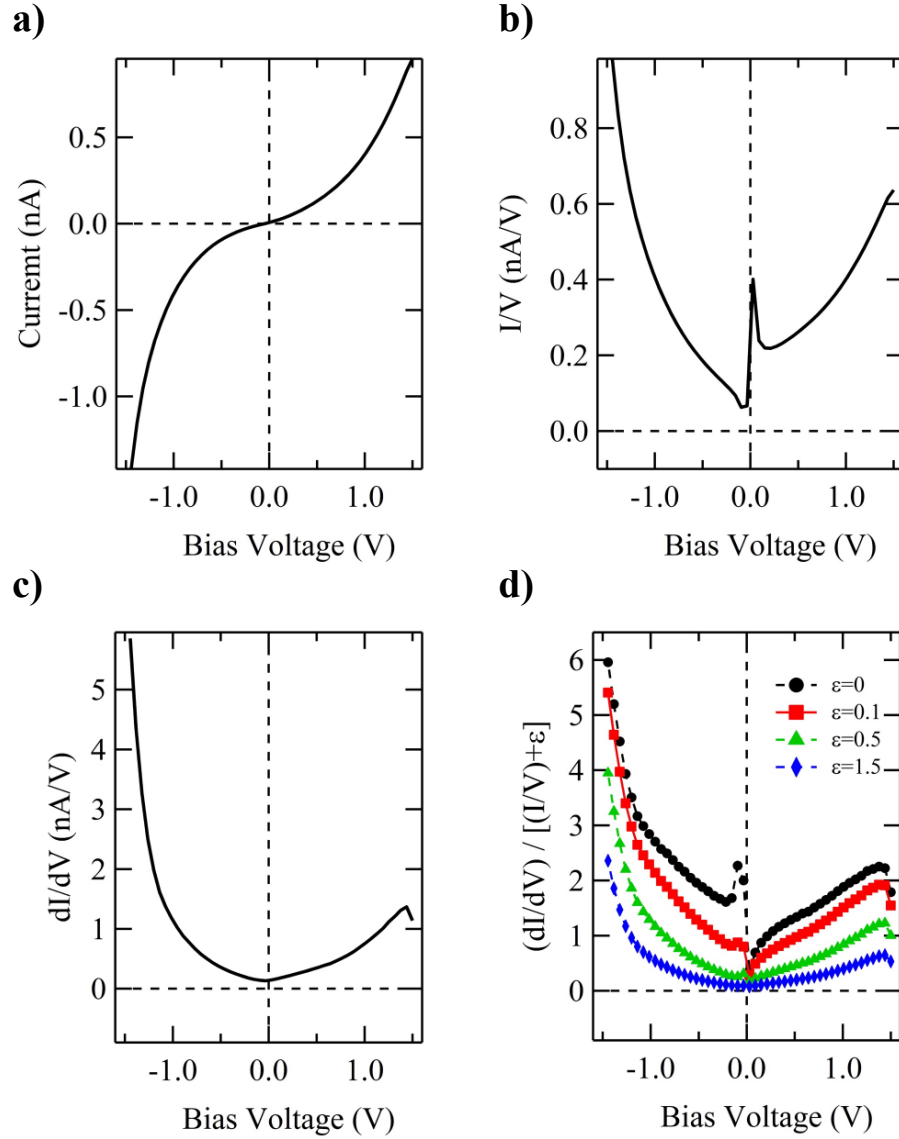


Figure 5.1: Spectrum acquired from graphene on copper sample. a) I-V curve. c) The normalization parameter (I/V) , where a divergence is observed at $V \sim 0$. c) After differentiation of I-V curve and before normalization. d) Normalized dI/dV for several ϵ values.

Another method to correct the divergence issues for current values close to zero is to broaden I/V values with a one pole Fourier low pass filter.^{17,18}

$$\text{normalized spectra (II): } \frac{dI/dV}{\left(\frac{\bar{I}}{\bar{V}}\right)} \quad (5.4)$$

where the $\left(\frac{\bar{I}}{\bar{V}}\right)$ is the broadened total conductivity (I/V). This method is often used for materials with large bandgap (bandgap > 1.5 eV).

In a grid STS, after acquiring the normalized spectra with one of the methods explained above, there are two ways to illustrate all the data:

- i) Differential conductivity (dI/dV) maps at specify energy, which correlate to LDOS of the sample in the image area. To acquire a data point for an individual pixel in this map, a single value in the voltage range has to be selected. Selecting different voltages is equivalent to plotting the LDOS of every single X-Y point at corresponding energy. These types of calculation have to be done for every single point of the maps, which often includes more than ten thousand points.
- ii) The band gap map, which generate a bandgap value from each I-V characteristic.

In this GUI, there are two methods available to calculate a single value for the bandgap from each normalized dI/dV curve.

Bandgap by Method I: The simplest method to calculate the bandgap from I-V characteristics is to assign the range of energies with near zero conductance (or zero current) as the bandgap, since in this range there are no available states (Figure 5.2a), i.e. the energy range where:

$$\frac{dI/dV}{\left(\frac{\bar{I}}{\bar{V}}\right) + \varepsilon} \sim 0 \quad (5.5)$$

To determine the near zero conductance region, the background noise level for the instrument is used. This method is proven to be successful in determining the bandgap values from different types of samples (e.g. oxide, metallic, semiconducting surface).^{7,10,19}

Bandgap Method II: Another way of calculating the bandgap from normalized differential conductance is to determine the valence band (VB) and conduction band (CB) edges from differential conductance curves.^{20,21} In this method, two lines are tangent to the valence and conduction band edges and the third line is fitted to describe the data points in the bandgap region. The intersection of these lines determines the edges of CB and VB, which allows the calculation of the band gap (Figure 5.2b).

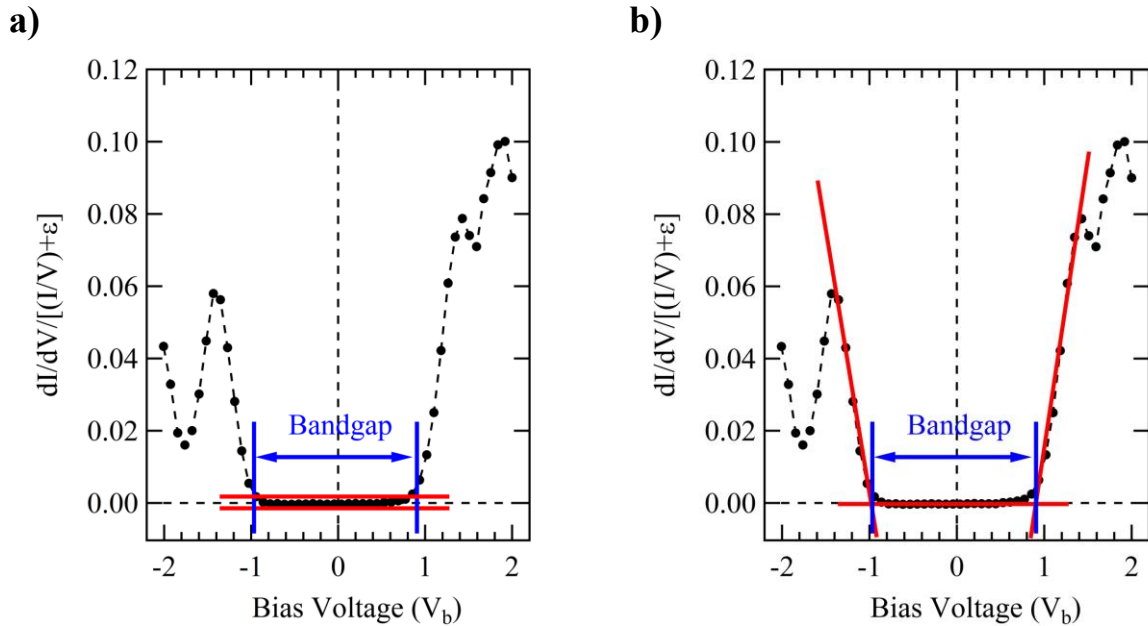


Figure 5.2: Spectrum acquired from multilayer of C_{60} molecules on graphene. The dashed line indicates the Fermi energy. a) Determination of the band gap by method I. the cutoff value is determined by noise level in instrument. b) Determination of the band gap by method II.

This method always works well in materials with a steep VB/CB slope. All these calculations are applied to every normalized dI/dV curves to generate a bandgap map. In this thesis,

conductance or bandgap maps were used to differentiate between different species on the surface, and to compare the initial surface and the surface after chemical modification (e.g. oxidation, carburization, diffusion, chemisorption, and nanomaterial synthesis). In addition, the GUI allows the user to extract the spectroscopy curves from small regions of interest on the surface.

Figure 5.3 shows a snapshot of this GUI after importing a grid point STS map. The two contour maps on the left side represent the dI/dV map and the normalized dI/dV map. The slide bar allows to select various voltage plane and replot the dI/dV and normalized dI/dV contour maps at new selected voltage. The two contour plots at the right side, represent the bandgap map calculated from dI/dV data before and after normalization. The two plot at the right side of the snapshot, illustrate the extracted dI/dV and normalized dI/dV curves from a selected area. These maps are a critical tool for the study of nanoscale reaction and material manipulation studied in this thesis.

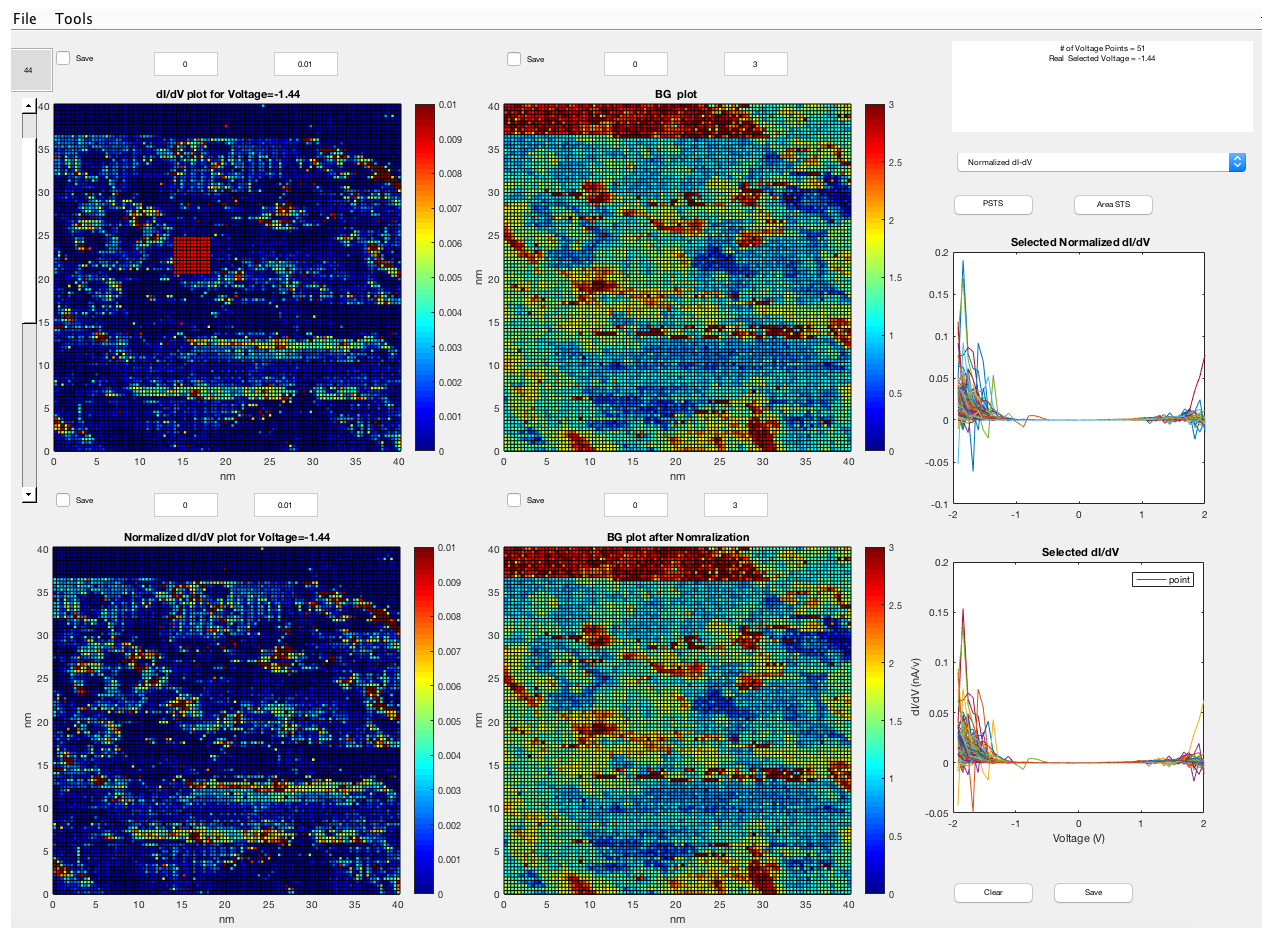


Figure 5.3: Snapshot of the GUI designed for grid STS analysis. The red square in top-left contour map highlights the area that the spectra were extracted.

5.3. References

- (1) Hamers, R. J. Atomic-Resolution Surface Spectroscopy with the Scanning Tunneling Microscope. *Annu. Rev. Phys. Chem.* **1989**, 40 (1), 531–559.
- (2) Wiesendanger, R. *Scanning Probe Microscopy: Analytical Methods*; Springer Science & Business Media, 1998.
- (3) Coombs, J. H.; Gimzewski, J. K.; Reihl, B.; Sass, J. K.; Schlittler, R. R. Photon Emission Experiments with the Scanning Tunnelling Microscope. *J. Microsc.* **1988**, 152 (2), 325–336.
- (4) Payne, M. C.; Inkson, J. C. Measurement of Workfunctions by Tunnelling and the Effect of the Image Potential. *Surf. Sci.* **1985**, 159 (2), 485–495.
- (5) Baratoff, A.; Binnig, G.; Fuchs, H.; Salvan, F.; Stoll, E. Tunneling Microscopy and Spectroscopy of Semiconductor Surfaces and Interfaces. *Surf. Sci.* **1986**, 168 (1), 734–743.
- (6) Becker, R. S.; Golovchenko, J. A.; McRae, E. G.; Swartzentruber, B. S. Tunneling Images of Atomic Steps on the Si(111)7×7 Surface. *Phys. Rev. Lett.* **1985**, 55 (19), 2028–2031.
- (7) Volders, C.; Monazami, E.; Ramalingam, G.; Reinke, P. Alternative Route to Silicene Synthesis via Surface Reconstruction on H-MoSi₂ Crystallites. *Nano Lett.* **2017**, 17 (1), 299–307.
- (8) Monazami, E.; McClimon, J. B.; Rondinelli, J.; Reinke, P. Electronic Structure and Band Gap of Fullerenes on Tungsten Surfaces: Transition from a Semiconductor to a Metal Triggered by Annealing. *ACS Appl. Mater. Interfaces* **2016**.
- (9) McClimon, J. B.; Monazami, E.; Reinke, P. Interaction of C₆₀ with Tungsten: Modulation of Morphology and Electronic Structure on the Molecular Length Scale. *J. Phys. Chem. C* **2014**, 118 (42), 24479–24489.
- (10) Monazami, E.; Bignardi, L.; Rudolf, P.; Reinke, P. Strain Lattice Imprinting in Graphene by C₆₀ Intercalation at the Graphene/Cu Interface. *Nano Lett.* **2015**.
- (11) Selloni, A.; Carnevali, P.; Tosatti, E.; Chen, C. D. Voltage-Dependent Scanning-Tunneling Microscopy of a Crystal Surface: Graphite. *Phys. Rev. B* **1985**, 31 (4), 2602–2605.
- (12) Lang, N. D. Spectroscopy of Single Atoms in the Scanning Tunneling Microscope. *Phys. Rev. B* **1986**, 34 (8), 5947–5950.
- (13) Stroscio, J. A.; Feenstra, R. M.; Fein, A. P. Electronic Structure of the Si(111)2×1 Surface by Scanning-Tunneling Microscopy. *Phys. Rev. Lett.* **1986**, 57 (20), 2579–2582.
- (14) Feenstra, R. M. Scanning Tunneling Spectroscopy. *Surf. Sci.* **1994**, 299–300, 965–979.
- (15) Mårtensson, P.; Feenstra, R. M. Geometric and Electronic Structure of Antimony on the GaAs(110) Surface Studied by Scanning Tunneling Microscopy. *Phys. Rev. B* **1989**, 39 (11), 7744–7753.
- (16) Feenstra, R. M.; Lee, J. Y.; Kang, M. H.; Meyer, G.; Rieder, K. H. Band Gap of the Ge (111)c(2×8) Surface by Scanning Tunneling Spectroscopy. *Phys. Rev. B* **2006**, 73 (3), 35310.
- (17) Feenstra, R. M. Tunneling Spectroscopy of the (110) Surface of Direct-Gap III-V Semiconductors. *Phys. Rev. B* **1994**, 50 (7), 4561–4570.
- (18) Stroscio, J. A.; Kaiser, W. J. *Scanning Tunneling Microscopy*; Academic Press, 1993.
- (19) Ramalingam, G.; Monazami, E.; Reinke, P. Evolution of Atomic and Electronic Structure of Ni(001) Surface during Oxidation. *in preparation*.

- (20) Ritter, K. A.; Lyding, J. W. The Influence of Edge Structure on the Electronic Properties of Graphene Quantum Dots and Nanoribbons. *Nat. Mater.* **2009**, 8 (3), 235–242.
- (21) Kwon, S.-Y.; Ciobanu, C. V.; Petrova, V.; Shenoy, V. B.; Bareño, J.; Gambin, V.; Petrov, I.; Kodambaka, S. Growth of Semiconducting Graphene on Palladium. *Nano Lett.* **2009**, 9 (12), 3985–3990.

Chapter 6

Strain Lattice Imprinting in Graphene by C₆₀ Intercalation at the Graphene/Cu Interface

E. Monazami¹, L. Bignardi^{2,3}, P. Rudolf² and P. Reinke¹

(1) University of Virginia, 395 McCormick Road, P.O. Box 400745,
Charlottesville, Virginia 22904- 4745, United States

(2) Zernike Institute for Advanced Materials, University of Groningen, Nijenborgh
4, NL-9747AG Groningen, The Netherlands

(3) *Present address: Physikalisches Institut, Universität Münster, Wilhelm-
Klemm Str. 10, 48149 Münster, Germany

6. Strain Lattice Imprinting in Graphene by C₆₀ Intercalation

6.1. Abstract

Intercalation of C₆₀ molecules at the graphene-substrate interface by annealing leads to amorphous and crystalline structures. A comparison of topography and electronic structure with wrinkles and moiré patterns confirms intercalation. The intercalated molecules imprint a local strain/deformation on the graphene layer whose magnitude is controlled by the intermolecular distance. The crystalline intercalated structure exhibits a superlattice peak in the local density of states. This work provides control of local strain in graphene.

6.2. Introduction

The unique physical, chemical and mechanical properties of graphene have attracted unprecedented attention and have lead in the past decade to the development and augmentation of a wide range of applications. These include electronic devices that make use of the unique Dirac-type band structure at the K-point.¹⁻³ Graphene's two-dimensional structure allows modulation of its properties through the interaction with the substrate or by surface adsorbates.⁴⁻¹⁷ This approach is highly versatile and can modify graphene's properties while simultaneously conserving the Dirac cone. The challenge is to find suitable pathways to achieve the desired graphene modulation. We focus in our work on the implementation of well-defined strain fields^{18,19} by intercalation of C₆₀ molecules at the graphene-Cu interface. This creates highly localized strain states introduced in the graphene layer by the buried molecules, whose spatial distribution can be controlled by the intercalation process.

The main strategies to modify graphene and achieve new functionalities are currently (i) doping by intercalation,^{13,20,21} (ii) superposition of a periodic potential by superlattices,^{22,23} (iii) introduction of local strain,²⁴ (iv) electrostatic modulation,⁹ (v) chemical functionalization, (vi) ionic-liquid induced doping,²⁵ and (vii) nanoscale patterning to form nanoribbons and achieve control of the edge states and electronic confinement.²⁶ Our study combines strategies i to iii and expands the available intercalation strategies by use of molecular intercalants. Intercalation is a well-known method to achieve charge doping in layered van der Waals bonded materials such as graphite or h-BN. For graphene, the intercalation of alkali metals at the graphene-SiC interface has been used to achieve charge doping as a means to introduce a bandgap.¹⁵ On the other hand, graphene can be electronically decoupled from a metal substrate by the intercalation of weakly interacting metal atoms nearly restoring the Dirac cone.²¹ The intercalation of Pb islands at the

graphene–Ir(111) interface introduces a significant enhancement in the spin–orbit splitting for charge carriers residing in graphene which potentially leads to novel physical phenomena.²⁷

The introduction of localized strain modifies the charge transport in graphene through a change in the on-site energies of the pz orbitals of adjacent carbon atoms and in turn influences the hopping parameter. The impact of strain on graphene’s electronic structure has been discussed in numerous theoretical studies^{9,18,23,24,28–33} and has recently been described in the framework of a pseudo-magnetic field, whose strength depends on the magnitude and symmetry of the strain field.^{19,34} The experimental challenges in creating well-defined and stable strain states are considerable and have been approached by substrate patterning with trenches, electrostatically driven deformation, thermally induced ripple structures,³⁵ and by gas intercalation to form nanobubbles.¹⁹

The work on C₆₀ intercalation at the graphene–Cu interface presented in this study establishes a new strategy to control local strain and achieves at the same time positional control of the strained regions in amorphous and crystalline structures. Scanning tunneling microscopy (STM) and spectroscopy (STS) are used to study the electronic and topographic signatures of the intercalated material. The intercalation of C₆₀ at the graphene–Cu interface was achieved for a polycrystalline Cu substrate by a thermally activated process. The direct comparison between wrinkles,^{24,36,37} moiré patterns and intercalated structures is used to confirm the intercalation process and establish a set of criteria for the assessment of molecular intercalants.

6.3. Methods

This study was performed in an Omicron Variable Temperature ultrahigh vacuum scanning probe microscope with a base pressure of $<2 \times 10^{-10}$ mbar, which is connected to a preparation chamber. The graphene sample 1 (SA1) was purchased from Graphene Supermarket, and sample

2 (SA2) was grown by CVD on polycrystalline copper. The growth process for SA2 is described in ref.³⁸ Both sample surfaces were dominated by single layer graphene, albeit SA2 had a lower graphene coverage as deduced from STM imaging. Both samples show extended regions of Cu(100) grains, which was the focus of our work. Atomic resolution images of graphene as well as the Cu-surface were obtained for both samples. The samples were annealed prior to STM measurements and intercalation experiments to about ~623 K for 20 min to remove adsorbates and reduce the Cu-surface. Atomically resolved STM images of the bare Cu(100)-surface³⁹ recorded in close proximity to graphene and intercalated structures of interest, confirm that the oxide has been removed in all areas used for study in the present manuscript. In addition, moiré patterns seen on SA1 and SA2 are commensurate with a clean Cu-graphene interface and an example is included in Figure 6.1. Higher annealing temperatures were avoided to minimize ripple formation caused by the different thermal expansion coefficient in Cu and graphene. Yang et al.⁴⁰ demonstrated that oxide formed on Cu by oxidation in ambient can indeed be removed completely by annealing in vacuum at 573 K, which is commensurate with our observations, whereas oxidation at higher temperatures forms a more resilient oxide. We assume that oxygen contamination in the gas phase during graphene growth can lead to a much more persistent oxide layer, and details of graphene growth on Cu-oxide have been discussed by Gottardi et al.⁴¹

C₆₀ was deposited by thermal evaporation of high purity C₆₀ powder (MerCorp) from a h-BN crucible with graphite liner. The deposition rate was measured with a quartz crystal monitor and kept constant at 1 ML/min; the C₆₀ layer was deposited at room temperature and the thickness of the initial C₆₀ layer was between 2 and 20 ML. The Cu-graphene-C₆₀ sample was then annealed at temperatures between 573 and 753 K for 5–20 min to drive the molecules into the interfacial space and achieve intercalation. Intercalation was observed for annealing temperatures above 623

K (above the sublimation temperature of C_{60}), shorter annealing times (<10 min), and shorter ramp up-times to annealing temperature (<10 min) likewise favor intercalation over complete desorption. A shorter overall time (ramp-up plus annealing time) is favorable for the formation of an ordered (crystalline) over a disordered (amorphous) intercalate.

The initial graphene surface and each deposition step were studied with STM and STS. The sample preparation and deposition was performed in a preparation chamber, which shares the vacuum with the microscope, and the samples, therefore, were kept under UHV conditions for the entirety of the experiment. STM images were recorded in constant current mode at room temperature with electrochemically etched tungsten tips. A tunneling current of 1 nA was used for all STM images. Typically, graphene was measured with $V_{\text{bias}} = +0.085$ V for the best image quality, and the voltage was varied between 0.085 and 0.3 V for some of the intercalated structures. STS data sets were measured on graphite and Au to confirm reproducibility and reliability of the tip performance. STM and STS data were analyzed with WSxM 5.0,⁴² Igor Pro 6.22, and a Matlab program was developed for analysis and visualization of STS maps.

The STS maps were measured on a grid of 103×103 equidistant spectra within a 512×512 pixel topography image. The feedback-loop was switched off for every ST spectrum, and switched on for topography imaging in between spectra. The derivative dI/dV and normalized conductance $dI/dV/(I/V)$ [differential conductance] spectra were obtained numerically using the methods described by Feenstra and Tromp.^{43–45} Topography images, which were recorded simultaneously with the STS maps, were used to calculate drift between subsequent STS maps. In the analysis of the crystalline intercalated structure, we averaged over five drift-corrected STS maps measured consecutively to improve the signal-to-noise ratio.

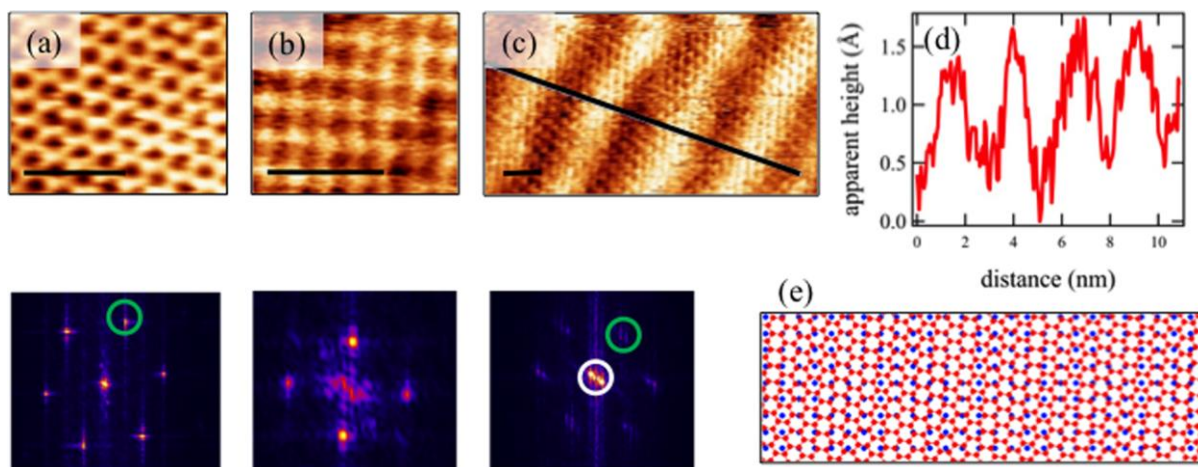


Figure 6.1: STM topography images of (a) graphene surface, (b) Cu(001), (c) moiré pattern with superimposed graphene honeycomb lattice, and (d) linescan along the diagonal of (c). The bottom row shows the corresponding Fourier transforms illustrating the hexagonal and square lattices, respectively. The green circles mark graphene spots, and the white circle marks the moiré pattern with its longer wavelength. (E) Geometric simulation of the moiré pattern for a 5° rotation between graphene and Cu lattice, which corresponds to the one seen in (c). The scalebar is 1 nm in all images.

6.4. Results and Discussion

The results section first discusses the wrinkles in graphene as an example for a free-standing graphene, and will then move on to moiré patterns between graphene and Cu(001) as examples of a superlattice imprinted on graphene. We will then introduce amorphous intercalates (where the intercalated molecules are arranged in an irregular manner) and crystalline intercalates (where the C_{60} molecules are arranged in a regular, square pattern) and compare the topographic and electronic structure of wrinkles, moiré pattern, and intercalated material. This comparison is used to confirm successful intercalation and it illustrates the significant variation between the structures.

Figure 6.2 displays the STM and STS data obtained for wrinkles, which form after sample annealing due to the mismatch of thermal expansion coefficients of graphene and Cu. Wrinkles are regions on the surface where graphene has detached from the substrate but is not folded over.⁴⁶ Figure 6.2a shows an example of a complex 4-fold wrinkle on SA2, and Figure 6.2b is a single

wrinkle; both were observed after deposition of 18 molecular layers of C_{60} on SA2, and annealing at 723 K for 5 min with a ramp-up time of 15 min to drive the intercalation. The intercalate seen on other sections of this sample had an amorphous structure as discussed in the next section. The images of the wrinkles, and the atomic resolution of the honeycomb lattice (Figure 6.2c), confirm that the graphene is not folded in on itself. The graphene lattice is resolved across the entire wrinkle and Figure 6.2d–f summarize the spectroscopy data. The black square in Figure 6.2d is the same image section as the 3D depiction in Figure 6.2b, and marks the region of the STS map in Figure 6.2e. The map is a cut through all dI/dV spectra at 9.2 mV in the conduction band. The higher dI/dV values on the wrinkle itself are distinguished in the color-coded map by a green color, whereas blue corresponds to a lower dI/dV value characteristic of the Cu– graphene signature expected on either side of the wrinkle. The ST spectra of the fullerene layers prior to intercalation show the fullerene bandgap of 2.3 eV are identical to spectra measured previously with STS⁴⁷ and agree with the spectra of the occupied and unoccupied electronic states of C_{60} on graphite as determined by photoemission and X-ray absorption.⁴⁸ The fullerene layer has a thickness of a few MLs and the bandgap is fully developed with E_F positioned at the center of the gap.

The corresponding differential conductance spectra are shown in Figure 6.2f, which includes the spectra for graphene on Cu recorded at the edge of the measurement window, graphene at the center of the wrinkle, and graphene at the boundary of the wrinkle. Each of these spectra is averaged over the area marked by the green and blue lines, respectively; the error bar indicates the variation of spectral signatures along this line. E_D is tentatively assigned to the lowest dI/dV value and is marked with an arrow. The STS for graphene on Cu is measured at the left side of the images and several nanometer removed from the wrinkle. The shape of the spectra at the

edge of the fold along the blue line replicate the general shape of the graphene on Cu spectra except for a slight shift of E_D by ~ 0.06 eV, and superposition of several weak, step-like features.

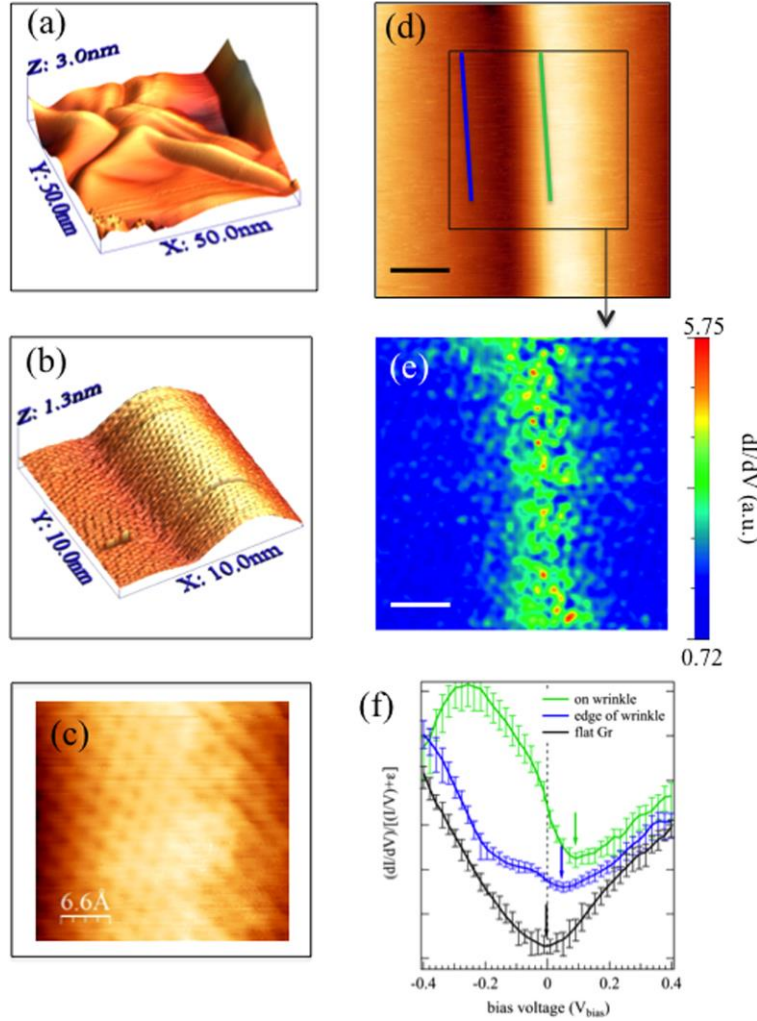


Figure 6.2: (a) 3D image of a four-way wrinkle in graphene, (b) 3D image of a single wrinkle with atomically resolved graphene lattice as shown in (c), which was recorded at the center of the wrinkle. (d) Top view of the same wrinkle shown in (b) (scale bar = 5 nm); the green (blue) line corresponds to the line along which the ST spectra from (f) were collected and averaged. (e) STS map for $V_{bias} = 9.2$ mV within the boxed area marked in (d). The wrinkle coincides with the higher dI/dV values in agreement with the spectra displayed in (f), which includes the spectra averaged along the lines indicated in (d). (f) Displays representative dI/dV spectra; the error bars indicate the variation in the spectra used for averaging: parallel to the wrinkle axis on top of the wrinkle (green), and at the edge of the wrinkle (blue). The spectrum for graphene on Cu prior to C_{60} intercalation (black) is included for comparison. The spectrum for the C_{60} layer prior to intercalation is identical to spectra shown in the literature^{47,48} and has a bandgap of 2.3 eV.

For the spectra measured on the wrinkle, the overall shape is more strongly modified and the minimum is shifted by ~ 0.09 eV with respect to E_F . The number of very noisy spectra with significant signal excursions, which are unsuitable for analysis, is considerably higher for measurements on the wrinkle. Without the ability to control E_F with a gate the assignment of Dirac energies should be taken with a grain of salt.⁴⁹ However, if the tentative assignment is correct then E_D on the fold corresponds to a slight p-type doping possibly caused by the strain field in the wrinkle. The higher dI/dV values and step-like fluctuations for spectra measured on the wrinkle can be attributed to deformations of graphene during measurement.³⁶ The local electrostatic field around the tip exerts a force on the graphene leading to a small “dent” or a “pull” on the surface. The tunneling current will therefore be modified by contributions from the interactions with the tip side, consequently leading to variability in the spectral shape.⁵⁰ In addition to the contributions from the mechanical deformation, a modulation of the local density of states (LDOS) can contribute to the increased dI/dV to E_F , although the work by P. Xu et al.³⁶ indicates that the contribution from the mechanical distortion dominates. This analysis demonstrates that wrinkles in graphene are suitable model systems for free-standing graphene, and high resolution topography and spectroscopic data can be obtained.

The second type of surface structure, which is ubiquitous in the study of graphene, are moiré patterns caused by the lattice mismatch between graphene and the substrate which imprint a superlattice on graphene whose periodicity depends on the structure of the substrate and the orientation of graphene with respect to the substrate lattice.²³ The characterization of moiré patterns for graphene on Cu will be used later for comparison of corrugations observed in the intercalated structures. Moiré patterns were observed on all samples and the example in Figure 6.1 is from SA2. A recent publication by Gottardi et al.⁴¹ report a selection of moiré patterns for

graphene on Cu-oxides/ Cu(111) surface with a similar corrugation but different periodicity compared to the ones reported here for the Cu(001) surface. Figure 6.1 shows atomically resolved graphene, a Cu(100) surface adjacent to this graphene island, a moiré pattern, and the corresponding Fourier transforms presented below each image. The combination of a hexagonal graphene with a square Cu(100) structure yields a striped pattern for 5° rotation, which was confirmed by using a purely geometric model with rigid lattices (see sketch next to the Fourier transform). The profile along the black line of Figure 6.1c reveals a corrugation across the moiré pattern of 0.15 nm with a wavelength close to 3 nm, and this value was found to be insensitive to variations in V_{bias} during imaging.

A representative example of intercalated fullerenes with an amorphous structure (SA1, $T = 723$ K, 5 min anneal with a 10 min ramp to temperature) is shown in Figure 6.3. We prepared several samples with similar conditions (see experimental section for details) and observed amorphous intercalated structures on different areas with variable molecule density. Figure 6.3a shows a typical STM image of the amorphous intercalated structure with intermolecular distances between 3 and 8 nm. The average diameter of the molecule shape imprinted on the graphene layer is about 1.3 nm, which is consistent for all samples and slightly larger than the C_{60} diameter of 1 nm measured for isolated molecules on a graphite surface due to “blanketing” by the graphene overlayer. Figure 6.3b includes several intercalated fullerene molecules, and two representative linescans marked A and B for intermolecular distances of 3.0 and 4.5 nm, respectively, are shown below the image.

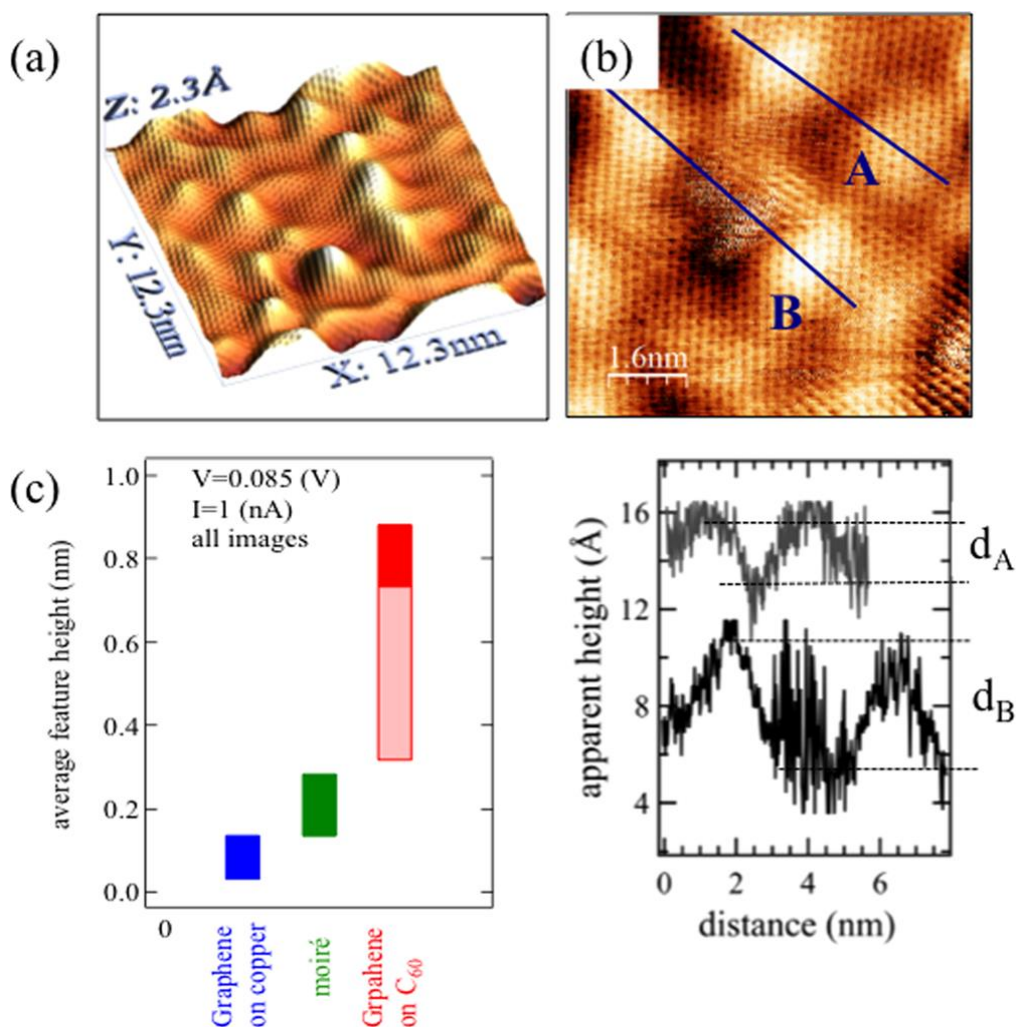


Figure 6.3: (a) 3D STM topography image of an amorphous intercalated structure; the graphene lattice on top of the C₆₀ molecules is resolved (Note: this image was Fourier filtered to reduce noise, image b is an unfiltered 2D image of same sample). (b) Image section of the amorphous intercalated structure and two linescans are shown below the image. Molecules along line A (line B) are separated by 3 nm (4.1 nm) and d_A (d_B) in the linescans indicates the apparent height for the respective intermolecular distances. (c) Summary of average feature heights observed for graphene on Cu, moiré patterns such as the one shown in Figure 6.1, and the wide range of feature heights observed in the intercalated structures. Isolated fullerene molecules will have an apparent height of about 0.8 nm when buried beneath graphene.

The feature height depends on the intermolecular distance and is defined as the magnitude of the dip between two fullerene molecules, d_A and d_B as marked in the linescans. d_A for the closer spaced molecules is considerably smaller than d_B for the larger intermolecular distance. The

smaller dip is related to a detachment of graphene from the substrate in between closely spaced molecules and appears as a “ridge” in the 3D image. A comparison of the corrugation between graphene on Cu, the moiré pattern shown in Figure 6.1, and the range of feature heights observed in intercalated structures in Figure 6.3c visualizes the impact of intercalation on the deformation of the graphene layer. Graphene on top of an amorphous intercalated structure shows a significantly larger feature height, and feature height variability than any other substrate-induced corrugation.

Figures 6.4 and 6.5 present the crystalline intercalated structure prepared on SA1 [annealed at 673 K for 5 min with a 4 min ramp up to temperature]. The linescan across the crystalline intercalated structure seen in Figure 6.4a illustrates the significant change in apparent height as a function of bias voltage, which has been observed for all intercalated structures. The average apparent height (AH) of the intercalated fullerenes changes significantly as a function of V_{bias} for the amorphous and the crystalline intercalated structures in the same manner and the largest corrugation is observed for $V_{\text{bias}} = 0.085$ V. The strong variation of apparent height with bias voltage has been reported previously^{51,52} for C_{60} intercalated at the Ni/graphene interface and is independent of spatial arrangement and substrate material albeit this behavior of intercalated molecules is currently not well understood.

Figure 6.4b summarizes the reduced AH defined by [AH at a given voltage]/[maximum AH measured for the respective bias voltage observed for intermolecular distances above 4 nm] as a function of intermolecular distance. All data for amorphous and crystalline structures (data point for 3.4 nm intermolecular distance) collapse onto a step-like function where the magnitude of the dip between the molecules depends only on the intermolecular distance. The reduced AH is 1 for fullerenes with an intermolecular distance >4.0 nm but decreases rapidly for shorter distances. A

high strain state with large local deformation of graphene is achieved if the graphene layer is in contact with Cu in between the molecules, and a low strain state is seen if graphene becomes detached from the substrate and is only in contact with the molecules. The transition between the low and high strain states occurs between 3.0 and 4.0 nm, and is controlled by the interfacial energies for Cu–C₆₀, graphene–C₆₀, and Cu–graphene and by contributions from the deformation energy of graphene.⁵³ The detachment of graphene from the substrate is driven by its inherent stiffness with a high in-plane Young's modulus.^{26,35,36,46,54,55}

The work by Yamamoto et al.⁵⁶ provides insight in the stability of wrinkles in graphene, which form in response to the presence of nanoscale particles placed between substrate and graphene. This work used SiO₂ particles with an average diameter of 7.5 nm nearly an order of magnitude larger than the fullerene molecules and a concise description of wrinkle deformations was developed. The maximum wrinkle length X_c is defined as the distance over which a wrinkle is sustained due to the rigidity of the graphene lattice and given by $X_c \sim d(E_{2D}/\Gamma)^{1/4}$. E_{2D} is the tensile rigidity with 2.12×10^2 eV/nm², d is the height of the deflection. The adhesion or interaction energy per unit area Γ between graphene and Cu(100) is given as 0.0826 eV/carbon atom or 3.28 eV/nm², respectively.^{53,57} Using $d = 1$ nm, which is equivalent to the center-to-center intermolecular distance in the solid, and $d = 0.8$ nm, which is the radius of the carbon cage, the maximum wrinkle length is ~ 5 nm, or ~ 4 nm, respectively.^{58,59} If the distance between the molecules is larger than the wrinkle will “sag” and graphene touches the substrate. This value is in surprisingly good agreement with our experimental values, where the graphene will contact the Cu-substrate for a wrinkle length (= intermolecular distance) of more than 4 nm. This comparison strongly indicates that the mechanical behavior of graphene can still be described within the continuum-type models used by Yamamoto et al.⁵⁶ even on length scales which are close to the

C–C bond length. In summary, the graphene strain field can be manipulated on a nanometer scale by controlling the geometry of the intercalation structure.

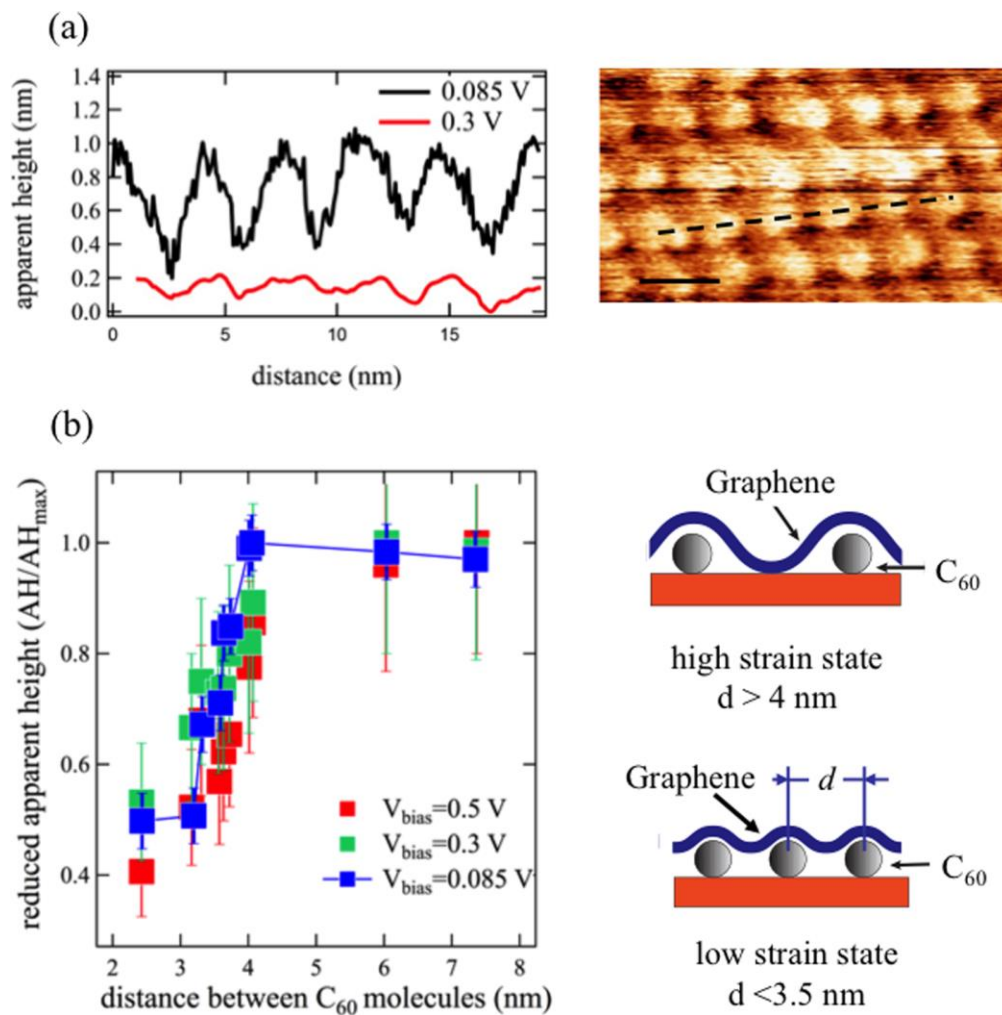


Figure 6.4: (a) shows a crystalline intercalated structure and a linescan for V_{bias} of 0.085 and 0.3 V of the same image section. The corresponding data points are included in (b) for 3.4 nm intermolecular distance. (b) Reduced apparent height calculated by division of the apparent height (AH) of the molecules by the maximum AH measured for the largest molecule distance at the same V_{bias} . The reduced apparent height for three bias voltages is included and they collapse onto a single step-like function. The drawing on the right-hand side visualizes the high and low strain states.

Figure 6.5 showcases all aspects of the crystalline intercalated structure including topography images and differential conductance maps. Figure 6.5a and b show islands and

extended regions covered with the square lattice, which is characteristic for the crystalline intercalated structure. These regions are observed all over the sample, and short annealing and ramp-up times favor the crystalline intercalated structure. In contrast to the imaging of the amorphous intercalated structure, atomic resolution was not achieved for the crystalline structure. The short intermolecular distance of about 3.4 nm and the small dip in AH correspond to a low strain state and the graphene layer is detached from the Cu substrate between the molecules. The graphene layer, therefore, is susceptible to motion under the influence of the tip during measurement, which prevents atomic resolution and might account for the increased magnitude of dI/dV at E_F (Figure 6.5c). A section in Figure 6.5a marked by the purple rectangle is shown separately in a different color scheme to enhance contrast: the square symmetry of the intercalated structure is apparent and it is even possible to identify a point defect: a missing molecule in the upper left-hand corner marked by a circle.

An area where graphene is in contact with Cu is located at the bottom edge of the image in Figure 6.5a and the corresponding ST spectra are included in Figure 6.5c. The good agreement with the spectroscopy signature of graphene on Cu recorded prior to intercalation confirms this assignment. The electronic structure of the crystalline intercalated material is summarized in Figure 6.5c which includes a spectroscopy map of the area marked by a black rectangle in (a) for $V_{\text{bias}} = 0.037$ V. The spectra for the intercalated structure show a minimum close to E_F albeit with a higher value of the differential conductance. The ST spectra shown in Figure 6.5c were obtained by averaging over the selected areas in the STS map; each segment includes about 250 individual spectra, and ~10% of the spectra were rejected due to a very poor signal-to-noise ratio. The most striking difference in the crystalline intercalated surface regions compared to graphene on Cu are two additional peaks, minima in the empty and filled states, respectively, which are symmetrically

positioned at ± 0.9 eV. These minima are seen in all spectra recorded in the crystalline intercalated region including those outside the marked segment.

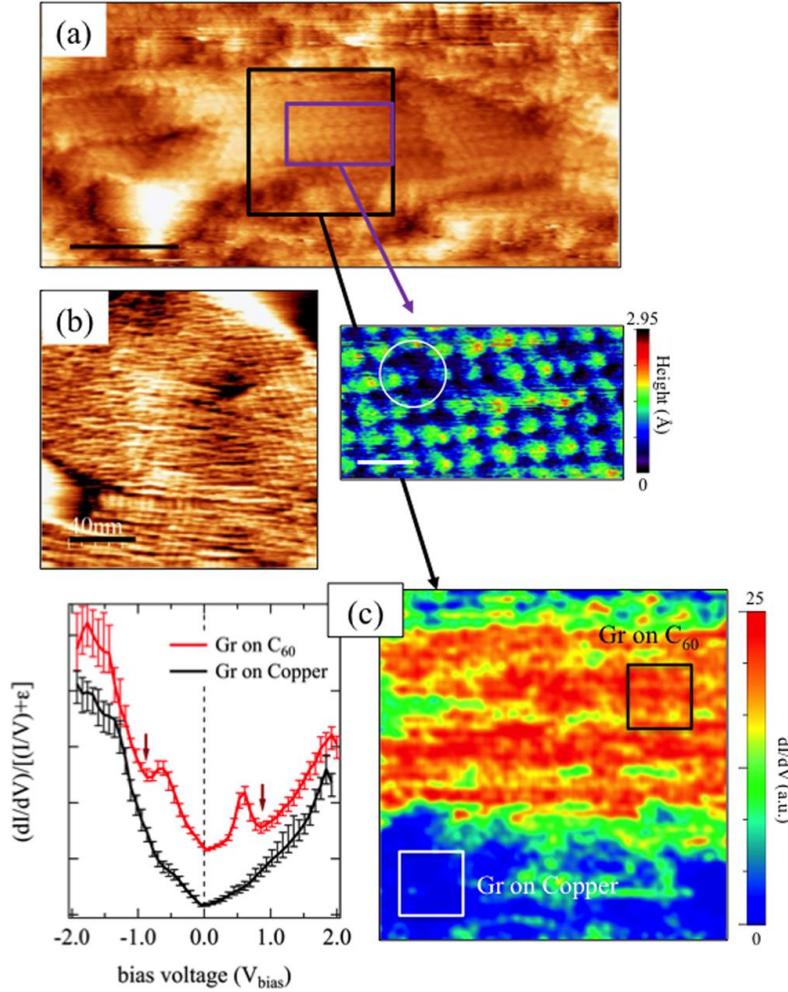


Figure 6.5: (a) and (b) Representative STM topography images of the crystalline intercalated structure (scale bar = 40 nm). The image region marked with a purple rectangle is enlarged and shown in a different color scheme to enhance image contrast. The white circle marks a vacancy in the intercalant lattice. (c) ST spectra from the crystalline intercalated structure (Gr on C₆₀, red) and graphene on Cu for comparison (Gr on copper, black). The arrows mark the position of the spectral minimum, most likely the Dirac energy, and the two minima associated with the superlattice peaks from the crystalline intercalated structure. The spectroscopy map at $V_{\text{bias}} = 37$ mV reflects the spatial distribution of the crystalline intercalation region with a higher dI/dV (red and yellow color) and includes a section with graphene on Cu at the bottom of the frame with a significantly lower dI/dV value (blue) in agreement with the spectra. The ST spectra were obtained by averaging over the area indicated by the black and white squares in the map (see text for details).

The expression given by Yankowitz et al.³³ can be used to calculate superlattice signatures in graphene:

$$E_s = \pm \frac{2\pi}{\sqrt{3}\lambda} \hbar v_f \text{ obtained by substituting } |G| = \frac{4\pi}{\sqrt{3}\lambda} \text{ in } E_s = \pm \frac{\hbar v_f |G|}{2}$$

with E_s as the energy of the superlattice signature, $|G|$ as the reciprocal lattice vector of the superlattice, λ the wavelength of the topographic superlattice as measured from the STM images, and v_F the Fermi velocity of 1.1×10^6 m/s.²² For the crystalline intercalated structure, the wavelength is about 3.4 nm, and yields a superlattice minimum at 0.78 eV, which is very close to the experimentally observed position at 0.9 eV. An alternative interpretation for the presence of additional peaks in the ST spectra is a resonant tunneling through the molecular energy levels in the fullerene molecules, albeit the symmetry of the peaks (minima) with respect to E_F , and the good agreement with the above calculation supports the interpretation as superlattice peaks. This assessment strongly indicates that the fabrication of a crystalline intercalated structure leads to the formation of topographic as well as electronic superlattices defined by the local strain field, where Dirac cone replicas lead to the appearance of a superlattice peak.

The intercalation of C_{60} molecules at the graphene–Cu interfaces is confirmed using the following set of criteria:

- (i) The features imprinted in graphene, which are correlated with the molecules have a diameter slightly larger than the free-standing molecule and exhibit only a small variability in diameter.
- (ii) Atomic resolution of the graphene lattice is achieved if the intermolecular distances exceed about 4 nm when the graphene is still in contact with Cu. Atomic

resolution can be limited by the detachment of graphene from the substrate,^{54,56} which can contribute to the tip induced motion of the graphene layer

(iii) The electronic structure as expressed in the ST spectra is different from molecules residing on a graphene surface.

(iv) The corrugation of the surface is significantly larger than the corrugation observed for moiré patterns. The square symmetry of the crystalline intercalated structure cannot be achieved by moiré patterns in combination with the hexagonal graphene lattice.

(v) In addition, the height variations as a function of V_{bias} observed in the amorphous and crystalline intercalated structures are in agreement with intercalation experiments reported in the literature,⁵² and these results have been reproduced for several samples, using different tips, and are not observed for other surface structures

In combination, these observations allow us to state with confidence that molecule intercalation has been achieved, and establish general guidelines for assessing molecule intercalation processes. This is particularly important since the intercalation of a large molecule is initially counterintuitive but has been observed previously, albeit not widely reported, for C_{60} intercalation in graphite.^{24,60,61}

Recent experiments, which produce localized strain fields in graphene, are microbubbles at the Pt-graphene interface, exhibiting locally a Landau level splitting equivalent to a 300 T pseudo-magnetic field, nanobubbles at the Ru-graphene interface created by local oxidation and strain-driven detachment of graphene, and Pb-islands made by intercalation at the Ir-graphene interface.^{13,19,34} The intercalation of C_{60} is comparable to these structures in terms of the magnitude of strain and curvature induced in graphene and is likely to provide a better long-term stability

than nanobubbles, which are prone to lose their inventory of smaller molecules over time by diffusion along the interface or through the graphene membrane.⁶² In our experience, the C₆₀ intercalated structures are stable for up to several weeks in an ultrahigh vacuum environment. Their stability in air has not been tested and will depend on the interaction/adhesion of the graphene layer and C₆₀ molecules to a substrate, which might oxidize over time. On the other hand, the strain field is defined by molecule dimensions, which do not change over time, and are identical for each intercalated molecule.

The position of E_D in pristine graphene–Cu, and the crystalline intercalated structures is close to E_F indicating that doping is not significant in either structure. The graphene–Cu interface frequently shows n-type doping of graphene, and the shift of E_D on clean Cu(111) and Cu(100) measured with electron spectroscopy has often been reported to be around –0.3 eV.⁶³ A recent study⁶⁴ demonstrated that short annealing of graphene on Cu(100) at moderate temperatures will not induce n-type doping, which only emerges after annealing at higher temperatures. The temperature-dependence of graphene doping is attributed to a reorganization/restructuring at the Cu(100)-graphene interface.⁶⁵ The intercalation of oxygen, and the presence of an oxygen-induced reconstruction^{39,63} are both associated with a more dramatic shift of E_D by –0.6 eV, whereas graphene on Cu-oxide surfaces will effectively decouple graphene from the underlying metal.⁴¹ Because we were able to measure a pristine Cu(100) surface adjacent to graphene islands, an electronic decoupling of graphene from a complete Cu-oxide layer is currently excluded, and the graphene–Cu interface in our work can be compared to the interfaces present during the lower temperature range annealing reported in ref ⁶⁴.

The absence of significant doping in the intercalated structure is somewhat surprising considering the fact that charge transfer from all low index Cu surfaces to C₆₀ is well

documented,^{48,66,67} however no charge transfer is observed between C₆₀ and graphite, which can serve as a reasonable model system for graphene.⁶⁸ The charge density n in graphene is related to E_D by:

$$n = \frac{(E_D)^2}{\pi \hbar^2 v_f}$$

If we assume that each C₆₀ molecule is charged with one elementary charge q – the charge density using the molecule distribution from the crystalline intercalated structure is $n = 1 \times 10^{14} \text{ cm}^{-2}$. This charge density corresponds to a shift in $E_D = 0.35 \text{ eV}$, which is clearly much larger than the experimentally observed value. However, it is expected that C₆₀ acts overall as an acceptor in this triple layer system.⁴⁸ The charge distribution and consequently position of E_D in the Cu–fullerene–graphene system clearly warrants a more detailed study and will be investigated in the future by integration of the intercalated structure in a device with a backgate.

A critical challenge in advancing the manipulation of graphene by molecule intercalation is the control over the formation of crystalline or amorphous structures, and ideally, the lattice constant of crystalline structures. Our work indicates that duration of the annealing process, annealing temperature, and ramp-up time to annealing temperature are decisive to achieve significant intercalation products for graphene on Cu, whereas the thickness of the initial C₆₀ layer plays only a minor role. The temperature to achieve intercalation is above the sublimation temperature of C₆₀ and the success of the process is influenced by the competition between intercalation and sublimation.

The intercalation process for molecules is currently not well understood, and we suggest starting by framing the discussion using the following energy balance:

$$- E_{\text{def}}(\text{G}) - E_{\text{interface}}(\text{G-M}) + E_{\text{interface}}(\text{C}_{60}\text{-G}) + E_{\text{interface}}(\text{C}_{60}\text{-M})$$

where $E_{\text{def}}(\text{G})$ is the energy required to deform the graphene sheet to insert the molecules, and then to adapt to the deformation required to accommodate the intercalated molecule, $E_{\text{interface}}(\text{G-M})$ is the interfacial term which describes the interaction between graphene and the metal substrate (M), $E_{\text{interface}}(\text{C}_{60}\text{-G}) / E_{\text{interface}}(\text{C}_{60}\text{-M})$ are the interface energy between C_{60} and graphene/metal, respectively. The first two terms of this equation refer to the energy of the system before intercalation and the other two terms refer to the energy of the system after intercalation process. Therefore, if the total value of this equation becomes positive, it means that the intercalation is energetically favorable.

Their relative contributions have to be weighted correctly, and this simple energy balance includes only interfacial interactions. Intercalation is likely to occur if the energetic cost of the combined reactions of deformation, and reduction of the Cu–graphene contact area is small compared to the gain made by formation of the C_{60} –graphene and C_{60} –Cu interfaces albeit kinetic limitations might be significant. These limitations pertain to the activation energy required to initiate intercalation by detaching the graphene edges from the Cu–surface, and include the diffusion of intercalated C_{60} at the interface. The intercalation of a C_{60} molecule cannot proceed by transition through the plane of the graphene layer for geometric reasons, but it has to start at a defect, grain boundary, or edge of a graphene flake/island or use a wrinkle as a conduit.

We hypothesize that the structure of the Cu–substrate surface influences the symmetry of the crystalline molecule structure, leading to the square symmetry. The lattice constant of the crystalline intercalated structures fluctuates by about 20% across the surface, which indicates that a well-defined epitaxial relation between molecule position and orientation is not achieved. The formation of amorphous structures, which are observed for longer annealing times and higher temperatures, on the other hand, is probably the result of a competition between deintercalation

leading to desorption and motion of molecules in the interfacial space leading to a breakdown of the crystalline structure. In contrast, reports for C₆₀ intercalation at the Ni(111)–graphene interface show only 1D wormlike channels along which the molecules accumulate but with no extended intercalation in 2D.^{51,52} Ni interacts strongly with graphene, whereas the interaction between graphene and Cu is much weaker with a larger interlayer distance promoting diffusion at the interface. The impact of the strain field imparted by the graphene deformation on the crystallinity of the intercalated structure remains at present speculative. Overall, our observations are commensurate with a relatively narrow stability region of the crystalline intercalated structure. The next step to develop a better understanding of the intercalation process, and to achieve control of the crystallography of the intercalated structure, will be to extend the present work and establish an “intercalation phase diagram”, which covers a wider range of temperatures, annealing times, substrate materials, and substrate crystallography.

The intercalation of molecules at the Cu–graphene interface is a unique and, versatile approach to the manipulation of graphene. Considering the large size of the fullerene molecule, it seems likely that other molecules can be intercalated although for a reliable prediction of the feasibility of intercalation a better understanding of the process has to be achieved. Specifically, the intercalation of the relatively large C₆₀ molecule leads to the formation of amorphous or crystalline strain lattices where the intermolecular distance tunes the magnitude of the strain state. The intercalation of molecules is a complex process, where the mutual interactions between graphene, substrate, and intercalant as well as the mechanical deformation in graphene have to be considered. A full understanding of the intercalation process needs to be achieved to fully exploit molecule intercalation as a means to adapt graphene properties and reach the desired charge carrier transport characteristics to tailor device performance in the future. Our work has shown the

feasibility and richness of molecule intercalation structures and opens the path to build a wide range of materials.

Acknowledgement

This work by E. Monazami and P. Reinke was supported by NSF-Division of Materials Research (Ceramics) DMR- 1005809. Petra Rudolf and Luca Bignardi acknowledge the financial support by the “Graphene-based electronics” research program of the Foundation for Fundamental Research on Matter (FOM); FOM is part of The Netherlands Organization for Scientific Research (NWO).

6.5. References

- (1) Castro Neto, A. H.; Peres, N. M. R.; Novoselov, K. S.; Geim, A. K. The electronic properties of graphene. *Rev. Mod. Phys.* 2009, 81, 109–162.
- (2) Andrei, E. Y.; Li, G.; Du, X. Electronic properties of graphene: a perspective from scanning tunneling microscopy and magnetotransport. *Rep. Prog. Phys.* 2012, 75, 056501.
- (3) Das Sarma, S.; Adam, S.; Hwang, E. H.; Rossi, E. Electronic transport in two-dimensional graphene. *Rev. Mod. Phys.* 2011, 83, 407–470.
- (4) Britnell, L.; Gorbachev, R. V.; Jalil, R.; Belle, B. D.; Schedin, F.; Mishchenko, A.; Georgiou, T.; Katsnelson, M. I.; Eaves, L.; Morozov, S. V.; Peres, N. M.; Leist, J.; Geim, A. K.; Novoselov, K. S.; Ponomarenko, L. A. Field-effect tunneling transistor based on vertical graphene heterostructures. *Science* 2012, 335, 947–950.
- (5) Giovannetti, G.; Khomyakov, P.; Brocks, G.; Karpan, V.; van den Brink, J.; Kelly, P. Doping Graphene with Metal Contacts. *Phys. Rev. Lett.* 2008, 101, 026803.
- (6) Gyamfi, M.; Eelbo, T.; Wasniowska, M.; Wehling, T. O.; Forti, S.; Starke, U.; Lichtenstein, A. I.; Katsnelson, M. I.; Wiesendanger, R. Orbital selective coupling between Ni adatoms and graphene Dirac electrons. *Phys. Rev. B: Condens. Matter Mater. Phys.* 2012, 85, 161406.
- (7) Jeong, H. M.; Lee, J. W.; Shin, W. H.; Choi, Y. J.; Shin, H. J.; Kang, J. K.; Choi, J. W. Nitrogen-doped graphene for highperformance ultracapacitors and the importance of nitrogen-doped sites at basal planes. *Nano Lett.* 2011, 11, 2472–2477.
- (8) Lauffer, P.; Emtsev, K. V.; Graupner, R.; Seyller, T.; Ley, L. Molecular and electronic structure of PTCDA on bilayer graphene on SiC(0001) studied with scanning tunneling microscopy. *Phys. Status Solidi B* 2008, 245, 2064–2067.
- (9) Low, T.; Guinea, F.; Katsnelson, M. I. Gaps tunable by electrostatic gates in strained graphene. *Phys. Rev. B: Condens. Matter Mater. Phys.* 2011, 83, 195436.
- (10) Park, J. U.; Nam, S.; Lee, M. S.; Lieber, C. M. Synthesis of monolithic graphene-graphite integrated electronics. *Nat. Mater.* 2011, 11, 120–125.
- (11) Petrovic, M.; Srut Rakic, I.; Runte, S.; Busse, C.; Sadowski, J. T.; Lazic, P.; Pletikoscic, I.; Pan, Z. H.; Milun, M.; Pervan, P.; Atodiresei, N.; Brako, R.; Sokcevic, D.; Valla, T.; Michely, T.; Kralj, M. The mechanism of caesium intercalation of graphene. *Nat. Commun.* 2013, 4, 2772.
- (12) Pollard, A. J.; Perkins, E. W.; Smith, N. A.; Saywell, A.; Goretzki, G.; Phillips, A. G.; Argent, S. P.; Sachdev, H.; Muller, F.; Hufner, S.; Gsell, S.; Fischer, M.; Schreck, M.; Osterwalder, J.; Greber, T.; Berner, S.; Champness, N. R.; Beton, P. H. Supramolecular assemblies formed on an epitaxial graphene superstructure. *Angew. Chem., Int. Ed.* 2010, 49, 1794–1799.
- (13) Sicot, M.; Leicht, P.; Zusan, A.; Bouvron, S.; Zander, O.; Weser, M.; Dedkov, Y. S.; Horn, K.; Fonin, M. Size-selected epitaxial nanoislands underneath graphene moire on Rh(111). *ACS Nano* 2012, 6, 151–158.
- (14) Silien, C.; Pradhan, N.; Ho, W.; Thiry, P. Influence of adsorbatesubstrate interaction on the local electronic structure of C₆₀ studied by low-temperature STM. *Phys. Rev. B: Condens. Matter Mater. Phys.* 2004, 69, 115343.
- (15) Tadich, A.; Edmonds, M. T.; Ley, L.; Fromm, F.; Smets, Y.; Mazej, Z.; Riley, J.; Pakes, C. I.; Seyller, T.; Wanke, M. Tuning the charge carriers in epitaxial graphene on SiC(0001) from electron to hole via molecular doping with C₆₀F₄₈. *Appl. Phys. Lett.* 2013, 102, 241601.
- (16) Zan, R.; Bangert, U.; Ramasse, Q.; Novoselov, K. S. Evolution of gold nanostructures on graphene. *Small* 2011, 7, 2868–2872.

- (17) Zhang, Y.; Brar, V. W.; Girit, C.; Zettl, A.; Crommie, M. F. Origin of spatial charge inhomogeneity in graphene", *Nat. Nat. Phys.* 2009, 5, 722–726.
- (18) Pereira, V.; Castro Neto, A. Strain Engineering of Graphene's Electronic Structure. *Phys. Rev. Lett.* 2009, 103, 046801.
- (19) Qi, Z.; Kitt, A. L.; Park, H. S.; Pereira, V. M.; Campbell, D. K.; Castro Neto, A. H. Pseudomagnetic fields in graphene nanobubbles of constrained geometry: A molecular dynamics study. *Phys. Rev. B: Condens. Matter Mater. Phys.* 2014, 90, 125419.
- (20) Varykhalov, A.; Sanches-Barriga, J.; Shikin, A. M.; Biswas, C.; Vescovo, E.; Rybkin, A.; Marchenko, D.; Rader, O. Electronic and magnetic properties of quasifreestanding graphene on Ni. *Phys. Rev. Lett.* 2008, 101, 157601.
- (21) Gierz, I.; Suzuki, T.; Weitz, R. T.; Lee, D. S.; Krauss, B.; Riedl, C.; Starke, U.; Hoechst, H.; Smet, J. H.; Ast, C. R.; Kern, K. Electronic coupling of an epitaxial graphene monolayer by gold intercalation. *Phys. Rev. B: Condens. Matter Mater. Phys.* 2010, 81, 235408.
- (22) Xue, J.; Sanchez-Yamagishi, J.; Bulmash, D.; Jacquod, P.; Deshpande, A.; Watanabe, K.; Taniguchi, T.; Jarillo-Herrero, P.; LeRoy, B. J. Scanning tunnelling microscopy and spectroscopy of ultra-flat graphene on hexagonal boron nitride. *Nat. Mater.* 2011, 10, 282–285.
- (23) Ponomarenko, L. A.; Gorbachev, R. V.; Yu, G. L.; Elias, D. C.; Jalil, R.; Patel, A. A.; Mishchenko, A.; Mayorov, A. S.; Woods, C. R.; Wallbank, J. R.; Mucha-Kruczynski, M.; Piot, B. A.; Potemski, M.; Grigorieva, I. V.; Novoselov, K. S.; Guinea, F.; Fal'ko, V. I.; Geim, A. K. Cloning of Dirac fermions in graphene superlattices. *Nature* 2013, 497, 594–597.
- (24) Kim, K.; Lee, Z.; Malone, B. D.; Chan, K. T.; Aleman, B.; Regan, W.; Gannett, W.; Crommie, M. F.; Cohen, M. L.; Zettl, A. Multiply folded graphene. *Phys. Rev. B: Condens. Matter Mater. Phys.* 2011, 83, 245433.
- (25) Ye, J.; Craciun, M. F.; Koshino, M.; Russo, S.; Inoue, S.; Yuan, H.; Shimotani, H.; Morpurgo, A. F.; Iwasa, Y. Accessing the transport properties of graphene and its multilayers at high carrier density. *Proc. Natl. Acad. Sci. U. S. A.* 2011, 108, 13002–13006.
- (26) Lee, J. K.; Yamazaki, S.; Yun, H.; Park, J.; Kennedy, G. P.; Kim, G. T.; Pietzsch, O.; Wiesendanger, R.; Lee, S.; Hong, S.; DettlaffWeglikowska, U.; Roth, S. Modification of electrical properties of graphene by substrate-induced nanomodulation. *Nano Lett.* 2013, 13, 3494–3500.
- (27) Calleja, F.; Ochoa, H.; Garnica, M.; Barja, S.; Navarro, J. J.; Black, A.; Otrokov, M. M.; Chulkov, E. V.; Arnau, A.; Vazquez de Parga, A. L.; Guinea, F.; Miranda, R. Spatial variation of a giant spin– orbit effect induces electron confinement in graphene on Pb islands. *Nat. Phys.* 2014, 11, 43–47.
- (28) Guinea, F. Strain engineering in graphene. *Solid State Commun.* 2012, 152, 1437–1441.
- (29) Guinea, F.; Katsnelson, M.; Vozmediano, M. Midgap states and charge inhomogeneities in corrugated graphene. *Phys. Rev. B: Condens. Matter Mater. Phys.* 2008, 77, 075422.
- (30) Guinea, F.; Katsnelson, M. I.; Geim, A. K. Energy gaps and a zero-field quantum Hall effect in graphene by strain engineering. *Nat. Phys.* 2010, 6, 30–33.
- (31) Isacsson, A.; Jonsson, L.; Kinaret, J.; Jonson, M. Electronic superlattices in corrugated graphene. *Phys. Rev. B: Condens. Matter Mater. Phys.* 2008, 77, 035423.
- (32) Katsnelson, M. I.; Novoselov, K. S.; Geim, A. K. Chiral tunnelling and the Klein paradox in graphene. *Nat. Phys.* 2006, 2, 620–625.
- (33) Yankowitz, M.; Xue, J.; Cormode, D.; Sanchez-Yamagishi, J. D.; Watanabe, K.; Taniguchi, T.; Jarillo-Herrero, P.; Jacquod, P.; LeRoy, B. J. Emergence of superlattice Dirac points in graphene on hexagonal boron nitride. *Nat. Phys.* 2012, 8, 382–386.

- (34) Lu, J.; Neto, A. H.; Loh, K. P. Transforming Moire blisters into geometric graphene nanobubbles. *Nat. Commun.* 2012, 3, 823.
- (35) Bai, K.-K.; Zhou, Y.; Zheng, H.; Meng, L.; Peng, H.; Liu, Z.; Nie, J.-C.; He, L. Creating One-Dimensional Nanoscale Periodic Ripples in a Continuous Mosaic Graphene Monolayer. *Phys. Rev. Lett.* 2014, 113, 086102.
- (36) Xu, P.; Yang, Y.; Barber, S. D.; Ackerman, M. L.; Schoelz, J. K.; Qi, D.; Kornev, I. A.; Dong, L.; Bellaiche, L.; Barraza-Lopez, S.; Thibado, P. M. Atomic control of strain in freestanding graphene. *Phys. Rev. B: Condens. Matter Mater. Phys.* 2012, 85, 121406.
- (37) Li, X.; Cai, W.; An, J.; Kim, S.; Nah, J.; Yang, D.; Piner, R.; Velamakanni, A.; Jung, I.; Tutuc, E.; Banerjee, S. K.; Colombo, L.; Ruoff, R. S. Large-area synthesis of high-quality and uniform graphene films on Copper foils. *Science* 2009, 324, 1312–1314.
- (38) Bignardi, L.; van Dorp, W. F.; Gottardi, S.; Ivashenko, O.; Dudin, P.; Barinov, A. V.; de Hosson, J. T. M.; Stoehr, M.; Rudolf, P. Microscopic characterization of suspended graphene grown by chemical vapour deposition. *Nanoscale* 2013, 5, 9057–9061.
- (39) Jensen, F.; Besenbacher, F.; Laegsgaard, E.; Stensgaard, I. Dynamics of oxygen-induced reconstruction of Cu(100) studied by scanning tunneling microscopy. *Phys. Rev. B: Condens. Matter Mater. Phys.* 1990, 42, 9206–9209.
- (40) Yang, J. C.; Yeadon, M.; Olynick, D.; Gibson, J. M. Anomalous desorption of Copper oxide observed by in situ transmission electron microscopy. *Microsc. Microanal.* 1997, 3, 121–125.
- (41) Gottardi, S.; Mueller, K.; Bignardi, L.; Moreno-Lopez, J. C.; Pham, T. A.; Ivashenko, O.; Yablonskikh, M.; Bjoerk, J.; Rudolf, P.; Stoehr, M.; Barinov, A. Comparing graphene growth on Cu(111) versus oxidized Cu(111). *Nano Lett.* 2015, 15, 917–922.
- (42) Horcas, I.; Fernandez, R.; Gomez-Rodriguez, J. M.; Colchero, J.; Gomez-Herrero, J.; Baro, A. M. WSXM: A software for scanning probe microscopy and a tool for nanotechnology. *Rev. Sci. Instrum.* 2007, 78, 013705.
- (43) Feenstra, R. M.; Lee, J. Y.; Kang, M. H.; Meyer, G.; Rieder, K. H. Band gap of the Ge(111)c(2 × 8) surface by scanning tunneling spectroscopy. *Phys. Rev. B* 2006, 73, 035310.
- (44) Tromp, R. M. Spectroscopy with the scanning tunnelling microscope: a critical review. *J. Phys.: Condens. Matter* 1989, 1, 10211–10228.
- (45) Feenstra, R. M. A prospective: Quantitative scanning tunneling spectroscopy of semiconductor surfaces. *Surf. Sci.* 2009, 603, 2841–2844.
- (46) Kim, K.; Lee, Z.; Malone, B. D.; Chan, K. T.; Aleman, B.; Regan, W.; Gannett, W.; Crommie, M. F.; Cohen, M. L.; Zettl, A. Multiply folded graphene. *Phys. Rev. B: Condens. Matter Mater. Phys.* 2011, 83, 245433.
- (47) McClimon, J. B.; Monazami, E.; reinke, P. Interaction of C₆₀ with tungsten: modulation of morphology and electronic structure on the molecular length scale. *J. Phys. Chem. C* 2014, 118, 24479.
- (48) Rudolf, P.; Golden, M. S.; Bruehwiler, P. A. Studies of fullerenes by the excitation, emission and scattering of electrons", *J. J. Electron Spectrosc. Relat. Phenom.* 1999, 100, 409–433.
- (49) Zhang, Y.; Brar, V. W.; Wang, F.; Girit, C.; Yayan, Y.; Panlasigui, M.; Zettl, A.; Crommie, M. F. Giant phonon-induced conductance in scanning tunnelling spectroscopy of gate-tunable graphene. *Nat. Phys.* 2008, 4, 627–630.
- (50) Gao, L.; Guest, J. R.; Guisinger, N. P. Epitaxial graphene on Cu(111). *Nano Lett.* 2010, 10, 3512–3516.

- (51) Lu, J.; Zheng, Y.; Sorkin, A.; Loh, K. P. Growing suspended graphene on C₆₀ molecules. *Small* 2012, 8, 3728–3732.
- (52) Varykhalov, A.; Gudat, W.; Rader, O. Imaging buried molecules: fullerenes under graphene. *Adv. Mater.* 2010, 22, 3307–3310.
- (53) Lee, C.; Wei, X.; Kysar, J. W.; Hone, J. Measurement of the elastic properties and intrinsic strength of monolayer graphene. *Science* 2008, 321, 385–388.
- (54) Kushima, A.; Qian, X.; Zhao, P.; Zhang, S.; Li, J. Ripplations in van der waals layers. *Nano Lett.* 2015, 15, 1302–1308.
- (55) Lu, J.; Bao, Y.; Su, C. L.; Loh, K. P. Properties of strained structures and topological defects in graphene. *ACS Nano* 2013, 7, 8350–8357.
- (56) Yamamoto, M.; Pierre-Louis, O.; Huang, J.; Fuhrer, M. S.; Einstein, T. L.; Cullen, W. G. “The Princess and the Pea” at the nanoscale: wrinkling and delamination of graphene on nanoparticles. *Phys. Rev. X* 2012, 2, 041018.
- (57) Klaver, T. P. C.; Zhu, S.-E.; Sluiter, M. H. F.; Janssen, G. C. A. M. Molecular dynamics simulation of graphene on Cu(100) and Cu(111) surfaces. *Carbon* 2015, 82, 538–547.
- (58) Goel, A.; Howard, J. B.; Vander Sande, J. B. Size analysis of single fullerene molecules by electron microscopy. *Carbon* 2004, 42, 1907–1915.
- (59) Zhou, O.; Fischer, J. E.; Coustel, N.; Kycia, S.; Zhu, Q.; McGhie, A. R.; Romanow, W. J.; McCauley, J. P.; Smith, A. B.; Cox, D. E. Structure and bonding in alkali-metal-doped C₆₀. *Nature* 1991, 351, 462.
- (60) Fuhrer, M. S.; Hou, J. G.; Xiang, X.-D.; Zettl, A. C₆₀ intercalated graphite: predictions and experiments. *Solid State Commun.* 1994, 90, 357–360.
- (61) Gupta, V.; Scharff, P.; Risch, K.; Romanus, H.; Müller, R. Synthesis of C₆₀ intercalated graphite. *Solid State Commun.* 2004, 131, 153–155.
- (62) Nair, R. R.; Wu, H. A.; Jayaram, P. N.; Grigorieva, I. V.; Geim, A. K. Unimpeded Permeation of Water Through Helium-Leak-Tight Graphene-Based Membranes. *Science* 2012, 335, 442–444.
- (63) Walter, A. L.; Nie, S.; Bostwick, A.; Kim, K. S.; Moerschini, L.; Chang, Y. J.; Innocenti, D.; Horn, K.; McCarty, K.; Rotenberg, E. Electronic structure of graphene on single-crystal copper substrates. *Phys. Rev. B: Condens. Matter Mater. Phys.* 2011, 84, 195443.
- (64) Marsden, A. J.; Asensio, M.-C.; Avila, J.; Dudin, P.; Barinov, A.; Moras, P.; Sheverdyaeva, P. M.; White, T. W.; Maskery, I.; Costantini, G.; Wilson, N. R.; Bell, G. R. Is graphene on copper doped? *Phys. Status Solidi RRL* 2013, 7, 643–646.
- (65) Tian, J.; Cao, H.; Wu, W.; Yu, Q.; Guisinger, N. P.; Chen, Y. P. Graphene induced surface reconstruction of Cu. *Nano Lett.* 2012, 12, 3893–3899.
- (66) Schull, G.; Neel, M.; Becker, M.; Kroeger, J.; Berndt, R. Spatially resolved conductance of oriented C₆₀. *New J. Phys.* 2008, 10, 065012.
- (67) Rowe, J. E.; Rudolf, P.; Tjeng, L. H.; Malic, R. A.; Meigs, G.; Chen, C. T.; Chen, J.; Plummer, E. W. Synchrotron radiation and low energy electron diffraction studies of ultrathin C₆₀ films deposited on Cu(100), Cu(111) and Cu(110). *Int. J. Mod. Phys. B* 1992, 6, 3909–3913.
- (68) Reinke, P.; Feldermann, H.; Oelhafen, P. C₆₀ bonding to graphite and boron nitride surfaces. *J. Chem. Phys.* 2003, 119, 12547–12552.

Chapter 7

Electronic Structure and Band Gap of Fullerenes on Tungsten Surfaces: Transition from a Semiconductor to a Metal Triggered by Annealing

Ehsan Monazami¹, John B. McClimon², James Rondinelli³, and Petra Reinke⁴

(1) Department of Materials Science and Engineering, University of Virginia,
Charlottesville, Virginia 22901, United States

(2) Department of Materials Science and Engineering, University of
Pennsylvania, Philadelphia, Pennsylvania 19104, United States

(3) Department of Materials Science and Engineering, Northwestern University,
Evanston, Illinois 60208, United States

7. Electronic Structure and Band Gap of Fullerenes on Tungsten Surfaces

7.1. Abstract

The understanding and control of molecule–metal interfaces is critical to the performance of molecular electronics and photovoltaics devices. We present a study of the interface between C_{60} and W, which is a carbide-forming transition metal. The complex solid-state reaction at the interface can be exploited to adjust the electronic properties of the molecule layer. Scanning tunneling microscopy/spectroscopy measurements demonstrate the progression of this reaction from wide band gap (>2.5 eV) to metallic molecular surface during annealing from 300 to 800 K. Differential conduction maps with 104 scanning tunneling spectra are used to quantify the transition in the density of states and the reduction of the band gap during annealing with nanometer spatial resolution. The electronic transition is spatially homogeneous, and the surface band gap can therefore be adjusted by a targeted annealing step. The modified molecules, which we call nanospheres, are quite resistant to ripening and coalescence, unlike any other metallic nanoparticle of the same size. Densely packed C_{60} and isolated C_{60} molecules show the same transition in electronic structure, which confirms that the transformation is controlled by the reaction at the C_{60} –W interface. Density functional theory calculations are used to develop possible reaction pathways in agreement with experimentally observed electronic structure modulation. Control of the band gap by the choice of annealing temperature is a unique route to tailoring molecular-layer electronic properties.

7.2. Introduction

Interfaces between metals and organic molecules are critical to the performance of a wide range of devices from organic photovoltaic cells to self-organized molecular switches and motors.^{1,2} The interaction between metal surfaces and molecules is complex and controls the geometric arrangement of the molecules as well as their electronic properties, which are modulated by local charge-transfer and polarization effects.^{3–5} The majority of molecule adsorption studies are performed on noble and noncarbide-forming metals and thus exclude chemical reactions and covalent bonding across the interface. Here we show that chemical reactions at the molecule–metal interface can be used to tailor the molecule’s electronic and chemical properties in unexpected ways. This work establishes a broader design palette of molecule-based device structures and contributes to an understanding of the contact performance in organic solar cells, which is still a subject of intense discussion.

Small volatile organic molecules such as methane and acetylene dissociate rapidly on many transition-metal surfaces, and a carbide layer will form as a result of the significant thermodynamic driving force. This process is used in the industrial-scale synthesis of carbides and carbide particles, which serve as catalysts, hard coatings, and electrodes in corrosive environments.⁶ The dissociation of larger organic molecules presents a much more complex situation with potentially multiple stable intermediate reaction products on the way to the carbide. In the present work, we investigate the interfacial reaction between carbon-60 (C_{60}) molecules, which possess a high degree of symmetry and near-aromatic bonding configuration, and tungsten (W), which is a transition metal with only two stable carbides. The C_{60} –metal interaction is particularly well-studied, although the majority of those studies are performed on noble and noncarbide-forming metals, and the number of studies on carbide-forming substrates and metals is much smaller.

Charge transfer from a metal substrate to a fullerene molecule is seen for many surfaces including silver (Ag),⁷ gold (Au),⁸ copper (Cu), and iron (Fe).⁹ For other surfaces, an adsorbate-driven surface reconstruction is initiated [palladium Pd(110) and germanium Ge(111)],^{10,11} and sometimes C₆₀ even “burrows” into the metal surface,^{12,13} and the dissociation of C₆₀ on ruthenium Ru(0001) leads to the formation of graphene layers.¹⁴ The formation of W–carbide from C₆₀ on W surfaces has been reported only in a few studies, and any detailed understanding of the reaction pathways leading from molecule to carbide is missing.^{15,16}

We analyze the solid-state reaction at the interface between C₆₀ and the W surface, which leads to the formation of so-called nanospheres, which retain (mostly) the geometry of the original molecule until the temperature exceeds 800 K. At the same time, the band gap is reduced and a fully metallic nanosphere surface is seen above 700 K. The transition from an intact C₆₀ molecule at room temperature to a metallic nanosphere at 700 K < T < 850 K and ultimately a carbide surface for T > 850 K is in essence the stepwise dissociation of C₆₀ controlled by the interfacial reaction. This temperature driven reaction sequence affords unique control of the electronic structure while retaining the molecular surface morphology. We observe the reactions of C₆₀ with the carbide-forming W-metal surface at the atomic scale with scanning tunneling microscopy and spectroscopy. The interpretation of the experimental results is supported by density functional theory (DFT) calculations.

7.3. Methods

The work was performed on an Omicron variable-temperature scanning probe microscope connected to a preparation chamber with a base pressure of $<2 \times 10^{-10}$ mbar. Scanning tunneling microscopy (STM) and spectroscopy (STS) measurements were used to observe the C₆₀ layer and its modification as a function of the temperature. The STS measurements were integrated in grid

measurements, where for every fifth pixel an I–V curve was recorded with the feedback loop switched off. The feedback loop was switched on for topography imaging between spectra. For an image size of 512×512 pixels, a total of 10609 (103×103) I–V spectra were measured for each scan direction (forward and backward). The dI/dV spectra and normalized conductance $(dI/dV)/[(I/V) + \epsilon]$ were obtained numerically, and the latter is proportional to the density of states (DOS).^{39,40} The voltage range corresponding to zero conductance was assigned to the band-gap region. The results are visualized in maps at specific V_{bias} values and in band-gap maps. About 10–20% of the I–V curves showed significant noise or excursions likely due to changes in the tip termination or shape and were eliminated in the analysis. The large number of ST spectra included in the maps yields a high degree of redundancy, allows for selective averaging over identical areas to reduce noise, and establishes the error bar included in the ST spectra. For band-gap histograms, the forward and backward spectra were averaged for each data point. The band gap is assigned to the voltage range where the normalized dI/dV is close to zero and the slope is negligible. To establish reproducibility, ST spectra on graphite and Au were recorded prior to most experiments. STM and STS data were analyzed with WSxM 5.0⁴¹ and Igor Pro 6.22, and a MATLAB program was developed to manage the large data sets, normalization, and visualization of all STS maps.

W thin films were deposited on a MgO(100) substrate followed by deposition of the C_{60} layer. The as-received MgO (CrysTec) was (1) etched for 30 s in 14.6 M H_3PO_4 and rinsed with deionized water and acetone and (2) annealed 10 h in air at 1273 K in a box furnace, and (3) the calcium (Ca) spires from impurity segregation^{42,43} were removed in a second etching step followed by a 5 h annealing in air.⁴⁴ All MgO surfaces were checked with atomic force microscopy prior to use. W thin films with thicknesses between 50 and 80 nm were subsequently deposited at 1073 K by electron-beam evaporation at a deposition rate of 0.5–0.8 nm/min. C_{60} was added at a rate of 1

monolayer (ML)/min by thermal evaporation of high-purity C₆₀ (MerCorp) from an h-BN crucible with a graphite liner. All deposition rates were calibrated using of a quartz crystal monitor. The frequency change of the quartz crystal microbalance, which corresponds to 1 ML of C₆₀, was calibrated in a separate experiment using X-ray photoelectron microscopy. The C₆₀ layer was deposited at room temperature, and the thickness of the initial C₆₀ layer was 2–4 ML. STM measurements were performed with an etched W tip, and typical imaging conditions for the C₆₀ layer are $I_t = 0.1$ nA and $V_{\text{bias}} = 2$ V, and those for the W surface are $I_t = 0.1$ nA and $V_{\text{bias}} = 6$ mV. The MgO–W–C₆₀ samples were annealed at temperatures between 473 and 1073 K. All STM/STS measurements were performed at room temperature. After each annealing step, the samples were kept at ultrahigh vacuum until they cooled to room temperature prior to measurement. Oxidation during this time was not observed with STS.

The geometry, bonding, band gap, and stability of several C₆₀–W bonding combinations including C₅₈W₂, C₅₈W, C₅₉W, C₆₀W, and C₆₀ on W(110) were studied with DFT. All of the simulations were carried out using DFT, as implemented in the Atomistic Toolkit (ATK 2015.rc2) package. The local-spin-density approximation (LSDA) with the Perdew–Zunger exchange–correlation parametrization was used.⁴⁵ The valence-electron wave functions were simulated using a double- ζ -polarized basis set for both C and W.^{46,47} For self-consistent calculations, a global break point of 10^{–5} eV in total energy was used. Geometry optimizations were performed using the limited memory Broyden–Fletcher–Goldfarb–Shanno algorithm until the maximum force on all atoms was less than 0.05 eV/Å.

7.4. Results and Discussions

Figure 7.1 illustrates the progression from the bare W surface to the C₆₀ layer and finally to the nanosphere-covered surface. Parts a and b of Figure 7.1 show a representative image and a

corresponding linescan, respectively, of the W thin film deposited on MgO(100), which is composed of grains with an average size of $10 \times 10 \text{ nm}^2$, an intragranular surface with height variation as small as 0.3 nm, and grain boundary grooves with a depth of $\geq 1 \text{ nm}$. The relatively small grain size can be attributed to W's high melting temperature and, consequently, low adatom surface mobility. The relatively small thickness of the W layers inhibits a conclusive determination of its orientation. Unfortunately, atomic resolution was not achieved on a regular basis, and X-ray diffraction techniques used on these films are not entirely conclusive. Grazing-incidence X-ray diffraction results show a weak and not entirely conclusive signature of a W(110) texture, and the presence of some W(100) surfaces is likely. Epitaxial W thin films on MgO with W(110)||MgO(100) have a lattice misfit of 5.9% with a 45° rotation at the interface, and this orientation has been reported previously for W and Mo.¹⁷ The W(100)||MgO(100) orientation presents a significantly larger misfit of 22% and indicates that W(110) is likely the preferred surface orientation. Owing to this uncertainty, the W(110) and W(100) surfaces were included in the DFT calculation of the C₆₀-W interaction described in the Supporting Information.

Figure 7.1c shows the surface morphology after deposition of 4 ML of C₆₀ on W. This image shows a densely packed, crystalline layer on the left-hand side, in agreement with the face-centered-cubic FCC(111) packing, and a disordered layer on the right-hand side. The center-to-center intermolecular distance in the FCC regions is 1 nm, commensurate with fullerenes on Cu,¹⁸ lead (Pb),¹⁹ and Au.²⁰ The disordered packing is attributed to a high density of step edges and defects in the W surface. A similar transition from a well-ordered to a disordered structure has been observed in C₆₀ layers on graphite and amorphous C, where the defect-rich amorphous C surface pins the molecules.²¹

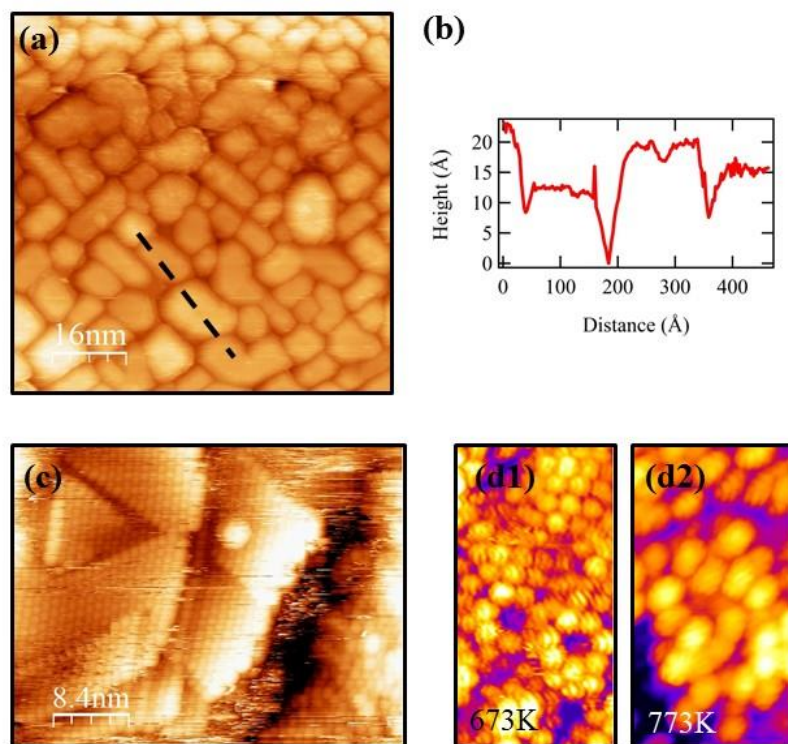


Figure 7.1: Summary of surfaces observed before and after deposition of C_{60} on W/MgO(100) surfaces (a–c) and after annealing of this surface to 673 K (d1) and 773 K (d2). The MgO sample is etched with phosphoric acid and subjected to a two-step annealing process to minimize the development of Ca spires and achieve a smooth surface. The MgO terraces are prior to W deposition on average 100×100 nm in size and provide smooth terraces for W thin-film growth (a and b). The fullerene layer (c) is composed of regions with high crystallinity (FCC packing) and amorphous regions (right-hand side of the image). After annealing (d1 and d2), the surface morphology of the fullerenes is maintained, and the majority of the molecules exhibit two or three surface grooves, which are consistent with a 6–6 orientation (d1 and d2; image size 8×15 nm).

The surface morphology of C_{60} is conserved after annealing to 673 K, and the molecule shape can still be clearly recognized after annealing to 773 K, as shown in Figure 7.1(d1,d2). At this point, only the molecular layer in contact with the W surface is retained (T-desorption of the multilayer is 540 K due to weaker C_{60} – C_{60} interaction).¹⁵ Nearly all molecules show a set of two or three parallel grooves, which emerge after annealing and are due to the cessation of molecule

rotation. At room temperature, rapid rotation of the molecules leads to averaging over all orientations, yielding a featureless image. If molecule rotation ceases, the molecule's frontier orbital related to the molecule's orientation can be imaged (see in supplementary information Figure 7.7). The groove structure seen here agrees with C_{60} molecules, where the 6–6 bond is at the apex.²² Because of the molecule's symmetry, the 6–6 bond is also the contact point to the W surface. The preferred molecule orientation on the W(110) surface was confirmed with DFT, and the geometry, lowest unoccupied molecular orbital, and DOS for this configuration are shown in Figure 7.7. The orientation of the grooves on C_{60} rotates with the scanning direction, and while experimental issues can never be entirely excluded, the grooving does not appear to be an artifact of the measurement.

The surface motion of C_{60} at room temperature is illustrated in Figure 7.8, which shows sequential images of C_{60} molecules (0.2 ML coverage). Prior to annealing, the C_{60} molecules move to the step edges over time and this motion ceases after annealing. The cessation of molecule rotation and motion indicates that a reaction between the W surface and the C_{60} molecule is initiated by annealing, and this process pins the molecule in place. This can be understood as the initiation of fullerene degradation on their path to the thermodynamically stable carbide. Figures 7.2 and 7.3 show the impact of annealing on the electronic structure starting with the discussion of the as-deposited C_{60} layer.

Figure 7.2, which shows the as-deposited C_{60} layer on a W thin film, includes regions with thicknesses corresponding to 1 ML of C_{60} , 2 ML of C_{60} , and amorphous regions and is therefore ideal to study the modulation of the electronic structure. After the first annealing at 593 K, only a single layer of C_{60} is retained; the multilayers have desorbed, in agreement with the sublimation temperature of C_{60} . A topography image and the corresponding band-gap map are given in Figures

7.2a,b, and line scans confirm the transition from single layer to double layer at the center of the image. Three regions can be distinguished in the topography image as well as the band-gap map: (1) a well-ordered structure with a band gap of ~ 1.6 eV, (2) multilayer patches with a larger average band gap of ~ 1.9 eV, and (3) areas that include an amorphous structure, which tend to have slightly larger band gaps (~ 2.5 eV and higher).²³ The statistical analysis of the band gap map included in Figure 7.2c shows a bimodal shape reflecting the contributions of the different layers, and Figure 7.2d includes selected spectra for the single-layer and amorphous regions. The same type of analysis will be used in the assessment of annealing-induced modifications. The difference in the band gap between regions 1 and 2 (single layer vs multilayer) agrees well with the literature.^{24–26} The screening of the intermolecular Coulomb repulsion by the metal substrate results in a generally smaller gap compared to molecules in the second layer, where the larger distance from the metal greatly reduces the screening. The origin of the increased gap with a loss of crystallinity remains unclear, although we tentatively ascribe it to a subtle change in the screening due to changes in the intermolecular distance. Modeling of these effects was not undertaken because most DFT functionals cannot simulate the long-range interactions required for quantitative assessment.³

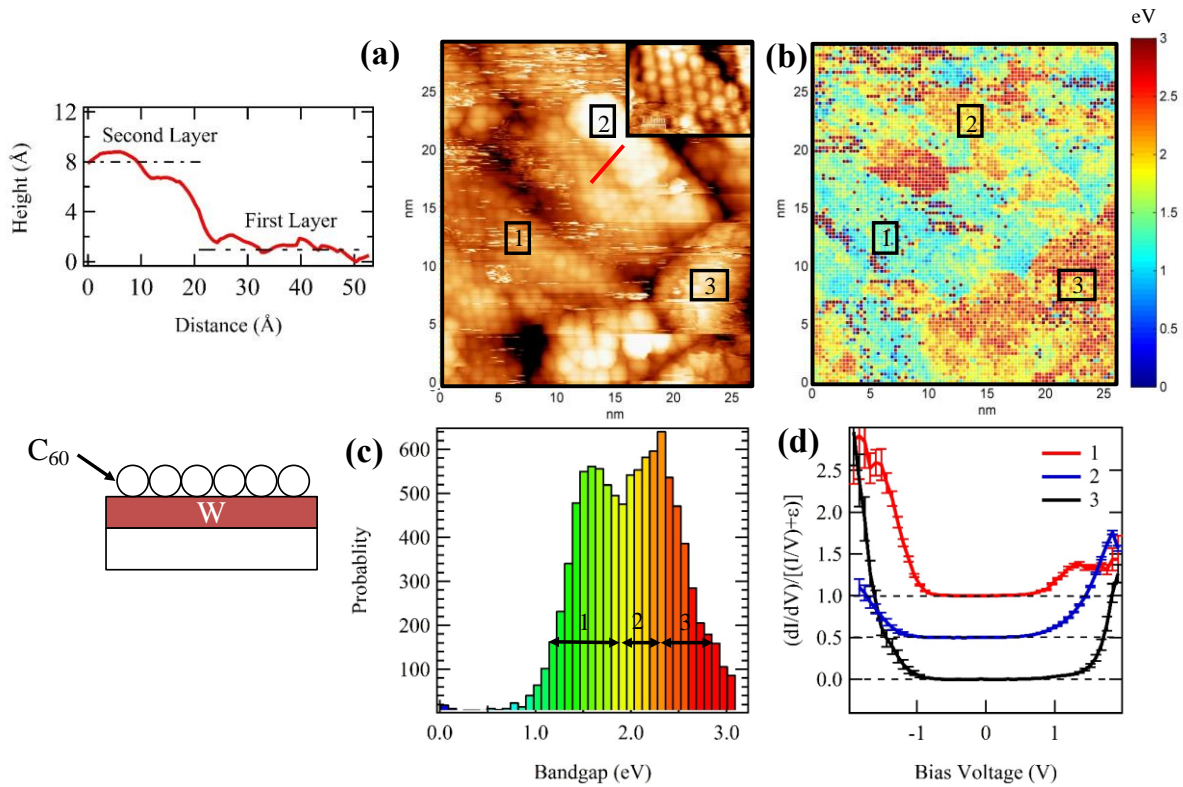


Figure 7.2: Topography and LDOS including a band-gap map for C₆₀ layers on W. (a) Topography image, which has regions with single-layer and multilayer C₆₀, as evidenced by the line scan at the center of the image. The regions marked in the image correspond to the following structure: region 1 is a C₆₀ single layer, region 2 is a C₆₀ double layer, and region 3 is an amorphous structure. (b) Band-gap map. The gap was determined from the I–V curves measured at 102×102 image points. (d) Representative examples of the normalized dI/dV spectra. The error bar is the standard error of the data set. (c) Distributions of band gaps measured in part b in the form of a histogram. All data points from the band-gap map are included. Labels 1–3 in the histogram correspond to the respective regions in the image.

To deepen our understanding of the experimental results, DFT calculations are used for two distinct systems: first, to describe the orientation and electronic structure of the C₆₀ molecule on W(110) and W(100) surfaces and, second, to capture the changes in the electronic structure for isolated molecules, which is induced by modification of the bonding and the introduction of W atoms in the C₆₀ cage. The DFT calculations generally reproduce the spectral shape of the DOS and relative changes in the band gap rather well, despite the underestimation of the band-gap values

by the LSDA. LSDA does not account correctly for van der Waals and long-range interactions. However, a precise representation of the van der Waals forces for the C_{60} -W interaction is not necessary for the present work because the intermolecular interaction is small compared to the bonding between C_{60} molecules on W, where covalent bonds dominate. The bonding at this interface can reasonably be assumed to be independent of the intermolecular interaction.^{8,27-29} The DOSs calculated for C_{60} on W(110) and W(100) are included in the Supporting Information. The observed ST spectra for the first layer of molecules show also a shift of E_F toward the conduction band edge (valence band edge at ~ -1 eV and conduction band edge at ~ 0.7 eV in Figure 7.2d) in agreement with the calculated DOS (Figure 7.7). This shift follows from the band alignment for the W(110) surface with a work function of 4.52 eV and compares well with the Ag(100) surface with a near-identical work function.

Figure 7.3 summarizes the impact of annealing on the electronic structure. By annealing, the electronic structure changes rather dramatically, as seen in Figure 7.3a, which shows the normalized differential conductivity spectra extracted from the STS maps. The error bars are the standard error accumulated for all spectra within the respective map. The transition from the wide-band-gap C_{60} molecules to a metallic surface is gradual and progresses over a temperature range of at least 150 K. Parts b and c of Figure 7.3 show the surface at 673 K, where the transition to a metallic surface is nearly complete. This surface is particularly inhomogeneous in terms of its electronic structure; the STS map for $V_{\text{bias}} = 0.08$ eV shows the emergence of nanometer-sized metallic islands such as region 1. Other regions are still semiconducting and typically have a larger apparent height, which can be seen in a direct comparison with the topography image (Figure 7.3b). The larger apparent height is due to a topography variation and not an increased local density

of states (LDOS); if the apparent height was controlled by the LDOS, we expect a larger height for metallic regions.

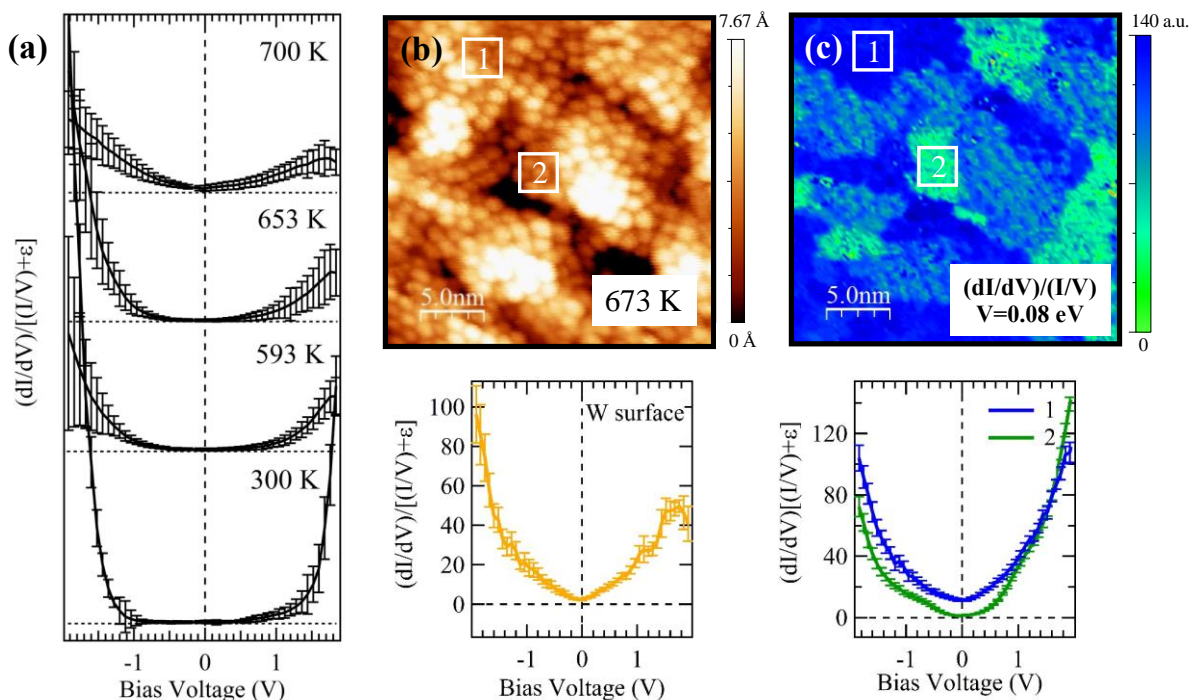


Figure 7.3: Modulation of LDOS as a function of the annealing temperature (300–700 K) and topography image in addition to the normalized dI/dV map for 673 K. (a) LDOS derived from spectroscopy maps for C_{60} layers annealed at the temperatures indicated in the figure. The width of the error bar is related to the spatial homogeneity of the respective map and the experimental error in STS acquisition. Data points with clearly unphysical excursions and noise were removed (%10). The topography image in part b and the corresponding normalized dI/dV map in part c illustrate the spatial variation of the LDOS for an annealing step at 673 K. Examples for normalized dI/dV spectra for the two regions marked in the map are included (blue and green). For comparison, the normalized conductance spectrum for the W surface is included (yellow).

Simultaneously, the sizes of the fullerene molecules and nanospheres were measured by analyzing several STM images for each annealing step (Figure 7.4). The molecules and nanospheres are densely packed and appear to also move slightly on top of each other in some images, leading to a significant error in the distribution, which is therefore only a rough measure

of the nanosphere diameter. However, it still shows an increase in the most likely diameter (the maximum in the diameter distribution) by about 30–40% during the annealing process. The origin of this diameter increase is not entirely clear; we assume that some molecules are deformed as the interfacial reaction progresses and then adopt a more elliptical shape. However, the general expression of the frontier orbital with the grooves from the 6–6 termination is still present in the STM images, which indicates that the top part of C₆₀ remains structurally intact despite distortion of the shape. Pascual et al.³⁰ reported a similar observation and a decrease in the sizes of the fullerene molecules adsorbed on Si(111) after annealing to 873 K. The size modification was attributed to the formation of a stronger adsorption state and consequently a reduction in the molecule vibrations. However, this seems intuitively not a suitable explanation for the size increase observed in our experiments. We therefore suggest that the incorporation of W atoms in the cage structure or partial fracture of the molecule cage might be responsible for the size change.

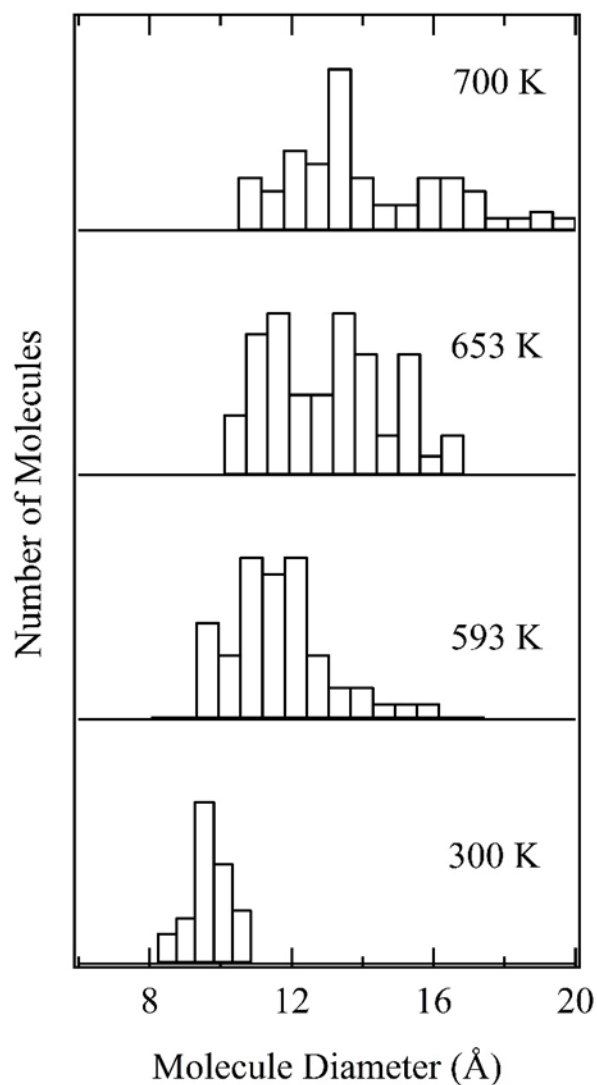


Figure 7.4: Distribution of the molecule diameter as a function of the annealing temperature. Each distribution includes several hundred molecules, and the annealing steps are identical with those discussed in Figures 2 and 3. The distribution is normalized to the unit height.

Quantitative information on the progression from a wideband-gap semiconductor to a metallic surface is obtained from the analysis of the STS maps, and the results are summarized in Figure 7.5. Figure 7.5a shows the band-gap histograms for four temperatures straddling the transition from fullerene layers with a wide band gap to nanospheres with a reduced band gap (1.2– 0.7 eV) and finally to fully metallic nanospheres at 700 K. Each histogram includes 21218

spectra (10609 I–V curves from forward and backward scans) and data from several maps for each annealing step. The band-gap histograms for different areas on different samples, which have identical initial C_{60} coverage (single layer, multilayer, and amorphous) and annealing treatment, show only minor differences.

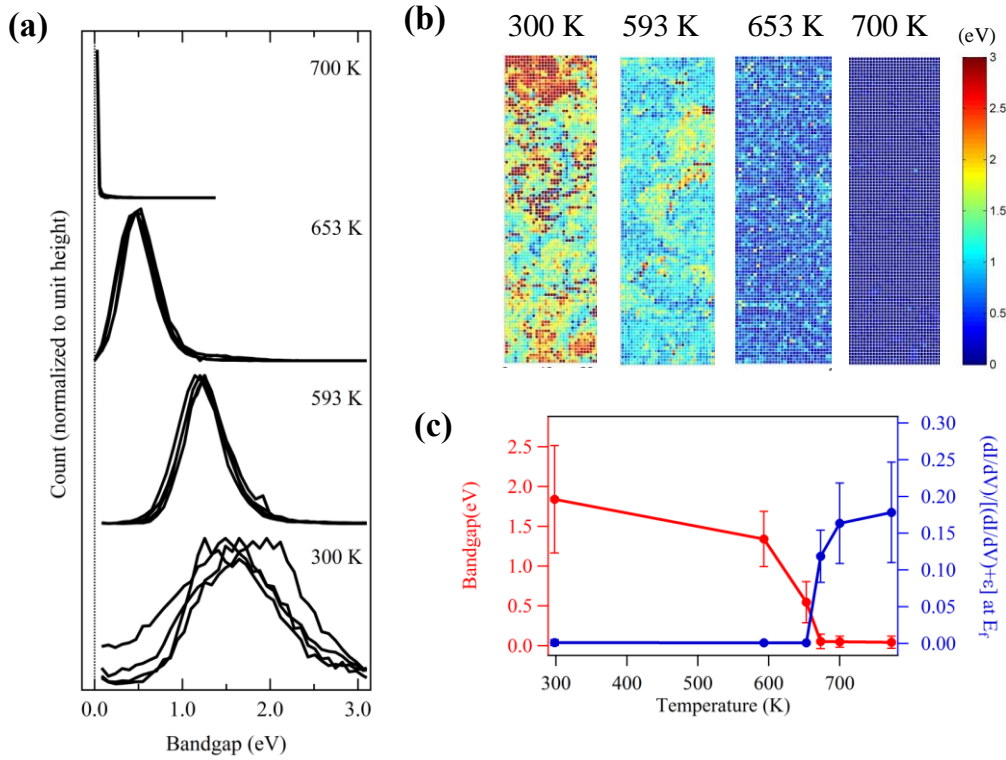


Figure 7.5: Band-gap evolution as a function of the temperature from 300 to 773 K. (a) Band-gap distributions measured after annealing at the temperature indicated in the graph. The distributions measured for several images are included for each temperature. The distribution at 300 K is relatively broad, which can directly be traced back to the differences between the single, double, and amorphous C_{60} layers shown in Figure 7.1. The distributions are normalized to the unit height, and for 700 K, only metallic spectral signatures are observed. (b) Corresponding band-gap maps. Each representative strip is 20×80 nm in size and part of a larger map. (c) Change of the average gap and normalized conductance at E_F as a function of the temperature.

The band-gap histograms become narrower during annealing because only a single layer is retained, and some patches can be identified in the band-gap maps where the transformation has progressed slower or faster (Figure 7.4b). This decrease in the width of the distribution histograms

can be interpreted as an indication of an electronically more uniform surface after annealing. The full width at half-maximum (fwhm) of the bandgap distributions for intermediate temperatures of 593 and 653 K are 0.7 and 0.5 eV, respectively. The 300 K distribution includes multilayers (Figure 7.1), and the 700 K sample is fully metallic with a fwhm of <0.2 eV. The width of the band-gap distribution is influenced by inhomogeneities in the initial substrate and C_{60} layer but can also be attributed to the nature of the chemical reaction, which will occur over a range of temperatures and cannot be expected to be as abrupt as a phase transition process. In addition, some error is introduced by the STM measurement itself, which depends on many factors including the surface roughness. The largest band gap associated with the map from Figure 7.3b,c (673 K) is only about 0.3 eV, while other regions are fully metallic. Figure 5c summarizes these results: the band-gap maps and the DOS at E_F reflect the transition from fullerenes to nanospheres until a fully metallic nanosphere surface is established. Ultimately, a carbide surface is observed for $T > 850$ K, and the nanosphere morphology disappears.

The same reaction sequence is observed for isolated C_{60} molecules on W surfaces; the molecules, which are mobile at 300 K (Figures 7.12 and 7.13), will become immobile as soon as the annealing process is initiated, and their band gap subsequently decreases. Our observations indicate that the reaction at the W- C_{60} interface drives modulation of the electronic structure, while the nanosphere surface probed with STM still presents the geometric structure of the fullerene molecules. The inverse relationship between the annealing temperature and band gap of nanospheres provides a unique platform to engineer molecular surfaces.

The experimental results show the gradual transition from a wide-band-gap molecular semiconductor to a metallic surface with a near-identical topography, and this transition is driven by a reaction with the W substrate. The experimental results are complemented by DFT

calculations, which provide a detailed understanding of the C_{60} –W interactions leading to such profound changes in the molecule’s electronic structure. We consider three models and test whether they can be used to describe the transition to a metallic nanostructure while conserving essentially the molecule shape probed with STM: (i) W atoms placed on the outside of the fullerene cage (on cage), (ii) gradual substitution of C atoms with W atoms (substitutional), and (iii) C_{60} fragmentation followed by local carbide formation at the interface. Model iii is by far the most complex situation, but a significant knowledge gap about the local reaction pathways prevents at present a meaningful description with DFT. The presence of fullerene fragments alone is insufficient to explain the experimental findings because their band gap never closes to reach a fully metallic state.^{31,32} We therefore focus on models i and ii, which isolate possible scenarios of W integration with C_{60} . To our knowledge, no prior DFT calculations have been performed for substitutional W, and we tested the validity of our approach by assessing C_{58} – $_{59}$ Pt, C_{59} Fe, and C_{58} – $_{59}$ Ni, which have been discussed in the literature.^{33–36} We were able to reproduce the LDOS for these hetrofullerenes by following similar procedures as described in literature. The binding energy of the metal atoms (Pt, Fe, and Ni), electron affinity, and ionization potential of the hetrofulleneren structures were replicated in our simulation within ± 0.8 eV agreement.

Figure 7.6 shows the DOS for the most stable isomers of C_{60} W (on-cage) and C_{59} W and C_{58} W₂ (both substitutional) and the DOS of pristine C_{60} for comparison. The computed geometry for C_{59} W is quite similar to that of other metal heterofullerenes, and 3-fold-coordinated W atoms move slightly away from the C_{60} surface. The W–C distance in C_{59} W (0.1905–0.1934 nm) is slightly larger than that for nickel (Ni), cobalt (Co), and Fe and smaller than that for platinum (Pt) and iridium (Ir), as expected based on the atomic sizes.^{36–38} Because all vertices in C_{60} are equivalent, there is only one bonding configuration for C_{59} W, but several possible configurations

were tested for $C_{58}W_2$ and $C_{60}W$. For $C_{60}W$, the lowest-energy configuration is achieved if the W atom is placed in the center of a hexagonal face, and the 6-fold-coordinated W atom moves slightly away from the molecule surface. The W–C distances for this structure are 0.203–0.208 nm. Adding more W atoms on-cage is energetically unfavorable.

For the heterofullerenes, the binding energies were calculated and compared by placing W at different sites and using the following expressions:

$$C_{60} + W = C_{60}W \quad \Delta H_r = (E)_{C_{60}W} - (E)_{C_{60}} - E_W$$

$$C_{60} + W_2 = C_{58}W_2 + C_2 \quad \Delta H_r = (E)_{C_{58}W_2} + (E)_{C_2} - (E)_{C_{60}} - E_{W_2}$$

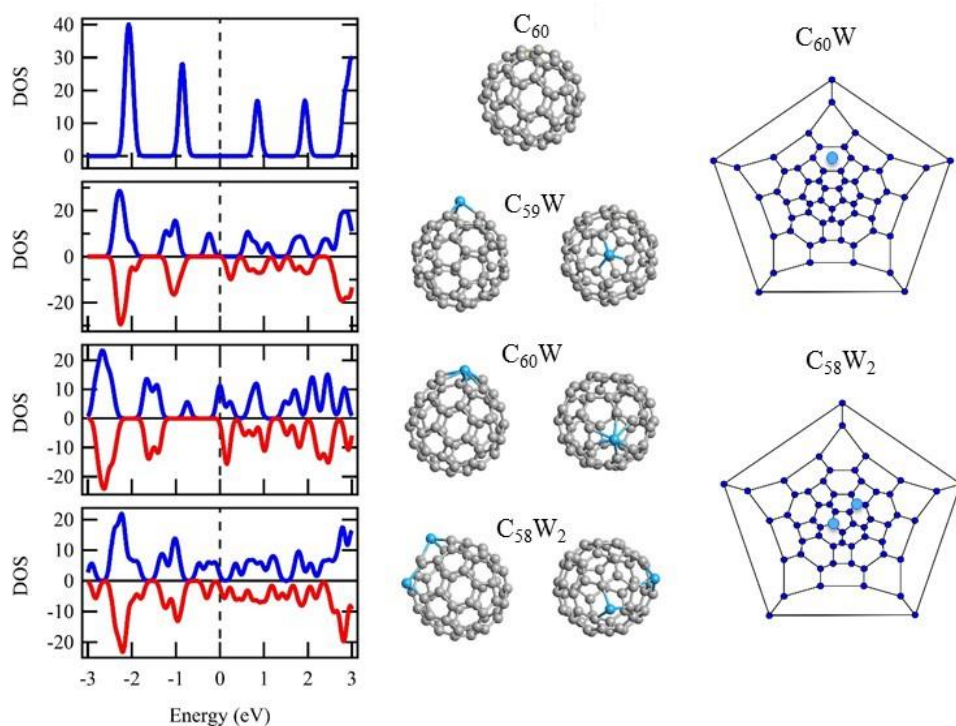


Figure 7.6: Results from DFT calculations for the most stable $C_{59}W$ and $C_{58}W_2$ substitutional configurations and $C_{60}W$ with W atoms added on the outside of the C_{60} cage. The calculations for C_{60} are included for comparison. For the open-shell structures $C_{60}W$, $C_{59}W$, and $C_{58}W_2$, spin-resolved DOS is depicted, with the spin-up DOS

marked in blue and the spin-down DOS marked in red. The DOS is summed over the entire molecule. Gray and light-blue atoms indicate C and W, respectively.

In the most stable $C_{58}W_2$ configuration, the W–C distance is slightly larger than that for $C_{59}W$ (0.1906–0.1950 nm) and the W atoms are separated by two C atoms. Intuitively, this configuration will induce the least amount of strain. The reduction in the band gap is quite dramatic, and two substitutional W atoms yield already a metallic DOS, although with a rather small intensity at E_F . The DFT calculations demonstrate that reaction pathways that introduce C–W bonds ultimately lead to the formation of metallic nanospheres passing through intermediate reaction steps with reduced band gaps. Experimentally, the reaction is only activated by annealing at >500 K and then progresses over an extended temperature range. The relatively narrow band-gap distributions in the intermediate temperature range indicate a preferred reaction pathway rather than the coexistence of a wide range of bonding geometries. The selectivity of the reaction pathway then leads to the preferred 6–6 orientation of the nanospheres. The current DFT work includes a narrow selection of possible intermediate structures, and a larger variety can be constructed to reflect intermediate band gaps, which are not well represented in the current W– C_{60} structures.

7.4. Conclusions

In conclusion, we have demonstrated that the reaction at the interface between C_{60} and W leads to a gradual transformation to metallic nanospheres. Control of the band gap is reasonable, and it can be adjusted within a 0.7 eV interval by the choice of the annealing temperature. The good agreement between experimental and DFT calculations supports the hypothesis that the interfacial reaction between the molecule and metal surface drives the electronic structure modulation. On the other hand, the geometry and orientation of the nonsubstrate facing part of C_{60} remain intact. This unique situation offers a wonderful new test bed to study and modulate the molecular layers.

Associated Contents

*S Supporting Information: DFT calculations of bonding between C₆₀ molecules and W(100) and W(110) and a description of the optimized bonding geometry and tests for several molecule orientations. The electronic structure of the C₆₀/ W(110) and -W(100) interfaces is also calculated with DFT and compared to the literature on C₆₀–metal interfaces. The motion of C₆₀ molecules on the W surface is shown as observed experimentally with STM, and the topography and spectroscopy data for single molecules on W are discussed and compared to the data described in the main body of the manuscript for continuous layers.

Author Contributions

The majority of the experimental work and DFT calculations was conducted by E.M., and J.B.M. performed exploratory experiments on nanosphere formation. The study was initially conceived by P.R. and further developed by E.M.. DFT calculations were performed in collaboration with J.R.. The manuscript was written by E.M. and P.R., with significant input and discussion from J.B.M. and J.R. The final version was commented and agreed upon by all authors. Data from this work are stored on Libra, the University of Virginia's institutional repository. Visit the site or contact P.R. about gaining access to these data. Notes The authors declare no competing financial interest.

Acknowledgements

The authors gratefully acknowledge support of this work by the National Science Foundation through Award DMR-1005809 by the Division of Materials Research (Ceramics) and

Award CHE-1507986 by the Division of Chemistry (Macromolecular/ Supramolecular and Nanochemistry).

7.5. References

- (1) Dennler, G.; Scharber, M. C.; Brabec, C. J. Polymer-Fullerene Bulk-Heterojunction Solar Cells. *Adv. Mater.* **2009**, *21* (13), 1323–1338.
- (2) Martin, C. A.; Ding, D.; Sørensen, J. K.; Bjørnholm, T.; van Ruitenbeek, J. M.; van der Zant, H. S. J. Fullerene-Based Anchoring Groups for Molecular Electronics. *J. Am. Chem. Soc.* **2008**, *130* (40), 13198–13199.
- (3) Neaton, J. B.; Hybertsen, M. S.; Louie, S. G. Renormalization of Molecular Electronic Levels at Metal-Molecule Interfaces. *Phys. Rev. Lett.* **2006**, *97* (21), 216405.
- (4) Lu, X.; Grobis, M.; Khoo, K. H.; Louie, S. G.; Crommie, M. F. Charge Transfer and Screening in Individual C₆₀ a Scanning Tunneling Spectroscopy and Theoretical Study. *Phys. Rev. B* **2004**, *70* (11), 115418.
- (5) Refaely-Abramson, S.; Sharifzadeh, S.; Jain, M.; Baer, R.; Neaton, J. B.; Kronik, L. Gap Renormalization of Molecular Crystals from Density-Functional Theory. *Phys. Rev. B* **2013**, *88* (8), 081204.
- (6) Decker, S.; Löfberg, A.; Bastin, J.-M.; Frennet, A. Study of the Preparation of Bulk Tungsten Carbide Catalysts with C₂H₆/H₂ and C₂H₄/H₂ Carburizing Mixtures. *Catal. Lett.* **1997**, *44* (3-4), 229–239.
- (7) Wang, L.-L.; Cheng, H.-P. Density Functional Study of the Adsorption of a C₆₀ Monolayer on Ag(111) and Au(111) Surfaces. *Phys. Rev. B* **2004**, *69* (16), 165417.
- (8) Tamai, A.; Seitsonen, A. P.; Baumberger, F.; Hengsberger, M.; Shen, Z.-X.; Greber, T.; Osterwalder, J. Electronic Structure at the C₆₀ Metal Interface: An Angle-Resolved Photoemission and First-Principles Study. *Phys. Rev. B* **2008**, *77* (7), 075134.
- (9) Tran, T. L. A.; Çakır, D.; Wong, P. K. J.; Preobrajenski, A. B.; Brocks, G.; van der Wiel, W. G.; de Jong, M. P. Magnetic Properties of Bcc-Fe(001)/C₆₀ Interfaces for Organic Spintronics. *ACS Appl. Mater. Interfaces* **2013**, *5* (3), 837–841.
- (10) Weckesser, J.; Cepek, C.; Fasel, R.; Barth, J. V.; Baumberger, F.; Greber, T.; Kern, K. Binding and Ordering of C₆₀ on Pd(110): Investigations at the Local and Mesoscopic Scale. *J. Chem. Phys.* **2001**, *115* (19), 9001–9009.
- (11) Xu, H.; Chen, D. M.; Creager, W. N. C₆₀-Induced Reconstruction of the Ge(111) Surface. *Phys. Rev. B* **1994**, *50* (12), 8454–8459.
- (12) Murray, P. W.; Pedersen, M. Ø.; Lægsgaard, E.; Stensgaard, I.; Besenbacher, F. Growth of C₆₀ on Cu(110) and Ni(110) Surfaces: C₆₀-Induced Interfacial Roughening. *Phys. Rev. B* **1997**, *55* (15), 9360–9363.
- (13) Li, H. I.; Pussi, K.; Hanna, K. J.; Wang, L.-L.; Johnson, D. D.; Cheng, H.-P.; Shin, H.; Curtarolo, S.; Moritz, W.; Smerdon, J. A.; McGrath, R.; Diehl, R. D. Surface Geometry of C₆₀ on Ag(111). *Phys. Rev. Lett.* **2009**, *103* (5), 056101.
- (14) Lu, J.; Yeo, P. S. E.; Gan, C. K.; Wu, P.; Loh, K. P. Transforming C₆₀ Molecules into Graphene Quantum Dots. *Nat. Nanotechnol.* **2011**, *6* (4), 247–252.
- (15) Wertheim, G. K.; Buchanan, D. N. E. Reaction of C₆₀ with Metals: W. *Solid State Commun.* **1993**, *88* (2), 97–100.
- (16) Gall', N. R.; Rut'kov, E. V.; Tontegode, A. Y. Interaction of C₆₀ Molecules with the (100)W Surface: Adsorption, Initial Stages of Film Growth, and Thermal Transformation of the Adsorption Layer. *Semiconductors* **38** (9), 1023–1029.
- (17) Palmquist, J.-P.; Czigany, Z.; Odén, M.; Neidhart, J.; Hultman, L.; Jansson, U. Magnetron Sputtered W–C Films with C₆₀ as Carbon Source. *Thin Solid Films* **2003**, *444* (1–2), 29–37.

- (18) Silien, C.; Pradhan, N. A.; Ho, W.; Thiry, P. A. Influence of Adsorbate-Substrate Interaction on the Local Electronic Structure of C₆₀ Studied by Low-Temperature STM. *Phys. Rev. B* **2004**, *69* (11), 115434.
- (19) Franke, K. J.; Pascual, J. I. Effects of Electron–vibration Coupling in Transport through Single Molecules. *J. Phys. Condens. Matter* **2012**, *24* (39), 394002.
- (20) Randel, J. C.; Niestemski, F. C.; Botello-Mendez, A. R.; Mar, W.; Ndabashimiye, G.; Melinte, S.; Dahl, J. E. P.; Carlson, R. M. K.; Butova, E. D.; Fokin, A. A.; Schreiner, P. R.; Charlier, J.-C.; Manoharan, H. C. Unconventional Molecule-Resolved Current Rectification in Diamondoid–fullerene Hybrids. *Nat. Commun.* **2014**, *5*, 4877.
- (21) Büttner, M.; Reinke, P. Fullerene Nanostructures on Defect-Rich Graphite Surfaces. *J. Phys. Chem. C* **2009**, *113* (19), 8107–8111.
- (22) Bozhko, S. I.; Krasnikov, S. A.; Lübben, O.; Murphy, B. E.; Radican, K.; Semenov, V. N.; Wu, H.-C.; Levchenko, E. A.; Chaika, A. N.; Sergeeva, N. N.; Shvets, I. V. Correlation between Charge-Transfer and Rotation of C₆₀ on WO₂/W(110). *Nanoscale* **2013**, *5* (8), 3380–3386.
- (23) McClimon, J. B.; Monazami, E.; Reinke, P. Interaction of C₆₀ with Tungsten: Modulation of Morphology and Electronic Structure on the Molecular Length Scale. *J. Phys. Chem. C* **2014**, *118* (42), 24479–24489.
- (24) Wertheim, G. K.; Buchanan, D. N. E. Interfacial Reaction of C₆₀ with Silver. *Phys. Rev. B Condens. Matter* **1994**, *50* (15), 11070–11073.
- (25) Hunt, M. R. C.; Modesti, S.; Rudolf, P.; Palmer, R. E. Charge Transfer and Structure in C₆₀ Adsorption on Metal Surfaces. *Phys. Rev. B Condens. Matter* **1995**, *51* (15), 10039–10047.
- (26) Rowe, J. E.; Rudolf, P.; Tjeng, L. H.; Malic, R. A.; Meigs, G.; Chen, C. T.; Chen, J.; Plummer, E. W. Synchrotron Radiation and Low Energy Electron Diffraction Studies of Ultrathin C₆₀ Films Deposited on Cu(100), Cu(111) and Cu(110). *Int. J. Mod. Phys. B* **1992**, *06* (23n24), 3909–3913.
- (27) Girifalco, L. A. Molecular Properties of C₆₀ in the Gas and Solid Phases. *J. Phys. Chem.* **1992**, *96* (2), 858–861.
- (28) Nakamura, J.; Nakayama, T.; Watanabe, S.; Aono, M. Structural and Cohesive Properties of a C₆₀ Monolayer. *Phys. Rev. Lett.* **2001**, *87* (4), 048301.
- (29) Bozhko, S. I.; Krasnikov, S. A.; Lübben, O.; Murphy, B. E.; Radican, K.; Semenov, V. N.; Wu, H. C.; Bulfin, B.; Shvets, I. V. Rotational Transitions in a C₆₀ Monolayer on the WO₂/W(110) Surface. *Phys. Rev. B* **2011**, *84* (19), 195412.
- (30) Pascual, J. I.; Gómez-Herrero, J.; Rogero, C.; Baró, A. M.; Sánchez-Portal, D.; Artacho, E.; Ordejón, P.; Soler, J. M. Seeing Molecular Orbitals. *Chem. Phys. Lett.* **2000**, *321* (1–2), 78–82.
- (31) Petrukhina, M. A.; Scott, L. T. *Fragments of Fullerenes and Carbon Nanotubes: Designed Synthesis, Unusual Reactions, and Coordination Chemistry*; John Wiley & Sons, 2011.
- (32) Chen, M. K.; Hsin, H. J.; Wu, T. C.; Kang, B. Y.; Lee, Y. W.; Kuo, M. Y.; Wu, Y. T. Highly Curved Bowl-Shaped Fragments of Fullerenes: Synthesis, Structural Analysis, and Physical Properties. *Chem. – Eur. J.* **2014**, *20* (2), 598–608.
- (33) Hayashi, A.; Xie, Y.; Poblet, J. M.; Campanera, J. M.; Lebrilla, C. B.; Balch, A. L. Mass Spectrometric and Computational Studies of Heterofullerenes ([C₅₈Pt][−], [C₅₈Pt]⁺) Obtained by Laser Ablation of Electrochemically Deposited Films. *J. Phys. Chem. A* **2004**, *108* (12), 2192–2198.

- (34) Gabriel, M. A.; Genovese, L.; Krosnicki, G.; Lemaire, O.; Deutsch, T.; Franco, A. A. Metallofullerenes as Fuel Cell Electrocatalysts: A Theoretical Investigation of Adsorbates on C₅₉Pt. *Phys. Chem. Chem. Phys. PCCP* **2010**, *12* (32), 9406–9412.
- (35) Billas, I. M. L.; Massobrio, C.; Boero, M.; Parrinello, M.; Branz, W.; Tast, F.; Malinowski, N.; Heinebrodt, M.; Martin, T. P. First Principles Calculations of Iron-Doped Heterofullerenes. *Comput. Mater. Sci.* **2000**, *17* (2–4), 191–195.
- (36) Changgeng, D.; Jinlong, Y.; Xiangyuan, C.; Chan, C. T. Geometric and Electronic Structures of Metal-Substituted Fullerenes C₅₉M (M=Fe, Co, Ni, and Rh). *J. Chem. Phys.* **1999**, *111* (18), 8481–8485.
- (37) Poblet, J. M.; Muñoz, J.; Winkler, K.; Cancilla, M.; Hayashi, A.; Lebrilla, C. B.; Balch, A. L.; Winkler, K. Geometric and Electronic Structure of Metal-Cage Fullerenes, C₅₉M (M = Pt, Ir) Obtained by Laser Ablation of Electrochemically Deposited Films. *Chem. Commun.* **1999**, No. 6, 493–494.
- (38) Feenstra, R. M. A Prospective: Quantitative Scanning Tunneling Spectroscopy of Semiconductor Surfaces. *Surf. Sci.* **2009**, *603* (18), 2841–2844.
- (39) Tromp, R. M. Spectroscopy with the Scanning Tunnelling Microscope: A Critical Review. *J. Phys. Condens. Matter* **1989**, *1* (51), 10211.
- (40) Horcas, I.; Fernandez, R.; Gómez-Rodríguez, J. M.; Colchero, J.; Gómez-Herrero, J.; Baro, A. M. WSXM: A Software for Scanning Probe Microscopy and a Tool for Nanotechnology. *Rev. Sci. Instrum.* **2007**, *78* (1), 013705–013705.
- (41) Minamikawa, T.; Suzuki, T.; Yonezawa, Y.; Segawa, K.; Morimoto, A.; Shimizu, T. Annealing Temperature Dependence of MgO Substrates on the Quality of YBa₂Cu₃O_x Films Prepared by Pulsed Laser Ablation. *Jpn. J. Appl. Phys.* **1995**, *34* (8R), 4038.
- (42) Cukauskas, E. J.; Kirchoefer, S. W.; Chang, W. Morphology and Dielectric Properties of Ba_{0.5}Sr_{0.5}TiO₃ Thin Films on Annealed (1 0 0) MgO. *J. Cryst. Growth* **2002**, *236* (1–3), 239–247.
- (43) McClimon, J. B. Synthesis and oxidation of non-stoichiometric tungsten carbide studied by scanning tunneling microscopy/spectroscopy. Master. University of Virginia (2014). <http://libraprod.lib.virginia.edu/catalog/libra-oa:3096>.
- (44) Perdew, J. P.; Zunger, A. Self-Interaction Correction to Density-Functional Approximations for Many-Electron Systems. *Phys. Rev. B* **1981**, *23* (10), 5048–5079.
- (45) Brandbyge, M.; Mozos, J.-L.; Ordejón, P.; Taylor, J.; Stokbro, K. Density-Functional Method for Nonequilibrium Electron Transport. *Phys. Rev. B* **2002**, *65* (16), 165401.
- (46) Soler, J. M.; Artacho, E.; Gale, J. D.; García, A.; Junquera, J.; Ordejón, P.; Daniel Sánchez-Portal. The SIESTA Method for Ab Initio Order- N Materials Simulation. *J. Phys. Condens. Matter* **2002**, *14* (11), 2745.
- (47) Byrd, R.; Lu, P.; Nocedal, J.; Zhu, C. A Limited Memory Algorithm for Bound Constrained Optimization. *SIAM J. Sci. Comput.* **1995**, *16* (5), 1190–1208.

7.7. Supporting Information

7.7.1. DFT Calculation of C₆₀ / W

DFT calculations are used to gain insight in the bonding of C₆₀ molecules to the W atoms and surface. For this goal, two separate approaches are used. First configurations/orientations for a C₆₀ molecule on W(110) and W(100) surface are illustrated and in the second approach, conceivable tungsten hetrofullerenes structures were considered. Hetrofullerene calculations are described in the main body of the manuscript and several adsorption geometries for C₆₀ molecule are compared. In this section, the DFT results for C₆₀ on tungsten surface is discussed in details.

7.7.2. C₆₀ / W-bulk Energies and Adsorption Geometries

As it was explained in the main text, the W-thin films in this works are mainly oriented in (110) orientation, but minor contributions from other plane orientations is possible. Therefore, DFT calculations for both C₆₀/ W(110) and C₆₀/ W(100) systems were performed. For the first approach, a single C₆₀ molecule was placed on a slab with a thickness of six layers of W in the bcc structure with a total of 126 atoms for (110) and 96 for (100) surface. Four possible orientation for fullerene on the W(110) surface were explored: h hexagon face, p pentagon face, h-h bond between two hexagons, or p-h bond between a hexagon and pentagon were closest to the W surface (Figure 7.7). The most stable configuration, which is shown in Figure 7.7a, is the h-h orientation and due to the symmetry of the molecule the same bond is visible at the apex of the molecule facing the STM tip.

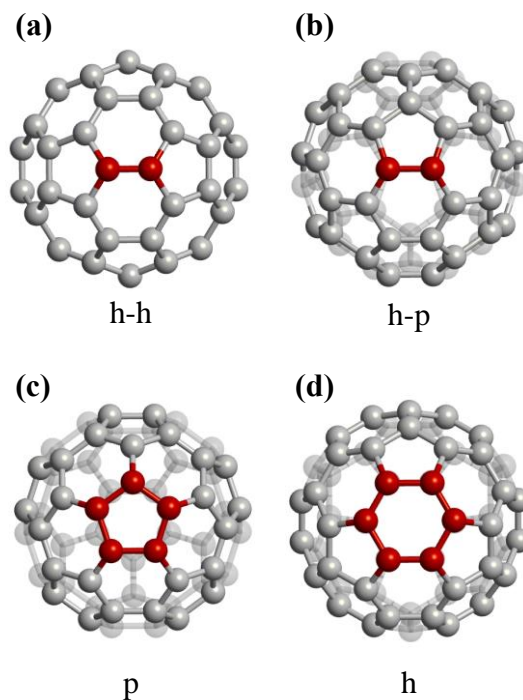


Figure 7.7: Possible adsorption orientation for C_{60} molecule on substrate. The red circles show the closest carbon atoms to the W-substrate. (a) h-h bridge between two hexagons (b) p-h bridge between a hexagon and pentagon (c) pentagon face (d) hexagon face.

Both W(110) and W(100) surface were considered for the simulations. To find the most energetically favorable adsorption site of C_{60} on tungsten surface, for each tungsten plane, four possible relative position of C_{60} to the tungsten surface were simulated. These adsorption sites are shown in Figure 7.8. We acknowledge that there are more possible configurations for such material systems, at the same time we believe for the purpose of this work these configurations are sufficient. For W(110), the minimum energy was found where the h-h bridge in C_{60} molecule was placed at the center of 4 tungsten atoms in 110 plane.).

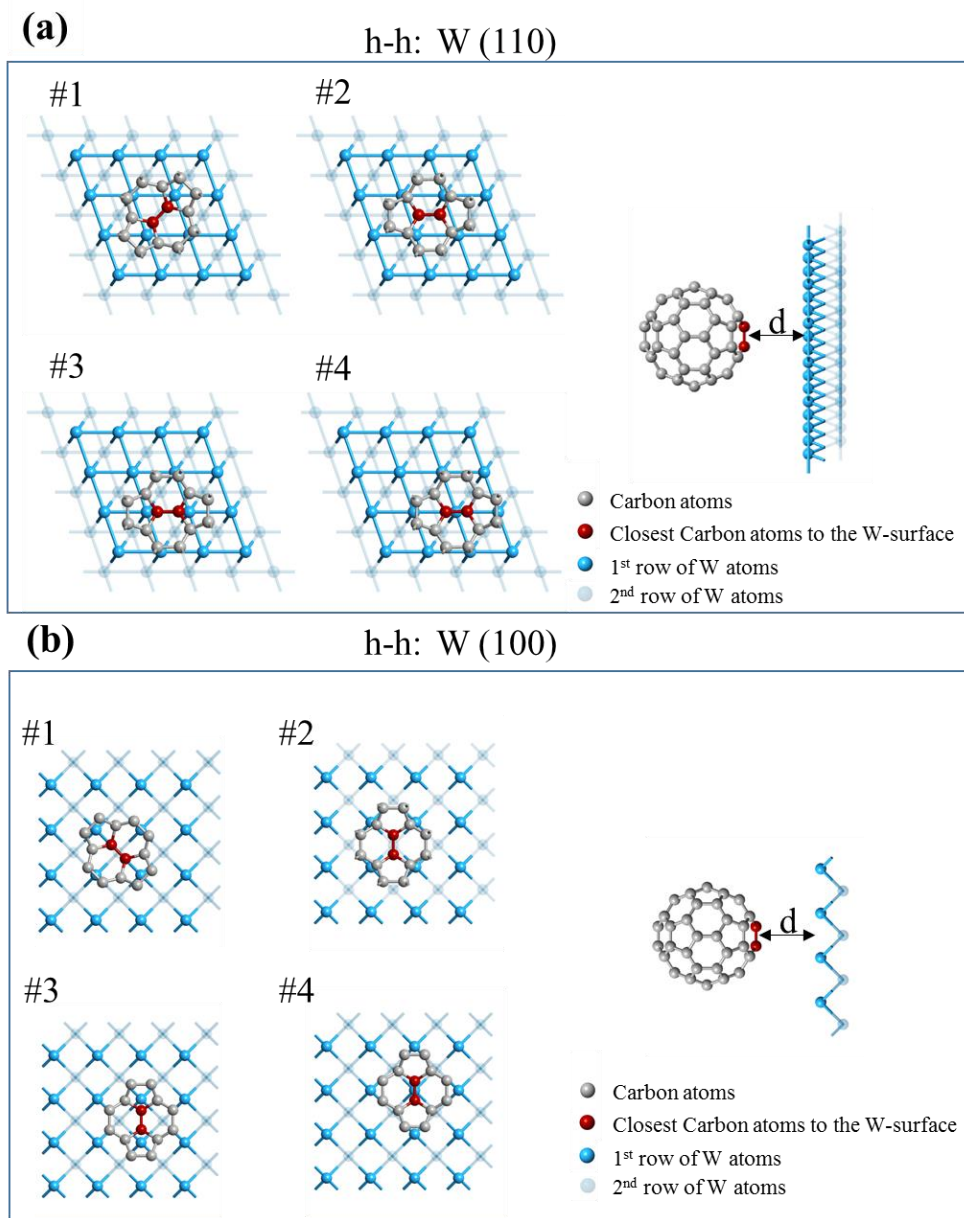


Figure 7.8: Considered adsorption geometries of C_{60} molecule on a) W(110) and b) W(100) surface. To display the adsorption position clearly, only the lowest 14 carbon atoms from C_{60} are shown. (a) Four possible adsorption site for W(110) where the h-h bond in C_{60} positioned at (#1) at the center (#2) at the center with 45o rotation (#3) on bridge (#4) on top .(b) Four possible adsorption site for W(100) where the h-h bond in C_{60} positioned at (#1) the center (#2) at the center with 45o rotation (#3) on bridge (#4) on top.

This configuration is marked as #2 in Figure 7.8a. A similar analysis was applied for W(100) plane. For this system, the minimum energy was found when the h-h bridge of C_{60}

molecule was positioned at the center of 4 tungsten atoms. This configuration is marked as #1 in Figure 7.8b.

To find the equilibrium distance between C_{60} and tungsten surface for each of these configurations, the molecule was placed above the surface in various distance from substrate and the total energy of the systems were calculated. Figure 7.9 (a,b) illustrates the results for the total energy versus distance, where each curves include one global minimum. For W(110) the global minimum energy was find for configuration #2 at 1.8 (Å), and for W(100) the minimum energy was achieved for configuration #1 at 1.6 (Å) .

After finding the approximate equilibrium distance/adsorption geometry for C_{60} /W-surface system, to achieve the most stable structure the W(110)-Conf# 2 and W(100)-Conf# 1 were allowed to relax. In the relaxation process, a tungsten slab with thickness of six atomic layers in the bcc structure was used. During the relaxation process, the three bottom layer of the metal were fixed and the top three layers of substrate in addition to C_{60} molecule were allowed to relax. This also leads to a slight compression of the molecule perpendicular to the surface. The binding energy of C_{60} to the surface of W(110) is ~7.3 eV, which indicate a very strong interaction between C_{60} and the surface. This strong interaction is comparable to the results reported for C_{60} molecule on Ir(111) with binding energy of 7.67 eV.¹ This strong binding energy is in consistent with our experimental results from fullerene surface after annealing, where the motion of C_{60} molecules was restricted after annealing. This binding energy is even larger for W(100) surface (~9.05 eV), where due to lower density of tungsten atoms in the surface in comparison to W(110), more perturbation of W atoms in the surface is possible. Therefore, this stronger binding energy leads to a lower distance between molecule and W surface.

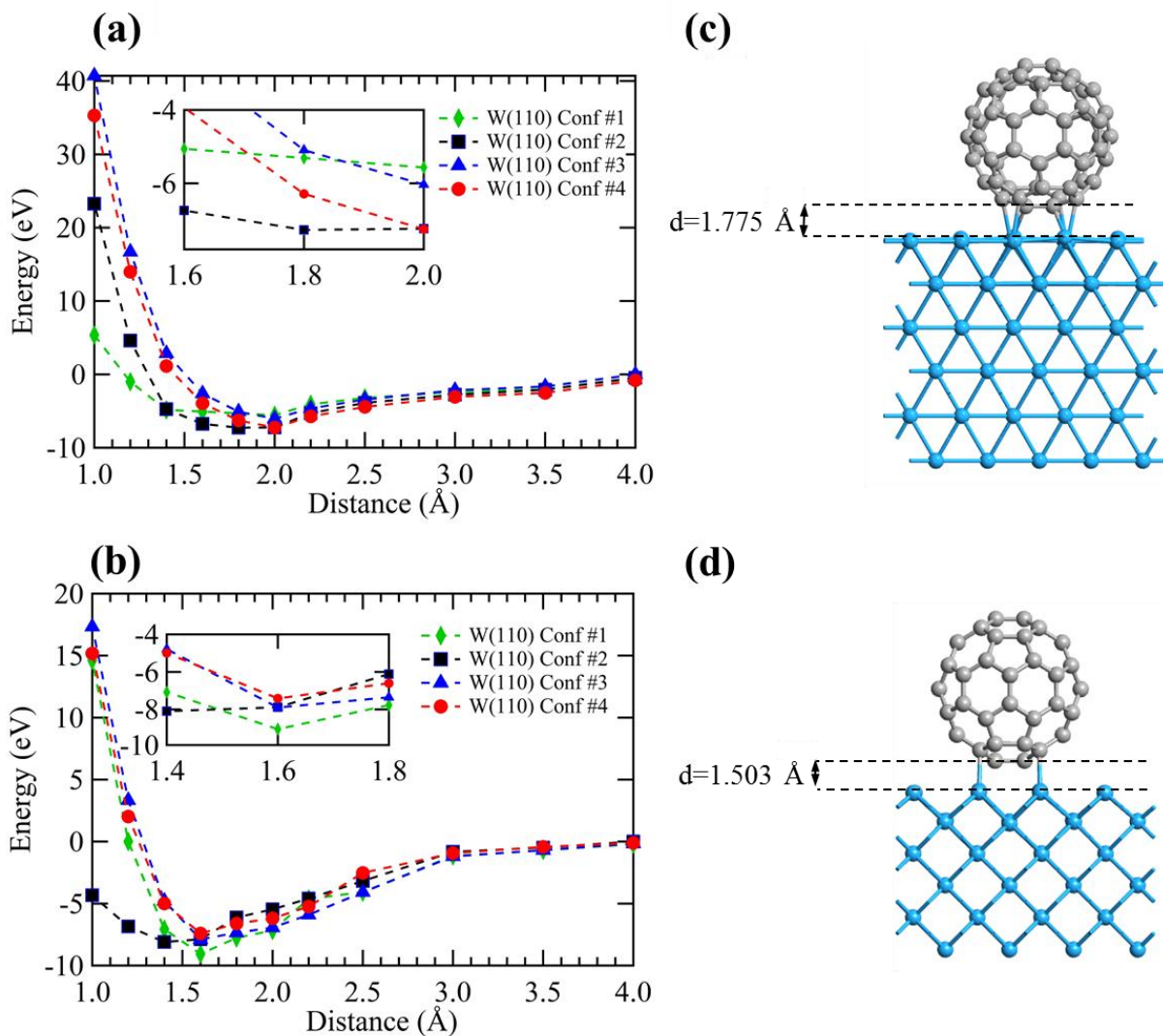


Figure 7.9: Total energy analysis of the systems to find the most stable adsorption configuration/distance for C_{60} molecules on (a) W(100) and (b) W(110) (c) the relaxed configuration for W(110) (d) the relaxed configuration for W(100).

7.7.3. Electronic structure of C_{60} / W(110) and C_{60} / W(100)

The relaxed structure for C_{60} / W(110) is shown in Figure 7.10a. The DOS integrated over the whole molecule after bonding to the W surface is shown in Figure 7.10b where a k-point sampling of $4 \times 4 \times 1$ was used. The calculated DOS for a free C_{60} molecule is included for comparison. We are aware that the absolute magnitude of the molecule band gap is not reproduced

particularly well with DFT, however, the qualitative changes in the band gap moving from a free molecule to a molecule adsorbed on a surface are described in a reliable manner. A similar result has been shown previously for C_{60} on Au, Ag and other surfaces and we were able to faithfully reproduce these published results.^{2,3} The electronic gap of a free C_{60} molecule is 4.9 eV, in the solid the gap drops to 2.3 eV (conduction band to valence band edge),⁴ which is close to the value measured in our work for multilayers. The DFT calculation yields 1.7 eV gap for an isolated C_{60} (Figure 7.10b). Upon bonding to the surface, the gap is and E_F shifts to higher energy in the LUMO due to mixing with the d-states in W. This replicates the response as seen in the ST spectra included in Figure 7.1d, and the observations reported in a recent publication.⁵ The lowest unoccupied molecular orbital (LUMO) is visualized in the Figure 7.10, and reflects closely the surface structure observed in STM after the molecule is immobilized at the onset of the interfacial reaction. A weak peak near the fermi energy arise from splitting of LUMO state of C_{60} on W(110), a similar peak has been observed for C_{60} / Ag(100) surface.³

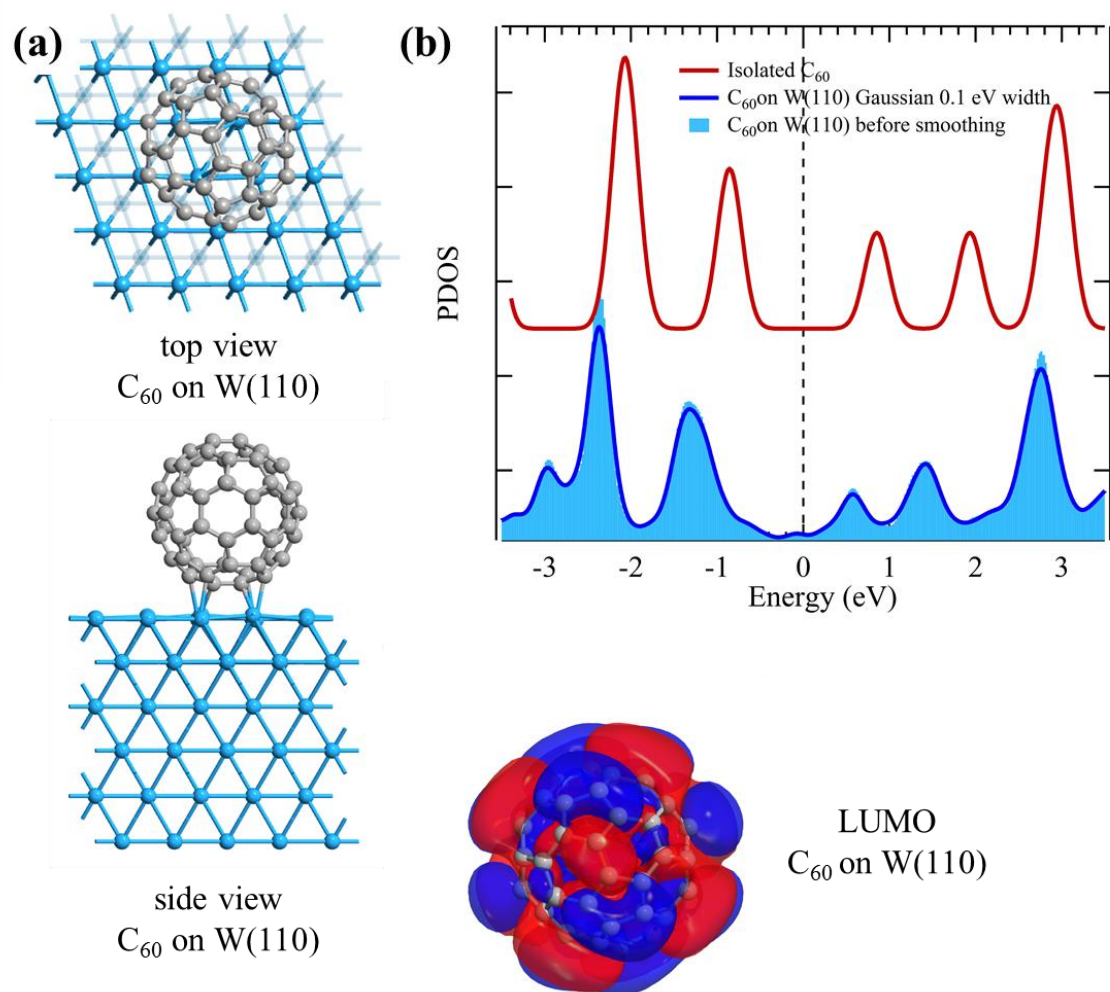


Figure 7.10: Configuration and calculated projected density of states (DOS) on C₆₀ molecules after adsorption on W(110) surface. (a) the most stable molecule orientation with the h-h bond facing the W-surface - top and side view. The LUMO for C₆₀ on W(110) is depicted in the same orientation and reflects the molecule as it is seen on the vacuum-facing side imaged with STM, in which blue and red represent the positive and negative wave function. (b) DOS of the C₆₀ molecule, and C₆₀ positioned on W(110) in the orientation shown in (a) before smoothing and after smoothing with a Gaussian with a full half width of 0.1 eV. The dashed vertical line indicates E_F.

A similar type of analysis was performed for C₆₀ /W(100) system and it is shown in Figure 7.11. The LUMO peak in the DOS of these two system can be taken as the main difference between C₆₀ / W(110) and C₆₀ / W(100) systems. While C₆₀ molecule adsorbed on W(110) surface shows a clear LUMO peak in PDOS, this peak illustrates a more complex nature for C₆₀ adsorbed on

(100) surface.

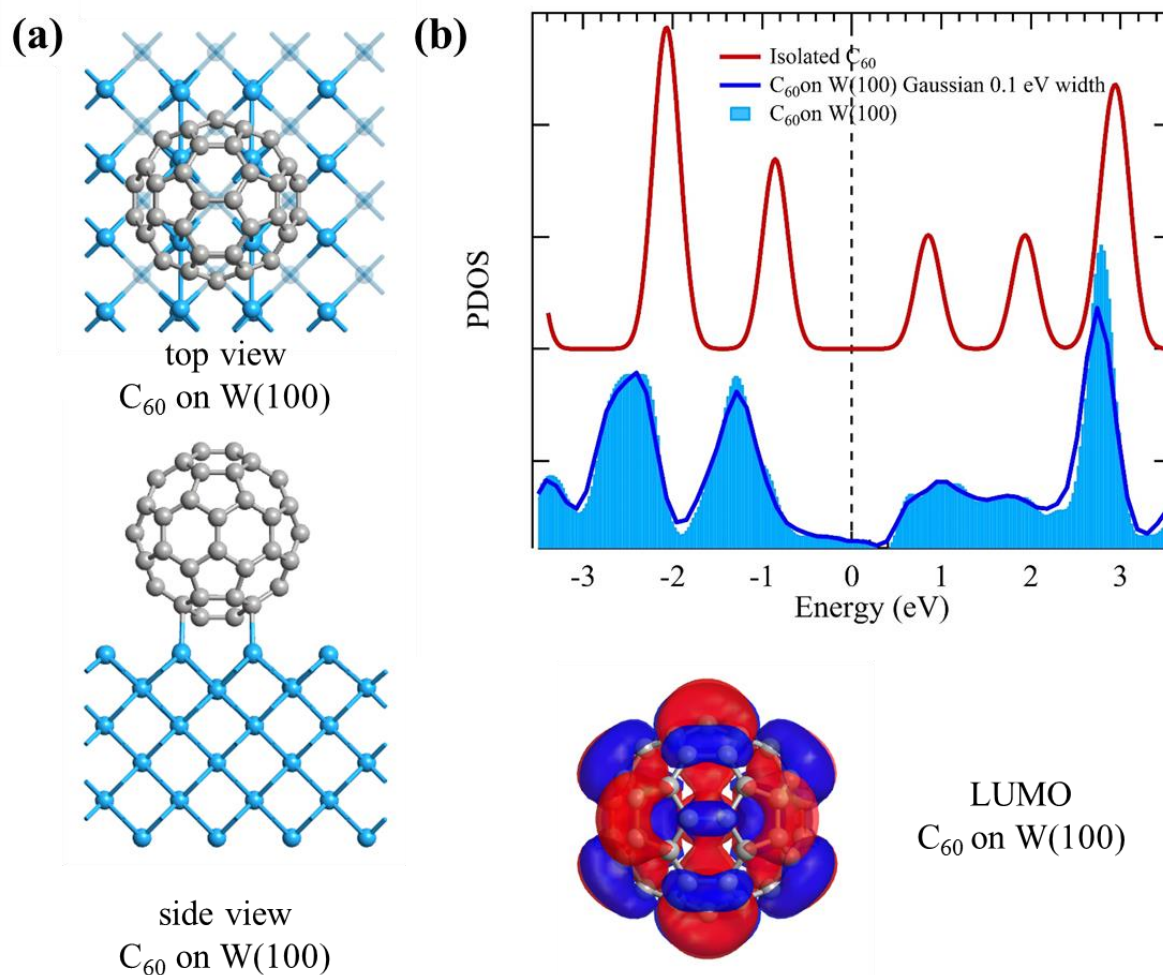


Figure 7.11: Configuration and calculated projected density of states (DOS) on C_{60} molecules after adsorption on W(100) surface. (a) the most stable molecule adsorption geometry with the h-h bond facing the W-surface - top and side view. The LUMO for C_{60} on W(100) is depicted in the same orientation and reflects the molecule as it is seen on the vacuum-facing side imaged with STM, in which blue and red represent the positive and negative wave function. (b) DOS of the C_{60} molecule, and C_{60} positioned on W(100) in the orientation shown in (a) before smoothing and after smoothing with a Gaussian with a full half width of 0.1 eV. The dashed vertical line indicates E_F .

7.7.4. C_{60} Molecule Motion at Room Temperature

Figure 7.8 shows two STM images taken sequentially to track the motion of C_{60} molecules prior to annealing. The C_{60} coverage is about 0.2 ML and the W-surface exhibits several step edges

and terraces. The molecules decorate the step edges, where about 75% of the molecules reside, while the remaining 25% is located on the terraces. The two image frames included in S2 are representative examples of molecule motion seen in room temperature imaging. The images are taken from bottom to top, line by line with alternating scan direction. The individual molecules are marked in the images and isolated in the frames shown in the bottom row of S2. We distinguish between fullerene molecules (blue), a few instances where the signature in the image is most likely a molecule (light blue), and in the second image frame those molecules which were added are marked in red, and those which are missing compared to frame 1 are marked in green. The acquisition time for each of these images is about 5 minutes.

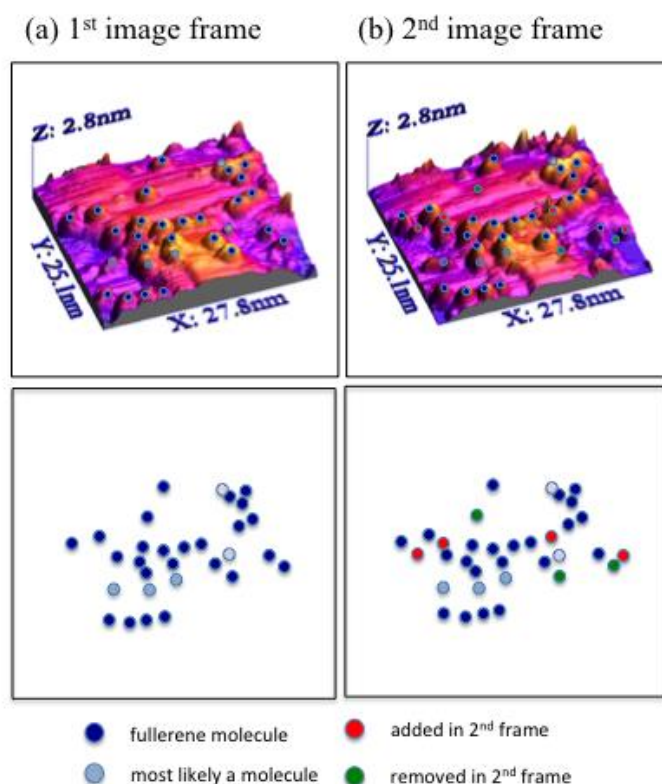


Figure 7.12: Sequential image frames of C_{60} molecules on a W-surface ($V_{\text{bias}}=1$ V $I=0.02$ nA). Frame 1 (a) and 2 (b) were recorded sequentially. The molecule positions are marked in the images, and their position is isolated in frames shown in the bottom row.

7.7.5. Single Molecules on the W-surface

This experiment shows a sub-monolayer coverage ~ 0.3 ML with C_{60} molecules on the W-surface. The topography image was recorded during the measurement of the spectroscopy maps and has therefore a lower resolution compared to images in the main section of the manuscript. The differential conductance map clearly shows the position of the molecules on the conducting surface. The differential conductance is increased locally when the bias voltage corresponds to the position of the LUMO ($V_{\text{bias}}=+1.2$ V) and the HOMO ($V_{\text{bias}}=-1.76$ V). The HOMO and LUMO

can also be recognized in the spectra included in Figure 7.2d, which correspond to a single C_{60} layer on W. The isolated molecules exhibit the same LDOS which is seen in the complete molecule layer, and also show an identical response to annealing.

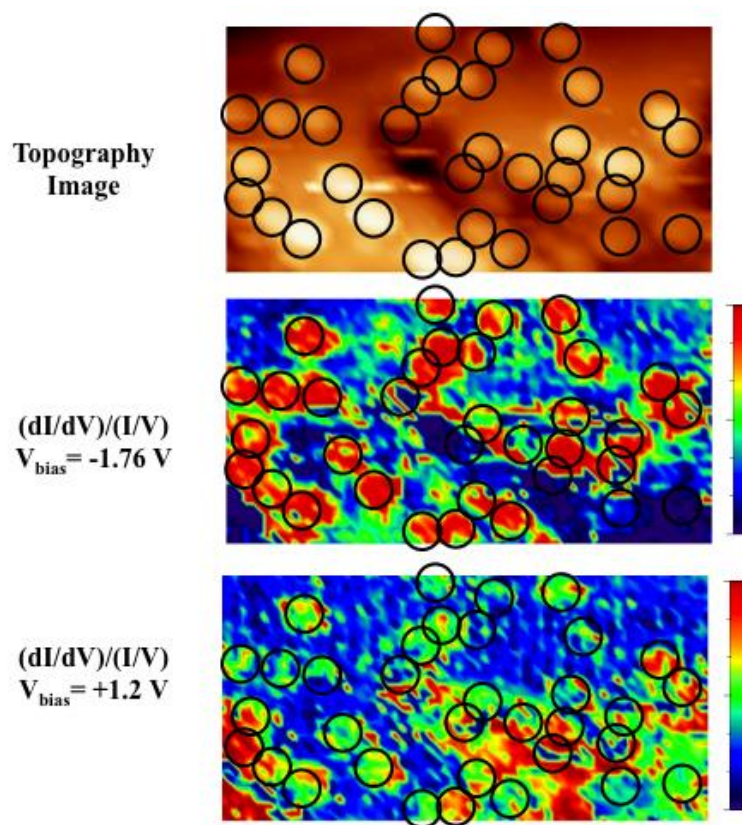


Figure 7.13: Topography image, and differential conductance maps for V_{bias} of -1.76 V (filled states) and $+1.2$ V (empty states) recorded simultaneously. The C_{60} coverage is ~ 0.3 ML and the molecules are marked with circles to allow for ease of comparison between image and maps. Every 5th image pixel corresponds to a ST spectrum. The enhanced LDOS at the molecule positions is readily apparent against the constant LDOS from the metal substrate. The section in the center bottom of the image, which corresponds to a substrate inhomogeneity yields a higher LDOS from the metal substrate and the fullerene molecules are hard to locate in this region for the empty states, but easily seen in the filled state map.

7.7.6. References

- (1) Fei, X.; Zhang, X.; Lopez, V.; Lu, G.; Gao, H.-J.; Gao, L. Strongly Interacting C₆₀/Ir(111) Interface: Transformation of C₆₀ into Graphene and Influence of Graphene Interlayer. *J. Phys. Chem. C* **2015**, *119* (49), 27550–27555.
- (2) Wang, L.-L.; Cheng, H.-P. Density Functional Study of the Adsorption of a C₆₀ Monolayer on Ag(111) and Au(111) Surfaces. *Phys. Rev. B* **2004**, *69* (16), 165417.
- (3) Lu, X.; Grobis, M.; Khoo, K. H.; Louie, S. G.; Crommie, M. F. Charge Transfer and Screening in Individual C₆₀ a Scanning Tunneling Spectroscopy and Theoretical Study. *Phys. Rev. B* **2004**, *70* (11), 115418.
- (4) Lof, R. W.; van Veenendaal, M. A.; Koopmans, B.; Jonkman, H. T.; Sawatzky, G. A. Band Gap, Excitons, and Coulomb Interaction in Solid C₆₀. *Phys. Rev. Lett.* **1992**, *68* (26), 3924–3927.
- (5) McClimon, J. B.; Monazami, E.; Reinke, P. Interaction of C₆₀ with Tungsten: Modulation of Morphology and Electronic Structure on the Molecular Length Scale. *J. Phys. Chem. C* **2014**, *118* (42), 24479–24489.

Chapter 8

Oxidation and Carburization of Carbon Rich Tungsten Carbide Thin Films

8. Oxidation and Carburization of Carbon Rich Tungsten Carbide Thin Films

8.1. Introduction

Transition metal carbides such as tungsten carbide, possess unique bonding characteristics with covalent, ionic and metallic contributions, which leads to their specific physical and mechanical properties.¹⁻³ An early work by Levy and Boudart in 1973 showed that tungsten carbide density of state at near the Fermi energy is similar to Pt leading to the speculation that it might have similar catalytic properties.⁴ Since then, several studies have explored this aspect of tungsten carbide.⁵⁻⁷ Although the performance of tungsten carbide has been proved inferior in direct comparison to Pt and other noble metals, its lower cost and superior resistance to catalyst poisons like H₂S and CO have kept research interest high for applications such as anode catalyst in primary metabolite based microbial fuel cells.⁸ Although tungsten carbide is isoelectronic to Pt, it is susceptible to oxidation (unlike Pt), which degrades the catalytic activity of the surface.⁹⁻¹¹

In this work, an approach for synthesis of nonstoichiometric carbon rich carbide is presented. The free carbon in these thin films are expected to provide a pathway to carburize the oxidized regions by annealing of the sample at UHV. To verify this hypothesis, several sample with different C:W ratio was prepared and their morphology and electronic properties were measured by in-situ STM/STS measurement. In addition, AP-XPS measurements were performed to examine the effect of temperature in kinetics of oxidation and carburization cycles.

8.2. Methods

Tungsten carbide thin films were synthesized in UHV ($<2 \times 10^{-10}$) chamber by e-beam evaporation of tungsten, and thermal evaporation of C_{60} molecules as carbon precursor. MgO (100) was used as the substrate and held at 1073 K during deposition. This temperature significantly exceeds the temperatures used in the nanosphere experiments described in chapter 7. At this temperature, C_{60} molecules were dissociated to individual carbon atoms upon the impact with the hot substrate, then incorporate with tungsten atoms to form tungsten carbide. After the deposition, all samples were annealed at 1073 K for an additional 10 minutes to promote complete carburization. An advantage of this method over conventional growth techniques is the possibility to trap the extra carbon during the synthesis, which makes it a viable method to grow non-stoichiometric carbide thin films. Other growth techniques, which often are involved with carburization of tungsten oxide using a carburizing agent (e.g. CH_4/H_2 gas mixture),^{12–14} control over the carbon concentration of non-carbide carbon (free carbon inventory) throughout the thin film is difficult.

MgO was selected as the substrate for two reasons: first, MgO is a diffusion barrier against tungsten and carbon atoms and therefore, allows control of the carbon inventory in the thin films. Second, the relatively flat and large terraces of MgO promote formation of the smoothest films possible. The MgO surface preparation process is described in our previous publications and chapter 4 of this thesis.^{15,16}

Use of C_{60} molecule as carbon precursor has been shown to provide high quality carbide thin films.^{17,18} Three different composition of carbide thin films were targeted and up to 3 samples for each composition were synthesized for STM, and AP-XPS measurements. Summary of descriptions for the thin films are presented in Table 8.1.

	Sample	W- Atomic Ratio	C-Atomic Ratio	C _{ext} -Ratio	Labeled as
STM	S1, S2	50% W	50% C	0%	50/50
	S3, S4, S5	40% W	60% C	20%	40/60
	S6	25% W	75% C	50%	25/75
AP-XPS	S7	50% W	50% C	0%	50/50
	S8	40% W	60% C	20%	40/60
	S9, S10	25% W	75% C	50%	25/75

Table 8.1: Summary of carbide thin films used in this work. The term C_{ext} represent the ratio of extra carbon in thin films if tungsten and carbon form WC. This assumption is confirmed by XPS analysis.

The compositions of the thin films were calculated by controlling the ratio of deposited tungsten to carbon atoms. All deposition rates were calibrated by using of a quartz crystal monitor (QCM) prior to deposition. However, the XPS results illustrate a higher carbon concentration in thin films than it was expected (5-10 % more).

8.3. Results

8.3.1 STM/STS Results and Discussions

After each processing step, which include synthesis of the thin film, oxidation, and annealing at UHV (carburization), the samples (S1-S6) were transferred to the STM without breaking the vacuum and their morphology and electronic properties were studied. The technical aspect of STM/STS measurements are described in chapter 5. The typical imaging conditions for thin films before the oxidation were ($I_t = 1$ nA and $V_{bias} = 10$ mV), and for surface after oxidation were ($I_t = 1.5$ nA and $V_{bias} = 1$ mV). To be able to compare the spectroscopy results for oxidized

and carburized sample, an identical voltage range of (-2.5 – +2.5 V) was used for all STS measurements.

The STM and STS results are organized as following. First, the topographical features of tungsten carbide thin films and the effect of carbon concentration on their morphology is presented. Second, the influence of oxygen on these carbide thin films is discussed, and third, an example of annealed oxide surface is illustrated. The STM/STS results were collected by Brandon McClimon, a former student in our group.

Figure 8.1 shows the STM images measured for two different tungsten carbide thin films samples (S1 and S2) with 50/50 tungsten to carbon ratio. Figure 8.1a,b show the largest scale images ($2000 \times 2000 \text{ nm}^2$), where the majority of the surface is covered with square islands. The morphology of these thin films at this scale is similar to the observed morphology of underlying MgO (100) substrate. Higher magnification STM images show that each of these islands consists of numerous nanoclusters with irregular shapes (Figure 8.1c,d).

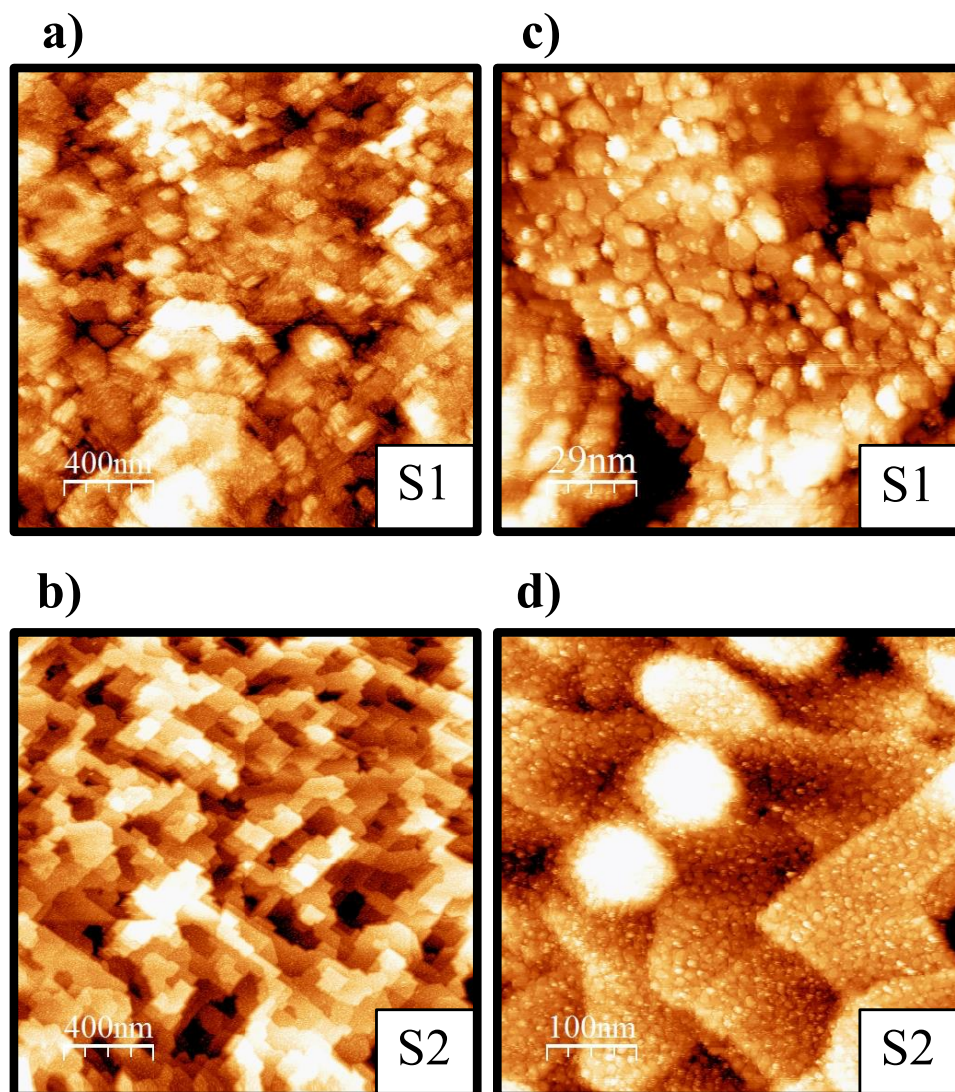


Figure 8.1: STM images from two different 50/50 tungsten carbide thin films (S1 and S2). a,b) 2000×2000 nm² images. The long ordering observed at this magnification is imprinted by the morphology of the underlying MgO substrate. c,d) Higher magnification images which show the fine structure on the surface. The image size of (c) is (145×145 nm²) and the image size of (d) is (500×500 nm²).

Two highest resolution images of these clusters (Figure 8.2a,b), exhibit a stripe pattern. Even though this strip pattern seems to be an irregular structure, a closer look at these images shows a portion of these areas contains local periodicity (Figure 8.2c,d). The nearest neighbor distance of the atoms in these regions is between (2.8-3.5 Å). These results indicate that the

observed structure possibly arises from (0001) plane of WC with the nearest neighbor distance of 2.9 (Å).¹⁹ The irregularity observed in the atomic structure of this surface is probably the result of carbon vacancy, which results in formation of WC_{1-x} compound. The existence of WC_{1-x} compound in thin films with W:C ratio of 50/50 is confirmed by XPS measurements.

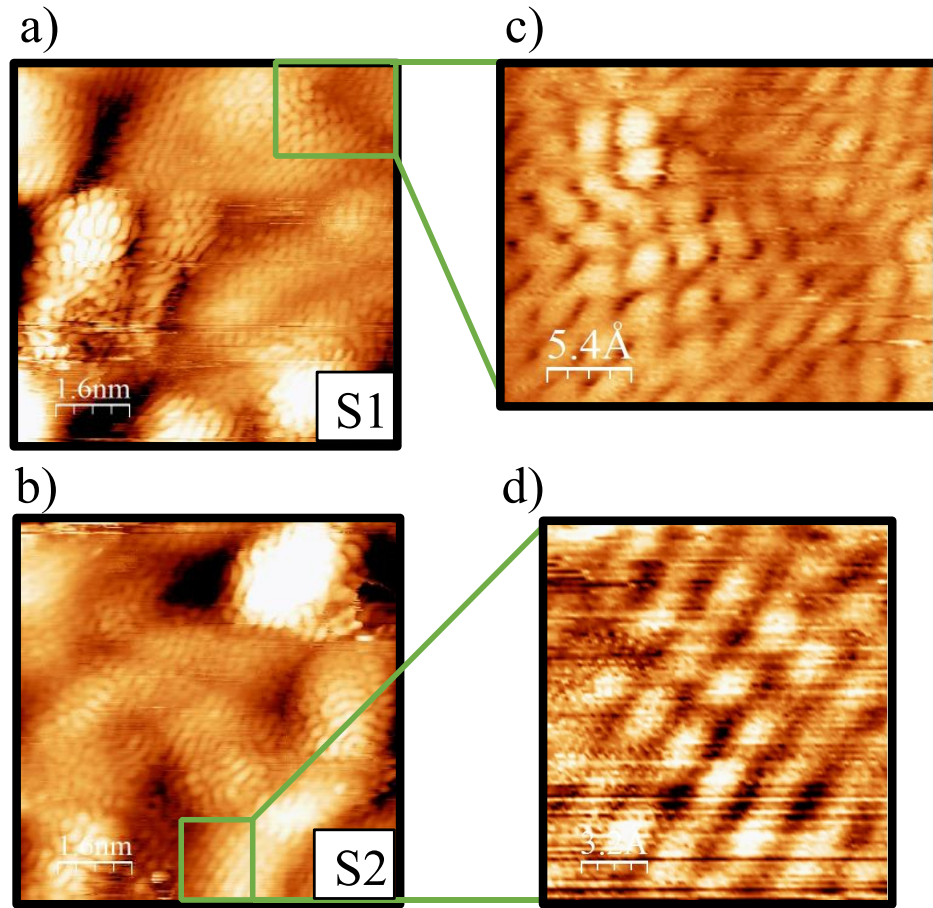


Figure 8.2: High resolution STM images ($8 \times 8 \text{ nm}^2$) of S1 and S2 samples.

The 40/60 carbide thin films show a different morphology at large scale ($2000 \times 2000 \text{ nm}^2$) in comparison to the 50/50 sample. Figure 8.3 illustrates that the sharp edges observed in 50/50 sample are replaced by a morphology which is consist of narrow and long features with smooth edges and more rounded terraces boundaries. At higher magnification (Figure 8.3c,d), it can be

seen that each island again consists of several nanoclusters. Atomic resolution was obtained and it shows that the majority of the surface is covered by graphite/graphene (Figure 8.3e,f). The appearance of distinct graphitic regions and the morphology of the surface at large scale, indicate that the 20% extra carbon embedded in thin films transforms the surface morphology and leads to the expected carbon segregation.

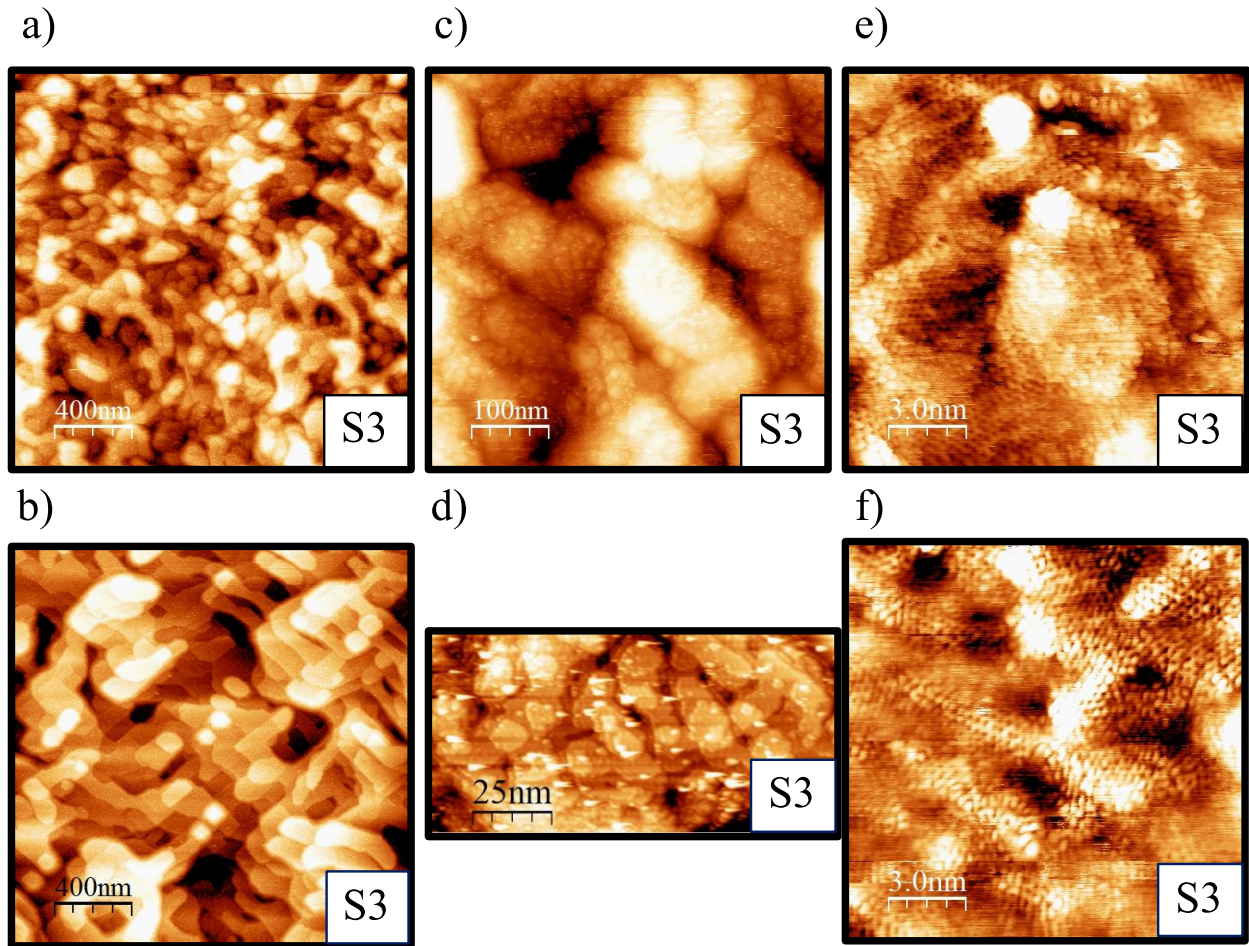


Figure 8.3: STM images from 40/60 tungsten carbide thin films (S3). a,b) 2000×2000 nm² images. The majority of the islands have smooth edges. c,d) Higher magnification where the nanoclusters inside each island are visible. The image size of (c) is (500×500 nm²) and the image size of (d) is (80×100 nm²). e,f) High resolution STM images (15×15 nm²).

Figure 8.4 illustrate an atomic resolution STM image from S3 sample in more details. With STM measurements, it is possible to differentiate between graphene and graphite. In Graphite, the carbon atoms that are placed on top of the carbon atom in lower layer (α atoms) show lower local density of states (LDOS) at near Fermi energy in comparison to the rest of carbon atoms (β atoms) (Figure 8.4d).^{20,21} Therefore, STM images of graphite show a triangular lattice with hexagonal symmetry (only β atoms are measured). The line-scan between atoms in graphite STM image, shows a nearest neighbor distance of 2.46 Å. In contrast, a STM images of graphene surface shows honeycomb lattice and all the carbon atoms are measured, and the line scan shows a nearest neighbor distance of 1.424 Å.

Figure 8.4a illustrates an example of Graphite and graphene regions on S3 sample. Graphite/graphene is indicated by red/blue circle, respectively, and they are confirmed by line-scans and fast Fourier transform (FFT). In addition to graphite/graphene, this surface exhibit small regions with striped pattern morphology reminiscent of S1 and S2. To highlight these regions the STM derivative image is included in Figure 8.3b and they are marked by green ellipsoids.

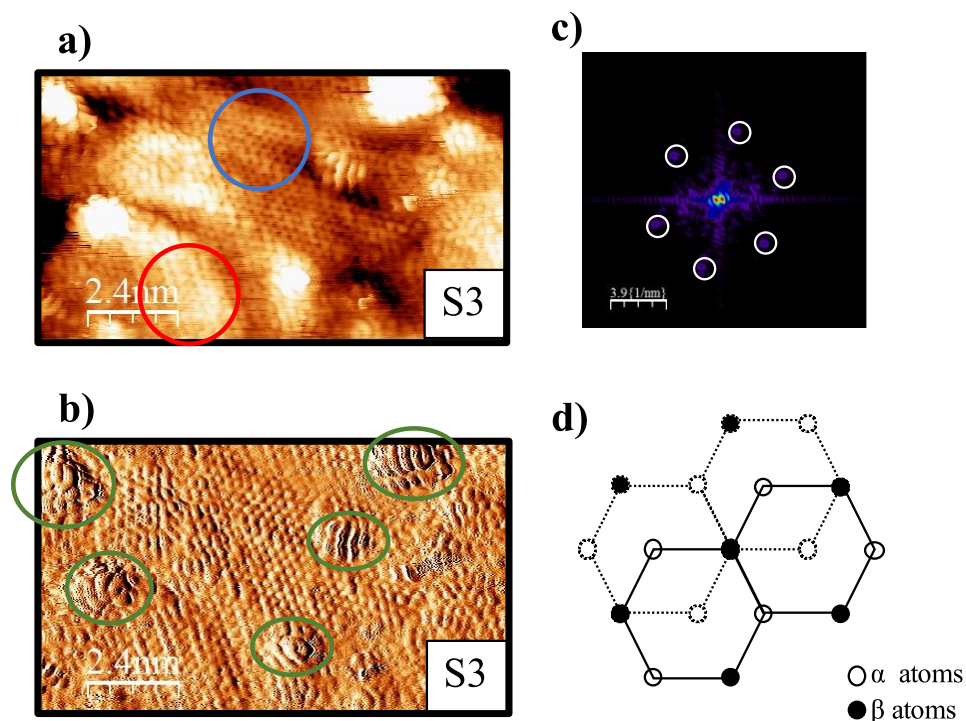


Figure 8.4: a) STM image from 40/60 tungsten carbide thin films ($7 \times 12 \text{ nm}^2$). The majority of the surface area is covered by graphene and graphite. b) the corresponding derivative STM image to highlight the striped regions from (a). c) The corresponding FFT illustrating the hexagonal lattices. d) The schematic representation of carbon atoms in graphite/graphene. The dashed lines show bottom layer and the solid lines show the top layer of carbon sheet.

By increasing the deposited carbon ratio even further (50% free carbon) during the growth process, the morphology of thin films was modified. Figure 8.5 shows the STM images for S5 sample (25/75) where 50% extra carbon atoms are incorporated in the thin film. The mobile island on the surface of this sample (Figure 8.5a,b) limit the resolution in the STM images. The islands are relatively large and smooth and reminiscent of STM images of graphite. The high surface coverage of graphite, is in a good agreement with large carbon inventory of the thin film.

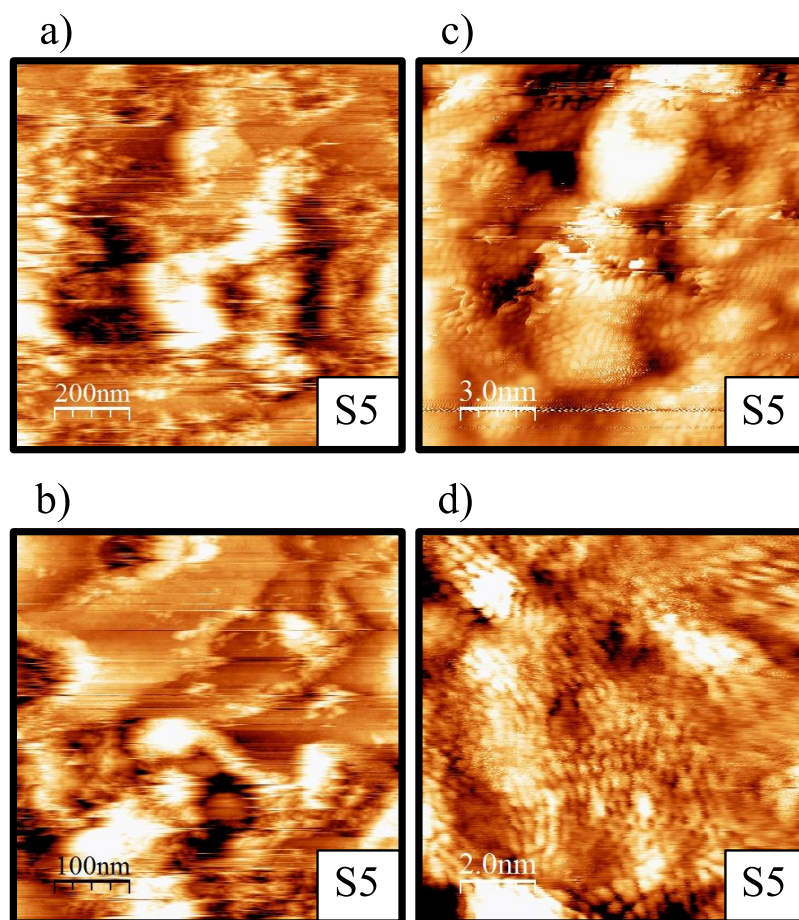


Figure 8.5: STM images of the 25/75 tungsten carbide thin films (S5). a,b) image size ($2000 \times 2000 \text{ nm}^2$). The large mobile islands are attributed to segregated graphite patches. c,d) Atomic resolution STM images, where the surface is covered by graphite.

In next step, oxidation of carbide thin films was studied by STM/STS measurements. Figure 8.6 illustrates the STM images of the S4 sample with 20% free carbon (40/60 W:C ratio), before and after oxidation. This sample was subjected to 1×10^{-7} mbar of O_2 for a total dose of $3.3 \times 10^{16} \text{ O}_2/\text{cm}^2$ at 573 K. At large scale ($2000 \times 2000 \text{ nm}^2$), the surfaces before and after oxidation are similar. At higher magnification, the oxidized image shows a higher density of circular bright spot, which are probably the oxide nuclei, while the overall morphology is comparable to the surface before oxidation (Figure 8.6c,d). The main contrast between the oxidized and pre-oxidation surfaces is noticeable at higher magnification close to or at atomic resolution. Similar to S3 sample

(both S3 and S4 are 40/60 carbide thin films), the majority of S4 surface illustrates graphite/graphene atomic resolution with small areas displaying stripe pattern. However, this morphology is modified after the oxidation, where only part of the surface is covered with graphite/graphene, and the rest of the surface shows a flat and featureless region (bottom-left section of Figure 8.6f). These newly formed featureless regions were observed in different part of surface and always show a lower LDOS in compare to graphite/graphene regions. This observation indicates that the oxygen etches away some of the graphite/graphene on the surface.

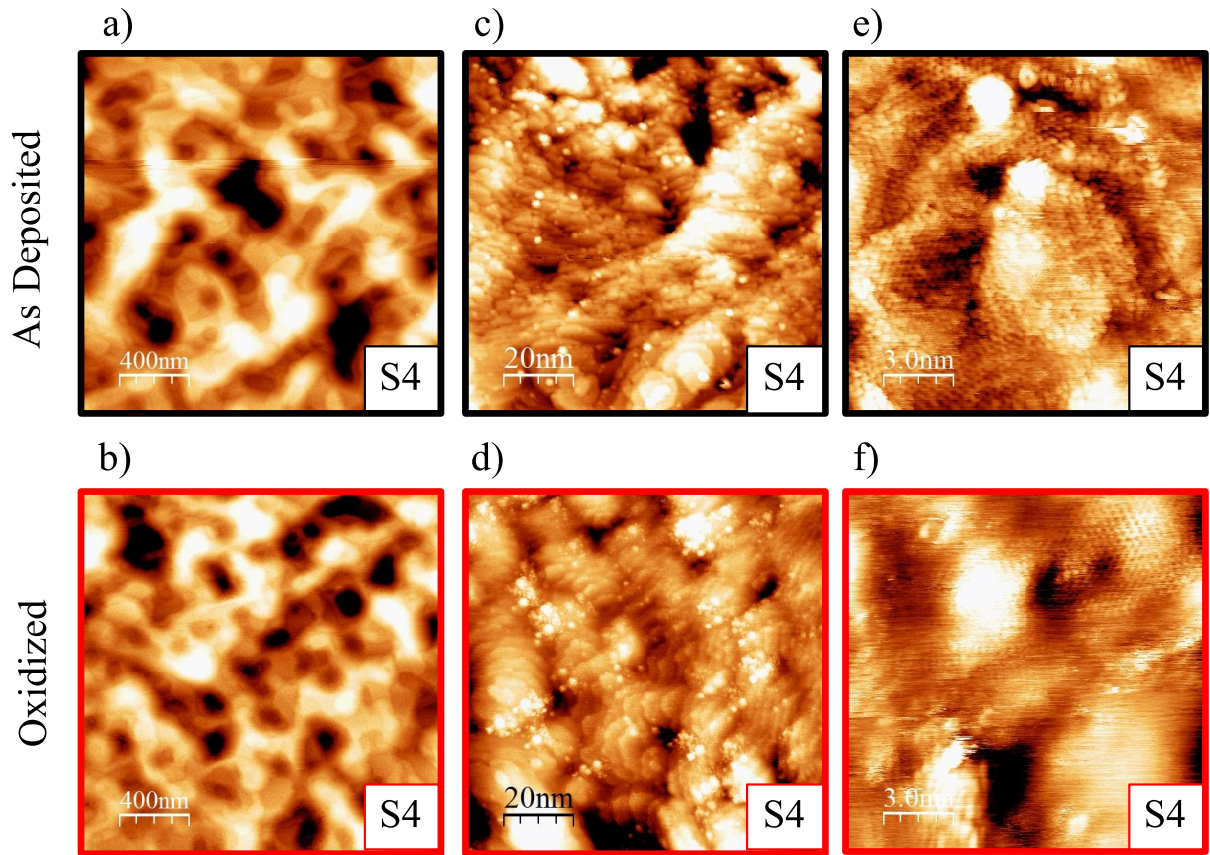


Figure 8.6: STM images from 40/60 tungsten carbide thin films. (a), (c), and (e) are STM images recorded before oxidation and (b), (d), and (f) are the STM images after oxidation. a,b) 2000×2000 nm² image size. c,d) 100×100 nm² STM images. e,f) High resolution STM images (15×15 nm²).

To verify the dissolution of graphite/graphene during oxidation, the data for oxidation at higher temperature for another 40/60 sample (S5) are presented in Figure 8.7. The pre-oxidized surface of this sample was similar to the ones shown for S3 and S4, which had the same tungsten to carbon ratio (Figure 8.3, 8.4, 8.6). This sample was subjected to 1×10^{-7} mbar of O_2 for a total dose of $4.95 \times 10^{16} O_2/cm^2$ at 873 K, 300 K higher than previous oxidation. After this oxidation step, the STM/STS data present no evidence of graphite/graphene regions.

The oxidized carbide thin film shows a large band gap over the entire surface with an average close to 2.2 eV. A few grains have a slightly larger band gap (2.8 eV), which is in a good agreement with the bandgap of WO_3 .¹⁵ The variation of the bandgaps in this surface indicates that the oxidation of WC does not fully progress to formation of WO_3 and several intermediate oxides ($WO_{2.9}$, $WO_{2.72}$, $WO_{2.5}$, and WO_2) or even mixed oxycarbides (WO_xC_y) form during the oxidation process (Figure 8.7d).^{22–25}

The spectra extracted from two surface regions (Figure 8.7b) have a much lower occupied LDOS (measured at negative bias voltage) than unoccupied LDOS (measured at positive bias voltage). Similar behavior has been reported for ST spectra measured on WO_3 surface.^{26,27} The spectra extracted from the ‘hatched’ region of the bandgap map exhibit high noise level and therefore, these spectra were not considered in calculation of bandgap histogram.

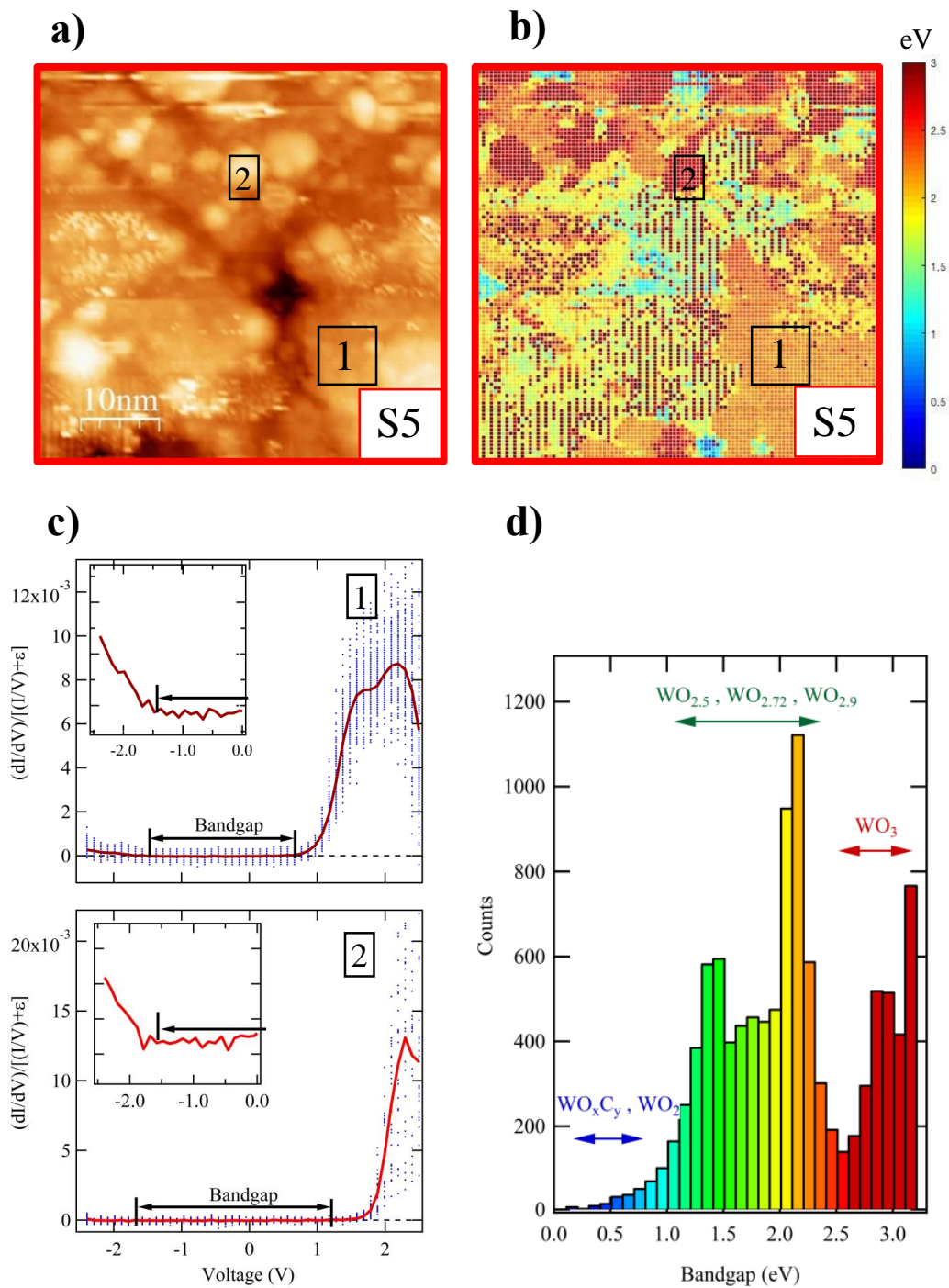


Figure 8.7: a) STM image of oxidized surface b) The corresponding bandgap of (a). c) Spectra extracted from regions marked by black rectangles in (a,b). The average spectrum is shown by the red line and all other spectra are displayed by blue dots. The inset is the average curve at (-2.5 – 0 V) energy range. d) The band gap histogram.

In next step, to determine the possibility of carburization of oxidized sample with free carbon embedded in thin films, S5 sample was annealed for 2 hours at 873 K in UHV. Annealing at UHV environment excludes any source of carbon other than those carbon atoms in thin film. STM/STS results illustrate that after this annealing step, the overall band gap of the surface decreases. In contrast to heavily oxidized surface (Figure 8.7) where the entire of surface was covered with tungsten oxide components, the annealed surface exhibit several grains with zero band gap. Figure 8.8 illustrates an example of a region where these new metallic grains were formed.

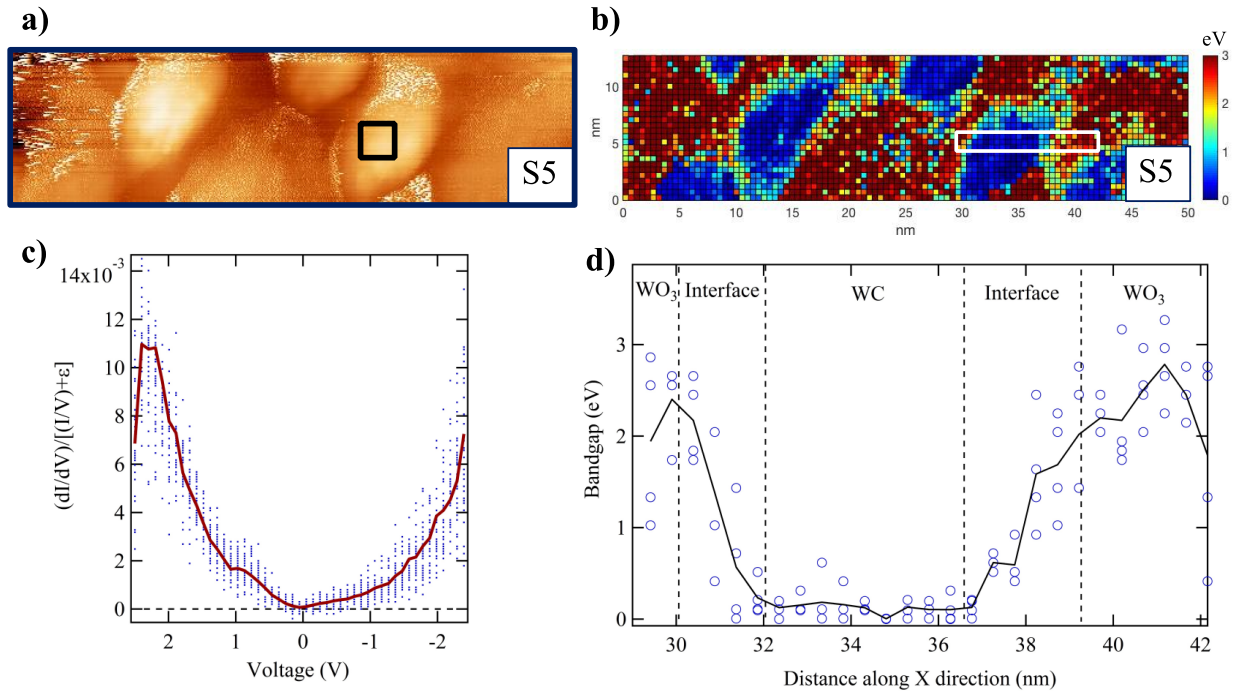


Figure 8.8: a) STM image of the S5 sample after UHV annealing of the oxidized surface. b) The corresponding bandgap of (a). c) Spectra extracted from region marked by black square in (a). All spectra are shown by blue dots and the average spectrum is shown by the red line. d) The band gap profile extracted from region marked by the white square in (c).

These results show that the annealing of the oxidized surface, give rise to diffusion of carbon atoms from lower layers and formation of new carbide nuclei. A gradual change in the

bandgap from oxide area to metallic grains is an indication of an interface regions between the WO_3 and newly formed WC (8.8 d). From the band gap values at interface, it can be concluded that the interface is consist of intermediate oxides and oxycarbides.

8.3.2. AP-XPS Results Discussions

In addition to STM/STS studies, four samples were synthesized for the study of oxidation/carburization of carbide thin films with AP-XPS. These samples were at ambient conditions for two weeks prior to AP-XPS measurements. These measurements were performed in MAX Lab synchrotron light source as described in chapter 3. These measurements allowed us to determine the chemical composition and electronic states of the thin films and investigate the effect of several oxidation/ carburization cycles on thin films.

In this section, a focus analysis of XPS spectra acquired from tungsten 4f (W4f) core levels with photon energy of 400 eV is presented. The information regarding to C1s and O1s spectra, and depth analysis with different photon energy are not included. However, for the purpose of publication which is in preparation, these data will be added to complete the analysis and adopt the model if necessary.

W4f core levels spectra. (30-41 eV)

Figure 8.9 shows the temperature and the time of the recorded XPS spectra for S9 sample. In this sample, the W:C atomic ratio is 25:75, therefore only 25% of the total carbon inventory is in WC and the rest are in form of graphite/graphene. In this experiment, several cycles of oxidation and carburization were performed. For all the oxidation cycles the partial pressure of oxygen was at 0.3 mbar, and the carburization process were performed in UHV environment.

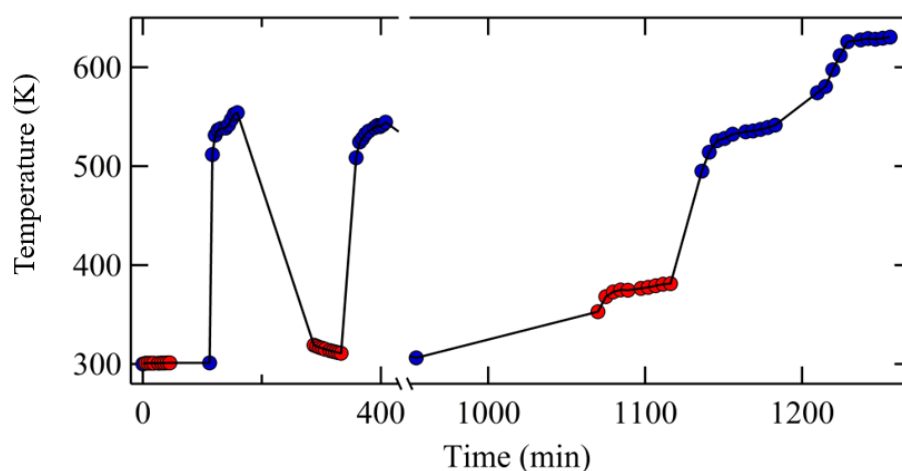


Figure 8.9: The processes performed on S9 sample. The blue/red circles indicate the time and temperature of recorded spectra during carburization/oxidation, respectively.

The spectra for the repeated oxidation/carburization cycles in sample S9 are summarized in Figure 8.10. This figure includes several spectra at specific point in the reaction cycles and their variation throughout the cycles is captured in a contour plot. The W4f spectra were normalized to unit area to facilitate comparison. These spectra show two main doublets, which can correlate to WC and WO₃ components. A significant intensity in oxide region of W4f core level in as introduced surface indicates that a portion of the surface of the thin film is oxidized due to exposure to the ambient environment during transfer.²⁸

The most prominent changes during the oxidation/carburization cycles are summarized as follows:

- i) The intensity of each spectrum in carbide region (31.5-34.6 eV) increases/decreases during the carburization/oxidation, respectively. In contrast, the intensity of each spectrum in oxide region of W4f core level (33.8-36.8 eV) increases/decreases during the oxidation/carburization, respectively.

- ii) In addition to the change in the intensity of the peaks, the width of XPS spectra in carbide region changes. This width become narrower during the oxidation and wider during carburization process.
- iii) The peaks in oxide region shift to lower binding energy during oxidation steps, and this shift is reversed within the carburization steps.

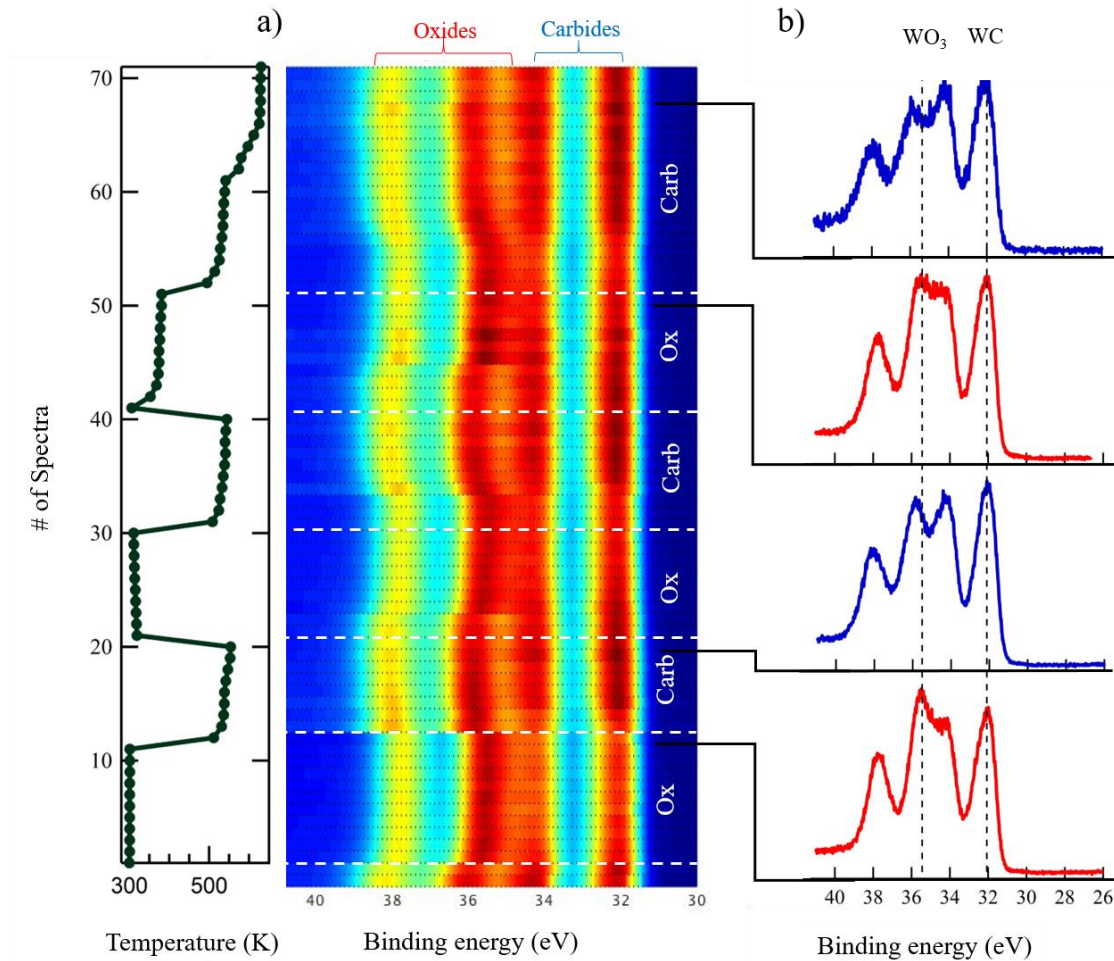


Figure 8.10: a) The intensity contour plot of the W4f spectra ($h\nu = 400$ eV) for S9 sample during oxidation/carburization cycles. b) Selected spectra from (a). The processing parameters (time and temperature) for this experiment are shown in Figure 8.9.

8.3.2.1. Fitting Procedure

To acquire a quantitative analysis about the changes in tungsten carbide and tungsten oxide components during the oxidation/ carburization cycles, a fitting procedure was performed. The binding energy was calibrated in respect to $\text{Au}4f_{7/2}$ peak at 84.0 eV. The backgrounds of the XPS data were corrected by Shirley method. The semiconducting and insulating components were fitted by a Lorentzian-Gaussian (L-G) mixed with L/G ratio of $30\% \pm 5$.²⁹ To describe the conductive components including WC and WC_{1-x} doublets, Doniac Sunjic (DS) function, i.e., a convolution of a Gaussian and a Lorentzian profile with an additional parameter to include asymmetry in curves, was used.^{30,31} The W_{4f} core levels were fitted by doublets with spin orbital splitting (ΔE) of 2.1 ± 0.1 eV. The relative intensity of the peaks used in the fitting procedure, in each doublet ($I_{\text{W}4f_{5/2}} / I_{\text{W}4f_{7/2}}$) was at 0.75. In addition to W_{4f} core levels, a small peak at higher binding energy was used to describe the $\text{W}5p$ core levels. The energy position and the intensity of $\text{W}5p$ peaks are as followings:

$$\text{Binding energies: } W_{4f_{7/2}} - W_{5p_{3/2}} = 5.8 \text{ eV}$$

$$\text{Relative intensity: } I_{\text{W}4f_{7/2}} / I_{\text{W}5p_{3/2}} = 0.08$$

Only the $\text{W}5p$ peak of WC component was included. The $\text{W}5p$ peak of WO_3 is out of the range of the measured spectra, and for the rest of components the intensity of this peak is very small and can be ignored. AP-XPS data were analyzed with KolXPD software. The fitting procedure is described in two parts. First, a simple fitting by only two doublets is discussed and in the second part, a more detailed fitting with considering all the possible components in carbide thin films is presented.

Fitting Considering Only WC and WO₃:

As shown in Figure 8.10, the W4f spectra acquired from the carbide thin films display two main doublets. The first doublet has a binding energy of ~32.2 eV which is the binding energy of WC, and the second doublet is positioned at binding energy of $\sim 35.5 \pm 0.2$ eV which is the binding energy of WO₃.^{24,28,32}

Therefore, in a first step only these two components were considered (WC and WO₃), and all the spectra were fitted with the doublets corresponding to these species. In addition, a small peak corresponding to W5p from WC was included. The results of this fitting procedure are summarized in Figure (8.11, 8.12, and 8.13) and the information regarding to these doublets are shown in Table 8.2.

Tungsten States	Binding energy	$I_{W4f_{5/2}} / I_{W4f_{7/2}}$	ΔE (eV)	Asymmetry (α)	fwhm (eV)
W ⁴⁺ in WC	32.2 ± 0.1	0.75	2.1 ± 0.1	0.02	1.2 ± 0.1
W ⁶⁺ in WO ₃	$35.75 \pm 0.2^*$	0.75	2.1 ± 0.1	-	1.8 ± 0.1

Table 8.2: XPS parameters used in fitting. (*) The BE energy of W⁶⁺ in WO₃ during the oxidation was always slightly lower and positioned at 35.55 ± 0.2 eV.

Several examples of the fitted curves in addition to the raw data are shown in Figure (8.11). The residual shown on bottom of each curve is calculated by subtracting the fitted curve from the raw data. These results show that it is possible to obtain a reasonable fit for W4f core levels spectra by using only two doublets. At the same time, the residual indicates that there are underestimations/overestimations at specific binding energy for all the spectra.

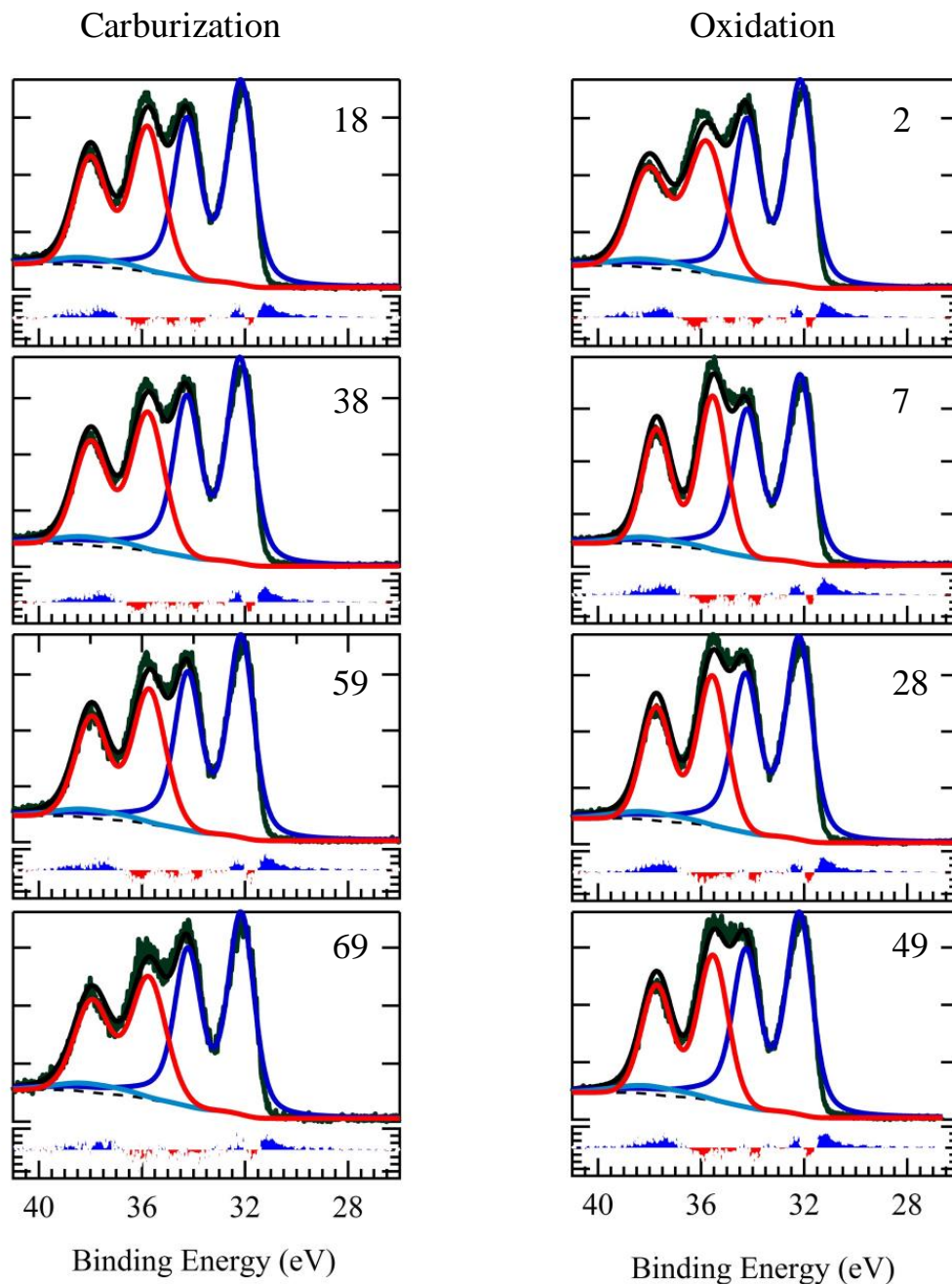


Figure 8.11: Several examples of the results for the fitting process. The spectra at the left-hand side were recorded during carburization and the ones at the right-hand side were measured during oxidation. The raw data (dark green), carbide doublet (dark blue), W5p peak from carbide doublet (light blue), oxide doublet (red), and the Shirley background is shown with the dashed line. The residuals are shown at the bottom of each graph where the blue color indicates an overestimation of the fitted results and the red color indicates an underestimation of the fitted curve. The numbers at the top of each graph specifies the number of XPS spectra recorded during experiment (same as Figure 8.8).

The Figure 8.12 shows the contour plot for the residuals, which were calculated after fitting all spectra measured at 26-42 eV binding energy (W4f core level). These results indicate that the fitted curves overestimate at 31.7, 32.3, 37.5, and 38.7 eV binding energies. Simultaneously, an underestimation of the fitted results at 31.9, 33.0, 35.0, and 36 eV are seen here. The analysis of the residuals clearly shows that WO₃ and WC are the main components in thin films, but the repetition of residuals at the specific binding energies mentioned above indicates that more components in fitting procedure need to be considered.

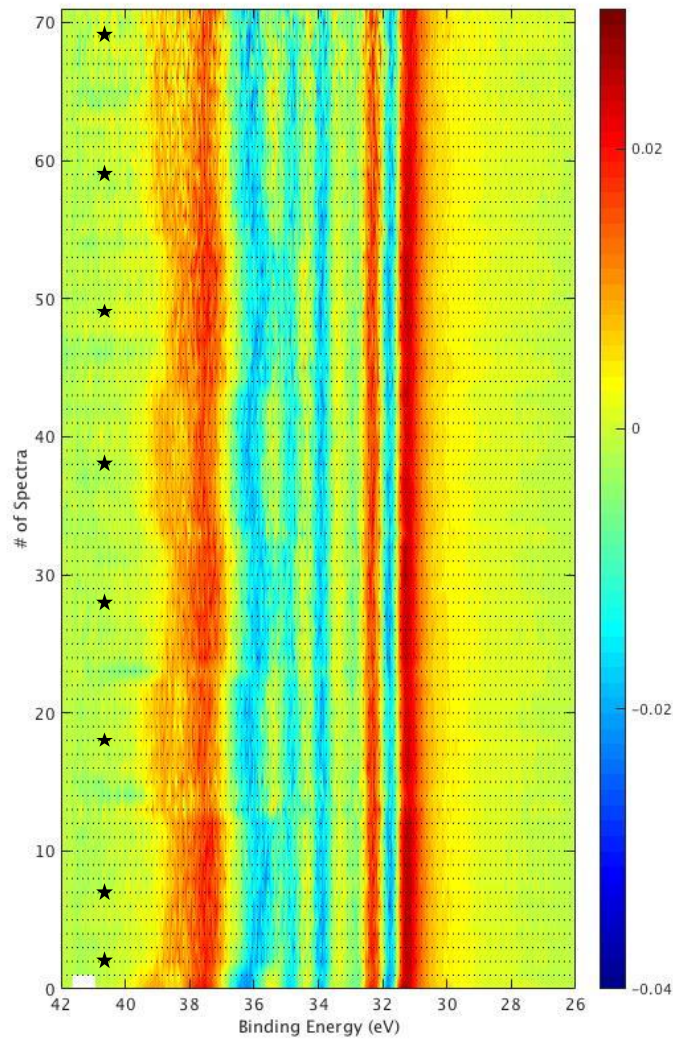


Figure 8.12: The calculated residuals after fitting. The star symbols indicate the spectra shown in Figure 8.11.

The limitation of fitting with only 2 chemically shifted components (4f core levels of WC and WO₃) and a single peak (5p core level of WC), can be illustrated by calculating the chemical changes during oxidation and carburization process.

To illustrate the changes in material chemistry, the variation of carbide concentration, which is calculated from the area of the carbide peak divided by the total area of spectrum, during oxidation and carburization process is shown in Figure 8.13. These results show after annealing at moderate temperature (510-630 K) in an UHV environment, at three different cycles, the WC concentration increases (carburization). However, the data obtained during oxidation process show a not well-defined trend in carbide concentration. This is in contrast with the results shown in Figure 8.10, where it is clear that the intensity of the spectra in the binding energy range that corresponds to tungsten carbide (31.5-34.6 eV) decreases during oxidation.

This observation highlights the limitation of fitting with only two doublets and the effect of the residuals on interpretation of the data. Therefore, to achieve an accurate picture of chemical changes during oxidation/ carburization, a more detailed fitting process with consideration of all possible chemical components in carbide thin films is discussed in next section.

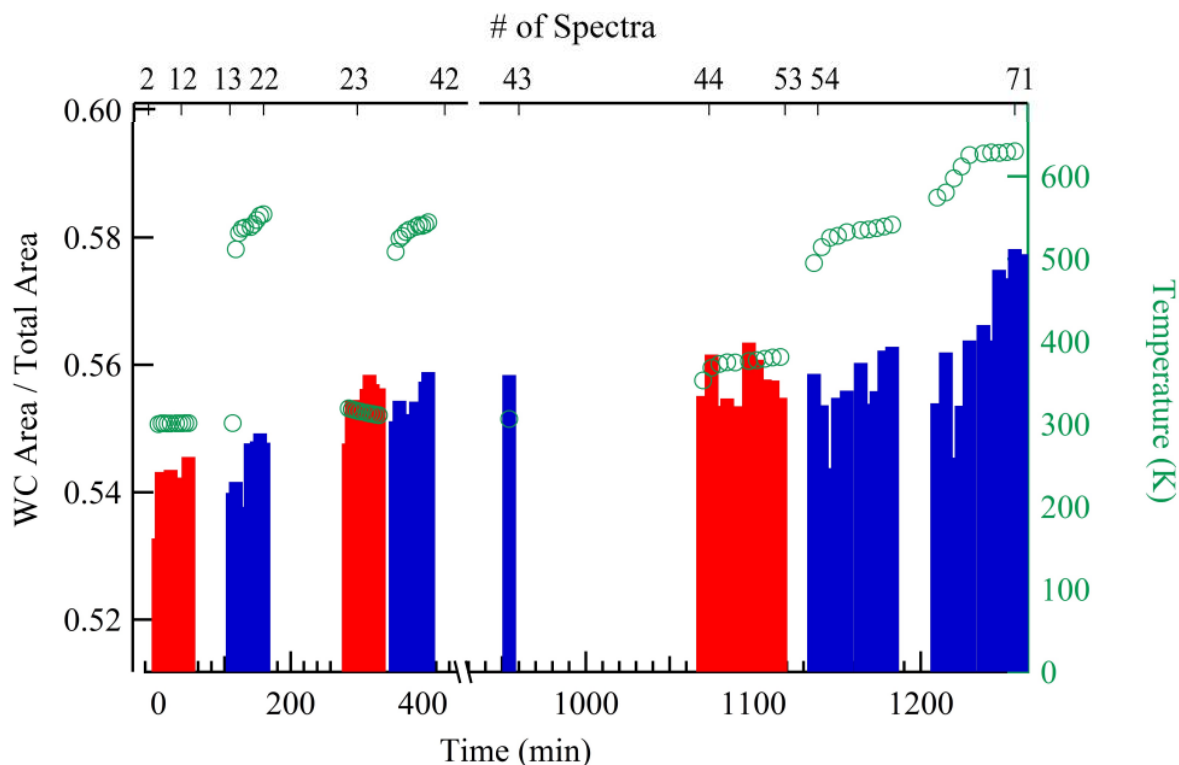


Figure 8.13: Evolution of the carbide component in XPS spectra for the S9 sample. These results obtained after fitting with two doublets. The red bars indicate the carbide concentration in presence of oxygen in the cell (oxidation). The blue bars show the carbide concentration during annealing in UHV (carburization). The green circles show the temperature when the spectra were measured.

Fitting Considering WC, WC_{1-x}, WO₂, W₂O₅, and WO₃

In this section, a fitting procedure with consideration of three additional components are discussed. To be able to compare this fitting with the fitting described in pervious section, the same spectra as the pervious section are fitted. At first, the reasons and justifications for addition of each new component in fitting procedure are discussed and afterwards, the chemical reactions in thin films by using the carbide area as a parameter to measure the carburization/ oxidation rate will be illustrated.

WC_{1-x}: As it was discussed, the width of the carbide doublets during oxidation/ carburization changes. This change, can be attributed to an additional peak with a binding energy

of 31.7 eV. This component is the metallic carbon deficient tungsten carbide (WC_{1-x}),³³ and to describe it in fitting process a DS curve was used.

W₂O₅: In all measured W4f level spectra, the ratio of intensity of each peak in oxide and carbide doublet is always different than the expected relative intensity of 0.75. For instance, these ratios for spectra shown in Figure 8.12 are summarized in following.

Sample	$I_{4f_{5/2}} / I_{4f_{7/2}}$ Carbide Doublet	$I_{4f_{5/2}} / I_{4f_{7/2}}$ Oxide Doublet
As received	0.85	0.65
Carburized	0.84	0.51

Table 8.3: Intensity of individual peaks in carbide and oxide doublet for two distinct spectra

For carbide doublet, the large intensity ratio arises from the overlap between $4f_{7/2}$ peak of W_2O_5 positioned at 34.6 eV with $4f_{5/2}$ peak of WC at 34.3 eV. Simultaneously, the small intensity ratio observed for the oxide doublet is caused by the overlap between the $4f_{5/2}$ peak of W_2O_5 at 36.8 eV and $4f_{7/2}$ of WO_3 35.75 eV. To describe the W_2O_5 in fitting procedure, a new L-G doublet was added.

WO₂: The last component that was added is WO_2 . The addition of this component can be justified from the difference spectra shown in Figure 8.14 (b). A shoulder which is appear at the left side of WC peak (33.2 eV), correlate well to the expected binding energy for WO_2 .³⁴

WO_xC_y: Tungsten oxycarbide (WO_xC_y) is another possible component that could be considered. This doublet is positioned somewhere between WC and WO_2 doublets.^{23,33} However, because it is not possible to identify the exact value of the x and y in oxycarbide formula, an exact

binding energy cannot be assigned to this component. Therefore, the peak that correlates to this component in XPS data was not involved in fitting.

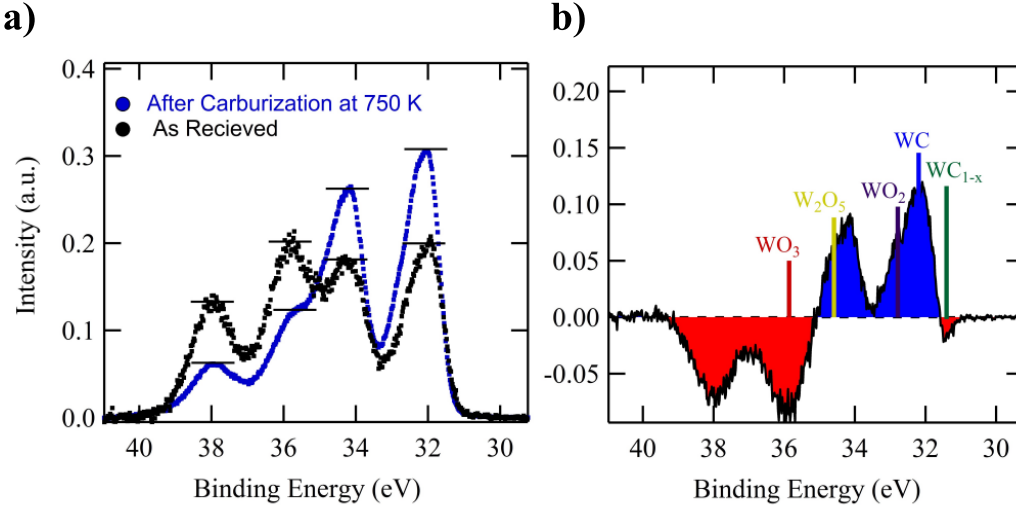


Figure 8.14: a) Two examples of XPS data from S10 sample. This sample has the same carbon to tungsten ratio as S9 (W:C 25:75). b) The difference between the spectra shown in (a).

In summary, the components that are considered in optimized fitting procedure are as followings: tungsten carbides (WC and WC_{1-x}) and tungsten oxides (WO_3 , W_2O_5 , and WO_2). The information regarding to XPS peaks of these components are listed in Table 8.4.

Tungsten States	BE (eV)	$I_{W_{4f_{7/2}}} / I_{W_{4f_{5/2}}}$	ΔE (eV)	Asymmetry (α)	fwhm (eV)
$W^{4(1-x)+}$ in WC_{1-x}	31.7	0.75	2.1 ± -0.1	0.02	0.7 ± 0.2
W^{4+} in WC	32.2	0.75	2.1 ± -0.1	0.03	1.2 ± 0.1
W^{4+} in WO_2	33.2 ± 0.2	0.75	2.1 ± -0.1	-	1.5 ± 0.1
W^{5+} in W_2O_5	34.6 ± 0.2	0.75	2.1 ± -0.1	-	1.5 ± 0.1
W^{6+} in WO_3	35.65 ± 0.1	0.75	2.1 ± -0.1	-	1.8 ± 0.1

Table 8.4: list of parameters used in fitting procedure.

For fitting purposes, the number of independent parameters for spin-orbit doublet (individual peaks in each doublet) can be reduced by keeping the full width at half maximum (fwhm), intensity ratio, and the doublet split distance constant.

Several examples of the fitted curves and the raw data are shown in Figure 8.15. The residuals at the bottom of each set is calculated by subtracting the fitted curve from the raw data. For comparison purpose, the y-axis of residual curves in this figure has the same maximum/minimum as the data shown in Figure 8.9. These curves show that the fitting procedure which considers all the components in tungsten carbide thin film, results to an excellent fit with almost zero residuals.

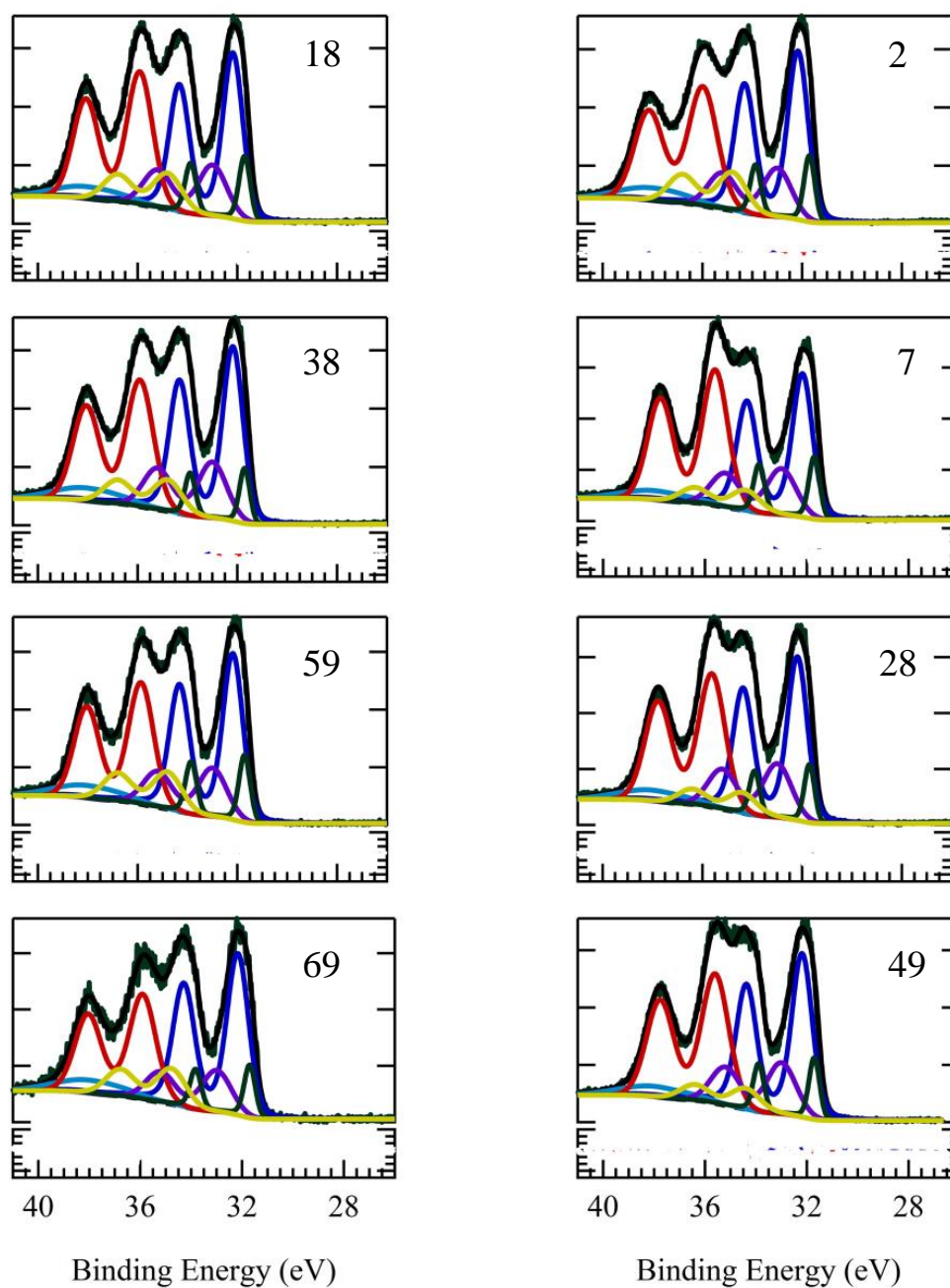


Figure 8.15: several examples of the results after the fitting process. The left-hand side spectra are recorded during carburization and the right-hand side spectra during oxidation. The raw data (dark green), carbide doublet (dark blue), W5p peak from carbide doublet (light blue), oxide doublet (red), and the Shirley background is shown with the dashed line. The residual for each curve is included at the bottom of each graph where the blue color indicates an overestimation of the fitted results and the red color indicates an underestimation of the fitted curve. The numbers at the top of each graph specifies the number of XPS spectra recorded during experiment (same as Figure 8.10).

The evolution of tungsten carbide components area ($WC+WC_{1-x}$) vs time is shown in Figure 8.16. For the first section of this graph ($t < 400$ minutes), in the course of oxidation the carbide concentration decreases, and carburization regenerates the carbide component to its initial concentration. In the second part of the graph ($t > 950$ minutes), the carbide concentration decreases during oxidation again, however, this time carburization at higher temperature not only results in carbide concentration to return to its initial value (after annealing at ~ 500 K for 30 min), the carbide concentration continues to increase even further.

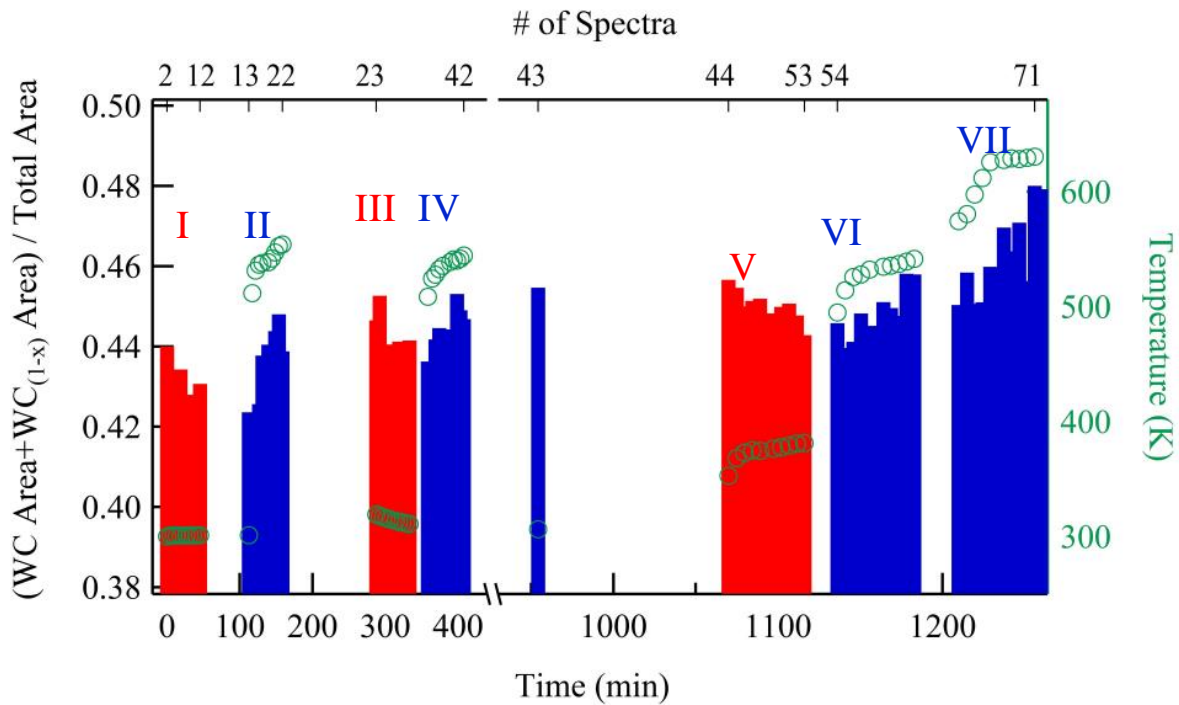


Figure 8.16: The red bars indicate the ratio of the carbide area in presence of oxygen in the cell. The blue bars show the ratio of carbide area during annealing at UHV (carburization). The oxidation/carburization cycles are labeled from I-VII.

To illustrate the relation between the annealing temperature and the carburization rates for each step (oxidation and carburization), the carbide concentration shown in Figure 8.15 were fitted

by lines and the slope of these lines were taken as carburization rate. The results of this fitting are shown in Figure 8.17.

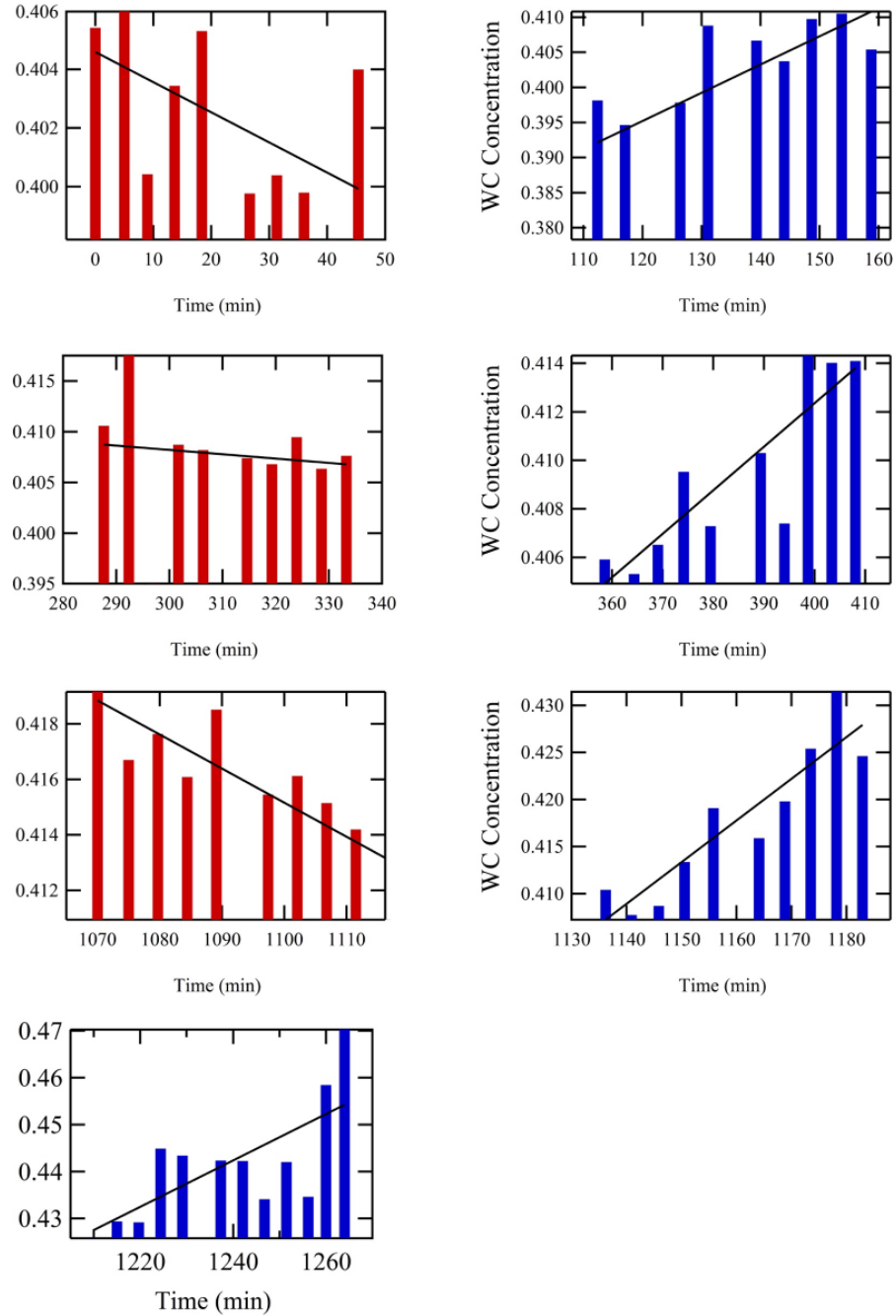


Figure 8.17: Several examples of linear fitting of the data shown in Figure 8.14. the vertical axis for all the graphs is area $(WC+WC_{I-x})/\text{total area}$.

Similar type of analysis was performed on the W4f level spectrum acquired on several samples (S7, S8, S10) with different W:C ratio, and the results of the measured carburization rates are shown in Figure 8.18. These results show that by increasing the annealing temperature the carburization rate is accelerated, which is caused by higher diffusion rate of carbon atoms. In addition, carburization process occurs faster in the samples with higher carbon concentration.

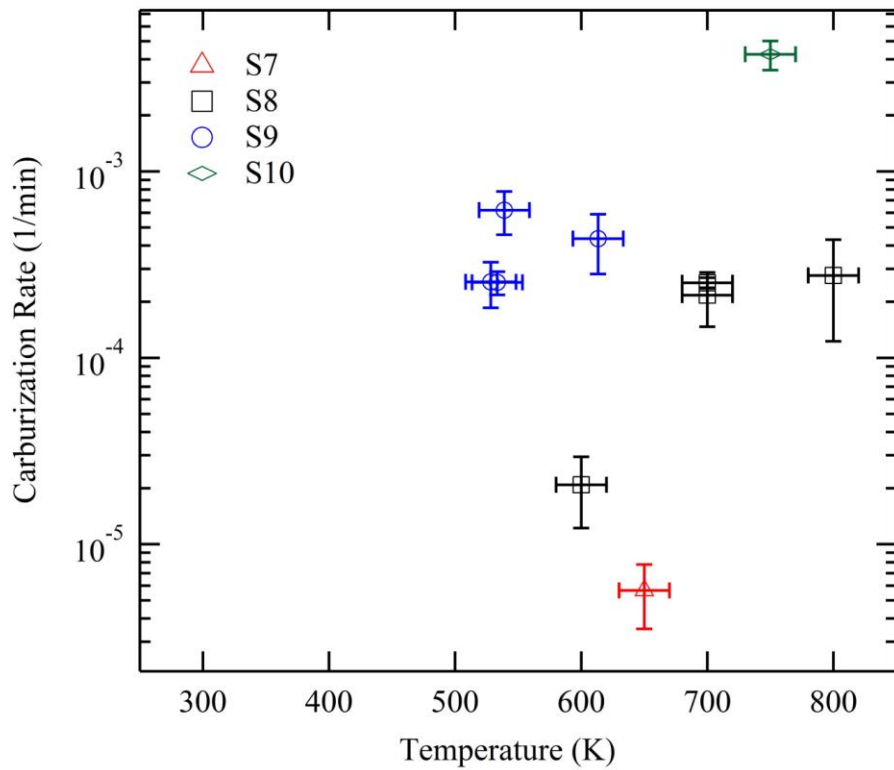
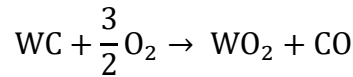
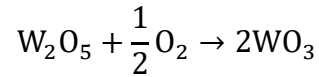


Figure 8.18: Calculated carburization rate from XPS data. Recall that the concentration of free carbon in both S9 and S10 is 50%, S8 is 20%, and S7 is 0%.

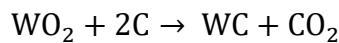
The concentration of the oxide components was also analyzed in this work. Figure 8.19 shows the concentration changes for the three types of tungsten oxide considered in fitting process. During oxidation cycles, the concentration of the WO₃ and WO₂ increases while the concentration of W₂O₅ decreases. For instance, at the first oxidation cycle the concentration of WO₃ increases

by ~2% and W_2O_5 Concentration decrease by the same amount. At the same cycle, the WO_2 concentration increases by about ~2.5%, and to the carbide concentration in this cycle decreases by about 2%. Similar observations for other oxidation cycles point to the following reactions as the pathway for oxidation of tungsten carbide films.



During the first three carburization process (II, IV, and VI) at 490-530 K, the concentration of WO_3 and WO_2 increases while the W_2O_5 concentration decreases. These results indicate that in carburization process, the two reactions that were occurring within oxidation cycle are reversed. The last step of carburization process (VII), which is performed at higher temperature (550-630 K) in comparison to pervious carburization steps, illustrates a different behavior in the change of concentration of oxide components. The W_2O_5 concentration in this step is decreasing which is an indication of another reduction reaction where W_2O_5 is transformed to WO_2 (W^{5+} to W^{4+}). The possible carburization reactions are summarized in followings:

At Temperature 480 – 540 K: $2WO_3 + C \rightarrow W_2O_5 + CO$



At Temperature above 540 K: $W_2O_5 + C \rightarrow 2WO_2 + CO$

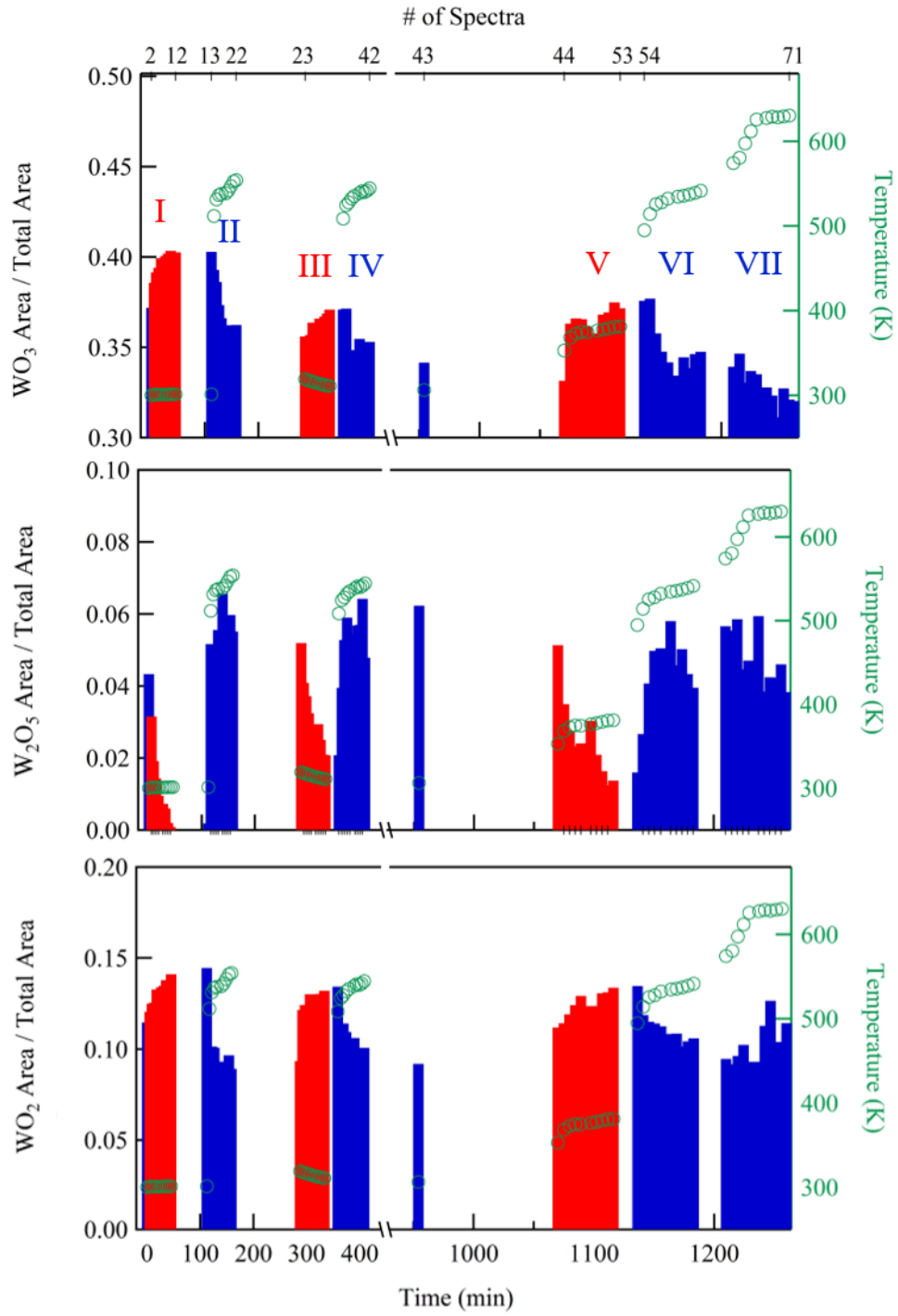


Figure 8.19: The red bars indicate the ratio of the several oxide components in presence of oxygen in the cell. The blue bars show the ratio of those oxide components during annealing at UHV (carburization). The oxidation/carburization cycles are labeled from I-VII.

8.5. Conclusions

STM results showed a distinct difference between the morphology of carbide thin films with W:C ratio of 50:50 and carbon rich carbide thin films with W:C ratio of 40:60 and 25:75. A major portion of the surface area of carbon rich tungsten carbide thin films was covered by graphene and graphite flakes. STM/STS results show that the oxidation at temperature above 573 K result in etching of graphite and graphene and formation of tungsten oxide. These results indicated that during oxidation, several intermediate oxide components will form. An example of self-carburization of a carbon rich thin film was demonstrated by annealing of a fully oxidized 40/60 sample at 873 K in UHV environment. This annealing gave rise in formation of carbide grains in a fully oxidized surface. An interface between the carbide and oxide regions with several nm thicknesses was observed.

AP-XPS results showed that a portion of carbide thin films were oxidized by exposure to ambient environment (during transfer from our lab to MAX Lab synchrotron). In the analysis of AP-XPS data, it was shown that fitting without considering intermediate oxide components does not capture the chemical changes correctly. Repeated oxidation and carburization cycles showed that it is possible to reverse the oxidation processes at room temperature, by annealing of the surface at moderate temperature (~530 K) for the same period of time as oxidation cycle. Also, annealing at temperature above 550 K gave rise to carbide concentration higher than its initial values. All the results together, indicate that the diffusion of free carbon from lower layers is a viable pathway to increase the life time of a catalytic surface of tungsten carbide.

Author Contributions

The majority of the STM/STS experiments were performed J.B. McClimon and the analysis of the results was completed by E.Monazami . The AP-XPS results were collected by E. Monazami and Prof. P. Reinke in collaboration with Prof, J.Schnadt.

8.6. Future work

In this work, the chemical reaction in carbon rich carbide thin films during oxidation and carburization were investigated by STM/STS and AP-XPS. In the analysis of AP-XPS data only the W4f were considered, however, to be able to create a complete model for oxidation and carburization more information is required. The next steps in this work are to analyze the C1s, O1s, and valence band spectra acquired by AP-XPS experiments, which will provide more information about chemical reactions. Also, depth profile concentration and assessment of the thickness of the oxide layers will help in a better understanding of these reactions.

8.7. References

- (1) Krzanowski, J. E.; Endrino, J. L. The Effects of Substrate Bias on Phase Stability and Properties of Sputter-Deposited Tungsten Carbide. *Mater. Lett.* **2004**, 58 (27–28), 3437–3440.
- (2) Tavsanoğlu, T.; Begum, C.; Alkan, M.; Yucel, O. Deposition and Characterization of Tungsten Carbide Thin Films by DC Magnetron Sputtering for Wear-Resistant Applications. *JOM* **2013**, 65 (4), 562–566.
- (3) Beadle, K. A.; Gupta, R.; Mathew, A.; Chen, J. G.; Willis, B. G. Chemical Vapor Deposition of Phase-Rich WC Thin Films on Silicon and Carbon Substrates. *Thin Solid Films* **2008**, 516 (12), 3847–3854.
- (4) Levy, R. B.; Boudart, M. Platinum-Like Behavior of Tungsten Carbide in Surface Catalysis. *Science* **1973**, 181 (4099), 547–549.
- (5) Kojima, I.; Miyazaki, E.; Inoue, Y.; Yasumori, I. Catalysis by Transition Metal Carbides. VI. Hydrogenation of Carbon Monoxide over WC, W₂C, and W Powder Catalysts. *Bull. Chem. Soc. Jpn.* **1985**, 58 (2), 611–617.
- (6) Delannoy, L.; Giraudon, J.-M.; Granger, P.; Leclercq, L.; Leclercq, G. Chloropentafluoroethane Hydrodechlorination over Tungsten Carbides: Influence of Surface Stoichiometry. *J. Catal.* **2002**, 206 (2), 358–362.
- (7) Ribeiro, F. H.; Dalla Betta, R. A.; Guskey, G. J.; Boudart, M. Preparation and Surface Composition of Tungsten Carbide Powders with High Specific Surface Area. *Chem. Mater.* **1991**, 3 (5), 805–812.
- (8) Palanker, V. S.; Gajyev, R. A.; Sokolsky, D. V. On Adsorption and Electro-Oxidation of Some Compounds on Tungsten Carbide; Their Effect on Hydrogen Electro-Oxidation. *Electrochimica Acta* **1977**, 22 (2), 133–136.
- (9) Hsu, I. J.; Kimmel, Y. C.; Dai, Y.; Chen, S.; Chen, J. G. Rotating Disk Electrode Measurements of Activity and Stability of Monolayer Pt on Tungsten Carbide Disks for Oxygen Reduction Reaction. *J. Power Sources* **2012**, 199, 46–52.
- (10) Harnisch, F.; Schröder, U.; Quaas, M.; Scholz, F. Electrocatalytic and Corrosion Behaviour of Tungsten Carbide in near-Neutral pH Electrolytes. *Appl. Catal. B Environ.* **2009**, 87 (1–2), 63–69.
- (11) A Combined Surface Science and Electrochemical Study of Tungsten Carbides as Anode Electrocatalysts - Springer.
- (12) Ribeiro, F. H.; Boudart, M.; Dalla Betta, R. A.; Iglesia, E. Catalytic Reactions of N-Alkanes on β -W₂C and WC: The Effect of Surface Oxygen on Reaction Pathways. *J. Catal.* **1991**, 130 (2), 498–513.
- (13) B. Rodella, C.; H. Barrett, D.; F. Moya, S.; A. Figueroa, S. J.; B. Pimenta, M. T.; S. Curvelo, A. A.; Silva, V. T. da. Physical and Chemical Studies of Tungsten Carbide Catalysts: Effects of Ni Promotion and Sulphonated Carbon. *RSC Adv.* **2015**, 5 (30), 23874–23885.
- (14) Ribeiro, F. H.; Dalla Betta, R. A.; Boudart, M.; Baumgartner, J.; Iglesia, E. Reactions of Neopentane, Methylcyclohexane, and 3,3-Dimethylpentane on Tungsten Carbides: The Effect of Surface Oxygen on Reaction Pathways. *J. Catal.* **1991**, 130 (1), 86–105.
- (15) McClimon, J. B.; Monazami, E.; Reinke, P. Interaction of C₆₀ with Tungsten: Modulation of Morphology and Electronic Structure on the Molecular Length Scale. *J. Phys. Chem. C* **2014**, 118 (42), 24479–24489.

- (16) Monazami, E.; McClimon, J. B.; Rondinelli, J.; Reinke, P. Electronic Structure and Band Gap of Fullerenes on Tungsten Surfaces: Transition from a Semiconductor to a Metal Triggered by Annealing. *ACS Appl. Mater. Interfaces* **2016**.
- (17) Palmquist, J.-P.; Czigány, Z.; Hultman, L.; Jansson, U. Epitaxial Growth of Tungsten Carbide Films Using C₆₀ as Carbon Precursor. *J. Cryst. Growth* **2003**, 259 (1–2), 12–17.
- (18) Palmquist, J.-P.; Czigany, Z.; Odén, M.; Neidhart, J.; Hultman, L.; Jansson, U. Magnetron Sputtered W–C Films with C₆₀ as Carbon Source. *Thin Solid Films* **2003**, 444 (1–2), 29–37.
- (19) Sun, Y.; Cui, H.; X. Jin, S.; X. Wang, C. Eutectic Solidification Applied to Nanofabrication: A Strategy to Prepare Large-Scale Tungsten Carbide Nanowalls. *J. Mater. Chem.* **2012**, 22 (32), 16566–16571.
- (20) Wong, H. S.; Durkan, C.; Chandrasekhar, N. Tailoring the Local Interaction between Graphene Layers in Graphite at the Atomic Scale and Above Using Scanning Tunneling Microscopy. *ACS Nano* **2009**, 3 (11), 3455–3462.
- (21) Tománek, D.; Louie, S. G. First-Principles Calculation of Highly Asymmetric Structure in Scanning-Tunneling-Microscopy Images of Graphite. *Phys. Rev. B* **1988**, 37 (14), 8327–8336.
- (22) Ribeiro, C. A.; Souza, W. R. de; Crespi, M. S.; Neto, J. A. G.; Fertonani, F. L. Non-Isothermal Kinetic of Oxidation of Tungsten Carbide. *J. Therm. Anal. Calorim.* **2007**, 90 (3), 801–805.
- (23) Brillo, J.; Kuhlbeck, H.; Freund, H.-J. Interaction of O₂ with WC(0001). *Surf. Sci.* **1998**, 409 (2), 199–206.
- (24) Calvillo, L.; Valero-Vidal, C.; Agnoli, S.; Sezen, H.; Rüdiger, C.; Kunze-Liebhäuser, J.; Granozzi, G. Combined Photoemission Spectroscopy and Electrochemical Study of a Mixture of (Oxy)carbides as Potential Innovative Supports and Electrocatalysts. *ACS Appl. Mater. Interfaces* **2016**, 8 (30), 19418–19427.
- (25) Wriedt, H. The O–W (Oxygen–Tungsten) System. *Bull. Alloy Phase Diagr.* **1989**, 10 (4), 368–384.
- (26) Jones, F. H.; Rawlings, K.; Foord, J. S.; Cox, P. A.; Egdell, R. G.; Pethica, J. B.; Wanklyn, B. M. R. Superstructures and Defect Structures Revealed by Atomic-Scale STM Imaging of WO₃ (001). *Phys. Rev. B* **1995**, 52 (20), R14392–R14395.
- (27) Dixon, R. A.; Williams, J. J.; Morris, D.; Rebane, J.; Jones, F. H.; Egdell, R. G.; Downes, S. W. Electronic States at Oxygen Deficient WO₃(001) Surfaces: A Study by Resonant Photoemission. *Surf. Sci.* **1998**, 399 (2–3), 199–211.
- (28) Warren, A.; Nylund, A.; Olefjord, I. Oxidation of Tungsten and Tungsten Carbide in Dry and Humid Atmospheres. *Int. J. Refract. Met. Hard Mater.* **1996**, 14 (5–6), 345–353.
- (29) Xie, F. Y.; Gong, L.; Liu, X.; Tao, Y. T.; Zhang, W. H.; Chen, S. H.; Meng, H.; Chen, J. XPS Studies on Surface Reduction of Tungsten Oxide Nanowire Film by Ar⁺ Bombardment. *J. Electron Spectrosc. Relat. Phenom.* **2012**, 185 (3–4), 112–118.
- (30) Ronning, C.; Feldermann, H.; Merk, R.; Hofsäuss, H.; Reinke, P.; Thiele, J.-U. Carbon Nitride Deposited Using Energetic Species: A Review on XPS Studies. *Phys. Rev. B* **1998**, 58 (4), 2207–2215.
- (31) Doniach, S.; Sunjic, M. Many-Electron Singularity in X-Ray Photoemission and X-Ray Line Spectra from Metals. *J. Phys. C Solid State Phys.* **1970**, 3 (2), 285–285.
- (32) Cappelli, E.; Bellucci, A.; Orlando, S.; Trucchi, D. M.; Mezzi, A.; Valentini, V. PLD Deposition of Tungsten Carbide Contact for Diamond Photodiodes. Influence of Process Conditions on Electronic and Chemical Aspects. *Appl. Surf. Sci.* **2013**, 278, 111–116.

- (33) Krasovskii, P. V.; Malinovskaya, O. S.; Samokhin, A. V.; Blagoveshchenskiy, Y. V.; Kazakov, V. A.; Ashmarin, A. A. XPS Study of Surface Chemistry of Tungsten Carbides Nanopowders Produced through DC Thermal Plasma/Hydrogen Annealing Process. *Appl. Surf. Sci.* **2015**, 339, 46–54.
- (34) Katrib, A.; Hemming, F.; Wehrer, P.; Hilaire, L.; Maire, G. The Multi-Surface Structure and Catalytic Properties of Partially Reduced WO_3 , WO_2 and $\text{WC} + \text{O}_2$ or $\text{W} + \text{O}_2$ as Characterized by XPS. *Proc. Sixth Int. Conf. Electron Spectrosc.* **1995**, 76, 195–200.